Semiconductors, Vol. 35, No. 5, 2001, pp. 491–498. Translated from Fizika i Tekhnika Poluprovodnikov, Vol. 35, No. 5, 2001, pp. 513–520.

ATOMIC STRUCTURE AND NONELECTRONIC PROPERTIES OF SEMICONDUCTORS

Oscillatory "Reactions" Involving the Oxygen and Carbon Background Impurities in Silicon Undergoing Heat Treatment

V. V. Lukjanitsa

Physics Department, Minsk State Medical Institute, Minsk, 220116 Belarus

Submitted September 19, 2000; accepted for publication September 25, 2000

Abstract—The effect of the heat treatment (for 1 h at 750–1100°C) of silicon on the transport of the oxygen and carbon impurities between the impurity–defect clusters, which are present in dislocation-free *n*-Si crystals, and the crystal matrix was studied. The observed nonmonotonic variations of oxygen and carbon concentrations in the above clusters are interpreted as resulting from oscillatory "reactions" that proceed during accommodation of these clusters when the crystal temperature varies (increases). The temperature limits of such oscillatory "reactions" are estimated. © *2001 MAIK "Nauka/Interperiodica".*

1. INTRODUCTION

A better understanding of defect formation in actual silicon crystals comes from studying the origin and properties of complex structural imperfections of the type of defect clusters [1–6]. These imperfections include impurity–defect clusters, which are formed in dislocation-free silicon during its growth and are not detected using selective etching [4]. It is believed [4, 7] that these clusters are inclusions of the second phase in the form of cores which are surrounded by elastic fields and an impurity atmosphere; the latter consists largely of oxygen and carbon atoms. The equilibrium between the impurity–defect clusters and the crystal matrix can be disturbed if the crystal temperature is varied significantly; this disturbance can be eliminated by the subsequent accommodation of the above clusters. Mechanisms for the accommodation of the impurity–defect clusters are different at low and high temperatures. If the temperature is lowered, the accommodation of these clusters occurs (as in the case of the compensation of a crystal by irradiation [8]) owing to electric interaction (recharging of defects, screening, changes in the space-charge region, etc.). At elevated crystal temperatures, the impurity–defect clusters can be accommodated as a result not only of electric interaction but also of the matter transfer between a cluster and the crystal matrix.

In this context, the objective of this study is to gain insight into the transport of matter between an impurity–defect cluster and the crystal matrix in relation to the heat treatment temperature.

With allowance made for the fact that irradiation of dislocation-free *n*-Si crystals leads to the accumulation of oxygen- (the *A* centers) and carbon-containing (the complexes of interstitial carbon atoms and substitutional carbon atoms, C_i–C_s) radiation defects located largely within impurity–defect clusters [4, 6], the production rates (η) obtained for these radiation defects were used to estimate the variation in the content of the oxygen and carbon impurities in an impurity–defect cluster during a heat treatment.

2. EXPERIMENTAL

2.1. Crystals and Samples

For the main experiments, we used silicon samples that had a surface area of 12×2.5 mm^2 and a thickness of 2 mm and were cut from the central part of an ingot. The ingot was a dislocation-free *n*-Si single crystal with a diameter of 55 mm and resistivity of $\rho = 100$ Ω cm; the ingot was grown at a rate of $V = 3$ mm/min by the floating-zone method in an argon atmosphere (the float-zone *n*-Si). The concentrations of the oxygen and carbon background impurities were determined from the infrared absorption spectra for the 5-mm-thick wafers and were found to be equal to $N_O = 3 \times 10^{16}$ cm^{-3} and $N_C = 2 \times 10^{16}$ cm^{-3}, respectively. We used metallography to assess the degree of structural perfection of the samples after selective etching of the surface.

In preliminary experiments performed to test the technique employed, we also used silicon crystals obtained using different technologies. These crystals included those of *n*-Si grown by the floating-zone (z) method in vacuum (v) and contained dislocations (d) with a low density of $N_d = 2 \times 10^4$ cm^{-2} [the *n*-Si(z, v, d) material]; the dislocation-free (df) *n*-Si crystals grown by the floating-zone method in an argon atmosphere (a) [the *n*-Si(z, a, df) material]; *n*-Si crystals obtained from the *n*-Si(z, a, df) material by neutron-transmutation doping [the neutron-transmutation-doped (NTD) *n*-Si material]; and the dislocation-free *n*-Si crucible-grown by the Czochralski (Cz) method in the argon atmosphere [the *n*-Si(Cz, a, df) material].

1063-7826/01/3505-0491$21.00

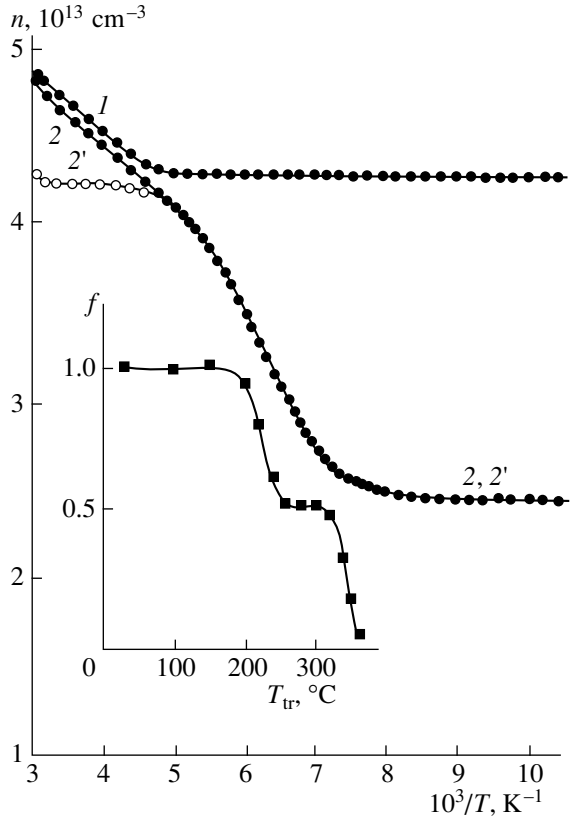

Fig. 1. Temperature dependences of the charge-carrier concentration in the (*1*) as-grown and (*2*) irradiated ($\Phi = 2.7 \times 10^{16}$ cm^{-2}) silicon samples. Curve *2*' represents the result of processing curve *2*. Dependence of the fraction *f* of unannealed defects with the levels at $E_c - (\sim 0.17$ eV) on the temperature of isochronous ($t = 15$ min) heat treatment is shown in the inset.

2.2. Thermal Treatment and Irradiation of the Samples

Isochronous (for a time of $t = 1$ h) thermal treatment of the samples was performed in air and in the temperature range $T_{tr} = 750$–1100°C (with an increment of 50°C) with subsequent rapid cooling (~100 K/s). A surface layer with a thickness of 100 μm was removed after the thermal treatment.

The thermally treated and as-grown (reference) samples were irradiated with ^{60}Co gamma-ray quanta with an intensity of 350 R/s at a temperature of $T_{irr} = 40$°C.

2.3. Measurements and Mathematical Processing of the Results

Experimental data on the formation rate (η) of radiation defects were obtained from the results of measurements and mathematical processing of the temperature (77–400 K) dependences of the Hall coefficient and electrical conductivity of the samples before and after irradiation. When measuring the temperature dependences of the Hall coefficient, special attention was given to the symmetry and quality of the nickel contacts deposited electrolytically onto the sample; the nonrectifying behavior of these contacts was assessed from the current–voltage characteristics measured preliminarily in the above temperature range using a characteriograph. In order to exclude the possible effect of electrical interferences and transient processes in the crystals studied, we measured the temperature dependences of the Hall coefficient in a massive dark screened box with low-rate cooling and heating (the sample was monitored for 1.5 h while being warmed to room temperature after having been kept at the liquid-nitrogen temperature for 5 minutes). The temperature dependences of the charge-carrier concentration $n = f(T)$ were calculated from the Hall coefficient temperature dependences with allowance made for the temperature dependence of the Hall factor [9].

The desired values $\eta = N/\Phi$ were determined using the linear portions of dependences of the defect concentration N on the irradiation flux Φ; the values of η were averaged over the results obtained for three samples.

We took into account that the C_i–C_s complexes and the *A* centers in *n*-Si have almost the same energy levels, equal to about $E_c - 0.16$ eV and $E_c - 0.18$ eV, respectively [10]. In order to determine the concentrations of these radiation defects separately, we developed a special computer program for minimization, in which the $n = f(T)$ dependence was analyzed on the basis of the electroneutrality equation in terms of a two-level model. In this program, the Marquardt, Powell, Newton–Raphson, steepest descent, and sliding descent (flexiplex) methods [11, 12] were employed; the search for the minimization direction was performed using the golden-section method [13]. The program made it possible to determine five parameters: the difference between the concentrations of the shallow-level donors and acceptors ($N_D - N_A$), the positions of two closely spaced energy levels E_1 and E_2, and their concentrations N_1 and N_2. According to [14], applying the above method to the analysis of the dependences $n(T)$ that include the portions corresponding to complete occupation and (or) complete depletion of the defect levels makes it possible to uniquely determine the defect parameters. Therefore, the samples to be studied were irradiated with low integrated fluxes so that the dependences $n(T)$ included the portions corresponding to both complete occupation and complete depletion (Fig. 1, curve *2*'). Each such dependence $n(T)$ involved 73 experimental points, which ensured a satisfactory statistical reliability of the sampling used.

Mathematical processing of $n = f(T)$ comprised two stages. In the first stage, the curves $n = f(T)$ for irradiated samples were "cleared." To this end, we first analyzed the dependences $n = f(T)$ for unirradiated and/or annealed samples (Fig. 1, curve *1*) and determined the parameters (energy levels and concentrations) of exist-

ing electrically active defects whose contribution to the temperature variation of n was then subtracted from $n = f(T)$ in irradiated samples (Fig. 1, curve *2*). The latter procedure is justified because there is no interaction between the quenched-in and radiation defects [15]. The dependence $n = f(T)$ (Fig. 1, curve *2'*) thus obtained represents the effect of radiation defects alone on the temperature dependence of n and is analyzed in the second stage. This stage begins with the separation of both temperature ranges of recharging and contributions (concentrations) of radiation defects with deep [E_c – (≥0.30 eV)] and relatively shallow [E_c – (~0.17 eV)] levels and is completed when the relation between the concentrations of C_i–C_s complexes and the A centers is determined.

2.4. Testing

Test runs of the program for minimization for the model curves $n = f(T)$ calculated for two types of defects with closely spaced energy levels yielded good results for all the methods used. In processing the actual curves, the Marquardt and Powell methods were found to be the most robust (convergent); both of these methods yielded almost the same values for the parameters of radiation defects (the C_i–C_s complexes and the A centers). At the same time, the Marquardt method was found to be the least sensitive to the choice of initial parameters. Therefore, it is this method in combination with the method of least squares [16] that was used primarily in the analysis of $n = f(T)$; other methods were used for checks.

In addition, the differential method [17] and the data on the isochronous annealing of radiation defects with the levels at E_c – (~0.17 eV) were also used for sampling. In accordance with the differential method, the bell-shaped curve $\varphi_H = f(F)$, where F is the Fermi level, obtained by differentiating the dependence $n = f(T)$ was analyzed. As shown previously [17], recharging of a single type of defect occurs if the half-width of the curve $\varphi_H = f(F)$ at half maximum is equal to $3.5kT$. If there are two or more defects with closely spaced energy levels, the half-width of the curve $\varphi_H = f(F)$ exceeds $3.5kT$. In this case, the curve $\varphi_H = f(F)$ was analyzed using the method of least squares in order to determine the fractional concentrations and energy levels of these defects. As for the concentration of the recharging defects of a single type, it is equal to the quadrupled height of the curve $\varphi_H = f(F)$ [17].

The table lists the results of studying the accumulation of radiation defects with the levels at E_c – (~0.17 eV) in gamma-ray irradiated n-Si crystals obtained using different technologies (the crystals having different concentrations of oxygen N_O and densities of grown-in dislocations N_d).

It can be seen that an attempt to separate the defects formed in n-Si(z, v, d) into two types yields the same positions of the energy levels E_1 and E_2: $E_1 \approx E_2 = E_c$ – 0.163 eV. According to [10], this level is inherent in the C_i–C_s complexes whose total concentration $N_{C_i-C_s}$ is equal in this case to the sum of concentrations N_1 and N_2 given in the table ($N_{C_i-C_s} = N_1 + N_2$). A similar situation ($E_1 \approx E_2$) takes place for n-Si(z, a, df), with the only (but essential) difference that, in this material, another energy level at E_c – 0.185 eV, which belongs to the A centers [10], is observed; here, we also have $N_A = N_1 + N_2$. In the case of irradiated n-Si(z, a, df) crystals and the NTD n-Si based on them, both of the radiation-defect types (the C_i–C_s complexes and the A centers) are observed and are reliably resolved with respect to both the energy position of the levels ($E_1 = E_c$ – 0.163 eV and $E_2 = E_c$ – 0.185 eV) and the concentra-

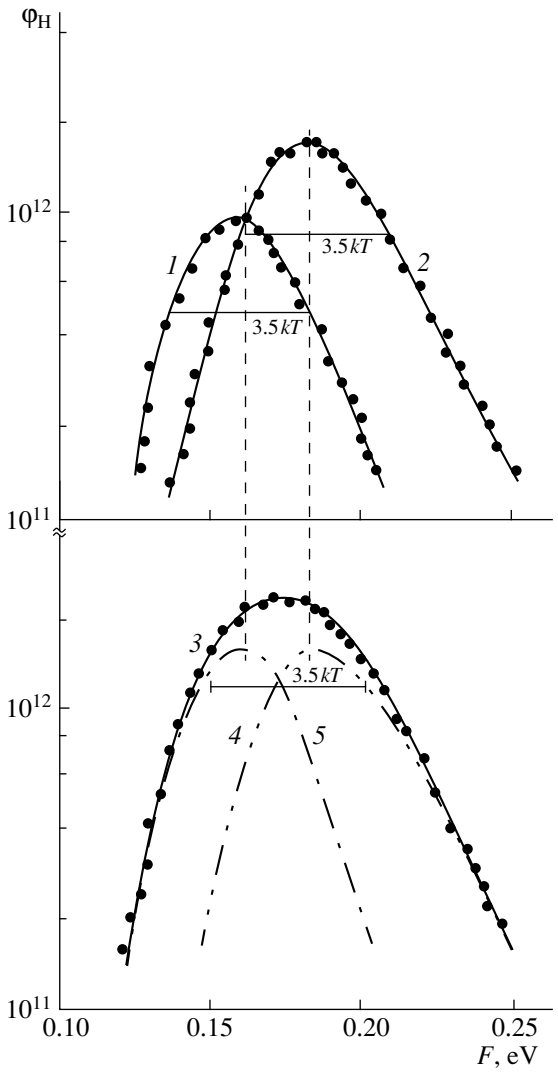

Fig. 2. Dependences of function φ_H on the Fermi level energy F for irradiated (*1*) n-Si(z, v, d) and (*2*) n-Si(Cz, a, df) crystals and for a (*3*) NTD n-Si. Curves *4* and *5* represent the components of curve *3*. The integrated fluxes Φ were (*1*) 9×10^{15}, (*2*) 1.14×10^{16}, and (*3*) 2.24×10^{16} cm^{-2}.

tions N_1 and N_2. Furthermore, as can be seen from the table, the concentrations N_1 and N_2 are almost the same ($N_1 \approx N_2$) in the NTD *n*-Si.

The differential method also yields the same result. The $\varphi_H = f(F)$ curves for *n*-Si(z, a, df) and NTD *n*-Si have half-widths larger than $3.5kT$ (Fig. 2, curve *3*), which is indicative of the recharging of two defect levels closely spaced in energy; these levels contribute identically to the $\varphi_H(F)$ curves (Fig. 2, curves *4*, *5*) and are separately observed (for each of them the half-width of the $\varphi_H(F)$ curve is equal to $3.5kT$) in the float-zone *n*-Si(z, v, d) (the C_i–C_s complexes (see Fig. 2, curve *1*) and the crucible-grown *n*-Si(Cz, a, df) (the *A* centers, see Fig. 2, curve *2*).

The reliability of the results obtained is supported by independent data on the annealing of radiation defects with the levels at E_c – (~0.17 eV) in the NTD *n*-Si (see the inset in Fig. 1). Two stages of annealing of these radiation defects are observed and are related to the annealing of the C_i–C_s complexes (T_{tr} = 180–260°C) and the *A* centers (T_{tr} = 300–360°C) [18]. As can be seen, the fractional concentrations of these defects are the same (amounting to about 50%), which agrees closely with the approximate equality $N_1 \approx N_2$; the latter equality was obtained from an analysis of $n = f(T)$ curves for the NTD *n*-Si using the Marquardt method (see table) and the differential method (Fig. 2, curves *4*, *5*).

In other words, the test of the method applied to various silicon crystals demonstrated the reliability of this method and of the results obtained for the separate determination of the concentration of radiation defects with closely spaced energy levels.

In addition, the above makes it possible to estimate the relation between the formation rates of the C_i–C_s complexes and the *A* centers in irradiated *n*-Si obtained by different methods. We believe that these data are of interest in their own right; therefore, these data are listed in the three rightmost columns of the table. As can be seen, the ratio between the introduction rates of the C_i–C_s complexes and the *A* centers $\eta_{C_i-C_s}/\eta_A$ may vary from a very large value [in *n*-Si(z, v, d), where $\eta_A \longrightarrow 0$], to virtually zero [in *n*-Si(Cz, a, df), where $\eta_{C_i-C_s} \longrightarrow 0$]. In *n*-Si(z, a, df) and NTD *n*-Si based on this material (see table, rows 2 and 3), the values of $\eta_{C_i-C_s}$ and η_A are comparable, and their ratio $\eta_{C_i-C_s}/\eta_A$ may be larger than unity and decreases as we pass from the starting to the NTD material; this is probably due to technological high-temperature treatment performed after the production of NTD Si.

We also note that, in the dislocation-free *n*-Si, grown by the floating-zone method and having the value $N_O \approx 5 \times 10^{15}$ cm^{-3}, η_A may be as high as 20% of $\eta_{C_i-C_s}$, whereas, sometimes, in the crucible-grown *n*-Si, C_i–C_s complexes are formed with a low rate, $\eta_{C_i-C_s} \leq 0.1\eta_A$, which is caused in our opinion by the different thermal history of the crystals.

3. RESULTS AND DISCUSSION

Figure 3 shows typical temperature dependences of the charge-carrier concentration in the as-grown, heat-treated, and irradiated crystals used in the main experiments. It follows from an analysis of these dependences that three groups of defects with levels at $E_1 = E_c - 0.16$ eV, $E_2 = E_c - 0.18$ eV, $E_3 = E_c - (\geq 0.40$ eV) are formed in all irradiated samples. Taking into account the results of annealing, we assign these defects to complexes consisting of interstitial carbon and substitutional carbon (C_i–C_s) (the level at $E_c - 0.16$ eV), to the *A* centers (the level at $E_c - 0.18$ eV), to the *E* centers (the level at $E_c - 0.42$ eV), to divacancies V_2 (the level at $E_c - 0.40$ eV), to carbon–oxygen divacancies COV_2 (the level at $E_c - 0.54$ eV), and, possibly, to other centers; the concentrations of divacancies are much lower than those of other defects.

Figure 4 shows the dependences of the production rates for the above defects on the temperature of the preliminary heat treatment of the crystals. As can be seen, η_A and $\eta_{C_i-C_s}$ are quantities of the same order of magnitude (albeit $\eta_A \leq \eta_{C_i-C_s}$), whereas the production rate for the defects with levels at $E_c - (\geq 0.40$ eV) $\eta_{0.40} \ll \eta_{C_i-C_s}$ and $\eta_{0.40} \ll \eta_A$ in almost the entire range of heat-treatment temperatures (except for T_{tr} =

Characteristics of *n*-Si crystals ($\rho \approx 100\ \Omega$ cm) and the parameters of defects produced in these crystals under irradiation

Material	N_O, cm^{-3}	N_C, cm^{-3}	N_d, cm^{-2}	Φ, cm^{-2}	E_c–E_1, eV	E_c–E_2, eV	N_1, cm^{-3}	N_2, cm^{-3}	$\eta_{C_i-C_s}$, cm^{-1}	η_A, cm^{-1}	$\eta_{C_i-C_s}/\eta_A$
n-Si(z, v, d)	$<10^{15}$	2.5×10^{16}	2×10^4	4.2×10^{16}	0.1631	0.1629	1.41×10^{13}	3.31×10^{12}	4.14×10^{-4}	~0	∞
n-Si(z, a, df)	3×10^{16}	2×10^{16}	~10	2.7×10^{16}	0.1636	0.1851	1.22×10^{13}	3.92×10^{12}	4.53×10^{-4}	1.45×10^{-4}	3.12
n-Si(NTD)	2×10^{16}	2×10^{16}	~10	2.7×10^{16}	0.1634	0.1843	7.81×10^{12}	7.62×10^{12}	2.89×10^{-4}	2.82×10^{-4}	1.02
n-Si(Cz, a, df)	6×10^{17}	3×10^{16}	~10	7.36×10^{16}	0.1845	0.1847	2.65×10^{13}	1.1×10^{12}	~0	3.75×10^{-4}	~0

1100°C). It can also be seen that the production rates for the vacancy-containing centers (the *A* centers, the *E* centers, and the V_2 and COV_2 centers) are higher in the heat-treated samples than those in as-grown samples. It is characteristic that all dependences shown in Fig. 4 are oscillatory: the quantities η_A, $\eta_{C_i-C_s}$, and $\eta_{0.40}$ increase and decrease alternately with increasing temperature of the preliminary heat treatment. It is significant that oscillatory variations in $\eta_{C_i-C_s}$ (curve *1*) and in η_A (curve *2*) are in "antiphase," whereas the variations in η_A (curve *2*) and in $\eta_{0.40}$ (curve *3*) occur "in phase." For $T_{tr} > 1050$°C, $\eta_{0.40}$ increases dramatically to values comparable to $\eta_{C_i-C_s}$; simultaneously, η_A decreases by almost the same amount.

The above results may be interpreted taking into account that anisotropic fields of compressive and tensile elastic stresses cause the primary radiation defects (vacancies *V* and interstitial atoms *I*) to migrate toward the impurity–defect clusters. Complexes involving *V* and *I* [4, 6] are actively formed within the clusters' impurity cloud, which mainly consists of background oxygen and carbon impurities. This redistribution of free *V* and *I* between the crystal matrix and the impurity–defect clusters leads to low production rates for the *E* centers η_E ($\eta_{0.40}$) and the C-containing complexes $\eta_{C_i-C_s}$ in the matrix and to relatively high rates η_A and $\eta_{C_i-C_s}$ in the impurity–defect clusters in which concentrations N_O and N_C are quite high. It is this mechanism that underlies the aforementioned relations $\eta_{0.40} \lll \eta_A$ and $\eta_{0.40} \lll \eta_{C_i-C_s}$.

In the as-grown samples, a large number of free vacancies are trapped at the interface between the interstitial-containing inclusion and the crystal matrix; annihilation and "freezing-out" of the vacancies may occur at this interface [6, 19]. Because of this, the experimentally observed relation $\eta_{C_i-C_s} > \eta_A + \eta_{0.40}$ is characteristic of unannealed crystals (Fig. 4). In the heat-treated crystals, the gettering properties of the interface are less pronounced (owing to the attachment of impurities), and the impurity cloud around the impurity–defect clusters is enriched with oxygen to a larger extent. Because of this, we observe a general trend towards an increase in the production rate for vacancy-containing radiation defects in annealed crystals compared to that in the as-grown crystals (Fig. 4, curves *2*, *3*). An oscillatory build-up of the *A* centers and vacancy-containing radiation defects with deep levels is observed against the background of the above trend. In our opinion, this form of annealing-temperature dependences of η_A and $\eta_{0.40}$ is related to the nonmonotonic variation in the oxygen concentration within the impurity cloud around the impurity–defect clusters in the course of heat treatment. The simultaneous "antiphase" oscillations of $\eta_{C_i-C_s}$ are indicative of inverse variation in the carbon concentration within the impurity cloud around the impurity–defect clusters. In other words, the impurity–defect clusters appear to respire during the heat treatment. In the course of subsequent irradiation, this "respiration" manifests itself in nonmonotonic (oscillatory) variation in the production rates of radiation defects that accumulate in the vicinity of the impurity–defect

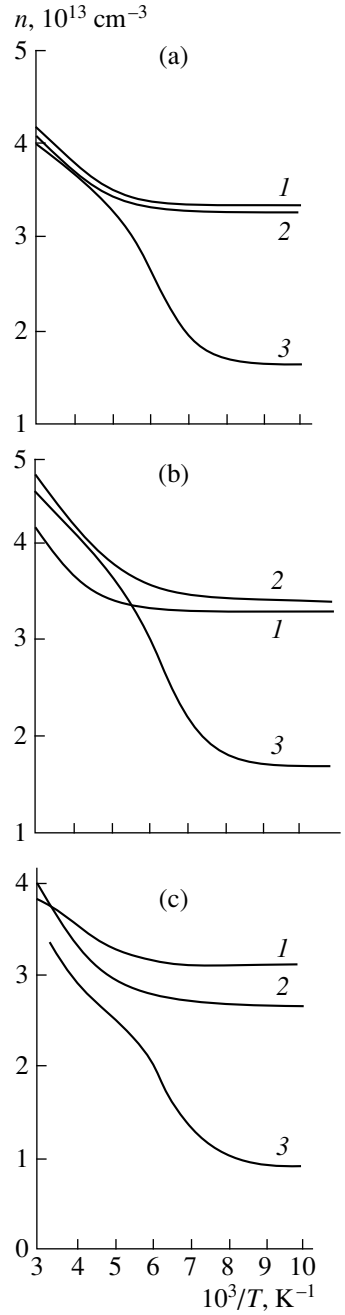

Fig. 3. Typical temperature dependences of the charge-carrier concentrations in the (*1*) as-grown, (*2*) heat-treated, and (*3*) irradiated *n*-Si(z, a, df) crystals. The heat-treatment temperature T_{tr} was (a) 800, (b) 1000, and (c) 1100°C. The integrated flux of radiation was $\Phi = 2.7 \times 10^{16}$ cm^{-2}.

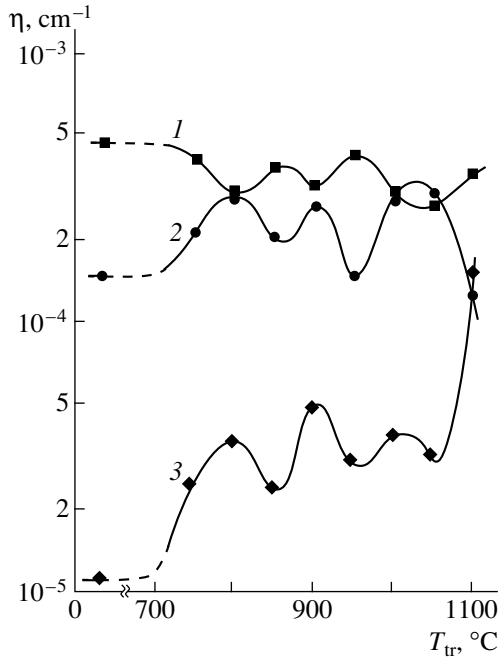

Fig. 4. Dependences of the production rates of radiation defects in *n*-Si grown by the floating-zone method on the temperature of its preliminary heat treatment (t = 1 h). The defects are (*1*) the C_i–C_s complexes, (*2*) the *A* centers, and (*3*) radiation defects with the levels at E_c – (≥0.40 eV).

clusters and contain oxygen (the *A* centers) and carbon (the C_i–C_s complexes). Furthermore, the observed "in-phase" variations in η_A and $\eta_{0.40}$ indicate that at least one type of radiation defect with deep levels formed in the vicinity of an impurity–defect cluster incorporates an oxygen atom (most probably, this is the CO_2V center).

Taking into account the fact that the vacancy- and interstitial-related channels of the radiation-defect formation are independent of one another and that the variations in η_A and $\eta_{C_i-C_s}$ are in antiphase, we may conclude that the oscillatory dependence of the build-up of the *A* centers and the C_i–C_s complexes on the temperature of preliminary heat treatment is caused by processes more complex than those related to variations in the probability of the direct annihilation of primary radiation defects or in the efficiency of the clusters to trap vacancies *V* [20]. Nevertheless, these processes have a common origin as is shown by the coincidence of the heat-treatment temperatures for which the temperature dependences of the production rates for radiation defects of various origins pass through the extreme points (Fig. 4, curves *1–3*).

Let us now compare the observed oscillatory variations in the oxygen and carbon concentrations in the impurity cloud around an impurity–defect cluster with the published data. Deep-level transient spectroscopy (DLTS) has been used previously [21] to study the uniformity of distribution of electron-irradiation-induced (the electron energy was equal to E_e = 2.5 MeV) *A* centers in the as-grown and heat-treated samples of crucible-grown *n*-Si. It was found that, in the as-grown material, the DLTS peak amplitude related to the *A* centers was independent of the temperature of the measurements. However, even after preliminary heat treatment for 1 h at T_{tr} = 600°C, such a dependence becomes distinct, which is interpreted as a consequence of the emergence of local *A*-center clusters. This is caused by the annealing-induced formation of local crystal regions enriched in oxygen. As the heat-treatment duration increases (to t = 10 h), the local oxygen content and, as a consequence, the local *A*-center concentration increase and then decrease for t > 10 h. Thus, according to [21], the local oxygen concentration may both increase and decrease with increasing duration of the heat treatment.

Figure 5 shows the typical temperature dependences of the charge-carrier concentration in the studied samples of the crucible-grown *n*-Si(Cz, a, df). The crucible-grown *n*-Si with a resistivity of ρ = 100 Ω cm has the following special features caused by certain relations between the concentrations of the doping (P) and background impurities (O, C) ($N_O \gg N_C$ and $N_O \gg N_P$) inherent in this material: as a result of the irradiation of this material, the *A* centers are preferentially formed [5], whereas the complexes consisting of interstitial carbon and interstitial oxygen (C_i–O_i) and having an energy level of E_v + 0.35 eV [22] are formed instead of the C_i–C_s complexes. In addition, the gettering properties of the impurity–defect clusters with respect to free vacancies are less pronounced in this material than in the floating-zone *n*-Si [6]. Nevertheless, our experiments with the crucible-grown *n*-Si ($N_O = 6 \times 10^{17}$ cm^{-3} and $N_C = 3 \times 10^{16}$ cm^{-3}) showed (Fig. 6, curve *1*) that oscillations in the production rate for the *A* centers (i.e., in the N_O concentration in the impurity–defect clusters) occur as a function of the temperature of preliminary heat treatment (T_{tr} = 750–1100°C, ΔT = 50°C, and t = 1 h). These oscillations are essentially similar to those of η_A in the float-zone *n*-Si studied (Fig. 4, curve *2*). It follows that, irrespective of the method of dislocation-free *n*-Si growth, interaction of inclusions with the background oxygen impurity occurs in the course of heat treatment of this material; as a result of this interaction, the local concentration of oxygen in the impurity–defect clusters varies with both the temperature and duration of the heat treatment. It is difficult to determine reliably the variations in N_C within the impurity–defect clusters in the crucible-grown *n*-Si using the method employed, the reason being that, in this material, the irradiation-produced carbon interstitials C_i are mainly involved (as was mentioned above) in the formation of C_i–O_i complexes whose energy level is located in the lower half of the band gap and is, therefore, undetected by the Hall effect measurements of the charge-carrier concentration in the *n*-Si crystals.

According to the data reported in [23], an oscillatory "reaction" of transformation of the defects with the level at $E_c - 0.18$ eV (the *A* centers) into the defects with the level at $E_c - 0.34$ eV was observed in silicon with an oxygen concentration of $N_O = 3 \times 10^{17}$ cm^{-3}. It was noted that, in Si crystals gamma-irradiated and then annealed at 100–200°C, the *A* centers transform into centers with the level at $E_c - 0.34$ eV; the reverse transformation is observed at temperatures higher than 200°C. The complete mutual rearrangement is interpreted [23] as being due to variation in the defect configuration (their bistability). It is important for the origination of oscillations that the *A* center binds a certain mobile component *M* and then releases it. Judging from the activation energy of the rearrangement (~0.7 eV), which may be approximately related to the migration energy E_m of defect *M*, it was inferred [23] that a carbon atom ($E_m = 0.8$ eV) may act as the mobile defect *M*. In this respect, the oscillations observed here in the production rates of the main radiation defects (η_A, $\eta_{C_i-C_s}$, and $\eta_{0.40}$) with increasing temperature of preliminary heat treatment may be interpreted as the consequences of oscillatory "reactions" directed at the establishment of equilibrium between the crystal matrix and the impurity–defect clusters (their accommodation), with technological oxygen and carbon impurities involved as mobile components *M*. If this is the case, the impurity–defect clusters should be treated as complex multistable defects whose configuration may change as the crystal temperature is varied. It is not inconceivable that the rotational motion of the cores of the impurity–defect clusters occurs as the heat-treatment temperature increases; this motion is accompanied by the subsequent accommodation of impurity–defect clusters via an exchange of matter (carbon and oxygen atoms) between the impurity–defect clusters (the inclusion–matrix interface) and the crystal matrix.

Glazov *et al.* [24] observed nonmonotonic (in our opinion, oscillatory) variations in the electrical properties of silicon and its linear expansion when the crystal was heated to temperatures in the range of T_{tr} = 200–1000°C. These variations were presumably caused by structural transformations in silicon, which occurred when temperature was varied. However, if it is assumed that the observed variations are also related to the "respiration" of impurity–defect clusters, the onset of this process may correspond to temperatures of 250–300°C. Incidentally, transformations of defects set in at these temperatures and lead to the radiation-stimulated formation of quenched-in donors-I in silicon grown by the floating-zone method [4]. According to the results of our additional experiments (Fig. 6, curves *2*, *3*), the onset temperature for transformations is lowered to 100°C if the heat treatment and irradiation are combined, i.e., if a "hot" irradiation of silicon is performed (in other words, if heat treatment is carried out in the course of irradiation).

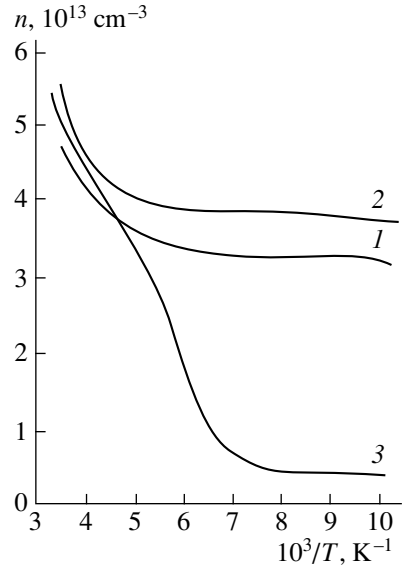

Fig. 5. Typical temperature dependences of charge-carrier concentrations in (*1*) as-grown, (*2*) heat-treated, and (*3*) irradiated *n*-Si crystals grown by the floating-zone method. The heat-treatment temperature was T_{tr} = 1000°C. The integrated flux of radiation was $\Phi = 7.36 \times 10^{16}$ cm^{-2}.

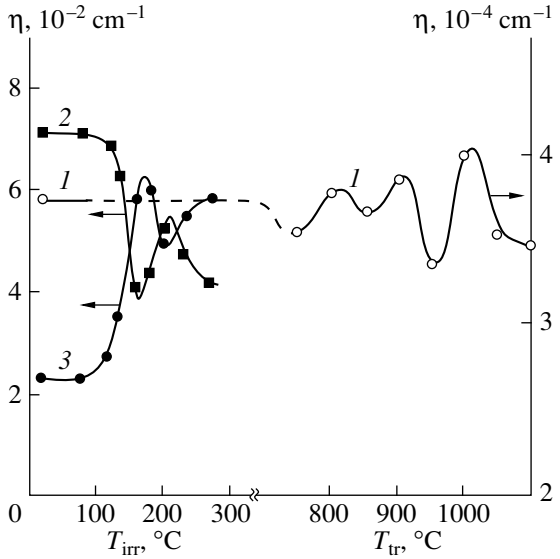

Fig. 6. Dependences of the production rates of radiation defects in *n*-Si (ρ = 100 Ω cm) on (*1*) the temperature of its preliminary heat treatment T_{tr} and (*2*, *3*) the irradiation temperature T_{irr}. Silicon was grown (*1*) in a crucible and (*2*, *3*) by the floating-zone method. Irradiation was performed with (*1*) ^{60}Co gamma-ray quanta, $\Phi = 7.4 \times 10^{16}$ cm^{-2}; and (*2*, *3*) electrons with E_e = 3.5 MeV and $\Phi = 8 \times 10^{13}$ cm^{-2}. The defects are (*1*, *3*) the *A* centers and (*2*) the C_i–C_s complexes.

However, the range of heat-treatment temperatures in which the "respiration" of impurity–defect clusters is observed (Fig. 4) is bound from above by a temperature of 1050°C; at higher temperatures, the impurity–defect clusters decompose and lose their gettering properties

[25]. Therefore, at $T_{tr} > 1000°C$, the efficiency of redistribution of the irradiation-generated vacancies between the impurity–defect clusters and the crystal matrix lowers; as a result, the build-up rate for the *A* centers in the vicinity of impurity–defect clusters decreases drastically (Fig. 4, curve *2*), and, correspondingly, the rate of the *E*-center production in the crystal bulk η_E increases steeply (Fig. 4, curve *3*).

4. CONCLUSION

On the basis of the above results, the following general conclusion may be made. In the course of the post-crystallization cooling of silicon from the melting temperature, the accommodation of the forming impurity–defect clusters is not completed due to lack of time and continues during the subsequent irradiation or heat treatment owing to the influx of primary radiation defects or to the transport of oxygen and carbon impurities from the impurity–defect clusters to the crystal matrix or in the opposite direction. The impurity–defect clusters may be treated as multistable formations, which can transform from one spatial configuration into another under irradiation or heat treatment. The concurring accommodation of the impurity–defect clusters is accompanied by oscillatory "reactions" with the participation of oxygen and carbon background impurities as mobile components. The lower (~100°C) and upper (~1050°C) boundaries of the temperature range in which such oscillatory reactions can proceed were estimated.

ACKNOWLEDGMENTS

I thank T.A. Kholopitsa who helped me with the development and debugging of computer program for minimization.

REFERENCES

1. V. V. Voronkov, G. I. Voronkova, B. V. Zubov, *et al.*, Fiz. Tekh. Poluprovodn. (Leningrad) **13**, 846 (1979) [Sov. Phys. Semicond. **13**, 498 (1979)].
2. R. F. Vitman, N. A. Vitovskiĭ, A. A. Lebedev, *et al.*, Fiz. Tekh. Poluprovodn. (Leningrad) **24**, 45 (1990) [Sov. Phys. Semicond. **24**, 27 (1990)].
3. A. N. Buzynin, S. E. Zabolotskiĭ, V. N. Kalinushkin, *et al.*, Fiz. Tekh. Poluprovodn. (Leningrad) **24**, 264 (1990) [Sov. Phys. Semicond. **24**, 161 (1990)].
4. I. I. Kolkovskii, P. F. Lugakov, V. V. Lukjanitsa, and V. V. Shusha, Phys. Status Solidi A **118**, 65 (1990).
5. V. V. Emtsev, G. A. Oganesyan, and K. Schmalz, Fiz. Tekh. Poluprovodn. (St. Petersburg) **27**, 1549 (1993) [Semiconductors **27**, 856 (1993)].
6. I. I. Kolkovskiĭ and V. V. Lukjanitsa, Fiz. Tekh. Poluprovodn. (St. Petersburg) **31**, 405 (1997) [Semiconductors **31**, 340 (1997)].
7. I. I. Kolkovskii, P. F. Lugakov, and V. V. Shusha, Phys. Status Solidi A **127**, 103 (1991).
8. P. F. Lugakov, V. V. Lukjanitsa, and Yu. M. Pokatilo, Fiz. Tekh. Poluprovodn. (Leningrad) **19**, 2014 (1985) [Sov. Phys. Semicond. **19**, 1239 (1985)].
9. H. J. Stein and F. L. Vook, Phys. Rev. **163**, 790 (1967).
10. A. G. Litvinko, L. F. Makarenko, L. I. Murin, and V. D. Tkachev, Fiz. Tekh. Poluprovodn. (Leningrad) **14**, 776 (1980) [Sov. Phys. Semicond. **14**, 455 (1980)].
11. N. Draper and H. Smith, *Applied Regression Analysis* (Wiley, New York, 1966; Statistika, Moscow, 1973).
12. D. M. Himmelblau, *Applied Nonlinear Programming* (McGraw-Hill, New York, 1972; Mir, Moscow, 1975).
13. D. D. McCracken and W. S. Dorn, *Numerical Methods and FORTRAN Programming* (Wiley, New York, 1965; Mir, Moscow, 1977).
14. M. I. Krivov, E. A. Popova, and E. V. Malisova, Izv. Vyssh. Uchebn. Zaved., Fiz. **6**, 156 (1973).
15. V. B. Neĭmash, T. R. Sagan, V. M. Tsmots', *et al.*, Fiz. Tekh. Poluprovodn. (Leningrad) **25**, 1857 (1991) [Sov. Phys. Semicond. **25**, 1117 (1991)].
16. D. Himmelblau, *Process Analysis by Statistical Methods* (McGraw-Hill, New York, 1970; Mir, Moscow, 1973).
17. H. I. Horffman, Appl. Phys. **19**, 307 (1979).
18. N. G. Kolin, P. F. Lugakov, V. V. Lukjanitsa, and A. A. Stuk, Izv. Vyssh. Uchebn. Zaved., Fiz. **33**, 98 (1990).
19. I. I. Kolkovskiĭ, P. F. Lugakov, and V. V. Shusha, Izv. Vyssh. Uchebn. Zaved., Fiz. **31**, 128 (1998).
20. A. V. Vasil'ev, S. A. Smagulova, and S. S. Shaĭmeev, Fiz. Tekh. Poluprovodn. (Leningrad) **19**, 952 (1985) [Sov. Phys. Semicond. **19**, 587 (1985)].
21. I. V. Antonova, A. Misiuk, V. P. Popov, and S. S. Shaĭmeev, Fiz. Tekh. Poluprovodn. (St. Petersburg) **31**, 998 (1997) [Semiconductors **31**, 852 (1997)].
22. L. I. Murin, Phys. Status Solidi A **101**, K107 (1987).
23. P. V. Kuchinskiĭ, V. M. Lomako, and L. N. Shakhlevich, Fiz. Tekh. Poluprovodn. (Leningrad) **22**, 1213 (1988) [Sov. Phys. Semicond. **22**, 769 (1988)].
24. V. M. Glazov, V. B. Kol'tsov, V. Z. Kutsova, *et al.*, Fiz. Tekh. Poluprovodn. (Leningrad) **25**, 588 (1991) [Sov. Phys. Semicond. **25**, 355 (1991)].
25. P. F. Lugakov and V. V. Lukjanitsa, Fiz. Tekh. Poluprovodn. (St. Petersburg) **26**, 1509 (1992) [Sov. Phys. Semicond. **26**, 848 (1992)].

Translated by A. Spitsyn

Semiconductors, Vol. 35, No. 5, 2001, pp. 499–501. Translated from Fizika i Tekhnika Poluprovodnikov, Vol. 35, No. 5, 2001, pp. 521–523.

ELECTRONIC AND OPTICAL PROPERTIES OF SEMICONDUCTORS

Thermal Conductivity and the Wiedemann–Franz Relation in Melts of Indium and Gallium Antimonides

Ya. B. Magomedov* and A. R. Bilalov

Institute of Physics, Dagestan Scientific Center, Russian Academy of Sciences, ul. 26 Bakinskikh komissarov, Makhachkala, 367003 Russia

** e-mail: kamilov@datacom.ru*

Submitted August 17, 2000; accepted for publication October 26, 2000

Abstract—The thermal and electrical conductivities of indium and gallium antimonides were studied in both solid and liquid states. It is shown that the calculated values of the Lorentz number (L) in InSb and GaSb, unlike in metals, increase with increasing temperature after melting. An anomalous increase in L is consistent with anomalous (for melts) temperature dependences of density, viscosity, and coordination number of these melts at the same temperatures. © *2001 MAIK "Nauka/Interperiodica".*

Much attention in recent years has been given to the problem of structural disordering and its effect on the kinetic properties of semiconductors and metals. Several models have been proposed to theoretically explain the effect of melting on charge transport in semiconductors. The most appropriate explanation appears to be offered by Mott's theoretical model [1]. According to this model, three types of transformations of the density of energy states of charge carriers in semiconductors are possible depending on the extent of the changes in short-range order during melting: the transition to a metallic state, the transition to a semimetallic state, or the preservation of semiconducting properties. Mott considers the magnitude of electrical conductivity as the most essential criterion which determines the semiconducting or metallic nature of the melts.

Arranging the melts studied at that time in decreasing order of magnitude of electronic conductivity, Allgaier [2] distinguishes three groups of melts (*A, B, C*) which correspond to the three types of energy-dependent transformation of electron density of states in Mott's model.

The *A* group includes, among the melts of common metals, the melts of semiconductors (germanium, silicon, and III–V compounds) with electrical conductivity exceeding $5 \times 10^5\ \Omega^{-1}\ m^{-1}$. The melting of these semiconductors is accompanied by drastic changes in the short-range order [3, 4], i.e., the disruption of the rigid system of interatomic covalent bonds; a drastic change in the electron energy spectrum (the conduction and valence bands are merged together); and an abrupt change in density, coordination number, electrical conductivity, thermal emf, viscosity, and Hall coefficient. The magnitudes of all these parameters become close to those existing in metallic melts. It is commonly assumed that the melting of such semiconductors causes their metallization.

A specific feature of the metallic state of a substance in both solid and liquid states is that the major heat and charge carriers in them are free electrons. According to the model of almost-free electrons developed by Ziman [5], the electron thermal conductivity (λ_e) is governed by the Wiedemann–Franz relation $\lambda_e = L\sigma T$, where σ is the electrical conductivity and L is the Lorentz number, which depends on the scattering mechanism and the degree of electron-gas degeneracy. If one assumes that the charge carriers in the semiconductor and metal melts are scattered elastically by molecular and atomic vibrations of structural elements, then, for the completely degenerate electron gas, the Lorentz number for metals is $L_0 = 2.44 \times 10^{-8}\ W^2/K^2$, and, for a nondegenerate state of electron gas in semiconductors, $L_{MB} = 1.55 \times 10^{-8}\ W^2/K^2$.

In metal melts, the Wiedemann–Franz law is obeyed, and the Lorentz number values near the melting temperature are close to L_0 [6]. However, as the temperature increases, the Lorentz number gradually decreases in liquid metals. The effect of inelastic scattering of electrons by relatively solitary ions in a gaseous-like state [6] is believed to be one of the causes of such a deviation from the Wiedemann–Franz law.

In metal-like semiconducting melts belonging, according to Mott, to the *A* group, the Wiedemann–Franz relation is not studied because of the lack of reliable experimental data on thermal conductivity. The available published data on the thermal conductivity of these melts [7–9] cover a narrow temperature range above the melting point and vary considerably in magnitude and temperature dependence.

In order to identify the mechanism of thermal conductivity and to verify the validity of the Wiedemann–Franz relation, we studied the thermal and electrical conductivities of indium and gallium antimonide melts in a wide temperature range.

1063-7826/01/3505-0499$21.00 © 2001 MAIK "Nauka/Interperiodica"

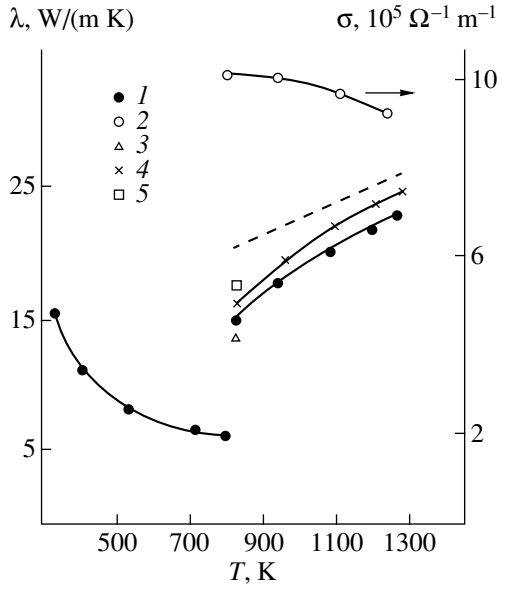

Fig. 1. Temperature dependences of (*1*) thermal, λ, and (*2*) electrical, σ, conductivities of an InSb melt; dashed line indicates the calculated thermal conductivity for a degenerate electron gas; *3*, *4*, and *5* are the data taken from [7], [9], and [8], respectively.

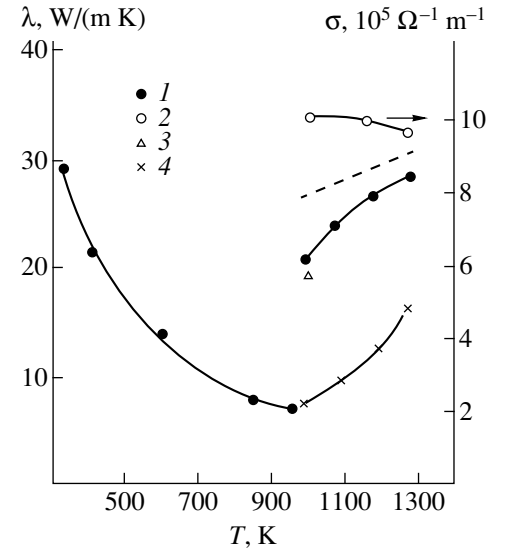

Fig. 2. Temperature dependences of (*1*) thermal, λ, and (*2*) electrical, σ, conductivities of a GaSb melt; dashed line indicates the calculated thermal conductivity for a degenerate electron gas; *3* and *4* are the data taken from [7] and [9], respectively.

The thermal conductivity was measured in a steady-state thermal mode by the method described in [10], and the electrical conductivity was studied by the four-probe compensation method [11]. The relative error of measurement did not exceed 4–5% for thermal conductivitiy and 3–4% for electrical conductivitiy. The studies were carried out for the same polycrystalline samples of InSb and GaSb obtained by fusing in quartz cells the pure starting compounds taken in stoichiometric proportion.

The temperature dependences of the thermal and electrical conductivity of InSb and GaSb are shown in Figs. 1 and 2. The available published data on the thermal conductivity of InSb and GaSb are also shown.

The experimental values of electrical conductivity obtained for the solid and liquid states are consistent with the published data [3, 4]. The experimental data on the thermal conductivity of melts immediately after melting are consistent with the data obtained for InSb [7, 9] and for GaSb [7]. We did not observe an abrupt decrease in thermal conductivity of melts upon further heating after melting as was reported in [7], since this was caused by inaccuracy in the experiment (a part of the melt apparently leaked out of the operating volume during heating after melting). A comparison of our results with the data published in [9] shows that in the entire temperature range studied the magnitudes and temperature dependences of thermal conductivity are consistent with the published data for InSb melts and are significantly inconsistent with the data for GaSb melts. The available published data on thermal and electrical conductivity were obtained for samples with a varied concentration of charge carriers because they were prepared by various authors using different technologies. It seems impossible to compare these data and verify the Wiedemann–Franz correlation.

In a solid-state region the data on thermal conductivity of indium and gallium antimonides presented in Figs. 1 and 2 are consistent with the data obtained in [7]. In this region, phonon and electron mechanisms are dominant in thermal conductivity (at temperatures close to the melting point). The deviation in the temperature dependence of phonon thermal conductivity from the T^{-1} law observed at high temperatures for InSb and GaSb can be explained on the basis of the results of the effect of hydrostatic pressure on these compounds [12] (by the thermal expansion of their crystal lattice [13]).

As can be seen in Figs. 1 and 2 (dashed lines), the electron thermal conductivity in InSb and GaSb melts, calculated from the Wiedemann–Franz relation using the data on electrical conductivity for a degenerate electron gas, is inconsistent with the experiment. The experimental data for λ_e in melts are also inconsistent with the results of calculation for a nondegenerate electron gas.

Using the data on the temperature dependence of density [4], we calculated the molecular thermal conductivity (λ_m) of the melts by Rao's formula [14]. The calculated values of λ_m for the entire temperature range do not exceed 0.46 and 0.65 W/(m K) for InSb and GaSb, respectively.

Using the experimental data on thermal conductivity of InSb and GaSb melts and taking into account the value of λ_m from the Wiedemann–Franz relation, the values of the Lorentz number for various temperatures

were also calculated. In contrast to the metallic melts, the Lorentz numbers increase with temperature in the range of 200–300 K after melting (from 1.7×10^{-8} to 2.1×10^{-8} W^2/K^2 for InSb and from 1.8×10^{-8} to 2.2×10^{-8} W^2/K^2 for GaSb). The values of the Lorentz number (2.1–2.2) $\times$ 10^{-8} W^2/K^2 at temperatures of T_m + (200–300) K (T_m is the melting temperature) are typical of metallic melts [6] and confirm the metallic nature of these melts in this temperature range.

The anomalous temperature dependence of the Lorentz numbers at temperatures near the melting point is consistent with anomalous (for metallic melts) temperature variations in density, viscosity, free energy, and entropy of activation of the viscous flow of melts of these compounds in the same temperature range [15]. The anomalous behavior of these parameters in the melts of III–V compounds is explained by the inherited features of solid-state structures in a certain temperature range after melting.

The increase in the Lorentz number and anomalies in the temperature behavior of other parameters upon further heating of the InSb and GaSb melts suggest that the process of structural transformation and metallization in these compounds is not completed at melting and is fully completed only after overheating by 200–300 K.

The valence and conduction bands are not completely merged together upon the melting of InSb and GaSb. It seems that the energy dependence of the density of states in the range corresponding to the band gap of the solid state still contains a certain minimum which flattens upon further heating of the melts. In our opinion, the melts of these compounds just after melting have intermediate properties between the metal melts and the *B* group melts according to Mott's classification.

ACKNOWLEDGMENTS

The authors are grateful to R.I. Bashirov for providing us with samples and to V.M. Guseĭnov for his help with the experiment.

REFERENCES

1. N. F. Mott and E. A. Davis, *Electronic Processes in Non-Crystalline Materials* (Clarendon, Oxford, 1971; Mir, Moscow, 1974).
2. R. S. Allgaier, Phys. Rev. **185**, 227 (1969).
3. A. F. Joffe and A. R. Regel, Prog. Semicond. **4**, 237 (1960).
4. V. M. Glazov, S. N. Chizhevskaya, and N. N. Glagoleva, *Liquid Semiconductors* (Nauka, Moscow, 1967; Plenum, New York, 1969).
5. J. M. Ziman, *Electrons and Phonons* (Clarendon, Oxford, 1960; Inostrannaya Literatura, Moscow, 1962).
6. L. P. Fillipov, *Investigation of Heat Conductivity of Liquids* (Mosk. Gos. Univ., Moscow, 1970).
7. Kh. I. Amirkhanov and Ya. B. Magomedov, Ukr. Fiz. Zh. **12** (2), 199 (1967).
8. B. M. Mogilevskiĭ and A. F. Chudnovskiĭ, in *Proceedings of the IX International Conference on Physics of Semiconductors* (Nauka, Moscow, 1969), Vol. 2, p. 1313.
9. V. I. Fedorov and V. I. Machuev, Teplofiz. Vys. Temp. **8**, 447 (1970).
10. Ya. B. Magomedov, Teplofiz. Vys. Temp. **28**, 396 (1990).
11. Kh. I. Amirkhanov, Ya. B. Magomedov, S. A. Aliev, G. B. Bagduev, Z. A. Isaev, and A. V. Shchegol'kova, in *Physical Properties of Tellurium* (Daguchledgiz, Makhachkala, 1969).
12. G. A. Slack, Solid State Phys. **34**, 1 (1979).
13. Ja. B. Magomedov, Sh. M. Ismailov, and N. L. Kramynina, High Temp.-High Press. **26**, 657 (1994).
14. M. R. Rao, Phys. Rev. **59**, 212 (1971).
15. A. R. Regel' and V. M. Glazov, *Laws of Electronic Melt Structure Formation* (Nauka, Moscow, 1982).

Translated by A. Zalesskiĭ

Semiconductors, Vol. 35, No. 5, 2001, pp. 502–505. Translated from Fizika i Tekhnika Poluprovodnikov, Vol. 35, No. 5, 2001, pp. 524–527.

ELECTRONIC AND OPTICAL PROPERTIES OF SEMICONDUCTORS

Specific Features of Photoconductivity in Thin *n*-PbTe:Ga Epilayers

B. A. Akimov*, V. A. Bogoyavlenskiĭ, L. I. Ryabova, and V. N. Vasil'kov

Moscow State University, Vorob'evy gory, Moscow, 119899 Russia

** e-mail: akimov@mig.phys.msu.su*

Submitted September 20, 2000; accepted for publication November 3, 2000

Abstract—Photoconductivity and transient processes in thin (0.2–0.3 μm) *n*-PbTe:Ga epilayers were studied. The films were grown by the hot-wall technique on $BaF_2\langle 111\rangle$ substrates. Photoelectric properties of the samples were investigated in the temperature range from 4.2 to 300 K. A GaAs light-emitting diode and miniature incandescent lamp were used as sources of pulsed and continuous infrared radiation, respectively. The most important characteristic of the films is the very wide temperature range of photosensitivity. At an illumination power density of 10^{-5} to 10^{-4} W/cm^2, the temperature at which the films become photosensitive T_C is as high as 150 K, which exceeds T_C for thicker films (2–3 μm) and high-resistivity single crystals of *n*-PbTe:Ga by 40 and 70 K, respectively. An analysis of the transient behavior of photoconductivity shows that photoexcited carriers are uniformly distributed over the volume of the thin films. A barrier for recombination of nonequilibrium charge carriers was estimated for slow relaxation processes. © *2001 MAIK "Nauka/Interperiodica".*

INTRODUCTION

Gallium in lead telluride produces deep impurity levels that pin the Fermi level within the band gap of the PbTe:Ga solid solution 70 meV below the conduction-band bottom [1–3]. At low temperatures ($T < 80$ K), the electron concentration in PbTe:Ga is close to that in the undoped material, and PbTe:Ga exhibits high photosensitivity and persistent photoconductivity. Therefore, PbTe:Ga is a promising material for infrared (IR) optoelectronics and can be used for the fabrication of lasers, thermal imagers, detectors, and other devices sensitive in the spectral range from 3 to 5 μm [2, 4, 5].

Most of the publications devoted to the photoelectric properties of *n*-PbTe:Ga dealt with single-crystal samples [6–9]. A synthesis of photosensitive films is complicated by the relatively narrow range of Ga concentrations corresponding to the semi-insulating state of the material [10]. Further difficulties arise from the nonuniform impurity distribution, namely, Ga segregation in the sample bulk [11]. High-resistivity *n*-PbTe:Ga films have been prepared and examined only recently. It was found [12, 13] that a temperature T_C, at which the persistent photoconductivity appears in *n*-PbTe:Ga epilayers 2–3 μm thick, is as high as 100–110 K, which exceeds T_C for the single-crystal samples by 30–40 K [2, 6]. In this study, we further optimized the hot-wall technique with the aim of preparing thinner (0.2–0.3 μm) high-resistivity epitaxial films of *n*-PbTe:Ga. This allowed us to compare the photoelectric characteristics of films of various thicknesses with those of single-crystal samples.

EXPERIMENTAL

The *n*-PbTe:Ga epitaxial films were grown by the hot-wall technique on $BaF_2\langle 111\rangle$ substrates from a starting charge containing 90% PbTe and 10% GaTe. To find conditions for the growth of most perfect films, we kept the source in the growth chamber at a temperature of 740°C and varied the substrate temperature in the range from 180 to 200°C. The growth duration was 4–6 h; the film thicknesses were about 0.2 μm. The structure of the grown films was examined by electron microscopy, acoustic microscopy, and X-ray diffraction.

The photoelectric properties of the *n*-PbTe:Ga films were studied in the temperature range from 4.2 to 300 K with the use of a low-temperature cell that completely shielded the samples from background radiation. A GaAs light-emitting diode (LED) operating at a wavelength of 1 μm with a power density of 10^{-5} W/cm^2 and a miniature incandescent lamp with a power density of 10^{-4} W/cm^2 were used as IR sources. Ohmic contacts were prepared from an In + Ag (4 at. %) + Au (1 at. %) alloy.

RESULTS

Figure 1 shows temperature dependences of resistivity ρ of the *n*-PbTe:Ga film 0.2 μm thick, which were measured in the dark (curve *1*) and under illumination with the LED (curve *2*) and the incandescent lamp (curve *3*). These results suggest that the ratio of dark resistivity to photoresistivity ρ^d/ρ^{ill} increases sharply as temperature decreases below the characteristic temperature T_C = 150 K at which the persistent photoconduc-

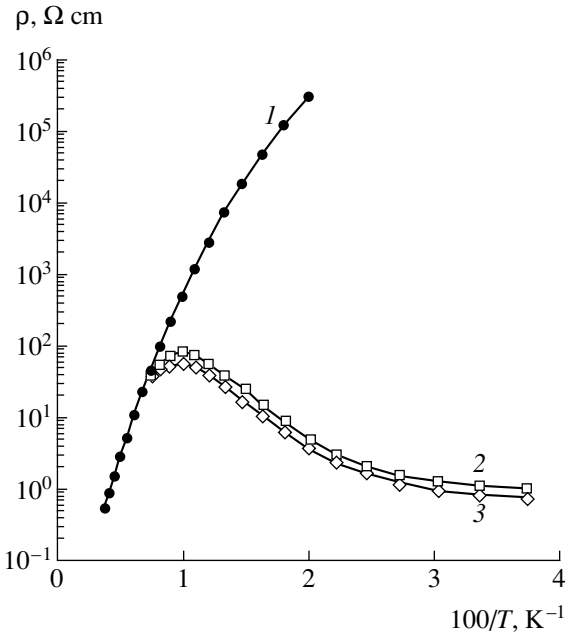

Fig. 1. Temperature dependences of resistivity of the *n*-PbTe:Ga film 0.2 μm thick measured (*1*) in the dark and under continuous IR illumination (*2*) with a LED and (*3*) an incandescent lamp.

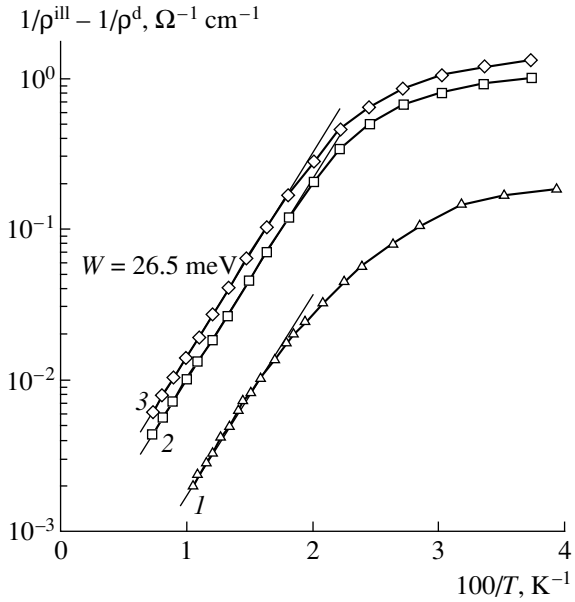

Fig. 2. Difference between photoconductivity and dark conductivity, $1/\rho^{ill} - 1/\rho^{d}$, vs. inverse temperature for (*1*) the *n*-PbTe:Ga film 2 μm thick illuminated with an incandescent lamp and (*2*, *3*) the *n*-PbTe:Ga film 0.2 μm thick illuminated with (*2*) a LED and (*3*) an incandescent lamp.

tivity appears. The ratio ρ^{d}/ρ^{ill} is 10, 10^3, and 10^5 at T = 100, 77, and 50 K, respectively. In the case of continuous illumination, the radiation-source spectrum and intensity variations have only a weak effect on the $\rho(T)$ dependences. This suggests that the curves measured under illumination characterize the highest sensitivity of the films in the IR spectral region.

Figure 2 presents a semilogarithmic plot of the difference of photoconductivity and dark conductivity, $1/\rho^{ill} - 1/\rho^{d}$, as a function of inverse substrate temperature for the *n*-PbTe:Ga films of various thicknesses. One can see that the difference $(1/\rho^{ill} - 1/\rho^{d})$ shows an exponential temperature dependence over a rather wide temperature range, from T = 50 K (this temperature is common to single crystals and films of *n*-PbTe:Ga) to the characteristic temperature T_C, which increases from 100 to 150 K as the film thickness decreases. Thus, a plot of $\log(1/\rho^{ill} - 1/\rho^{d})$ versus $1/T$ for the thin *n*-PbTe:Ga film is linear over a fairly wide temperature range (see curves *2*, *3*). We may assume that the exponential temperature dependence of the film conductivity is due to a variation in concentration of nonequilibrium electrons, which is described by the expression $\Delta n \propto \delta R/\tau$, where δR is the recombination rate of nonequilibrium charge carriers and τ is the characteristic recombination time. Assuming that, at relatively high temperatures (T > 50 K), δR at each point is equal to the generation rate, which remains constant under the experimental conditions, we may attribute the variation in the concentration of nonequilibrium electrons to the temperature dependence of the characteristic recombination time: $\tau \propto \exp(W/kT)$. Then, the barrier for recombination of nonequilibrium charge carriers (W) can be estimated from the formula

$$(1/\rho^{ill} - 1/\rho^{d}) \propto \exp(W/kT). \quad (1)$$

Thus the determined value of W is 26.5 meV.

Figure 3 shows the decay curves of photoconductivity $\Delta\sigma(t)$ measured after pulsed illumination with the LED for the *n*-PbTe:Ga films of various thicknesses. The time t = 0 corresponds to the instant at which the illumination was turned off. It easy to see a qualitative difference between the curves for the samples of different thicknesses. First, the conductivity of the thick *n*-PbTe:Ga film reaches its equilibrium value much more rapidly than the conductivity of the thin film. Second, a plot of $\log(\Delta\sigma)$ as a function of t for the thick film does not yield a straight line. By contrast, photoconductivity decay in the thin layer shows the classical exponential behavior described by the relation

$$\Delta\sigma(t) \propto \exp(-t/\tau) \quad (2)$$

virtually in the entire time range, except for a short period of time at the onset of the relaxation.

For quantitative comparison of the photoconductivity transient characteristics for the films of various

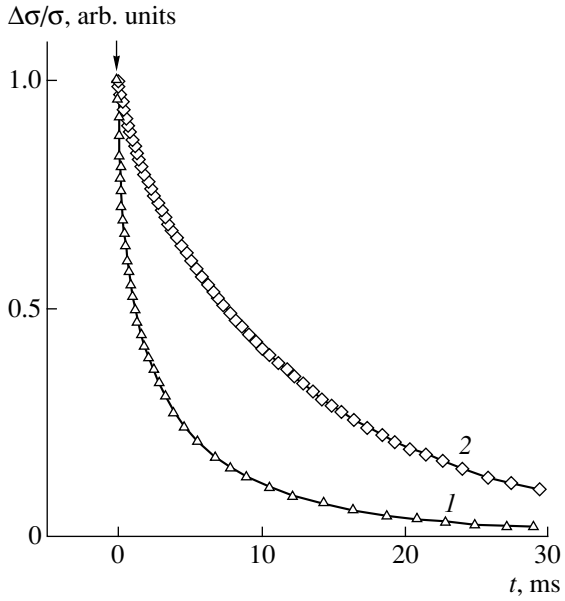

Fig. 3. Photoconductivity decay curves $\Delta\sigma(t)/\sigma$ measured for the *n*-PbTe:Ga films (*1*) 2 and (*2*) 0.2 μm thick after illumination with a 10-ms pulse from the LED at $T = 4.2$ K.

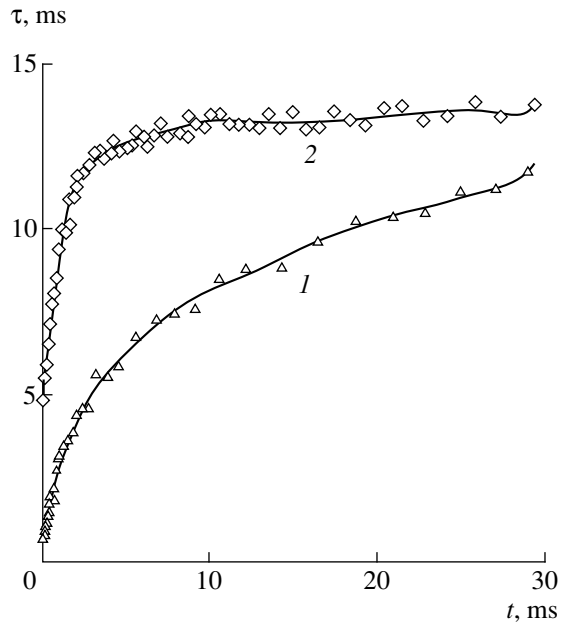

Fig. 4. Variation in the characteristic time relaxation calculated with formula (3) during the relaxation of photoconductivity in the *n*-PbTe:Ga films (*1*) 2 and (*2*) 0.2 μm thick (see Fig. 3).

thicknesses, we calculated the characteristic relaxation times by the equation

$$\tau(t) = \Delta\sigma/(-\partial\sigma/\partial t). \quad (3)$$

Figure 4 shows thus-calculated $\tau(t)$ dependences for the thick (curve *1*) and thin (curve *2*) films. For the thin layer, the characteristic relaxation time rapidly (in a time $t < 10$ ms) reaches the value $\tau \approx 13$ ms and then remains virtually unchanged. The characteristic relaxation time for the thick film increases progressively with time during the entire relaxation process and probably approaches asymptotically the same value $\tau = 13$ ms.

DISCUSSION

According to previous experimental studies [6, 7, 12, 13], photoconductivity in the *n*-PbTe:Ga films shows a quite complex transient behavior. To a first approximation, the photoconductivity transient may be considered as a superposition of fast and slow relaxation processes. Amplitudes of the fast and slow processes depend not only on the intensity and the duration of optical excitation but also on the thermal history of a sample, i.e., on heating–cooling conditions. For semiconductors doped with mixed-valence impurities, the recombination rate depends on concentrations of nonequilibrium carriers and impurity centers in a certain charge state [7, 13]. Therefore, a nonuniform distribution of nonequilibrium carriers over the volume in combination with a nonuniform distribution of impurity centers in various charge states can lead to nonequivalent conditions for recombination of different groups of carriers and can have a pronounced effect on the relaxation processes, which are manifested in the nonexponential behavior of the decay curves. In bulk samples, diffusion of nonequilibrium carriers from the surface to the crystal bulk can be considered as a factor that actually affects the relaxation curves. Analyzing the relaxation processes, we should take into account that, in *n*-PbTe:Ga, the slow processes prevail at a high excitation level, whereas the comparatively fast relaxation is observed under pulsed illumination with a low power density. As noted by Akimov *et al.* [13], this can be related to the fact that, at high concentrations of nonequilibrium electrons, the concentration of metastable impurity centers responsible for one-electron capture is low compared to the concentration of the impurity centers in the ground state (two-electron capture). The diffusion of nonequilibrium electrons into the crystal bulk gives the electrons an additional chance to arrive at a metastable center and recombine. The diffusion apparently plays an important part not only in bulk single crystals but in films 2–3 μm thick as well. This fact can be responsible for the lower values of $\tau(t)$ for the thicker films (see Fig. 4). Since the exponential transients are observed only for the thin films, we can presume that photoexcited carriers are uniformly distributed over the volume in these layers only. Thus, the results obtained in this study indicate that, in the thin films, the effects of diffusion and nonuniform distribution of nonequilibrium carriers over the volume are eliminated.

The persistent photoconductivity observed at $T < T_C$ predominates at temperatures of up to about 50 K. The

barrier W determined for the temperature range of $50\ \mathrm{K} < T < T_C$ characterizes the slow relaxation process proceeding under illumination with a high power density. It should be noted that the sample thickness affects only T_C, whereas the temperature at which the $\rho(T)$ curves measured under illumination level off is about the same for all the samples studied. As the temperature increases to 50 K, the accumulation of nonequilibrium carriers ceases, although the time constant of the slow relaxation should continue to increase exponentially. In particular, this is confirmed by the fact that, at 4.2 K, the persistent photoconductivity is observed after continuous high-intensity illumination is switched off. The characteristic time of the slow relaxation at $T = 50$ K was estimated from the expression $\tau = \tau_0 \exp(W/kT)$, where τ_0 was taken to be $\sim 10^{-8}$ s (characteristic time of band-to-band recombination in undoped PbTe). The obtained value of $\tau(T = 50\ \mathrm{K}) \sim 10\ \mu\mathrm{s}$ is almost identical to the characteristic times of negative photoconductivity in comparatively low-resistivity *n*-PbTe:Ga films [14], in which the Ga concentration is slightly higher than that in the samples with the pinned Fermi level. It should not be ruled out that the leveling-off of the $\rho(T)$ curves in the low-temperature range is due to a superposition of the negative and positive photoconductivity effects. In heavily doped samples, only the negative-photoconductivity effect is observed [14], whereas the negative photoconductivity in high-resistivity *n*-PbTe:Ga samples quenches positive photoconductivity only partially.

ACKNOWLEDGMENTS

This study was supported in part by the Russian Foundation for Basic Research, project nos. 98-02-17317 and 99-02-17531.

REFERENCES

1. G. Nimtz and B. Schlicht, *Narrow Gap Semiconductors*, Ed. by G. Hohler (Springer-Verlag, Berlin, 1983).
2. B. A. Akimov, A. V. Dmitriev, D. R. Khokhlov, and L. I. Ryabova, Phys. Status Solidi A **137**, 9 (1993).
3. *Lead Chalcogenides: Physics and Applications*, Ed. by D. Khokhlov (Gordon & Breach, New York, 2000).
4. J. Masek, T. J. Hoshino, C. Maissen, *et al.*, Proc. SPIE **1735**, 54 (1992).
5. H. Zogg, A. Fash, C. Maissen, *et al.*, Opt. Eng. **33**, 1440 (1994).
6. B. A. Akimov, A. V. Albul, V. Yu. Il'in, *et al.*, Fiz. Tekh. Poluprovodn. (St. Petersburg) **29**, 2015 (1995) [Semiconductors **29**, 1051 (1995)].
7. B. A. Akimov, A. V. Albul, and L. I. Ryabova, Fiz. Tekh. Poluprovodn. (St. Petersburg) **29**, 2158 (1995) [Semiconductors **29**, 1125 (1995)].
8. A. I. Belogorokhov, I. I. Ivanchik, S. V. Ponomarev, *et al.*, Pis'ma Zh. Éksp. Teor. Fiz. **63**, 342 (1996) [JETP Lett. **63**, 353 (1996)].
9. A. I. Belogorokhov, I. I. Ivanchik, Z. Popović, *et al.*, Fiz. Tekh. Poluprovodn. (St. Petersburg) **32**, 679 (1998) [Semiconductors **32**, 608 (1998)].
10. S. A. Belokon', L. N. Vereshchagina, I. I. Ivanchik, *et al.*, Fiz. Tekh. Poluprovodn. (St. Petersburg) **26**, 264 (1992) [Sov. Phys. Semicond. **26**, 148 (1992)].
11. B. A. Akimov, A. M. Gaskov, V. N. Glonty, *et al.*, Phys. Status Solidi A **142**, 85 (1994).
12. B. A. Akimov, V. A. Bogoyavlenskiy, L. I. Ryabova, and V. N. Vasil'kov, Proc. SPIE **3890**, 212 (1999).
13. B. A. Akimov, V. A. Bogoyavlenskiy, L. I. Ryabova, *et al.*, Semicond. Sci. Technol. **14**, 679 (1999).
14. B. A. Akimov, V. A. Bogoyavlenskiy, L. I. Ryabova, and V. N. Vasil'kov, Phys. Rev. B **61**, 16 045 (2000).

Translated by N. Izyumskaya

Semiconductors, Vol. 35, No. 5, 2001, pp. 506–511. Translated from Fizika i Tekhnika Poluprovodnikov, Vol. 35, No. 5, 2001, pp. 528–533.

ELECTRONIC AND OPTICAL PROPERTIES OF SEMICONDUCTORS

Dynamic Effect of a Constant Electric Field on the Kinetics of Photons Interacting with Electrons in a Semiconductor

R. Kh. Amirov and V. N. Gusyatnikov*

Research Institute of Mechanics and Physics, Saratov State University, Astrakhanskaya ul. 83, Saratov, 410026 Russia

** e-mail: victor@mail.saratov.ru*

Submitted July 26, 2000; accepted for publication November 4, 2000

Abstract—The Liouville–von Neumann equation and a nonequilibrium statistical operator were used to derive a kinetic equation for photons that interact with nonrelativistic electrons in a constant electric field. The collision integral is nonvanishing due to the effect of the field on the interaction of photons with electrons. The probabilities that photons are absorbed or emitted depend on the photon frequency and on the component of the electric field along the photon-momentum direction; these dependences may either obey the power law or be oscillatory. The oscillations are related to the energy–time uncertainty relation. The contribution of this effect to the photon spectrum in reference to the emission accompanying the scattering of electrons by phonons and ionized impurities is calculated for *n*-GaAs. The range of parameters for which this effect may significantly affect the spectrum is determined. *© 2001 MAIK "Nauka/Interperiodica".*

1. Optical methods for studying the kinetics of nonequilibrium processes occurring in external fields in semiconductor and gaseous plasmas have been recently used quite often. External fields affect not only the collective effects in the above media but also the mechanism of the particles' interaction. This brings about a modification of the collision integrals in the kinetic equations, which is well known for the electron-distribution function [1–3]. In particular, a constant electric field may affect the probability of scattering of electrons by phonons and impurity centers [4, 5] and may change the electrical conductivity of a semiconductor [6]. An external alternating electric field can also modify the integral for collisions of photons with the electron–phonon–impurity system [7, 8]. In this context, it is of interest to consider the effect of a constant electric field on the kinetics of interaction of photons with electrons in view of the fact that, in the absence of a field, the number of photons with a given frequency in a photon–electron system is unchanged in a nonrelativistic approximation owing to the laws of conservation of energy and momentum. In this study, we used the nonequilibrium statistical operator [3, 9] to derive a kinetic equation for the distribution function of photons interacting with nonrelativistic electrons; the collision integral for this equation is nonvanishing only if there is a constant electric field. The presence of a field brings about a violation of the delta-shaped law of conservation of energy in an elementary scattering event owing to two factors: the nonlinear dependence of electron energy on momentum and an explicit dependence of the coupling constant on the electron momentum. The extent to which one or the other factor manifests itself depends on the geometric relation between the field strength, momentum, and photon polarization vectors. We consider the form of the collision integral for electron distribution that is only slightly anisotropic, which is often the case in the aforementioned media. It is shown that variation in the probability of the photon emission and absorption with frequency may be both power-law and oscillatory depending on the component of the field in the photon-momentum direction. Oscillations are caused by "broadening" of the delta-function and, thus, by the energy–time uncertainty relation. Using *n*-GaAs as an example, we calculated the contribution of this effect to the free-electron emission spectrum in a semiconductor in reference to the electron emission in the course of scattering by phonons and ionized impurities. In addition to oscillations, this effect may manifest itself at frequencies for which the photon energy exceeds the electron temperature (expressed in energy units) but is lower than the optical-phonon energy. This makes it basically possible to verify the above effect experimentally.

2. The Hamiltonian of a system of nonrelativistic electrons that are in a constant electric field **E** with the potential $\varphi(\mathbf{r}) = -\mathbf{rE}$ and interact with a weak photon field is represented by the sum of the Hamiltonian of electrons in an external field H_e, the Hamiltonian of free photons H_r, and the Hamiltonian of electron–photon interaction H_{er}. We introduce the photon–electron

1063-7826/01/3505-0506$21.00

interaction in a conventional manner using the vector potential $\mathbf{A}(\mathbf{r})$ and its expansion

$$\mathbf{A}(\mathbf{r}) = \sqrt{\frac{2\pi\hbar\bar{c}}{V}}\sum_{j,\mathbf{K}}\frac{\mathbf{e}_j}{\sqrt{K}}[C_{j\mathbf{K}}\exp(i\mathbf{K}\mathbf{r}) + C^+_{j\mathbf{K}}\exp(-i\mathbf{K}\mathbf{r})].$$

Here, $C^+_{j\mathbf{K}}$ and $C_{j\mathbf{K}}$ are the creation and annihilation operators for photons with momentum $\mathbf{K}$ and the polarization vector $\mathbf{e}_j$; $\bar{c} = c/\sqrt{\varepsilon}$, where c is the speed of light in free space and ε is the permittivity of the medium; $\omega = K\bar{c}$ is the photon frequency; and V is the volume of the system. If the Coulomb gage $\mathbf{e}_j\mathbf{K} = 0$ ($j = 1, 2$) is used, the Hamiltonians can be written as

$$H_e = \sum_{\sigma,\mathbf{k},\mathbf{k}'}\left[\varepsilon_{\mathbf{k}}\delta_{\mathbf{k},\mathbf{k}'} + \frac{e}{V}\varphi(\mathbf{k}-\mathbf{k}')\right]a^+_{\sigma,\mathbf{k}}a_{\sigma,\mathbf{k}'},$$

$$H_r = \sum_{j,\mathbf{K}}\hbar\omega C^+_{j\mathbf{K}}C_{j\mathbf{K}},$$

$$H_{er} = \frac{1}{\sqrt{V}}\sum_{\sigma,j,\mathbf{k},\mathbf{K}}G_j(\mathbf{k},\mathbf{K})(C_{j,\mathbf{K}} + C^+_{j,-\mathbf{K}})a^+_{\sigma,\mathbf{k}+\mathbf{K}}a_{\sigma,\mathbf{k}},$$

where

$$\varphi(\mathbf{k}) = -\int_V d^3r(\mathbf{r}\mathbf{E})\exp(-i\mathbf{r}\mathbf{k}), \quad \varepsilon_{\mathbf{k}} = \frac{\hbar^2k^2}{2m},$$

$$G_j(\mathbf{k},\mathbf{K}) = -\frac{e\hbar}{m}\sqrt{\frac{2\pi\hbar}{\varepsilon\omega}}\mathbf{k}\mathbf{e}_j,$$

$a^+_{\sigma,\mathbf{k}}$ and $a_{\sigma,\mathbf{k}}$ are the operators of creation and annihilation of electrons with momentum $\hbar\mathbf{k}$; and σ, m, and e are the spin index, effective electron mass, and electron charge ($e < 0$), respectively. The term $\sim A^2$ accounting for two-photon processes is dropped in the expression for H_{er}.

Using the nonequilibrium statistical operator [9], the method for careful consideration of the external field in the collision integral of a generalized kinetic equation [3], and the Wick–Bloch–de Dominisis theorem [10], we obtain the following kinetic equation for the mean occupation numbers for photon states in the second order of iterations over the photon–electron coupling constant:

$$\frac{\partial N_j(\mathbf{K},t)}{\partial t} = \frac{2}{\hbar^2}\frac{1}{V}\sum_{\mathbf{k}}G_j^2(\mathbf{k},\mathbf{K})\{[N_j(\mathbf{K},t)+1]\times f(\mathbf{k},t)[1-f(\mathbf{k}-\mathbf{K},t)] - N_j(\mathbf{K},t)f(\mathbf{k}-\mathbf{K},t)\times[1-f(\mathbf{k},t)]\}\int_0^\infty d\tau\left(1+\tau\frac{e}{\hbar}\frac{\mathbf{E}\mathbf{e}_j}{\mathbf{k}\mathbf{e}_j}\right)\exp(-\varepsilon\tau) \times\left\{\exp\frac{1}{i\hbar}\left[(\varepsilon_{\mathbf{k}}-\varepsilon_{\mathbf{k}-\mathbf{K}}-\hbar\omega)\tau + \frac{e\hbar}{2m}\mathbf{K}\mathbf{E}\tau^2\right] + (\text{c.c.})\right\}. \quad (1)$$

Here,

$$f(\mathbf{k},t) \equiv f_\sigma(\mathbf{k},t) = \mathrm{Tr}\rho(t)a^+_{\sigma,\mathbf{k}}a_{\sigma,\mathbf{k}},$$

$$N_j(\mathbf{K},t) = \mathrm{Tr}\rho(t)C^+_{j,\mathbf{K}}C_{j,\mathbf{K}}$$

are the distribution functions for electrons and photons; $\rho(t)$ is the statistical operator of the system; (c.c.) denotes the term that is a complex conjugate to the preceding term; and $\varepsilon > 0$ and $\varepsilon \longrightarrow 0$ following the thermodynamic passage to the limit [9]. When deriving Eq. (1), we, as usual, assumed that the single-particle distribution functions remain virtually unchanged during the interaction time [11]; i.e.,

$$f(\mathbf{k},t-\tau) \approx f(\mathbf{k},t), \quad N_j(\mathbf{K},t-\tau) \approx N_j(\mathbf{K},t).$$

For $E = 0$, the right-hand side of Eq. (1) vanishes in the nonrelativistic limit. Compton scattering by nonrelativistic electrons is also absent [12]. Thus, the nonvanishing of the collision integral is caused only by the effect of the external field on the interaction of photons with electrons. For $\mathbf{K} \parallel \mathbf{E}$ ($\mathbf{e}_j\mathbf{E} = 0$), this integral is nonvanishing due only to the broadening of the delta-function, which is caused by the external field; in contrast, for $\mathbf{K} \perp \mathbf{E}$, the collision integral is nonvanishing due only to the dependence of the coupling constant $G_j(\mathbf{k},\mathbf{K})$ on the electron momentum [a term proportional to τ appears in Eq. (1)]. It is noteworthy that the dependence of G_j on $\mathbf{k}$ manifests itself if there is an anisotropy in the electron distribution [this follows from the inversion of the $\mathbf{k}$ component in the ($\mathbf{e}_1$, $\mathbf{e}_2$) plane in Eq. (1)]; in contrast, the delta-function broadens even if the function $f(\mathbf{k})$ is isotropic. In the general case, it is impossible to integrate with respect to τ. It is also impossible to pass to the nonrelativistic limit because the corresponding parameters are in the argument of the oscillating function. However, it is possible to integrate with respect to the electron momenta, for which it is necessary to specify the electron distribution function.

The following weakly anisotropic and nondegenerate distribution represents an adequate approximation to $f(\mathbf{k})$ in a fairly wide range of parameters (the tests are known; see, e.g., [13]) for both gaseous and semiconductor plasma:

$$f(\mathbf{k}) \cong f_0(\varepsilon_{\mathbf{k}})(1 + 2\lambda^2\mathbf{k}\mathbf{k}_0). \quad (2)$$

Here, $f_0(\varepsilon_{\mathbf{k}})$ is the Maxwell distribution function

$$f_0(\varepsilon_{\mathbf{k}}) = 4\pi^{3/2} n_0 \lambda^3 \exp(-\lambda^2 k^2), \quad \lambda = \frac{\hbar}{\sqrt{2mT_e}},$$

where n_0 is the electron concentration; the drift momentum $\hbar\mathbf{k}_0$ and the electron temperature are determined by solving the balance equations for the energy and momentum. After passing from summation to integration in Eq. (1) and calculating the integral for $\mathbf{k}$ with function (2), we find that the truncating multiplier $\exp(-\alpha\omega^2\tau^2)$ ($\alpha = T_e/2m\bar{c}^2$) appears in the integral for τ. This makes it possible to write the kinetic equation in the conventional form

$$\frac{\partial N_j(\mathbf{K}, t)}{\partial t} = [N_j(\mathbf{K}, t) + 1]W_j^+ - N_j(\mathbf{K}, t)W_j^- \quad (3)$$

and represent the probabilities for emission W_j^+ and absorption W_j^- of a photon in the following form:

$$W_j^{\pm} = \frac{T_e\omega_p^2}{\hbar\omega^2}\left\{\left[s\left(1 \pm \frac{\hbar\omega}{2m\bar{c}^2}\right)^{-1} + \frac{\lambda k_0}{\beta\gamma^2}\sqrt{\frac{\gamma^2-1}{\alpha}}\right.\right.$$
$$\times(1 + \beta^2\cos^2\varphi_j)\Big][\sigma_{\pm}(\xi\cos a_{\pm} + \sin a_{\pm})$$
$$+ (I_{\pm}^{(1)} - \xi I_{\pm}^{(2)})] + \frac{\lambda k_0\beta}{\gamma^2\sqrt{\alpha}}(\cos^2\varphi_j - \cos^2\varphi) \quad (4)$$
$$\left.\times[\sigma_{\pm}(\cos a_{\pm} - \xi\sin a_{\pm}) + (1 - \xi I_{\pm}^{(1)} - I_{\pm}^{(2)})]\right\}.$$

Here,

$$\sigma_{\pm} = \sqrt{\pi\frac{a_{\pm}}{2\xi}}\exp\left(-\frac{a_{\pm}}{\sqrt{\gamma^2-1}}\right)\left[s + \mathrm{erf}\left(\sqrt{\frac{a_{\pm}}{\xi}}\right)\right], \quad (5)$$

$$\begin{Bmatrix} I_{\pm}^{(1)} \\ I_{\pm}^{(2)} \end{Bmatrix} = a_{\pm}\int_0^1 dx \exp[\xi a_{\pm}(x^2-1)/2]\begin{Bmatrix} \cos a_{\pm}(1-x) \\ \sin a_{\pm}(1-x) \end{Bmatrix}, \quad (6)$$

$$\omega_p^2 = \frac{4\pi n_0 e^2}{\varepsilon m}, \quad \xi = \frac{\sqrt{\gamma+1}}{\sqrt{\gamma-1}},$$

$$a_{\pm} = \left(1 \pm \frac{\hbar\omega}{2m\bar{c}^2}\right)\frac{\sqrt{\gamma^2-1}}{4\alpha\gamma^2}, \quad \beta = \frac{|e|E\lambda}{\hbar\omega\sqrt{\alpha}},$$

$$\gamma^2 = 1 + \beta^2\cos^2\varphi, \quad \cos\varphi = \frac{\mathbf{KE}}{KE},$$

$$\cos\varphi_j = \frac{\mathbf{Ee}_j}{E}, \quad s = -\frac{\cos\varphi}{|\cos\varphi|}.$$

For $\mathbf{K} \parallel \mathbf{E}$, it follows from expression (4) that $W_1^{\pm} = W_2^{\pm}$, which is obvious if we consider the problem's symmetry. For $\mathbf{K} \perp \mathbf{E}$ ($a_{\pm} = 0$), by using Eq. (1) and expressions (3)–(6), calculating the relevant integrals, and passing then to the nonrelativistic limit, we obtain

$$\frac{\partial N_j(\mathbf{K}, t)}{\partial t} = -\frac{8\pi e^2}{\varepsilon V}\frac{e\mathbf{E}\mathbf{e}_j}{m^2\omega^3}\sum_{\mathbf{k}}\mathbf{k}\mathbf{e}_j f(\mathbf{k}, t)$$
$$\times[1 - f(\mathbf{k} - \mathbf{K}, t)] = -\frac{\omega_p^2}{\omega^2}\frac{|e|Ek_0}{m\omega}\cos^2\varphi_j. \quad (7)$$

The negative sign of the right-hand side in Eq. (7) may be interpreted qualitatively. In the presence of a field, the electron momentum is given by $\hbar\mathbf{k} + e\mathbf{E}t$. This momentum changes during an "interaction time" owing both to the photon momentum and to the presence of the field. If a photon is emitted by an electron with a momentum of $\hbar\mathbf{k}$, the law of conservation of energy and momentum is given by

$$\varepsilon_{\mathbf{k}} - \varepsilon_{\mathbf{k}+\mathbf{k}_e-\mathbf{K}} = \hbar\omega(\hbar\mathbf{k}_e = e\mathbf{E}\tau_i),$$

for photon absorption, we have

$$\varepsilon_{\mathbf{k}} + \hbar\omega = \varepsilon_{\mathbf{k}+\mathbf{k}_e+\mathbf{K}}.$$

For nonrelativistic electrons, these conservation laws can be obeyed only owing to the terms that contain $\mathbf{kk}_e$; it is important that $\mathbf{kk}_e < 0$ for emission and $\mathbf{kk}_e > 0$ for absorption. Since in the presence of a field $\mathbf{E}$ there are fewer electrons with $\mathbf{kk}_e < 0$ than with $\mathbf{kk}_e > 0$, the absorption of photons prevails over their emission.

For $\cos\varphi \neq 0$ ($\gamma \neq 1$), the simplest approximation is $a_{\pm} \ll 1$, which means that

$$\gamma \gg 1/4\alpha, \quad \Lambda = \frac{2|e|E\lambda|\cos\varphi|}{\hbar\omega} \gg \frac{1}{2\sqrt{\alpha}}, \quad (8)$$

where Λ is a quantity on the order of magnitude of the ratio between the energy gained by electron from the external field over the de Broglie wavelength and the energy of emitted or absorbed photon. In the lowest order of expansion in a power of $a_{\pm}$, we obtain

$$\frac{\partial N_j(\mathbf{K}, t)}{\partial t} = \frac{T_e}{\hbar}\frac{\omega_p^2}{\omega^2}[\sqrt{\pi a/2}(1 + a) + 2sa]$$
$$\times\left(1 - \frac{\lambda k_0}{\sqrt{\alpha}}\frac{\cos^2\varphi_j}{\cos^2\varphi}\right),$$

where $a \approx (2\Lambda\sqrt{\alpha})^{-1}$. It is obvious that, in the situations described by Eq. (7) and expression (8), oscillations of the terms proportional to $\sigma_{\pm}$ cannot manifest themselves; thus, we have the power-law dependences of occupation numbers on ω and E. In the reverse situation when $a_{\pm} \gg \pi^2/2$ and $\xi \approx 1$, which corresponds to $\gamma \geq 2$

and $\Lambda \ll 1/\pi^2\sqrt{\alpha}$, we can also derive an approximate analytical expression for $W_j^\pm$. If we change the variables as $y = a_\pm(1 - x)$ in the expressions for $I_\pm^{(1,2)}$ and convert the integrals to the interval $(0, \pi)$, we can show that we have the following expression for $I_\pm^{(1,2)}$ in the first order in $\pi^2/a_\pm$:

$$I_\pm^{(1)} - \xi I_\pm^{(2)} \approx -\frac{2\xi}{a_\pm(1+\xi^2)^2},$$
$$1 - \xi I_\pm^{(1)} - I_\pm^{(2)} \approx -\frac{\xi(\xi^2-1)}{a_\pm(1+\xi^2)^2}. \quad (9)$$

When deriving expressions (9), we treated the terms $\exp(-l\pi\xi)$ ($l \geq 4$) as small compared to 1.

It follows from formulas (4), (5), and (9) that, for $\mathbf{k}_0\mathbf{K} < 0$ ($\cos\varphi > 0$ and $s = -1$), $\sigma_\pm$ is an exponentially small quantity and $W_j^\pm$ are nonoscillating functions. For $\mathbf{k}_0\mathbf{K} > 0$ ($\cos\varphi < 0$ and $s = 1$), the terms containing $\sigma_\pm$ prevail over the terms (9) if $\Lambda \geq 1$ ($a_\pm/\sqrt{\gamma^2 - 1} \leq 1$), which is consistent with the condition for applicability of the given approximation. The probabilities $W_j^\pm$ may then depend in an oscillatory manner on ω and $E\cos\varphi$. Since an electron is localized in space to an accuracy of the de Broglie wavelength λ and since, over the distance λ, the electron energy ε changes by $\Delta\varepsilon \approx |e|E\lambda|\cos\varphi|$ owing to the electric field, the inequality $\Lambda \geq 1$ may be rewritten in the form of the energy–time uncertainty relation $\Delta\varepsilon\Delta t \geq \hbar$, where $\Delta t = 2\pi/\omega$. This is consistent with oscillations originating from the field-induced violation of the delta-shaped law of conservation of energy. The period of oscillations in their domain of existence is frequency-independent when the photon frequency is changed by the quantity

$$\frac{\Delta\omega}{\omega} \cong \pi\sqrt{\alpha}\Lambda \sim \frac{v}{\bar{c}} \ll 1, \quad (10)$$

where v is the thermal velocity of electrons. The estimate of the period as a function of the electric-field component along the photon-propagation direction has the form

$$\frac{\Delta|E\cos\varphi|}{|E\cos\varphi|} \cong 2\pi\alpha \propto \frac{v^2}{\bar{c}^2} \ll 1. \quad (11)$$

Inequalities (10) and (11) impose natural restrictions on the feasibility of observing the oscillations of the probabilities for the absorption and emission of photons. A pronounced anisotropy of the effect as a function of the photon-propagation direction in reference to the external-field direction is analogous to the classical situation when the Lienard–Wiechert potentials are considered [14], the reason being that the acceleration of electrons is accounted for in the scattering cross section in spite of a constant mean velocity of electrons.

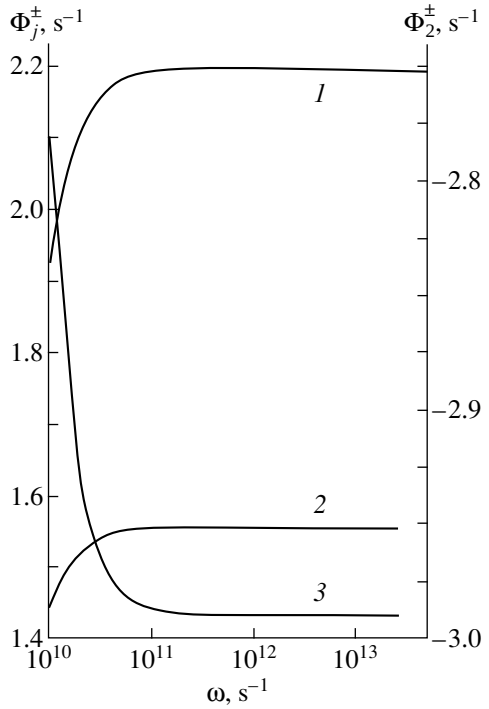

Fig. 1. The frequency dependences of probabilities for absorption and emission of photons $\Phi_j^\pm$. Curve *1* corresponds to $\Phi_{1,2}^\pm \times 10^{-9}$ and $\varphi = 0$; curve *2* is for $\Phi_1^\pm \times 10^{-9}$ and $\varphi = \pi/4$; and curve *3* is for $\Phi_2^\pm \times 10^{-11}$ and $\varphi = \pi/4$.

Figures 1 and 2 show the results of numerical calculations of the quantity $\Phi_j^\pm = \frac{2\hbar}{T_e}\frac{\omega^3}{\omega_p^2}W_j^\pm$ for free charge carriers in *n*-GaAs ($\varepsilon = 12.79$ and $m = 0.07m_0$) at the lattice temperature of $T = 80$ K and for $n_0 = 10^{16}$ cm^{-3}, $E = 367.6$ V/cm, $T_e = 101$ K, $\lambda k_0 = 0.34$ (the results of solving the balance equation for energy and momentum correspond to the data reported previously [8]), $\varphi_1 = \pi/2(\Phi_1^\pm)$ and $\varphi_2 = \varphi + \pi/2(\Phi_2^\pm)$. According to Eq. (7), $\Phi_1^\pm = 0$ and $\Phi_2^\pm$ = constant for $\varphi = \pi/2$. The functions Φ_j^+ and Φ_j^- cannot be distinguished in Fig. 2; the crowding of oscillations is due to logarithmic scale on the horizontal (ω) axis. A plot of $\Phi_{1,2}^\pm$ for $\varphi = \pi$ differs from a plot of $\Phi_1^\pm$ for $\varphi = 3\pi/4$ in a somewhat larger amplitude ($\sim 5 \times 10^{13}$ s^{-1}).

3. We now consider the contribution of the above effect to the intraband emission from a semiconductor in reference to the background emission in the situation when electrons interact with phonons and impurities.

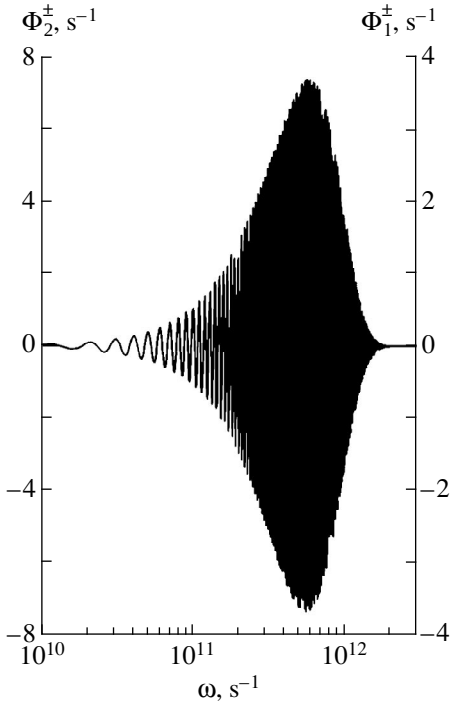

Fig. 2. The frequency dependences of normalized probability for the absorption and emission of photons $\Phi_j^{\pm}$ for $\Phi_1^{\pm} \times 10^{-13}$ and $\Phi_2^{\pm} \times 10^{-15}$; $\varphi = 3\pi/4$.

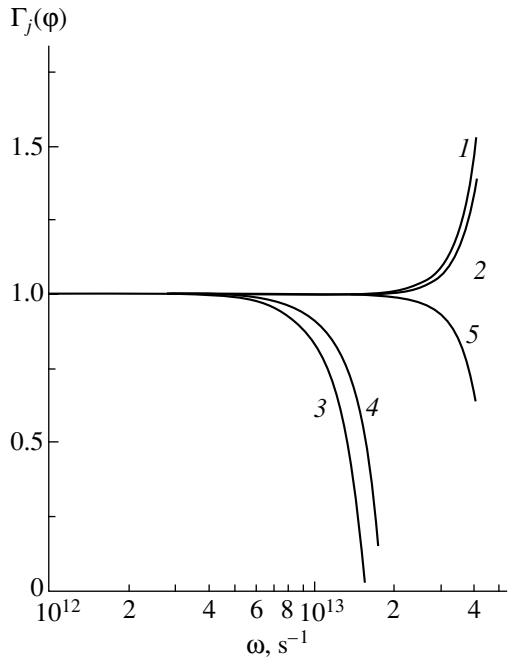

Fig. 3. Dependences of the relative number of photons $\Gamma_j(\varphi)$ on the frequency ω for various angles φ. The curves correspond to (*1*) $\Gamma_{1,2}$ for $\varphi = 0$; (*2*) Γ_1 for $\varphi = \pi/4$; (*3*) Γ_2 for $\varphi = \pi/4$; (*4*) Γ_2 for $\varphi = \pi/2$; and (*5*) Γ_1 for $\varphi = 3\pi/4$.

The corresponding kinetic equation has the same form as Eq. (3); however, the quantity $W_j^{\pm}$ in Eq. (3) should be replaced by

$$M_j^{\pm} = W_j^{\pm} + F_j^{\pm},$$

where

$$F_j^{+} = F_j^{\mathrm{po}}(\omega) + F_j^{\mathrm{im}}(\omega),$$

$$F_j^{-} = -F_j^{\mathrm{po}}(-\omega) - F_j^{\mathrm{im}}(-\omega).$$

The functions $F_j^{\mathrm{po}}(\omega)$ and $F_j^{\mathrm{im}}(\omega)$ correspond to the emission of a photon $\hbar\omega$ in the case of scattering by optical phonons and ionized impurities, whereas the functions $F_j^{\mathrm{po}}(-\omega)$ and $F_j^{\mathrm{im}}(-\omega)$ correspond to the absorption of a photon. These quantities were expounded in [8]. A solution to the kinetic equation has the following form:

$$N_j(\mathbf{K}, t) = N_{\mathrm{eq}}\exp[-B_j(t-t_0)] + N_{0j}\{1-\exp[-B_j(t-t_0)]\}.$$

Here, $N_{\mathrm{eq}} = N_j(\mathbf{K}, t_0)$ is the initial distribution, which is assumed to be the equilibrium one with a temperature of T; and

$$N_{0j} = A_j/B_j, \quad A_j = W_j^{+} + F_j^{+},$$

$$B_j = W_j^{-} - W_j^{+} + F_j^{-} - F_j^{+}.$$

The steady-state distribution N_{0j} exists if

$$\exp[-B_j(t-t_0)] \ll 1, \quad N_{\mathrm{eq}}\exp[-B_j(t-t_0)] \ll N_{0j},$$

i.e., if the emitted photon is absorbed in the same system, and if the stimulated processes are induced by the nonequilibrium distribution of photons. This means that the characteristic relaxation time B_j^{-1} should be much shorter than the time of transit of a photon through a specific medium; i.e., $B_j^{-1} \ll l/\bar{c}$ (l is the crystal size). In the opposite situation, we obtain the rate of emission of photons from the medium [8]. Estimations show that this situation is quite feasible in the studied frequency region of $\omega < \Omega$ (Ω is the optical-phonon frequency); thus, approximation (2) is valid.

It follows from numerical calculations for the same parameters that the quantity $B_j > 0$ does not oscillate, because $|W_j^{+} - W_j^{-}|$ is small and the relaxation is controlled by the background processes. Figure 3 shows the curves $\Gamma_j(\varphi) = N_{0j}/N_{pj}$, where N_{0j} ($N_{pj} = N_{0j}$ for $W_j^{\pm} = 0$) is the steady-state distribution of the nonequilibrium background emission. A profound effect of the phenomenon under consideration on the phonon spectrum manifests itself for $\omega > 10^{13}$ s^{-1} ($\hbar\omega/T_e \approx 1$) owing to the fact that F_j^{+} depends on frequency approximately as

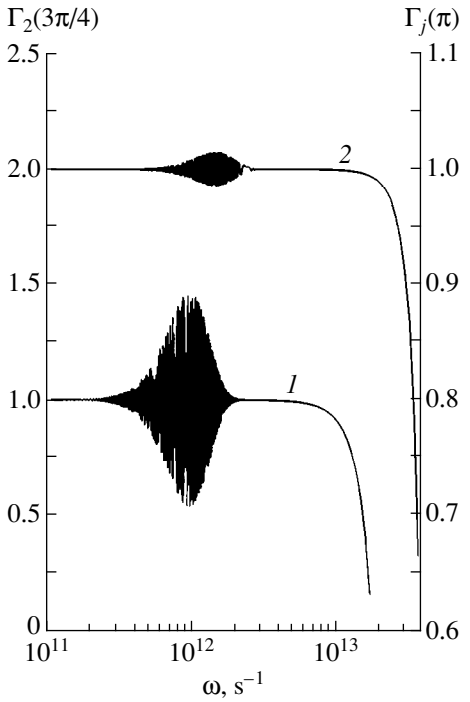

Fig. 4. Dependences of the relative number of photons $\Gamma_j(\varphi)$ on the frequency ω for various angles φ. Curve *1* corresponds to Γ_2 for $\varphi = 3\pi/4$ and curve *2* corresponds to Γ_j for $\varphi = \pi$.

$\exp(-\hbar\omega/T_e)$ [8], whereas W_j^+ decreases at these frequencies following approximately the power law (this can be seen from Fig. 1). For $\omega \approx \Omega \approx 5.5 \times 10^{13}$ s^{-1}, the emission from the crystal lattice becomes important and affects the background emission. Figure 4 shows the spectrum oscillations that correspond to Fig. 2. Oscillations in $\Gamma_1 = N_{01}/N_{p1}$ have a small amplitude for $\varphi = 3\pi/4$ and do not manifest themselves in the plot. It follows from the shape of curves *2* and *5* in Fig. 3 that the ratio $\Gamma_1(\pi/4)/\Gamma_1(3\pi/4)$ is not small for $\omega \approx 3$–4×10^{13} s^{-1}. In addition, $N_{p1}(\pi/4) = N_{p1}(3\pi/4)$ as a result of dependence on $(\mathbf{e}_j\mathbf{E})^2$ [8]. The same situation takes place for $\Gamma_j(0)/\Gamma_j(\pi)$ ($j = 1, 2$); i.e., the number of photons varies significantly (by a factor of 2–3) when the sign of **E** reverses. This makes it possible to verify experimentally this effect beyond the range of oscillations.

Thus, a constant electric field can affect the photon-emission spectrum not only due to the nonequilibrium nature of the electron distribution function but also because it changes the probabilities of the photon emission and absorption.

ACKNOWLEDGMENTS

We thank Professor M.I. Ryazanov for his participation in discussions concerning certain results of this study.

REFERENCES

1. V. P. Silin, *An Introduction to the Kinetic Theory of Gases* (Nauka, Moscow, 1971).
2. É. M. Épshteĭn, Izv. Vyssh. Uchebn. Zaved., Radiofiz. **18**, 785 (1975).
3. R. Kh. Amirov, S. A. Smolyanskiĭ, and L. Sh. Shekhter, Teor. Mat. Fiz. **21**, 247 (1974).
4. J. R. Barker, J. Phys. C **6**, 2663 (1973).
5. J. R. Barker, Solid-State Electron. **21**, 267 (1978).
6. R. Kh. Amirov and O. G. Zudeev, J. Phys.: Condens. Matter **2**, 6771 (1990).
7. R. Kh. Amirov, O. G. Zudeev, and V. A. Ivanchenko, Fiz. Tekh. Poluprovodn. (Leningrad) **18**, 1836 (1984) [Sov. Phys. Semicond. **18**, 1147 (1984)].
8. R. Kh. Amirov and O. G. Zudeev, Fiz. Tekh. Poluprovodn. (St. Petersburg) **30**, 3 (1996) [Semiconductors **30**, 1 (1996)].
9. D. N. Zubarev, *Nonequilibrium Statistical Thermodynamics* (Nauka, Moscow, 1971; Consultants Bureau, New York, 1974).
10. S. V. Tyablikov, *Methods in the Quantum Theory of Magnetism* (Nauka, Moscow, 1971, 2nd ed.; Plenum, New York, 1967).
11. N. N. Bogolyubov, in *Studies in Statistical Mechanics*, Ed. by J. de Boer and G. E. Uhlenbeck (Wiley, New York, 1961), p. 5; *Problems of Dynamic Theory in Statistical Physics* (Gostekhizdat, Moscow, 1946).
12. W. Heitler, *The Quantum Theory of Radiation* (Clarendon, Oxford, 1936; GITTL, Moscow, 1940).
13. F. G. Bass and Yu. G. Gurevich, *Hot Electrons and High-Power Electromagnetic Waves in a Plasma in Semiconductors and Gas Discharge* (Nauka, Moscow, 1975).
14. V. L. Ginzburg, *Theoretical Physics and Astrophysics* (Nauka, Moscow, 1981; Pergamon, Oxford, 1979).

Translated by A. Spitsyn

Semiconductors, Vol. 35, No. 5, 2001, pp. 512–515. Translated from Fizika i Tekhnika Poluprovodnikov, Vol. 35, No. 5, 2001, pp. 534–536.

ELECTRONIC AND OPTICAL PROPERTIES OF SEMICONDUCTORS

Studies of the Infrared Luminescence of ZnSe Doped with Copper and Oxygen

N. K. Morozova*, I. A. Karetnikov*, V. V. Blinov*, and E. M. Gavrishchuk**

** Moscow Power Institute (Technical University), ul. Krasnokazarmennaya 17, Moscow, 111250 Russia*
e-mail: MorozovaNK@mpei.ru
*** Institute of Chemistry of High-Purity Materials, Russian Academy of Sciences, ul. Tropinina 49, Nizhni Novgorod, 603600 Russia*

Submitted October 9, 2000; accepted for publication November 9, 2000

Abstract—The results of studying the poorly understood 700- to 2000-nm spectral region in ZnSe cathodoluminescence of condensates deposited from the vapor phase with deviations from stoichiometry and Cu and O introduction into a pure matrix are reported. The nature of cathodoluminescence in the region of 1300–1400 nm is refined: the conclusion is drawn that the emission is caused by isolated $V_{Zn}^{I(II)}$ vacancies. The behavior of V_{Se}-related luminescence bands at 830 and 960 nm, when the matrix composition changes, is considered. © *2001 MAIK "Nauka/Interperiodica".*

The data on the intense band that appears in the spectral range of 1250–1400 nm (80 K) of the ZnSe luminescence spectrum and depends on the presence of O, Cu, and Te impurities are reported in a number of publications [1–5].

It has been shown [5] that the cathodoluminescence (CL) in this range is caused by doping with Cu. Its spectral position approximately corresponds to the position of bands caused by intracenter transitions in Cu_{Zn}^{+2} ions with $3d^9$ configuration, which are well known for a number of II–VI compounds: ZnS, ZnO, and CdS (see table). Data on similar spectra for ZnSe are scanty and contradictory [11–13]. Previously [5], the band at ~1300 nm was attributed, according to the Bube scheme [11], to transitions $G(^2E) \longrightarrow E_{5/2}(^2T_2)$ and to corresponding emission Cu–*R* due to transitions from the conduction band to the level of Cu_{Zn}^{+2} ($3d^9$) ion. However, a more detailed study of ZnSe:Cu and ZnSe:O condensates formed by the chemical-vapor deposition (CVD) [9] involved the difficulties in using such an interpretation of the nature of the CL band at 1300–1400 nm (80 K). In addition, the condensates in [14] were grown with the Se excess, i.e., under conditions when the Cu ion transforms from the $3d^{10}$ into the $3d^9$ state.

The CL spectra of ZnSe:Cu and ZnSe:O samples reported previously [14] were not discussed for the range of 700–2000 nm; therefore, the data in this paper are complementary to those in [14]. Recall that CVD technology [15] was used for preparation of the samples; this technology allows one to obtain a rather pure ZnSe, to dope it controllably with Cu in the course of the growth by varying the Zn or Se excess with respect to the stoichiometric composition, and to introduce various amounts of oxygen. This made it possible to form various types of Cu centers or complexes [14]. At 700°C, a number of polycrystalline ZnSe samples were deposited. The content of other impurities in the undoped ZnSe samples were as follows: Na, K, Mg, Ca, B, Al, Sn, Pb, P, As, Cl, I, Ag, Cr, Mn, Fe, Co, Ni, and Cu ≤ 10^{15} cm^{-3}; Si, Cd, and N ≤ 10^{16} cm^{-3}; and O ≥ 10^{18} cm^{-3} [1].

The ZnSe:Cu–*A* sample had an increased oxygen concentration [O] ≈ 10^{20} cm^{-3} and was grown with the ratio of concentrations H_2Se/Zn in the vapor phase equal to 1.6. In the main part of samples *A* (as also *B*), the copper concentration was ~10^{16} cm^{-3}. The ZnSe:Cu–*B* sample with lower oxygen content (~10^{18} cm^{-3}) was obtained with the higher excess of Se compared to sample *A* due to an increase in concentration ratio H_2Se/Zn up to 1.7. By growing these samples from the H_2Se and Zn vapors, Cu was introduced in the growth process together with Zn via the vapor phase [4]. As is known, the most homogeneous crystal grows from the vapor phase and the formation of isolated Cu_{Zn} centers is pos-

Peaks of main emission bands for Cu_{Zn}^{+2} ($3d^9$)

Transitions	ZnS [6, 7]	ZnO [8]	CdS [4, 9, 10]
$G(^2E) \longrightarrow E_{5/2}(^2T_2)$	1490 nm	–	1631 nm
$G(^2E) \longrightarrow G(^2T_2)$	1636 nm	1730 nm absorption	1850 nm
Transitions to the valence band	1796 nm	1820 nm	2066 nm

sible. In addition, the ZnSe:Cu–*D* samples were obtained without the special introduction of oxygen but with Cu doping up to 10^{18}–10^{20} cm^{-3} by thermal diffusion (during the growth). The concentration ratio H_2Se/Zn was 1.2, and [O] was reduced in the range of 10^{20}–10^{18} cm^{-3} with [Cu] increasing.

The *C* and *C*' (ZnSe:O) samples were grown without the special doping with Cu using the same setup with addition of 0.9 and 4.3 vol % of O_2 in the vapor phase for the ratio H_2Se to Zn concentrations equal to 1.2 and 1.0, respectively. $[O]_p$ in the central part of samples was $<10^{19}$ and $\sim10^{20}$ cm^{-3}, respectively.

The CL spectra were studied at fresh cleavages of the samples by a step-by-step method. The details of the technique have been described recently [14].

We consider the CL study results in the range of 1300–1400 nm for the ZnSe:Cu and ZnSe:O CVD-samples, the CL spectra of which in the spectral range 400–2000 nm have been described previously [11]; for the range of 700–2200 nm, the typical spectra are shown in Fig. 1.

For the ZnSe:Cu–*A* sample (see [14]) in the initial part, where the introduction of zinc into the reactor occurs, the 1300- to 1400-nm band is absent, though the Cu concentration in this region is $>10^{17}$ cm^{-3}. At the end of sample *A*, under conditions of Se excess, with the increase of Cu concentration to $>10^{17}$ cm^{-3}, the intensity of the 1300- to 1400-nm band decreases too. For constant [Cu] and [O] in the central part of sample *A*, the intensity of the 1300- to 1400-nm band gradually increased (see Fig. 1 in [14]). In all these cases, an increase in the Se excess occurs. However, the correlation of the intensity change of the 1300-nm band and Cu–*R* is irrelevant, since, in the structure of the Cu–*R* center, Cu is present in the form of $3d^{10}$ ion, whereas the intracenter transitions in the vicinity of 1300 nm are considered for $3d^9$ ion (see Table 1 in [14]).

It turned out that the behavior of the 1300-nm band correlated with the intensity change of IR bands at 830 and 960 nm in the CL of sample *A*; i.e., the 1300–1400 nm band appears simultaneously with these two bands (see Fig. 1 in [14]). As is known [16, 17], the 830- and 960-nm bands in ZnSe are caused by V_{Se}: by the intracenter transition (between the excited and ground levels) and by the transition from the conduction band (E_c) to the ground level, respectively (Fig. 2a).

The 830-nm band ($V_{Se}^{\times}$) dominates under conditions of Zn excess in ZnSe [1–4]. As the concentration of [Zn] is reduced, both bands are observed. The 960-nm band increases in intensity when the charged states of the $V_{Se}^{\bullet}$ center dominate with the lowering of the Fermi level. One can observe both charged states of $V_{Se}^{\times(\bullet)}$ Se vacancies if the Fermi level is close to the ground level of the F^+ center (Fig. 2b). In this case, using the ratio of

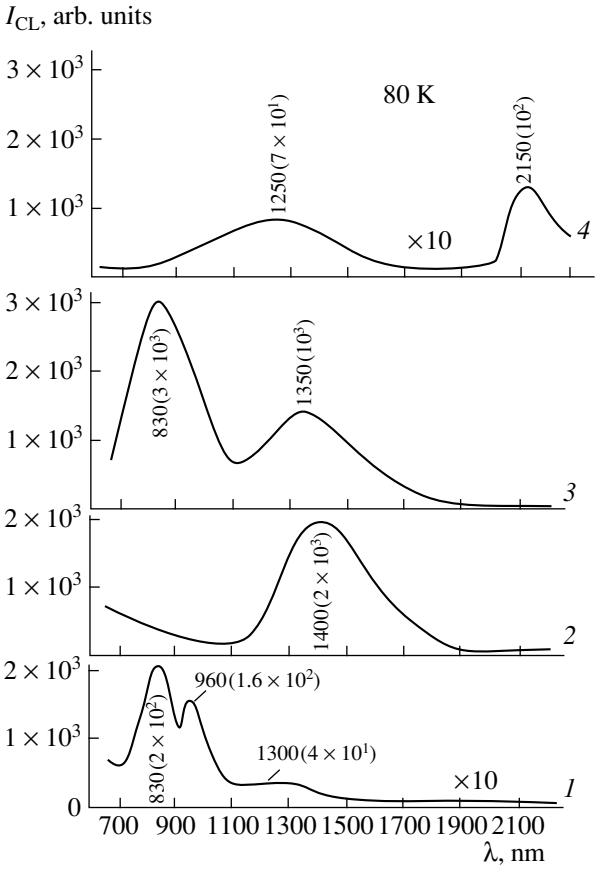

Fig. 1. Typical IR spectra of (*1*, *2*) ZnSe:Cu samples *A* and *B* obtained with the Se excess and [Cu] = 10^{16} cm^{-3} in the central part of the sample; (*3*, *4*) ZnSe:O samples *C* and *C*' obtained without special doping with Cu but with the introduction of 0.9 and 4.3% of O_2 into the vapor phase in the process of growth, respectively.

intensities of 960- and 830-nm bands, we can evaluate the change in the Fermi level position with respect to the level of $V_{Se}^{\times(\bullet)}$. The lowering of *F* is possible with an increase in concentration of intrinsic acceptors [V_{Zn}]. Simultaneously, the probability of transitions from E_c to $V_{Zn}^{I(II)}$ levels increases (Fig. 2b). According to the scheme in Fig. 2b, the CL band at 1300–1400 nm can be caused by the transitions mentioned above, and a certain difference in the band peak position can be explained by the presence of a shallow-level donor. Similar bands are characteristic of II–VI compounds, e.g., CL bands at 1030 nm in CdS [9], at 950 nm in ZnS [6], etc.

Actually, the facts considered above are not contradictory to the possibility of Zn vacancy origination under conditions of an increase in the intensity of 1300-nm band. In particular [2, 3], the intensity enhancement by 4 orders of magnitude for 1300-nm band in ZnSe CL was observed due to the excess of

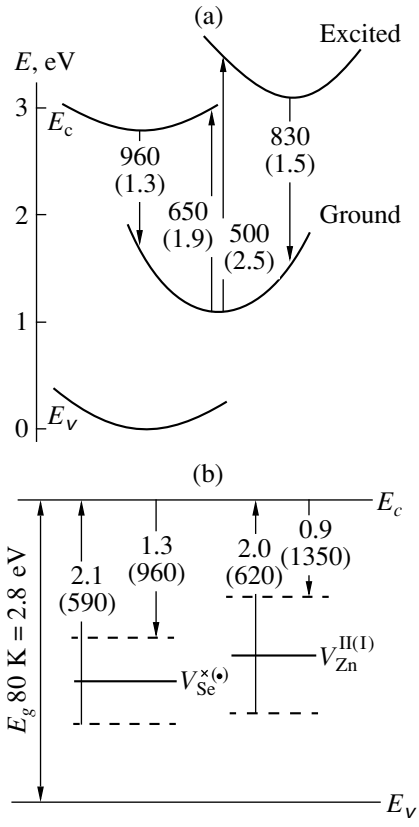

Fig. 2. (a) Model of F^+ center and (b) the scheme of level positions of Se and Zn vacancies in the ZnSe band gap [10–12].

metalloid (by Te introduction). It was noted [18] that in this case, the generation of Zn vacancies takes place.

In addition, the comparison of the intensities of 1300- to 1400-nm band for all samples (*A*, *B*, and *C*) was carried out for fixed (along length *L*) regions, for which a number of parameters are constant but only one changes. Thus, there is a region of constant [O] and [Cu] in sample *B*, but the Se excess increases along the length of the sample [14]. The CL intensity enhancement of the 1400-nm band correlates with an intensification of the 740-nm band (see Fig. 2a in [14]). A similar region is present also in sample *A* (Fig. 1 in [14]). For both cases, the intensity of 1300- to 1400-nm band increases with the Se excess, i.e., with the increase in $[V_{Zn}]$. Moreover, the intensity of the 1300- to 1400-nm band is higher by 1–3 orders of magnitude for sample *B* (grown under condition of the largest ratio of concentrations H_2Se/Zn equal to 1.7) than the intensity of this band for sample *A*.

In the region with a constant [Cu], such a large difference is likely associated also with [O], which reaches the value of 10^{20} cm^{-3} in sample *A*; as is shown in [2], the 1300- to 1400-nm CL is most efficient for a "low" oxygen concentration (about 10^{19} cm^{-3}). A decrease in the intensity of the 1300- to 1400-nm band is presumably caused by the reduction of the isolated Zn vacancy concentration $[V_{Zn}^{I(II)}]$. We may assume that, in the growth process with large Se and O_2 excess in a vapor phase, the intense formation of vacancies results in the origination of pores. This is confirmed by examining the cleavages of crystalline samples *C* and, especially, crystals *C*' using a scanning-electron microscope.[1]

To eliminate the Cu influence, we note that the intensity of the 1300- to 1400-nm band for sample *C* grown without doping with Cu with $[O] \approx 10^{20}$ cm^{-3} did not decrease; rather, it increased compared to that in sample *A*. The Cu introduction at a concentration of $>10^{18}$ cm^{-3} for sample *D* resulted in a complete disappearance of CL in the 1300- to 1400-nm region; i.e., Cu is not involved in this effect or affects V_{Zn} indirectly. Thus, Cu can occupy $[V_{Zn}]$ or, being an acceptor, can reduce the concentration of these defects.

Correlation of the 1300-nm band intensity with [Cu] reported in [5] can be caused by the [Cu] influence on the *F* level position and $[V_{Zn}]$. In addition, a number of CL bands with peaks at 1300, 1600, and 1750 nm were observed in ZnSe:Cu [5]. Such positions of peaks approximately correspond to the main components in the Cu ($3d^9$) ion spectrum (see the table). It is not improbable that the intracenter transitions in the Cu ion with $3d^9$ configuration can take place also for ZnSe:Cu. However, the more intense bands of native defects are superimposed upon the emission, whereas similar bands in the IR spectral range for other II–VI compounds (ZnS and CdS) are separated in the spectrum from the luminescence of Cu ($3d^9$) ion.

REFERENCES

1. N. K. Morozova, E. M. Gavrishchuk, O. R. Golovanova, *et al.*, Zh. Prikl. Spektrosk. **63**, 731 (1996).
2. L. D. Nazarova, Author's Abstract of Candidate's Dissertation (Moscow, 1995).
3. L. P. Gal'chinetskiĭ, I. A. Karetnikov, V. E. Mashchenko, *et al.*, Zh. Prikl. Spektrosk. **58**, 488 (1993).
4. N. K. Morozova, I. A. Karetnikov, V. V. Blinov, *et al.*, in *Proceedings of the XXX International Scientific and Technical Workshop on Noise and Degradation Processes in Semiconductor Devices* (Mosk. Énerg. Inst., Moscow, 2000), p. 204.
5. N. K. Morozova and O. R. Vinogradova, Neorg. Mater. **35**, 792 (1999).
6. G. N. Ivanova, V. A. Kasiyan, D. D. Nedeoglo, and S. V. Oprya, Fiz. Tekh. Poluprovodn. (St. Petersburg) **32** (2), 171 (1998) [Semiconductors **32**, 154 (1998)].

[1] In the CL of a similar sample (*C*') grown with the introduction of 4.3% O_2 in a vapor phase, a longer wavelength band at 2150 nm in the IR spectral region was observed (Fig. 1); at the same time, the bands caused by V_{Se} disappear by introducing O_2 in a significant amount (curve *4*), similar to a large Se excess (curve *2*).

7. *Physics and Chemistry of II–VI Compounds*, Ed. by M. Aven and J. S. Prener (North-Holland, Amsterdam, 1967; Mir, Moscow, 1970).
8. N. P. Golubeva and M. V. Fok, Zh. Prikl. Spektrosk. **35**, 551 (1981).
9. *Physics of II–VI Compounds*, Ed. by A. N. Georgobiani (Nauka, Moscow, 1986).
10. N. K. Morozova, I. A. Karetnikov, and E. M. Gavrishchuk, Neorg. Mater. **35**, 917 (1999).
11. G. B. Stringfellow and R. H. Bube, Phys. Rev. **14** (3), 903 (1968).
12. M. Godlewski, W. E. Lamb, and B. C. Cavenett, Solid State Commun. **39**, 595 (1981).
13. V. I. Sokolov, T. P. Surkova, M. V. Chukichev, and Vu Zoan M'en, Fiz. Tverd. Tela (Leningrad) **26**, 3681 (1984) [Sov. Phys. Solid State **26**, 2215 (1984)].
14. N. K. Morozova, I. A. Karetnikov, V. V. Blinov, and E. M. Gavrishchuk, Fiz. Tekh. Poluprovodn. (St. Petersburg) **35** (1), 25 (2001) [Semiconductors **35**, 24 (2001)].
15. G. G. Devyatykh, E. M. Gavrishchuk, and Yu. A. Dadanov, Vysokochist. Veshchestva **2**, 174 (1990).
16. F. J. Bryant and P. S. Manning, J. Phys. C **5**, 1914 (1972).
17. A. P. Okonechnikov, Author's Abstract of Doctoral Dissertation (Yekaterinburg, 1996).
18. V. D. Ryjikov, V. Havrushin, A. Klazlauskaz, *et al.*, J. Lumin. **52** (1–4), 71 (1992).

Translated by T. Galkina

Semiconductors, Vol. 35, No. 5, 2001, pp. 516–519. Translated from Fizika i Tekhnika Poluprovodnikov, Vol. 35, No. 5, 2001, pp. 537–540.

ELECTRONIC AND OPTICAL PROPERTIES OF SEMICONDUCTORS

On the Origin of the Luminescence Band with $h\nu_m$ = 1.5133 eV in Gallium Arsenide

K. D. Glinchuk*, N. M. Litovchenko, A. V. Prokhorovich, and O. N. Stril'chuk

Institute of Semiconductor Physics, National Academy of Sciences of Ukraine, pr. Nauki 45, Kiev, 03028 Ukraine

** e-mail: ria@isp.kiev.ua*

Submitted September 14, 2000; accepted for publication November 21, 2000

Abstract—The excitation-level dependence of intensities of the luminescence bands with $h\nu_m$ = 1.5133, 1.5141, and 1.5153 eV in semi-insulating GaAs crystals at 4.2 K was examined. The dependences obtained for all three bands are identical. The analysis of these results indicates that, in this material, the luminescence band with $h\nu_m$ = 1.5133 eV is related to the annihilation of the exciton–impurity complexes D^+X (excitons X being bound to ionized shallow donors D^+). © *2001 MAIK "Nauka/Interperiodica".*

1. INTRODUCTION AND PROBLEM FORMULATION

It is known that the edge luminescence spectrum of gallium arsenide at 4.2 K contains intense bands with peaks at $h\nu_m$ = 1.5133, 1.5141, and 1.5153 eV (see, e.g., [1–9]). The origin of the bands with $h\nu_m$ = 1.5153 and 1.5141 eV is established reliably: they are related to the radiative annihilation of the free excitons X (the emission intensity I_X, reaction $X \longrightarrow h\nu$) and the exciton–impurity complexes D^0X composed of an exciton X bound to a shallow neutral donor D^0 (reaction $D^0X \longrightarrow D^0 + h\nu$), respectively [1–4]; we denote the corresponding emission intensities by I_X and I_{D^0X}. Meanwhile, the origin of the luminescence band with $h\nu_m$ = 1.5133 eV (we denote its intensity by $I_{1.5133}$) is not yet established unambiguously. In some of the studies (see [1, 2, 5]), this band is related to the radiative annihilation of the exciton–impurity complexes D^+X composed of an exciton X bound to a shallow ionized donor D^+ (reaction $D^+X \longrightarrow D^+ + h\nu$; I_{D^+X} will denote the corresponding emission intensity). This assignment was substantiated by the agreement between the experimentally measured energy position of this band and the theoretically calculated photon energy corresponding to the radiative annihilation of the bound excitons D^+X [1], by an increase in the intensity of this band with a change of the conductivity type of the crystal from n to p (i.e., with an increase in the ionized donor concentration N_{D^+}) [1, 2], and by the analysis of the observed shift of the band maximum in the magnetic field [2, 5]. However, in other studies (see [3, 4, 6]), the luminescence band with $h\nu_m$ = 1.5133 eV is related to the recombination of the free holes h at the shallow neutral donors D^0, i.e., to the radiative annihilation of D^0h pairs (reaction $D^0h \longrightarrow D^+ + h\nu$; I_{D^0h} will denote the corresponding emission intensity). This assignment is based on the fact that the thermal dissociation energy of the centers responsible for the emission at 1.5133 eV is close to the ionization energy of the neutral donors D^0 [1, 2, 6]; on the analysis of the band shape [3], as well as the electric field dependence of the band shape [4]; and on the observation of quenching of the band intensity under the influence of an electric field [4]. It was originally assumed that the experimental data on the resonance excitation of the luminescence band with $h\nu_m$ = 1.5133 eV in GaAs also indicate that this band originates from the D^0h pair recombination radiation [3]. However, a detailed analysis carried out in [2], based on the data reported in [3] and on similar results reported in [2], revealed that measurements of the excitation spectra of this luminescence band do not give arguments in favor of this or any other model: these spectra may be attributed to radiative annihilation of both D^+X bound excitons and D^0h pairs. The authors of [3, 6] also believed that their data on the dependence of $I_{1.5133}$ and I_{D^0X} upon the excitation density L corroborate the assignment of the band with $h\nu_m$ = 1.5133 eV to the D^0h pair recombination. However, unambiguous evidence in support of any model of the origin of this band cannot be obtained from the comparison of the dependences $I_{1.5133}(L)$ and $I_{D^0X}(L)$ without careful analysis (see below); such an analysis was not carried out in [3, 6].[1]

[1] To analyze the excitation-level dependences of the emission intensity $I = \varphi(L)$ in detail, one needs to know the relationship between the concentrations of nonequlibrium and equilibrium charge carries, as well as the dependences of excess electron and hole concentrations and ionized and neutral donor concentrations on the excitation density L and the coordinate y.

1063-7826/01/3505-0516$21.00 © 2001 MAIK "Nauka/Interperiodica"

It follows from the above discussion that further investigations aimed at clarifying the origin of the $h\nu_m$ = 1.5133 eV luminescence band in GaAs are of considerable interest.

In this study, we carry out a detailed comparative analysis of the excitation-level dependence of the intensities of luminescence bands with $h\nu_m$ = 1.5133, 1.5141, and 1.5153 eV in semi-insulating GaAs crystals at 4.2 K. We demonstrate that the observed dependences of the edge-luminescence band intensities point to the D^+X bound-exciton-annihilation nature of the $h\nu_m$ = 1.5133 eV emission in GaAs.

2. EXPERIMENTAL

Semi-insulating GaAs crystals were grown by the Czochralski method in pyrolytic boron nitride crucibles with liquid B_2O_3 flux encapsulation at high pressure. The resistivity of the samples was $\rho \approx 10^8\ \Omega$ cm at T = 300 K and $\rho \longrightarrow \infty$ at $T \le 200$ K. The equilibrium electron concentration was $n_0 \approx 10^7$ cm^{-3} at T = 300 K and $n_0 \longrightarrow 0$ at $T \le 200$ K, and the electron mobility at 300 K was $\mu_n \approx 6000$ cm^2 V^{-1} s^{-1}; the equilibrium hole concentration $p_0 \ll n_0$. The dark conductivity of the samples was controlled by the ionization of the *EL*2 deep-level donors (antisite defects As_{Ga}, which form the level with the energy $\varepsilon_{EL2} \simeq 0.75$ eV) with the density $N_{EL2} \simeq 10^{16}$ cm^{-3} and are partially compensated by the residual shallow-level acceptors (C atoms with the concentration $N_C \simeq 3 \times 10^{15}$ cm^{-3}), and donors (Si atoms with the concentration $N_{Si} \simeq 10^{15}$ cm^{-3}) [10, 11].

The luminescence was excited by strongly absorbed He–Ne laser radiation (the photon energy equals 1.96 eV and the absorption coefficient $k = 2.5 \times 10^4$ cm^{-1}); the laser beam was directed along the *y*-axis, and the spot area on the sample surface was $s \simeq 10^{-2}$ cm^2. The typical crystal size was $1 \times 0.3 \times 0.2$ cm. Prior to taking the measurements, the samples were treated in a polishing etchant composed of $H_2SO_3 : H_2O_2 : H_2O$ in the proportion of 3 : 1 : 1. The luminescence spectra were recorded using an MDR-23 spectrometer with a resolution no worse than 0.2 meV. The shape of the spectra (the positions of the peaks $h\nu_m$ and the half-widths w of the bands and the intensity relationship between the bands) was virtually independent of L within the limits of the measurement error (±0.1 meV for $h\nu_m$ and w and ±10% for I).

The intensities of the luminescence bands under investigation (which, obviously, depended to a large extent on the concentrations of excess electrons δn and holes δp) were controlled by the processes in the bulk of the crystal (the diffusion length of the excess charge carriers $l_d \le 1/k$). The emission region was located near the crystal surface: its length in the *y* direction, approximately equal to $l_d + 1/k \simeq 10^{-4}$ cm, was significantly smaller than the corresponding sample dimension $d \simeq 0.2$ cm.

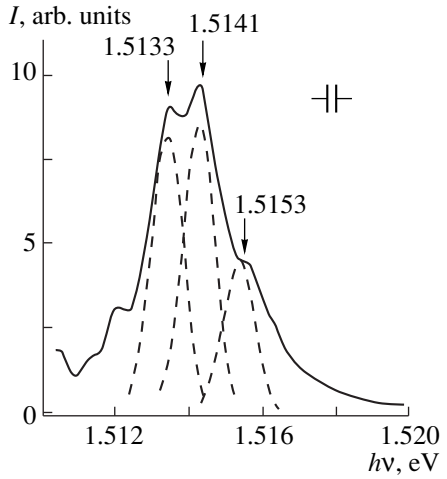

Fig. 1. Edge luminescence spectrum of semi-insulating GaAs at 4.2 K; $L = 2.5 \times 10^{18}$ photon cm^{-2} s^{-1}. The luminescence bands under study are separated from the net spectrum and are shown by dashed curves.

The spectra of the crystals were measured at a temperature of T = 4.2 K under excitation intensities L from 10^{17} to 10^{19} photon cm^{-2} s^{-1}. Under these conditions, the conductivity of the semi-insulating GaAs crystals was controlled by excess electrons and holes ($\delta n, \delta p \gg n_0 + p_0$). The total number of excess electrons $\delta N = s\int_0^\infty \delta n dy$ and holes $\delta P = s\int_0^\infty \delta p dy$ in the sample increased linearly with the excitation intensity L($\delta N, \delta P \propto L$). This means that the concentrations $\delta n(y)$ and $\delta p(y)$ increase linearly with L and decrease exponentially with y; i.e., $\delta n(y, L)$, $\delta p(y, L) \propto L\exp(-ay)$, where $a = \varphi(l_d, 1/k) \neq \varphi(y, L)$. The magnitudes of δn and δp were controlled by the rate of linear recombination of the nonequilibrium charge carriers at deep-level centers; this means that only a small fraction of the electrons and holes generated by the laser radiation became bound into excitons and, thus, recombined via excitonic states (i.e., the total intensity of excitonic luminescence was significantly lower than the excitation intensity).

To distinguish between different assumptions about the nature of the centers responsible for the luminescence band with $h\nu_m$ = 1.5133 eV, we undertook a comparative analysis of the dependences of intensities of this band and other exciton luminescence bands on the excitation intensity L. A typical luminescence spectrum recorded for one of the semi-insulating GaAs crystals under investigation is shown in Fig. 1; here, only the luminescence bands under study (with $h\nu_m$ = 1.5133, 1.5141, and 1.5153 eV), which are dominant in the spectrum, are separated out of the spectrum.

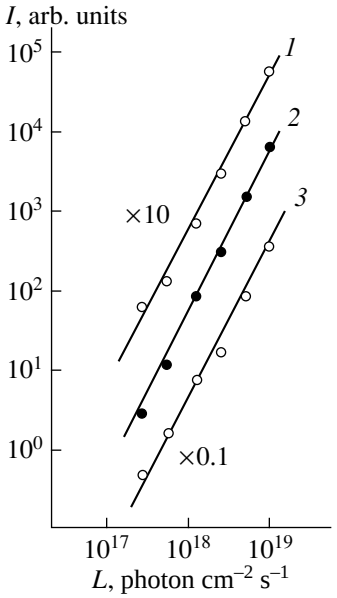

Fig. 2. Excitation-level dependences of the intensities of the luminescence bands under study in semi-insulating GaAs at 4.2 K: (*1*) D^0X bound-exciton band, (*2*) free-exciton band, and (*3*) band with $h\nu_m = 1.5133$ eV.

3. RESULTS AND DISCUSSION

The excitation-level dependences of the intensities of the bands related to annihilation of bound (D^0X) and free (X) excitons and the 1.5133-eV band in the luminescence spectra of semi-insulating GaAs samples at 4.2 K are shown in Fig. 2. One can see that the intensities I_{D^0X}, I_X, and $I_{1.5133}$ follow the same dependence, namely, they increase proportionally to L^2.

Let us examine the data presented. Obviously, luminescence intensities I_{D^0h}, I_{D^+X}, I_{D^0X}, and I_X depend on the concentrations of the free excitons n_e, holes δp, positively charged donors N_{D^+}, and neutral donors N_{D^0}; the probability b of the free-exciton radiative annihilation; the coefficient c_p^0 of the hole capture by donors; and the coefficients of the free-exciton capture by ionized and neutral donors β and γ, respectively. In the case of a semi-insulating GaAs crystal whose dimensions in the y direction significantly exceed $l_d + 1/k$, these intensities are given by the relationships [12, 13][2]

$$I_{D^0h} = c_p^0\int_0^\infty N_{D^0}\delta p\,dy, \quad I_{D^+X} = \beta\int_0^\infty N_{D^+}n_e\,dy, \qquad (1)$$

$$I_{D^0X} = \gamma\int_0^\infty N_{D^0}n_e\,dy, \quad I_X = b\int_0^\infty n_e\,dy, \qquad (2)$$

here,

$$N_{D^0} = \frac{c_n^+\delta n}{c_n^+\delta n + c_p^0\delta p}N_D, \quad N_{D^+} = \frac{c_p^0\delta p}{c_n^+\delta n + c_p^0\delta p}N_D, \qquad (3)$$

$$n_e = \frac{\alpha\delta n\delta p}{b + \beta N_{D^+} + \gamma N_{D^0}}, \qquad (4)$$

where N_D is the donor concentration, c_n^+ is the coefficient of the electron capture by the donors, and α is the coefficient of the electron–hole pair binding into an exciton.[3]

We consider the situation when

$$\delta n(y, L),\ \delta p(y, L) \propto L\exp(-ay).$$

This relationship, which holds under the actual experimental conditions (see above), follows from the fact that the main channel of excess electron and hole recombination is the linear recombination via deep-level centers; then, obviously, $I_{D^0h}, I_{D^+X}, I_{D^0X}, I_X \ll L$. In this case, it follows from (3) and (4) that $N_{D^+}, N_{D^0} \neq \varphi(y, L)$ and

$$n_e \propto \delta n\delta p \propto L^2\exp(-2ay).$$

Then, by evaluating the integrals in (1) and (2), we obtain the following dependences for the intensities of the luminescence bands under consideration:

$$I_{D^0h} \propto L, \qquad (5)$$

$$I_{D^+X}, I_{D^0X}, I_X \propto L^2. \qquad (6)$$

Since, according to (5) and (6) and to the experiments, the intensity $I_{1.5133}$, like I_{D^0X} and I_X, increases proportionally to L^2, we may conclude that the band with $h\nu_m = 1.5133$ eV is due to the annihilation of D^+X bound excitons ($I_{1.5133} = I_{D^+X}$). Evidently, if this band were related to the recombination of the free holes h at

[2] Evidently, the expressions for I_{D^0h}, I_{D^+X}, I_{D^0X}, and I_X written below are valid for GaAs crystals with any value of dark conductivity, not only for semi-insulating crystals, provided the excitation level is sufficiently high ($\delta n \gg n_0$ and $\delta p \gg p_0$).

[3] The expressions for N_{D^+}, N_{D^0}, and n_e are valid at low temperatures (in which case, the processes of donor thermal ionization and exciton thermal dissociation may be neglected) for $\delta n \gg n_0$ and $\delta p \gg p_0$. The expression for n_e was derived under the assumptions that (a) local equilibrium between electrons, holes, and excitons exists [14] and (b) free excitons are bound predominantly to donors (Fig. 1). The expressions for N_{D^+} and N_{D^0} were derived assuming that the occupancy of the donor states is governed by their interaction with the free carriers; in this case, $N_{D^+}, N_{D^0} \neq \varphi(y, L)$ if $\delta n/\delta p \neq \varphi(y, L)$.

the neutral donors D^0, a linear increase in $I_{1.5133}$ with L should be expected.

Thus, the observed dependence of the intensity of the luminescence band with $h\nu_m = 1.5133$ eV in semi-insulating GaAs at 4.2 K on the excitation intensity can be explained only under the assumption that this band originates from the D^+X bound-exciton annihilation, rather than from the free-hole recombination at the neutral donors (as was suggested in [3, 6]). This conclusion confirms once more the major role of the bound excitons D^+X in the origination of the luminescence band with $h\nu_m = 1.5133$ eV in GaAs.

4. CONCLUSION

The luminescence band peaked at $h\nu_m = 1.5133$ eV, observed in semi-insulating GaAs at 4.2 K, originates from the annihilation of the bound excitons D^+X. This result is important for the understand the physical basics of radiative electronic transitions in intermetallic semiconductors.

REFERENCES

1. E. H. Bohards and B. Bebb, Phys. Rev. **176**, 993 (1968).
2. U. Heim and P. Hiesinger, Phys. Status Solidi B **66**, 461 (1974).
3. R. Ulbrich and B. Moreth, Solid State Commun. **14**, 331 (1974).
4. W. Bludau and E. Wagner, Phys. Rev. B **13**, 5410 (1976).
5. S. Zeman and G. Lampert, J. Appl. Phys. **70**, 4909 (1991).
6. M. I. Kalinin, M. P. Lisitsa, and F. V. Motsnyĭ, Ukr. Fiz. Zh. **37**, 330 (1992).
7. K. S. Zhuravlev, A. K. Kalagin, N. T. Moshegov, *et al.*, Fiz. Tekh. Poluprovodn. (St. Petersburg) **30**, 1704 (1996) [Semiconductors **30**, 891 (1996)].
8. D. C. Reynolds, D. C. Look, and B. Jogai, Phys. Rev. B **53**, 1891 (1996).
9. V. A. Karasyuk, M. L. W. Trewalt, and A. J. Spring Thorpe, Phys. Status Solidi B **210**, 353 (1998).
10. A. N. Georgibiani and I. M. Tiginyanu, Fiz. Tekh. Poluprovodn. (Leningrad) **22**, 3 (1988) [Sov. Phys. Semicond. **22**, 1 (1988)].
11. K. D. Glinchuk, V. I. Guroshev, and A. V. Prokhorovich, Optoélektron. Poluprovodn. Tekh. **24**, 66 (1992).
12. E. L. Nolle, Fiz. Tverd. Tela (Leningrad) **9**, 122 (1967) [Sov. Phys. Solid State **9**, 90 (1967)].
13. T. M. Schmidt and K. Lischka, Phys. Rev. B **45**, 8989 (1992).
14. A. V. Sachenko and O. V. Snitko, in *Photoeffect in the Surface Layers of Semiconductors* (Naukova Dumka, Kiev, 1984), p. 158.

Translated by M. Skorikov

Semiconductors, Vol. 35, No. 5, 2001, pp. 520–524. Translated from Fizika i Tekhnika Poluprovodnikov, Vol. 35, No. 5, 2001, pp. 541–545.

ELECTRONIC AND OPTICAL PROPERTIES OF SEMICONDUCTORS

BeCdSe: A New Material for the Active Region in Devices Operating in the Blue–Green Region of the Spectrum

O. V. Nekrutkina[1,*], S. V. Sorokin[1,2], V. A. Kaĭgorodov[1,4], A. A. Sitnikova[1], T. V. Shubina[1], A. A. Toropov[1], S. V. Ivanov[1,2], P. S. Kop'ev[1], G. Reuscher[2], V. Wagner[2], J. Geurts[2], A. Waag[3], and G. Landwehr[2]

[1] *Ioffe Physicotechnical Institute, Russian Academy of Sciences, Politekhnicheskaya ul. 26, St. Petersburg, 194021 Russia*
** e-mail: olya.nekrutkina@pop.ioffe.rssi.ru*
[2] *Physicalisches Institut der Universität Würzburg, D-97074 Würzburg, Germany*
[3] *Abteilung Halbleiterphysik, Universität Ulm, 89081 Ulm, Germany*
[4] *St. Petersburg Electrotechnical University, St. Petersburg, 197376 Russia*
Submitted October 11, 2000; accepted for publication October 23, 2000

Abstract—Submonolayer cyclic epitaxy was used for the first time to obtain a bulk layer of BeCdSe solid solution 100 nm thick with a Be content close to 46%, which corresponded to the composition lattice-matched to the GaAs substrate. In addition, low-temperature lasing at a wavelength of 460 nm with a threshold power density of about 40 kW/cm^2 in a structure with multiple ZnSe/BeCdSe quantum wells was also attained for the first time. The band-bending parameter in the BeCdSe solid solutions was estimated at 4.5 eV. © *2001 MAIK "Nauka/Interperiodica".*

INTRODUCTION

In spite of rapid progress in research and development in the field of optoelectronic devices based on III–N materials, the wide-gap II–VI compounds remain the most suitable materials for the development of semiconductor lasers emitting in the blue–green region of the spectrum because this region is still beyond the reach of devices based on nitrides of Group III elements [1]. At present, the main impediment to the commercial application of II–VI compounds is the relatively short operating life of II–VI-based injection lasers (shorter than 400 h) [2]. Conventionally, the ZnCdSe compound having a relatively soft lattice is used to form the active regions of the lasers; this compound is characterized by a large lattice mismatch with the GaAs substrate, which brings about the formation and diffusion of point defects during laser operation. Thus, it is of much interest for scientists and technologists to produce new wide-gap II–VI compounds that emit in the blue–green spectral region, have a crystal lattice of enhanced rigidity, and are lattice-matched to GaAs.

The BeCdSe compound has been previously suggested [3] as a new material for the active region of optoelectronic devices for the blue–green region of the spectrum, the reason being that beryllium chalcogenides have the most rigid lattice among all II–VI compounds [4]. It has been shown theoretically [3] and experimentally [5] that it is possible to grow the $Be_xCd_{1-x}Se$ solid-solution layers lattice-matched to GaAs ($x \approx 0.46$) in spite of a wide range of instability in this solid-solution system ($x = 0.03$–0.38 for pseudomorphic growth on GaAs); this instability is caused by the large difference in lattice constants for the constituent binary compounds ($a_{CdSe} = 6.077$ Å, whereas $a_{BeSe} = 5.139$ Å). In this paper, we report the results of optical and structural studies of a bulk BeCdSe layer with a thickness of 100 nm and a Be content close to $x \approx 0.46$; the layer was grown for the first time by molecular-beam epitaxy (MBE). The same methods for growth and study were used for a structure with multiple ZnSe/BeCdSe quantum wells (QWs); low-temperature lasing was observed for the first time in this structure.

EXPERIMENTAL

The structures were grown by MBE on GaAs(001) substrates at a temperature of $T_s = 300$°C. Submonolayer digital alloying (SDA) was used to grow BeCdSe. The layer of solid solution was grown in the SDA mode by sequential alternate deposition of CdSe and BeSe submonolayers with widths less than 0.3 monolayers (ML); the resulting composition was governed by the ratio between the widths of the adjacent submonolayers. The structure used for obtaining the stimulated emission consisted of five 2-nm-thick BeCdSe QWs separated by 10-nm-thick ZnSe barriers and also of top and bottom $Zn_{0.97}Be_{0.03}Se$ confinement layers with thicknesses of 100 and 1000 nm, respectively. In a structure with a bulk BeCdSe layer, the top and bottom

$Zn_{0.97}Be_{0.03}Se$ confinement layers were 50 and 400 nm thick, respectively. The BeSe growth rate was determined by monitoring the oscillations in the pattern of the reflection high-energy electron diffraction (RHEED) in the course of growing the buffer 5-ML-thick BeTe layer. The thickness of the deposited CdSe layer grown either by MBE or in the epitaxy mode with enhanced migration of atoms was measured by optical and X-ray diffraction methods as reported previously [6, 7]. In order to assess the composition of the BeCdSe layer grown by MBE, we used the ratio between the BeTe and BeCdSe growth rates determined *in situ* from the RHEED data.

In structural studies, we employed two-crystal X-ray diffractometry, transmission electron microscopy (TEM), and scanning electron microscopy (SEM). The photoluminescence (PL) spectra were measured at a sample temperature of 80 K; a He–Cd laser with an emission wavelength of 325 nm was used as an excitation source. The lasing characteristics were studied under pulsed optical pumping (a nitrogen laser with a pulse duration of 8 ns and a wavelength of 337 nm was used).

RESULTS AND DISCUSSION

Theoretical calculations performed using the approximation of thermodynamic equilibrium and based on a model of a regular solid solution made it possible to determine the instability and immiscibility zones in a BeSe–CdSe system (Fig. 1). It can be seen that, at the temperature of epitaxy, the instability and immiscibility zones, which correspond to the areas above the intersection points of the binodal curve (curve *1*) and the spinodal curve (curve *2*) with the isotherm at 300°C, encompass almost the entire composition range. If elastic stresses emerging in the system owing to a mismatch between the lattice parameters of the layer and substrate are taken into account, then the shapes of the binodal (curve *3*) and spinodal (curve *4*) curves change significantly. The extent of the instability and immiscibility zones decreases, which makes it possible to obtain solid solutions with a high content of beryllium (>38%) under quasi-equilibrium conditions for pseudomorphic growth. If the elastic stresses in the layer are relaxed in part (for example, if the critical thickness is exceeded), the instability and immiscibility zones extend to higher Be contents. Thus, the calculation results show that pseudomorphic layers (with the Be content amounting to $x \approx 0.46$) lattice-matched to GaAs can be grown in a BeCdSe system.

Thin (0.8 nm) MBE-grown BeCdSe/ZnSe QWs with a Be content as high as several percent without any indication of phase decomposition were reported recently [3]. In order to extend the range of compositions within the instability domain, the use of a highly nonequilibrium method of SDA was suggested; we used this method (previously employed in the MBE growth of the III–V compounds [8]) for the first time to grow the II–VI compounds using MBE. The use of this method made it possible to grow QWs of high structural quality with a Be content of $x \approx 0.15$. It can be seen from Fig. 2 that the intensity of PL from a $Be_{0.14}Cd_{0.86}Se$/ZnSe QW exceeds the PL intensity from a CdSe QW by a factor of 50. It is noteworthy that lasing with the lowest pumping intensity ever attained at room temperature has been reported recently for a similar structure with a CdSe QW 2.8 nm wide [9]. However, even if nonequilibrium SDA is used, a further

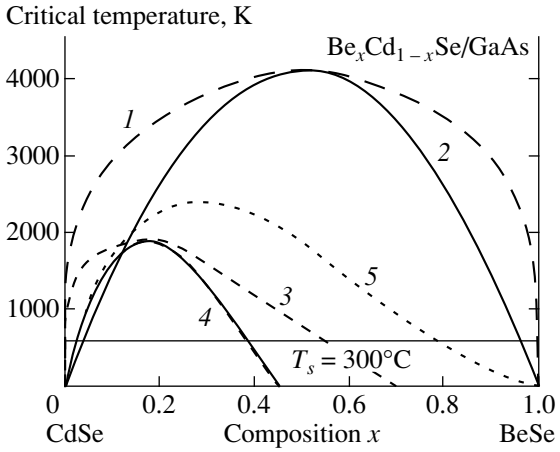

Fig. 1. The instability and immiscibility zones for a BeSe–CdSe system; these zones were calculated in the approximation of the model of a regular solid solution. Line *1* is for the chemical binodal curve; (*2*) corresponds to the chemical spinodal curve; (*3*) corresponds to the coherent binodal curve; (*4*) corresponds to the coherent spinodal curve; and (*5*) corresponds to the spinodal curve for a layer with partial relaxation of elastic stresses.

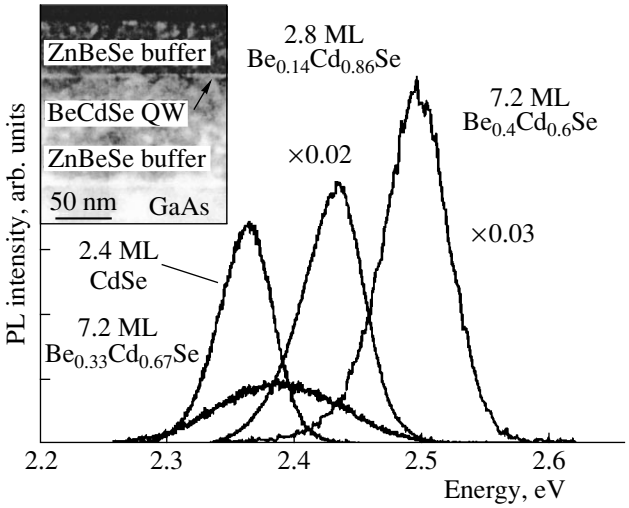

Fig. 2. The spectra of low-temperature photoluminescence of quantum wells with various contents of beryllium. The photograph obtained by transmission electron microscopy for a $Be_{0.4}Cd_{0.6}Se$ structure with a quantum well is shown in the inset.

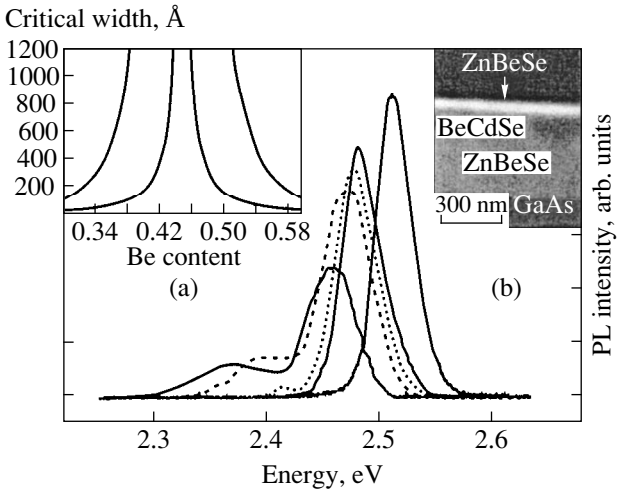

Fig. 3. Spectra of low-temperature photoluminescence observed in a bulk BeCdSe layer and measured at various sites of the sample along the direction corresponding to the gradient of Be concentration. The insets show (a) the calculated dependences of the critical thickness of BeCdSe on Be content according to different models and (b) scanning electron micrograph of cross section of the structure.

increase in the Be content results in the appearance of indications of phase decomposition [3]. Nevertheless, as the Be content increases further and the boundary of the instability zone ($x \approx 0.4$) is passed, the structures with BeCdSe/ZnSe QWs again demonstrate the same high-intensity PL as in the case of $Be_{0.14}Cd_{0.86}Se$/ZnSe QWs (see Fig. 2). Structural studies, in particular, those based on TEM, demonstrate that the morphology of the samples studied is good and that structural defects are absent (see the inset in Fig. 2). Thus, the use of SDA makes it possible to obtain BeCdSe/ZnSe QWs with a Be content within the instability zone of the system. Ivanov *et al.* [5] studied two structures, one of which was grown by conventional MBE and the other, by SDA; the structures featured a large gradient of Be content across the substrate surface area (from 40 to 48%) and contained multiple BeCdSe/ZnSe QWs. It was shown [5] that the optical characteristics of the two structures (in particular, the luminescence intensity) were approximately identical; however, the structural quality of QWs grown by SDA was slightly higher.

In order to study the properties of lattice-matched BeCdSe compositions, we used SDA to grow a structure with a 100-nm-thick BeCdSe layer. Since the substrate was not rotated during epitaxy, the gradient of the Be concentration in BeCdSe was appreciable. Figure 3 shows the PL spectra measured at various sites of the sample along the direction corresponding to the gradient in Be concentration. X-ray studies showed that the highest Be content in the sample was ~47%, which nearly corresponded to a solid solution lattice-matched to GaAs; therefore, we may expect that, as the Be content in the layer decreases, the PL intensity would also decrease owing to an increase in the lattice-constant mismatch and, correspondingly, to relaxation of elastic stresses in the layer, which gives rise to structural defects. The behavior of the main PL line supports this assumption, whereas the emergence of a new long-wavelength peak may indicate onset of phase decomposition. The instability zone extends as elastic stresses relax in the layer (Fig. 1); therefore, we may assume that the stresses in the structure relax in part, in spite of the fact that the lowest Be content in the layer lies significantly above the spinodal curve for the pseudomorphic layer (38%).

We grew several structures with a bulk BeCdSe layer using both conventional MBE and SDA. Only the SDA-grown structures featured a high structural quality. We may assume that, if MBE is used for growth, the relaxation of elastic stresses occurs when the critical thickness is exceeded, which may be caused by fluctuations in the intensities of molecular-beam fluxes. In contrast, SDA makes it possible to control to a high accuracy the composition and thickness of the layer during growth; in addition, this method is less sensitive to flux fluctuations. The dependence of the critical thickness of the BeCdSe layer on the Be content was calculated using the Matthews–Blakeslee equilibrium mechanical model [10] for estimating the lower bound for the Be content and the People–Bean energy balance model [11] for estimating the upper bound. It is evident (see the inset (a) in Fig. 3) that a thickness of 100 nm exceeds the critical one for the BeCdSe layer with a Be content lower than 38% (according to the People–Bean model) or even 44% (according to the Matthews–Blakeslee model). Thus, taking into account a significant gradient in the Be content across the surface area of the structure, we may expect that the layer morphology deteriorates appreciably in the region with a low Be content. Nevertheless, the layer morphology is uniform throughout the entire sample as can be deduced from a SEM cross-sectional image of the structure (see inset (b) in Fig. 3).

Figure 4 shows the complete collection of data available to us now and obtained from the PL for BeCdSe: the data for QWs with thicknesses of 0.8 nm [3] and 2 nm [5] and also for the structures described in this paper. The result of simulating the dependence of the band gap E_g on the Be content x is

$$E_g(\mathrm{BeCdSe}) = (1-x)E_g(\mathrm{CdSe}) + xE_g(\mathrm{BeSe}) - x(1-x)C,$$

where C, the band-bending parameter, is shown by the solid curve. The estimate based on the data for QWs represents a rather crude approximation because the effects of elastic stresses in the layer and the QW width on the PL line position were disregarded in this approach. An estimation based on the data on PL of a bulk BeCdSe layer yields the value of 4.5 eV for C. Such a large value of the band-bending parameter was previously observed in systems that also had an appre-

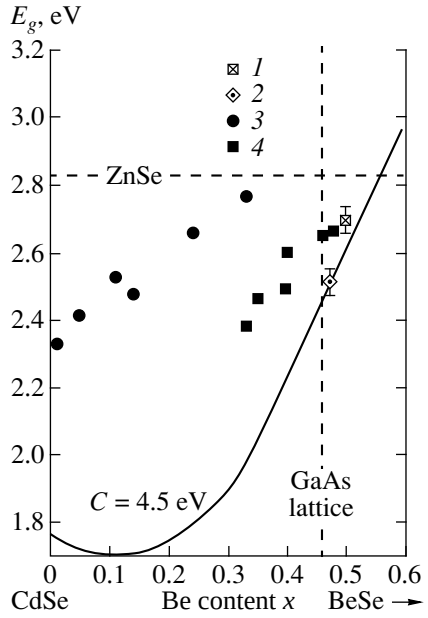

Fig. 4. The dependence $E_g(x)$ for $Be_xCd_{1-x}Se$. The data were obtained from luminescence measurements for the following structures: (*1*) a structure with $Be_xCd_{1-x}Se$/ZnSe multiple quantum wells, (*2*) a structure with a bulk BeCdSe layer (at the site corresponding to the highest Be content), (*3*) data for BeCdSe quantum wells with thicknesses of 0.8 nm [3] and 2 nm [5], and (*4*) our experimental data. The solid curve represents the calculated dependence $E_g(x)$ for the band-bending parameter C = 4.5 eV.

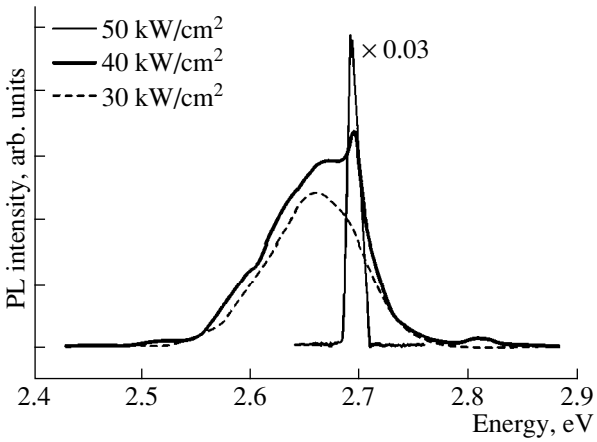

Fig. 5. Low-temperature spectra of spontaneous and stimulated emission from a structure with multiple quantum wells [(2 nm)-$Be_xCd_{1-x}Se$/(10 nm)-ZnSe]$_5$.

ciable mismatch between lattice constants for binary compounds, for example, in an $Al_xIn_{1-x}N$ system [12].

A large value of the band-bending parameter affects significantly the feasibility of using BeCdSe in laser-diode structures. Despite the absence of Mg in the confining layers, which results in a weak optical confinement, we managed to obtain stimulated emission from a structure consisting of five $Be_{0.5}Cd_{0.5}Se$/ZnSe QWs at a temperature of 80 K. Figure 5 shows the spectra of spontaneous and stimulated emission obtained under pumping with a pulsed nitrogen laser. Since the Be concentration in BeCdSe QWs exceeds 46% (the solid solution lattice-matched to the GaAs substrate), stresses in the layer give rise to additional energy states. The latter introduce a broad line in the emission spectrum; this line is positioned in the long-wavelength spectral region and is not involved in lasing. Stimulated emission emerges in the "blue" region of the spectrum.

Since there are no published data with a complete set of parameters, it is not possible to perform correct calculations and estimate the band offsets and the type of BeCdSe/ZnSe heterojunction (HJ) in relation to the Be content. Since, on the one hand, we should take into account the elastic stresses for compositions away from those lattice-matched to GaAs ($x \approx 0.46$) and, on the other hand, it is the Be content range in the vicinity of the above value that is of most interest, we estimated the band offsets for $x \approx 0.46$ with the factor of stresses in the layer disregarded.

The band offsets in a BeCdSe/ZnSe system were estimated according to the transitivity rule as the sum of the band offsets in the BeCdSe/CdSe and CdSe/ZnSe systems. The band offsets for a CdSe/ZnSe system can easily be calculated according to [13]; at the same time, it was assumed for the BeCdSe/CdSe HJ that ΔE_g is mainly caused by the conduction-band offset because, for this system, only the cations are changed when passing from one material to another. Notwithstanding the fact that the assumption of fixed distribution of ΔE_g between the conduction and valence bands obviously cannot be valid in the entire Be content range owing to the large value of the band-bending parameter, this assumption is quite valid for high Be concentrations, where the dependence $E_g(x)$ is almost linear. The results of this rather crude estimation make it possible to assume that, in the range of Be content close to $x \approx 0.46$, the BeCdSe/ZnSe HJ is a type I junction. Nevertheless, the value of the band offsets and the type of the BeCdSe/ZnSe HJ require further refinement.

CONCLUSION

Submonolayer digital epitaxy was used to grow a structure with multiple ZnSe/BeCdSe quantum wells, and a bulk BeCdSe layer with a thickness of 100 nm was obtained for the first time. In both structures, the Be content is close to $x \approx 0.46$, which corresponds to the solid solution lattice-matched to the GaAs substrate. Both structures featured high-intensity photoluminescence at temperatures as high as 295 K. A low-temperature lasing at a wavelength of 460 nm with a threshold pumping density of 40 kW/cm^2 was obtained for the first time in a ZnSe/BeCdSe structure with multiple QWs. A large band-bending parameter value in the BeCdSe system (about 4.5 eV) in combination with improved strength characteristics related to an

increased Be content make it possible to regard the unstressed BeCdSe layer lattice-matched to the GaAs substrate as a promising component for optoelectronic devices, in particular, for the lasers operating in the blue–green region of the spectrum.

ACKNOWLEDGMENTS

This study was supported by the Russian Foundation for Basic Research (project nos. 99-02-17097, 00-02-17022, and 00-02-16997), the Program of the Ministry of Science of the Russian Federation "Physics of Solid-State Nanostructures," the Volkswagen Foundation, and INTAS (grant no. 97-31907).

REFERENCES

1. S. Nakamura, M. Senoh, S. Nagahama, *et al.*, Appl. Phys. Lett. **76** (1), 22 (2000).
2. E. Kato, H. Noguchi, M. Nagai, *et al.*, Electron. Lett. **34**, 282 (1998).
3. S. V. Ivanov, A. A. Toropov, T. V. Shubina, *et al.*, J. Cryst. Growth **214/215**, 109 (2000).
4. C. Verie, J. Elecron. Mater. **27** (6), 782 (1998).
5. S. V. Ivanov, A. A. Toropov, T. V. Shubina, *et al.*, Phys. Status Solidi A **180**, 275 (2000).
6. S. V. Ivanov, A. A. Toropov, T. V. Shubina, *et al.*, J. Appl. Phys. **83**, 3168 (1998).
7. R. N. Kyutt, A. A. Toropov, S. V. Sorokin, *et al.*, Appl. Phys. Lett. **75**, 373 (1999).
8. R. Cingolani, O. Brandt, L. Tapfer, *et al.*, Phys. Rev. B **42**, 3209 (1990).
9. S. V. Ivanov, A. A. Toropov, S. V. Sorokin, *et al.*, Appl. Phys. Lett. **74**, 498 (1999).
10. J. W. Matthews and A. E. Blakeslee, J. Cryst. Growth **27**, 118 (1974).
11. R. People and J. C. Bean, Appl. Phys. Lett. **47**, 322 (1985).
12. T. Peng, J. Piprek, G. Qui, *et al.*, Appl. Phys. Lett. **71** (17), 2439 (1997).
13. H. J. Lozykovski and V. K. Shastri, J. Appl. Phys. **69**, 3235 (1991).

Translated by A. Spitsyn

Semiconductors, Vol. 35, No. 5, 2001, pp. 525–528. Translated from Fizika i Tekhnika Poluprovodnikov, Vol. 35, No. 5, 2001, pp. 546–549.

SEMICONDUCTOR STRUCTURES, INTERFACES, AND SURFACES

Method for Determining the Stoichiometric Composition of a Mercury Cadmium Telluride Solid Solution from Capacitance–Voltage Characteristics

I. M. Ivankiv, A. M. Yafyasov*, V. B. Bogevol'nov, and A. D. Perepelkin

Institute of Physics, St. Petersburg University, St. Petersburg, 198504 Russia

** e-mail: yafyasov@desse.phys.spbu.ru*

Submitted July 26, 2000; accepted for publication September 19, 2000

Abstract—A procedure is proposed for determining the stoichiometric composition of an intrinsic semiconductor $Hg_{1-x}Cd_xTe$, relying upon the field effect in an electrolyte. An original comparative analysis of experimental capacitance–voltage characteristics and those calculated in terms of a quantum description of the space charge region provides the x value in the surface layer of the semiconductor at a depth comparable with the Debye screening radius. The determined stoichiometric compositions are presented for four $Hg_{1-x}Cd_xTe$ samples (x = 0.205, 0.245, 0.290, and 0.330). © *2001 MAIK "Nauka/Interperiodica".*

1. INTRODUCTION

Electrical methods for investigating semiconductors by measuring capacitance–voltage (*C–V*) characteristics are widely used to determine the type and concentration of dopants and the spectrum of fast and slow surface states [1]. Additional possibilities in studying semiconductors are opened up when an electrolyte–insulator–semiconductor (EIS) system is used instead of the conventional metal–insulator–semiconductor (MIS) structure. The main advantage of the field effect technique in the case of the EIS system is the possibility of forming a practically oxide-free surface,[1] with the result that the measured capacitance is in fact the capacitance of the space charge region of the semiconductor (C_{sc}). Use of specially selected electrolytes and etching regimes yields a surface with a low density of surface states for various compositions of a mercury cadmium telluride (MCT) solid solution in a wide range of surface potentials.

With the field effect used in electrolytes, a direct comparison of theoretical and experimental *C–V* characteristics of MCT is hindered by the unavoidable error in determining the area and roughness factor of the surface of a sample subjected to chemical and electrochemical etching and by the additional capacitance associated with surface states (C_{ss}).

In this paper, a method is proposed for determining the stoichiometric composition of intrinsic MCT, free of the above experimental errors. The procedure consists in successively taking the logarithm of and differentiating the experimental *C–V* characteristics in a wide range of surface potentials, which eliminates the error in determining the area and roughness factor of the surface and allows a more precise comparison with a theoretical calculation. The capacitance associated with surface states may affect the obtained result only in the case when the inequality $C_{ss}(V_s) \ll C_{sc}(V_s)$, where V_s is the surface potential of the external electric field, is invalid.

2. THEORETICAL MODEL OF THE SPACE CHARGE REGION

To correctly describe the space charge region (SCR) in narrow-gap Kane semiconductors at room temperature, it is necessary to take into account the wave nature of electrons and holes in the bound state and in continuous spectrum. In terms of the one-particle Hartree approximation, the distributions of electron (ρ_e) and heavy-hole densities (ρ_{hh})[2] can be found from a self-consistent solution of the Poisson and Schrödinger equations for electrons and holes [3]:

$$\frac{d^2V(z)}{dz^2} = q\frac{\rho_e(z) - \rho_{hh}(z) + N_a - N_d}{\varepsilon_0\varepsilon_{sc}}, \quad (1)$$

$$-\frac{d^2\varphi_i(z, k_\parallel)}{dz^2} = [k^2(E_i(k_\parallel), V(z)) - k_\parallel^2]\varphi_i(z, k_\parallel), \quad (2)$$

[1] A Helmholtz layer 2–4 Å thick plays the part of an ultrathin insulating layer in the system semiconductor–electrolyte [2].

[2] The light-hole density can be neglected to a first approximation.

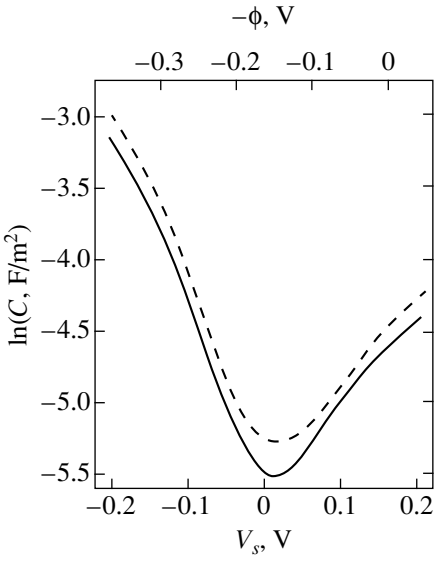

Fig. 1. Experimental (dashed line) and theoretical (solid line) *C–V* characteristics of MCT with $x = 0.245$.

$$\left[-\frac{\hbar^2}{2m_{hh}}\frac{d^2}{dz^2} - qV(z)\right]\varphi_j(z) = (-E_j - E_g)\varphi_j(z), \quad (3)$$

where $V(z)$ is the electrostatic potential profile in the SCR of the semiconductor; q is the electron charge; ε_{sc} is the dielectric constant of the semiconductor; ε_0 is the permittivity of free space; N_d and N_a are the concentrations of ionized donor and acceptor centers, respectively; and m_{hh} is the heavy-hole mass. Here, $\mathbf{k} = (k_x, k_y, k_z)$ is the wave vector; $k_\parallel^2 = k_x^2 + k_y^2$; as zero energy is taken the bottom of the conduction band in the semiconductor bulk; $\varphi_i(z, k_\parallel)$, $E_i(k_\parallel)$ and $\varphi_j(z)$, E_j are the envelopes of the wave functions and energy eigenvalues for, respectively, electrons and holes.

We assume that the dispersion law of heavy holes is parabolic and that of electrons is described by the formula [4]

$$k^2[E, V(z)] = \frac{1}{P^2} \times \frac{[E - qV(z)][E - qV(z) + E_g][E - qV(z) + E_g + \Delta]}{[E - qV(z) + E_g + (2/3)\Delta]}, \quad (4)$$

The determined composition (x) of $Hg_{1-x}Cd_xTe$ solid solutions

Method of determination	x			
Nominal values	0.205	0.245	0.290	0.330
Found from electron portion	0.209	0.245	0.295	0.330
Found from hole portion	0.150	0.255	0.305	0.320

where P is the matrix element of the momentum operator, E_g is the energy gap of the semiconductor, and Δ is the spin-orbit splitting of the valence band.

The concentrations of electrons and holes can be found from

$$\rho_e(z) = \frac{1}{\pi}\int_0^\infty dk_\parallel \sum_i \frac{k_\parallel \varphi_i(z, k_\parallel)\big|^2}{1 + \exp\{[E_i(k_\parallel) - E_F]/k_0T\}}, \quad (5)$$

$$\rho_{hh}(z) = \sum_{j=1}^{+\infty} \Gamma_j(E_j)\big|\varphi_j(z)\big|^2, \quad (6)$$

where

$$\Gamma_j(E_j) = \frac{m_{hh}k_0T}{\pi\hbar^2}\ln\{1 + \exp[(E_j - E_F)/k_0T]\},$$

E_F is the Fermi level, k_0 is the Boltzmann constant, and T is temperature.

The differential capacitance $C_{sc}(V_s)$ of the SCR in the semiconductor is found in the form

$$C_{sc} = \frac{dQ_{sc}}{dV_s}, \quad (7)$$

where $Q_{sc}(V_s) = q\int_0^\infty [\rho_e(z) - \rho_{hh}(z) + N_a - N_d]dz$ (in the case in question $N_d = N_a = 0$). By way of example, Fig. 1 shows a theoretical *C–V* characteristic for $Hg_{1-x}Cd_xTe$ with $x = 0.245$. The calculation was done with the following MCT parameters [5]:

$$\varepsilon_{sc} = 20.5 - 15.5x + 5.72x^2, \quad m_{hh}/m_0 = 0.5,$$
$$\Delta = 0.96 \text{ eV},$$

$$P[\text{eV cm}] = [(18 - 3x)\hbar^2/2m_0]^{1/2},$$

$$E_g[\text{eV}] = -0.302 + 1.93x + 5.35 \times 10^{-4}(1 - 2x)T - 0.81x^2 + 0.832x^3,$$

where m_0 is the free electron mass.

3. EXPERIMENTAL

The employed experimental procedure was based on measuring the impedance of a semiconductor–electrolyte interface probed with 1-μs-long voltage pulses, with current–voltage characteristics taken simultaneously. The semiconductor electrode was polarized in the potentiostatic regime with a continuous cyclic variation of the electrode potential at rates of $d\phi/dt$ = 10–100 mV/s at a temperature of $T = 295$ K. The electrode potential (ϕ) was measured relative to a standard hydrogen electrode. In the range of electrode potentials

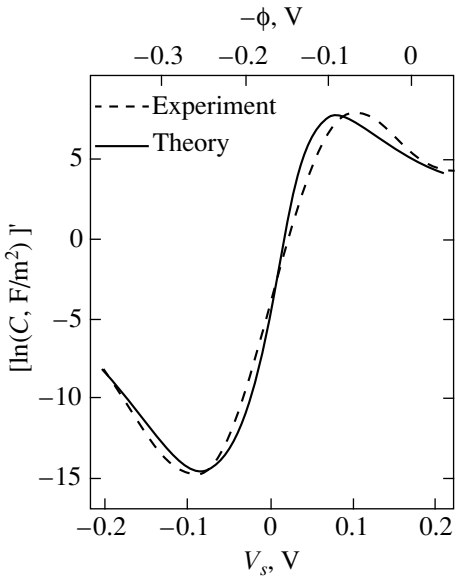

Fig. 2. Derivative of the logarithm of the experimental (dashed line) and theoretical (solid line) capacitance as a function of voltage for MCT with $x = 0.245$.

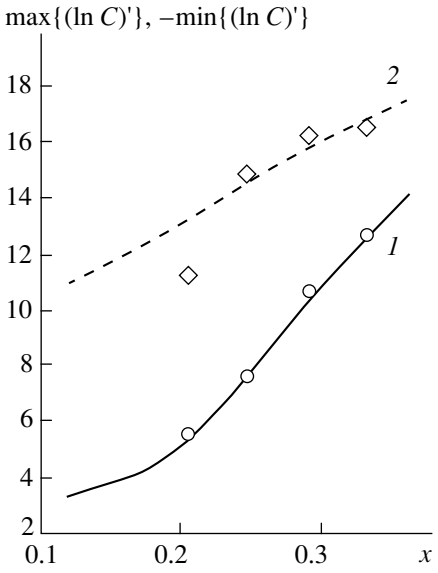

Fig. 3. Theoretical dependences (lines) of (*1*) maximum and (*2*) minimum values of $d(\ln C)/dV_s$ vs. MCT composition (x) and experimental values of extrema (points).

chosen for polarizing the semiconductor electrode, there were practically no currents across the interface associated with electrochemical reactions, and the field effect had an equilibrium nature.

Prior to measurements, the surface of MCT single crystals was subjected to chemical-dynamical polishing in a bromine–methanol solution. Immediately before an experiment, the sample surface was additionally etched electrochemically. Such a sample treatment removes oxides from the surface and ensures an extremely low density of surface states. As a result, the measured capacitance of the MCT–electrolyte interface is actually the capacitance of the SCR in the semiconductor, i.e., $C = C_{sc}$, with the relations $V_s = -(\phi - \phi_{FB})$ and $-\Delta\phi = \Delta V_s$, where ϕ_{FB} is the flat-band potential, valid over the entire range of electrode potentials.

In this study, the proposed procedure for determining the MCT composition was tested on four single-crystal samples with random crystallographic orientations (x = 0.205, 0.245, 0.290, and 0.330).[3] Figure 1 shows as an example experimental and theoretical C–V characteristics for a composition with $x = 0.245$. It can be seen that the experimental curve lies somewhat higher than the theoretical plot. The best agreement between the theoretical and experimental curves is achieved on making a correction to the sample area by 10%. In this case, the surface state density in the range $-0.1\ \text{V} < V_s < 0.1\ \text{V}$ is estimated to be no more than $3 \times 10^{11}\ \text{cm}^{-2}\ \text{eV}^{-1}$. Nevertheless, despite the error in determining the surface area, the proposed procedure allows the stoichiometric composition of the crystal to be determined with sufficient accuracy.

[3] Originally, the sample composition was certified using independent Hall-effect and optical measurements.

4. RESULTS AND DISCUSSION

Figure 2 presents curves obtained by taking the logarithm and subsequent differentiation of the theoretical and experimental C–V characteristics ($x = 0.245$). It can be seen that the theoretical (as well as the experimental) dependence of $d[\ln(C = C_{sc})]/dV_s$ on V_s shows a minimum in the hole portion ($V_s < 0$) and a maximum in the electron portion ($V_s > 0$). Plotting the derivative values at these extrema as a function of composition (x) yields the curves presented in Fig. 3. A good agreement between the theory and experiment is seen in the electron portion; a somewhat worse agreement is seen in the hole portion, which is presumably due to an uncontrollable oxide growth in anodic polarization.

Thus, the theoretical curves in Fig. 3 can be used as graphical charts for determining the composition of intrinsic MCT samples. This can be done by taking the logarithm of an experimental C–V characteristic, differentiating it, and plotting the obtained minimum and maximum values along the ordinate axis. The intersection of horizontal lines drawn through these points with the respective calculated curves will give the sought-for composition value x. The compositions of test samples, determined by this algorithm, are listed in the table.

5. CONCLUSION

The proposed method for determining the stoichiometric MCT composition by taking C–V characteristics

in an electrolyte–semiconductor system produced good results. Its distinctive feature is that it determines the composition locally (within the SCR). The method can be extended to the case of doped MCT and other semiconductors of the kind ($Hg_{1-x}Zn_xTe$, $Hg_{1-x}Mn_xTe$, etc.) with an appropriate choice of working electrolyte solutions and polarization modes in employing the field effect in electrolytes.

ACKNOWLEDGMENTS

This study was supported by the "Universities of Russia" Program (grant no. 99-27-32).

REFERENCES

1. P. Blood, Semicond. Sci. Technol. **1**, 7 (1986).
2. V. A. Myamlin and Yu. V. Pleskov, *Electrochemistry of Semiconductors* (Nauka, Moscow, 1965).
3. A. M. Yafyasov, I. M. Ivankiv, and V. B. Bogevolnov, Appl. Surf. Sci. **142**, 629 (1999).
4. O. E. Kane, J. Phys. Chem. Solids **1**, 249 (1957).
5. I. M. Nesmelova, *Optical Properties of Narrow-gap Semiconductors* (Nauka, Novosibirsk, 1992).

Translated by M. Tagirdzhanov

Semiconductors, Vol. 35, No. 5, 2001, pp. 529–532. Translated from Fizika i Tekhnika Poluprovodnikov, Vol. 35, No. 5, 2001, pp. 550–553.

SEMICONDUCTOR STRUCTURES, INTERFACES, AND SURFACES

Mechanism of the Current Flow in Pd–(Heavily Doped *p*-$Al_xGa_{1-x}N$) Ohmic Contact

T. V. Blank*, Yu. A. Goldberg*, E. V. Kalinina*, O. V. Konstantinov*, A. E. Nikolaev*, A. V. Fomin, and A. E. Cherenkov****

** Ioffe Physicotechnical Institute, Russian Academy of Sciences, Politekhnicheskaya ul. 26, St. Petersburg, 194021 Russia*
e-mails: tblank@delfa.net; mleb@triat.ioffe.rssi.ru; evk@pop.ioffe.rssi.ru
*** Center of Crystal Growth, St. Petersburg, 194021 Russia*
Submitted September 18, 2000; accepted for publication September 19, 2000

Abstract—The physical mechanism of the current flow in Pd–(heavily doped *p*-$Al_xGa_{1-x}N$) ohmic contact is studied. Chloride–hydride epitaxy was used to grow the *p*–$Al_{0.06}Ga_{0.94}N$ solid solution with uncompensated acceptor concentration $N_a - N_d$ ranging from 3×10^{18} up to 10^{19} cm^{-3}. Thermal vacuum deposition and subsequent thermal treatment were used to form an ohmic Pd contact. It is shown that, after the thermal treatment, the Pd–*p*-$Al_{0.06}Ga_{0.94}N$ barrier contact with a potential barrier height of about 2.3 V becomes ohmic and the barrier height decreases to approximately 0.05 V. For uncompensated acceptor concentration $N_a - N_d = 3 \times 10^{18}$ cm^{-3}, thermionic emission is found to be the main mechanism of the current through the Pd–*p*-$Al_{0.06}Ga_{0.94}N$ ohmic contact. An increase in $N_a - N_d$ to approximately 10^{19} cm^{-3} in the solid solution leads to a transition from thermionic emission (at high temperatures) to tunneling (at low temperatures). © *2001 MAIK "Nauka/Interperiodica".*

INTRODUCTION

Recently, much attention has been given to studying wide-gap semiconductors, $Al_xGa_{1-x}N$ solid solutions and GaN among them, in connection with technological progress in ultraviolet and visible light sources and photodetectors, field-effect transistors, and a number of other devices [1–3]. These structures include metal–semiconductor contacts either as an active element or as an ohmic contact. However, production of an ohmic contact to *p*-type nitrides involves difficulties, since they are hard to be doped up to the concentration of $\gtrsim 10^{18}$ cm^{-3} [4]. Moreover, in contrast to other III–V compound semiconductors, in GaN and GaN-based solid solutions, the Fermi level is not pinned at the surface, which leads to a considerable dependence of potential barrier height on the electron work function. There are no metals for which the work function exceeds the sum of electron affinity and GaN or AlN band gap (larger than 7 eV) [5]; this fact implies that production of an "ideal" ohmic contact is impossible.

Let us consider the two main mechanisms of the current flow through an ohmic contact: thermionic emission and tunneling [6].

According to the thermionic-emission model, the forward current I_f is an exponential function of voltage V and temperature T:

$$I_f = I_s \exp\left(\frac{qV}{nkT} - 1\right), \tag{1}$$

$$I_s = A^* S T^2 \exp\left(\frac{-q\varphi_B}{kT}\right), \tag{2}$$

where I_s is the saturation current, q is the electron charge, n is the ideality factor, k is the Boltzmann constant, φ_B is the potential barrier height, and A^* is the effective Richardson constant

$$A^* = A\frac{m^*}{m_0} \tag{3}$$

($A = 120$ A/(cm^2 K^2) is the Richardson constant, m^*/m_0 is the majority-carrier effective mass). Then, for the resistance of $R \equiv dV/dI$ contact at $V \longrightarrow 0$, we have

$$R = \left(\frac{k}{qA^*TS}\right)\exp\left(\frac{q\varphi_B}{kT}\right), \tag{4}$$

and for a unit area (S) resistance of the contact, $R_c = RS$. Being plotted in semilogarithmic scale, the $RT(1/T)$ dependence should be linear, with the slope characterizing the barrier height φ_B.

According to the model of tunneling [6], the unit-area resistance of a contact is given by

$$\frac{1}{R_c} = \frac{m^* q^2}{2\pi\hbar^3}\int_0^\infty \left(\frac{T(E)}{\exp[(E-\mu)/kT] - 1}\right) dE, \tag{5}$$

where $\hbar$ is the Planck constant, $T(E)$ is the probability of tunneling of carrier with energy E through the barrier

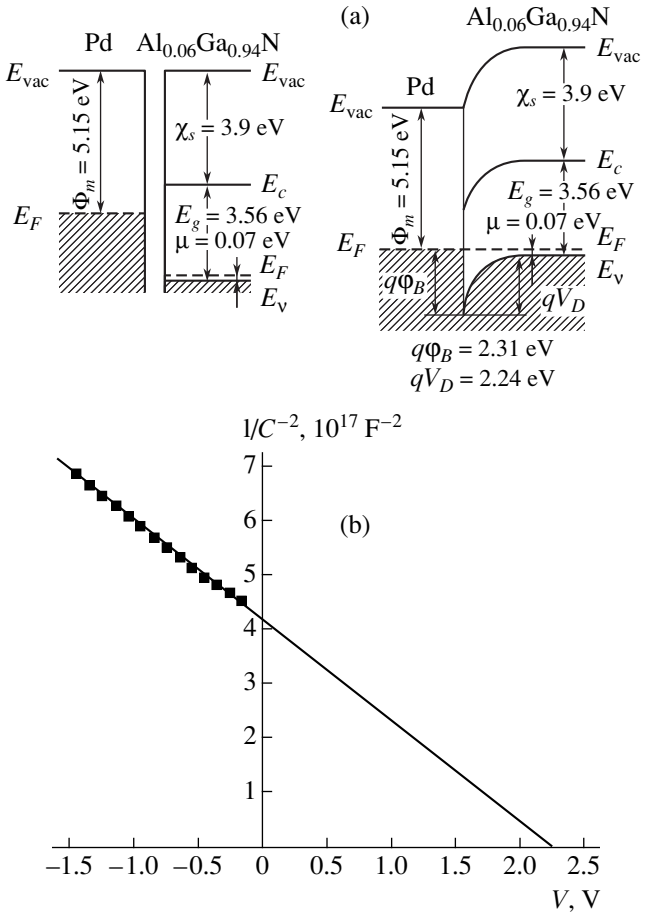

Fig. 1. (a) Energy-band diagram of Pd–*p*-$Al_{0.06}Ga_{0.94}N$ barrier contact and (b) the capacitance–voltage curve measured for this contact at T = 300 K. E_{vac} is the vacuum level, E_c is the conduction band bottom, E_v is the valence band top, and E_F is the Fermi level.

lower than $q\varphi_B$ by ΔE, and μ is the energy of the Fermi level (E_F) in the semiconductor.

In [7], it was found that

$$R_c \propto \exp\left[\left(\frac{2\sqrt{\varepsilon_s\varepsilon_0 m^*}}{\hbar}\right)\left(\frac{\varphi_B}{N^{1/2}}\right)\right], \qquad (6)$$

where ε_0 is the permittivity of free space, ε_s is the permittivity of a semiconductor and N is the uncompensated impurity concentration. Within this model, the resistance of contact exhibits an exponential dependence on $N^{-1/2}$ and depends on temperature only slightly.

There are few studies concerned with the mechanisms of the current flow through the ohmic contact in the structures based on semiconductor nitrides, especially, on those of *p*-type.

Thus, in [8], an ohmic contact of Ti/Ag with heavily doped *n*-GaN (uncompensated donor concentration $N_d - N_a$ falls in the range of 1.5×10^{17} to 1.7×10^{19} cm^{-3}) was considered, the tunneling mechanism of the current flow was ascertained, and the barrier height was determined to be 0.067 eV.

In [5], a nonalloyed Pt–*p*-GaN contact was studied for two values of uncompensated acceptor concentration: 1.8×10^{17} and 1.0×10^{18} cm^{-3}. It was found that, after a conventional surface treatment of a sample with $N_a - N_d = 1.8 \times 10^{17}$ cm^{-3}, thermionic emission is the main mechanism of current flow through the Pt–*p*-GaN contact. However, after an oxidation and $(NH_4)_2S$ surface treatment of the sample with $N_a - N_d = 1.0 \times 10^{18}$ cm^{-3}, it is tunneling that becomes the main mechanism of the current flow. Although the current–voltage characteristic of the nonalloyed contact was linear, the barrier height was determined to be as high as 0.42 eV.

In this paper, we report the results of studying the Pd–*p*-$Al_xGa_{1-x}N$ ohmic contact with high concentrations of holes in the semiconductor.

EXPERIMENTAL

Pd contacts were formed on the *p*-$Al_{0.06}Ga_{0.94}N$ epilayers grown by chloride–hydride vapor-phase epitaxy (HVPE) on the *n*-6*H*–SiC commercial substrates. The uncompensated acceptor concentration in the *p*-$Al_{0.06}Ga_{0.94}N$ epilayers of ~0.7 μm thickness was $N_a - N_d = 3 \times 10^{18}$–$10^{19}$ cm^{-3}. Pd was deposited by the thermal vacuum method on the epilayer surface pretreated in KOH solution. Then, the contacts were annealed in an N_2 atmosphere at 800°C for 20 s.

The $N_a - N_d$ concentration in the epilayers was measured with a mercury probe and was also derived from the capacitance–voltage (*C*–*V*) characteristics of Schottky barriers, formed by thermal vacuum deposition of Al or Au on the *p*-$Al_{0.06}Ga_{0.94}N$ layers. The measurements were performed at 300 K at a frequency of 10 kHz.

Resistance of the contacts was measured by the method outlined in [9] in the temperature range between 90 and 400 K.

On some of the samples, along with the ohmic contact, a barrier contact was formed by deposition of Pd; the barrier height of Pd–*p*-$Al_{0.06}Ga_{0.94}N$ contact was determined from the current–voltage (*I*–*V*) and *C*–*V* characteristics.

RESULTS AND DISCUSSION

It is well known that, in Pd–*p*-GaN and Pd–*p*-$Al_xGa_{1-x}N$ structures, the Schottky barrier height is controlled by the electron work function for the metal, and the electron affinity and the semiconductor band gap. The electron work function for Pd is Φ_m = 5.12–5.17 eV [6]. The band gap E_g amounts to 3.39 and 6.2 eV for GaN and AlN, respectively; the electron affinity χ_s = 4.1 eV for GaN and χ_s = 0.6 eV for AlN [10]. Let us assume that, for $Al_xGa_{1-x}N$ semiconductors with

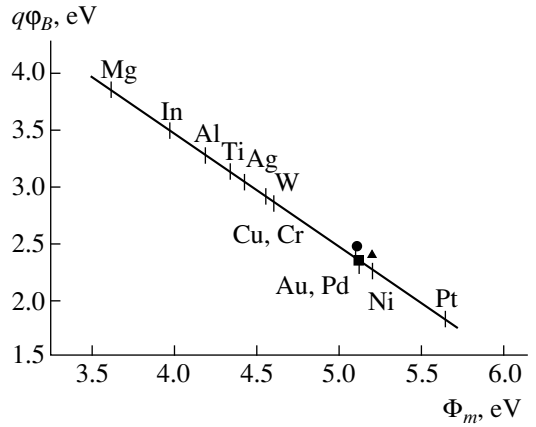

Fig. 2. The potential barrier height $q\varphi_B$ vs. the electron work function Φ_m for $Al_{0.06}Ga_{0.94}N$. Vertical bars stand for the calculated values $q\varphi_B = E_g - \Phi_m + \chi_s$; dots correspond to the experimental values obtained with Au–*p*-GaN [11], Ni–*p*-GaN [12], and Pd–*p*-$Al_{0.06}Ga_{0.94}N$ (this study).

compositions close to GaN, the band gap E_g and the electron affinity χ_s are linear in x. As a result, for $Al_{0.06}Ga_{0.94}N$, we have E_g = 3.56 eV and χ_s = 3.9 eV. Thus, in the Pd–*p*-$Al_{0.06}Ga_{0.94}N$, the barrier height should be $E_g - \Phi_m + \chi_s$ = 2.3 eV.

The experimental value of Pd–*p*-$Al_{0.06}Ga_{0.94}N$ barrier height derived from *C*–*V* characteristic was found to be 2.35 eV, which is in good agreement with the theoretical prediction (Fig. 1).

We note that, for Au–*p*-GaN structures with parameters close to those we consider ($N_a - N_d = 2 \times 10^{18}$ cm^{-3}, E_g = 3.39 eV, Φ_m = 5.1 eV, χ_s = 4.1 eV), the theoretical prediction for φ_B (2.4 V) is also consistent with the experiment (2.48 V) [11]. The barrier height of Ni–*p*-GaN (4×10^{16} cm^{-3}) calculated in [12] from the *I*–*V* and *C*–*V* characteristics amounted to 2.4 V (Fig. 2).

The results of our studying the resistance of Pd–*p*-$Al_{0.06}Ga_{0.94}N$ ohmic contacts are as follows.

(i) For contacts to solid solution with a concentration of $N_a - N_d = 3 \times 10^{18}$ cm^{-3}, the contact resistance decreased with temperature. In the wide temperature range from 90 up to 360 K, the dependence of *RT* on $1/T$ was found to be linear on a semilogarithmic scale (Fig. 3), which is consistent with thermionic emission

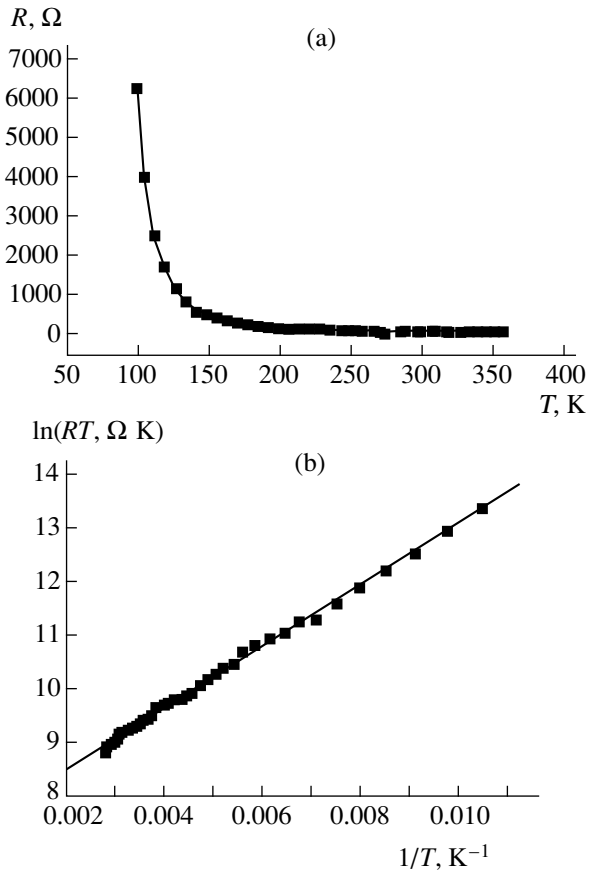

Fig. 3. (a) Temperature dependence of resistance *R* of Pd–$Al_{0.06}Ga_{0.94}N$ ($N_a - N_d = 3 \times 10^{18}$ cm^{-3}) ohmic contact and (b) the dependence of *RT* on $1/T$ for the same contact.

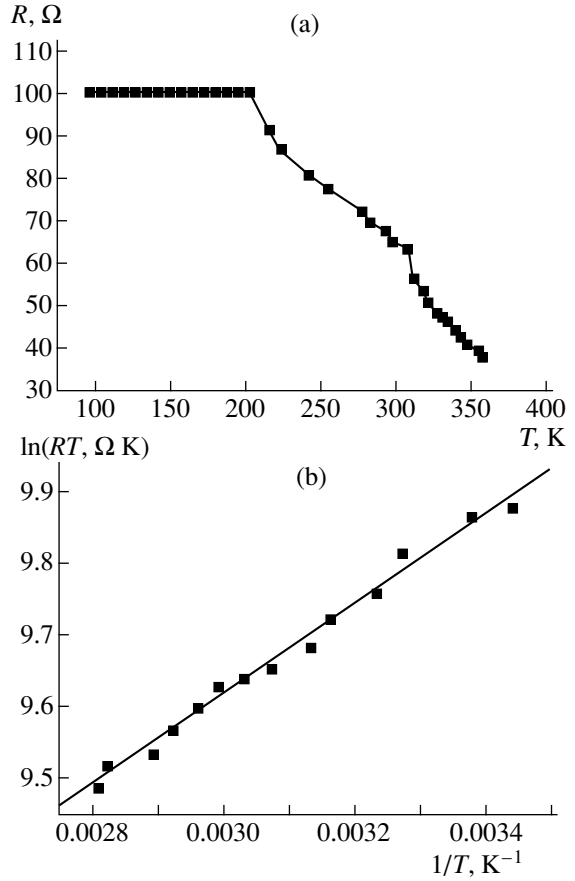

Fig. 4. (a) Temperature dependence of resistance *R* of Pd–$Al_{0.06}Ga_{0.94}N$ ($N_a - N_d = 10^{19}$ cm^{-3}) ohmic contact and (b) the dependence of *RT* on $1/T$ in the temperature range from 300 up to 360 K for the same contact.

theory. The potential barrier height φ_B derived from the curve is about 0.05 eV.

(ii) For contacts to solid solution with concentration $N_a - N_d = 10^{19}$ cm^{-3}, the contact resistance also decreased with temperature, as in the first case. In the temperature range from 300 up to 360 K, the dependence of RT on $1/T$ was found to be linear on a semilogarithmic scale (Fig. 4), which is consistent with thermionic emission theory. The potential barrier height φ_B derived from the curve was also close to 0.05 eV. At low temperatures (T = 90–190 K), however, the situation changes: the resistance becomes temperature-independent, which apparently indicates that thermionic emission has given way to tunneling as the main mechanism of the current flow through the ohmic contact. We note that, for a unit area resistance, we found that $R_c \approx 5 \times 10^{-3}$ Ω cm^2 for structures with $N_a - N_d = 3 \times 10^{18}$ cm^{-3} and $R_c \approx 3 \times 10^{-3}$ Ω cm^2 for structures with $N_a - N_d = 10^{19}$ cm^{-3} at T = 300 K.

CONCLUSION

Thus, the thermal treatment at 800°C transforms the Pd–*p*-$Al_{0.06}Ga_{0.94}N$ barrier contact with a potential barrier height of ~2.3 eV into an ohmic contact with a potential barrier height of ~0.05 V. For $N_a - N_d = 3 \times 10^{18}$ cm^{-3}, the thermionic emission is the main mechanism of the current flow through these ohmic contacts; in contrast, for $N_a - N_d = 10^{19}$ cm^{-3}, a transformation from thermionic emission (at high temperatures) to tunneling (at low temperatures) is observed.

REFERENCES

1. S. Nakamura, M. Senoh, N. Iwasa, and S. Nagahama, Jpn. J. Appl. Phys., Part 2 **34**, L797 (1995).
2. M. Asif Khah, J. N. Kuznia, A. R. Bhattarai, and D. T. Olson, Appl. Phys. Lett. **62**, 1786 (1993).
3. E. V. Kalinina, V. A. Soloviev, A. I. Babanin, *et al.*, in *Proceedings of the Second Conference on High Temperature Electronics (HITEN), Manchester, 1997*, p. 277.
4. J.-S. Jang, I.-S. Chang, H.-K. Kim, *et al.*, Appl. Phys. Lett. **74**, 70 (1999).
5. J.-S. Jang and T.-Y. Seong, Appl. Phys. Lett. **76** (19), 2743 (2000).
6. E. H. Rhoderick, *Metal–Semiconductor Contacts* (Claredon Press, Oxford, 1978).
7. A. Y. C. Yu, Solid-State Electron. **13**, 239 (1970).
8. J. D. Guo, C. I. Lin, M. S. Feng, *et al.*, Appl. Phys. Lett. **68** (2), 235 (1996).
9. G. K. Reeves, Solid-State Electron. **23** (5), 487 (1980).
10. *Handbook on Semiconductors Parameters*, Ed. by M. Levinshtein, S. Rumyantsev, and M. Shur (Wiley, New York, 2000), Vol. 3.
11. N. I. Kuznetsov, E. V. Kalinina, V. A. Soloviev, and V. A. Dmitriev, Mater. Res. Soc. Symp. Proc. **395**, 837 (1999).
12. K. Schiojima, T. Sugahara, and S. Sakai, Appl. Phys. Lett. **74** (14), 1936 (1999).

Translated by A. Sidorova-Biryukova

Semiconductors, Vol. 35, No. 5, 2001, pp. 533–538. Translated from Fizika i Tekhnika Poluprovodnikov, Vol. 35, No. 5, 2001, pp. 554–559.

SEMICONDUCTOR STRUCTURES, INTERFACES, AND SURFACES

Thermodynamic Analysis of the Growth of GaAsN Ternary Compounds by Molecular Beam Epitaxy

V. A. Odnoblyudov, A. R. Kovsh, A. E. Zhukov, N. A. Maleev, E. S. Semenova, and V. M. Ustinov

Ioffe Physicotechnical Institute, Russian Academy of Sciences, Politekhnicheskaya ul. 26, St. Petersburg, 194021 Russia

Submitted October 24, 2000; accepted for publication October 26, 2000

Abstract—A thermodynamic model describing the growth of GaAsN ternary solid solutions is presented. The model is able to predict the nitrogen content of GaAsN layers in relation to external parameters (flow rate of molecular nitrogen, arsenic flux, growth rate, and substrate temperature). The proposed model accounts for experimental observations such as the leveling-off dependence of the composition on the rate of the external flow of nitrogen, the existence of a plateau in the temperature dependence of the composition, and luminescence peak broadening with respect to the ideal case. *© 2001 MAIK "Nauka/Interperiodica".*

1. INTRODUCTION

During the growth of semiconducting materials by molecular beam epitaxy (MBE), the composition profile of ternary III–V compounds with a single volatile component of group V is readily controlled with a high precision, which is due to the unity incorporation efficiency of group III elements under standard growth conditions. Controlling the composition of compounds with two group V elements is a more complicated technological problem, requiring a great number of growth experiments. In this context, developing simple models that could predict the composition of one or other ternary compound on the basis of prescribed growth parameters (external fluxes and substrate temperature) is currently pressing. From the technological standpoint, the thermodynamic approach to the description of growth processes much surpasses the kinetic models, owing to its simplicity and clearness. It has been shown that MBE growth can be considered in terms of the thermodynamic approach on the assumption that the equilibrium between the gas and solid phases is attained at the surface of a growing film [1, 2]. In [3], we developed this approach for the growth of quaternary compounds with two volatile components and successfully applied it to the InGaAsP system. A good agreement was achieved between the experimental and calculated dependences.

At present, a new material of semiconductor electronics, (In)GaAsN, promising for the fabrication of 1.3 μm and, possibly, 1.55 μm light-emitting devices on GaAs substrates, is being intensively studied in quite a number of research centers all over the world [4]. The greatest progress in this field has been achieved with the use of the MBE technique [5, 6]. Therefore, developing an adequate theoretical model for describing the growth of nitrogen-containing compounds is an urgent task. The necessity for creating such a model is dictated by the novelty of investigations of the GaAsN system and the comparatively limited experimental experience that has been gained in this field. The complexity of this problem consists in that the content of nitrogen in GaN_xAs_{1-x} compounds is low and there exists a substrate temperature range ($T \approx 400$–500°C) in which the nitrogen incorporation efficiency remains constant. The question as to exactly which gas species of the plasma are incorporated into the growing layer has not been completely elucidated either. Nevertheless, extremely little attention has been given in the literature to creating a theoretical basis for describing the MBE growth of the given compound. In [7, 8], kinetic models were developed of GaAsN layer growth with two kinds of nitrogen plasma source driven by electron cyclotron resonance (ECR) and direct current (DC), respectively. However, these models fail to give the necessary numerical relations between the growth conditions and the parameters of a growing film. In [9], the growth process was regarded as the interaction of the gas and solid phases, and it was assumed that the growth occurs under strongly nonequilibrium conditions (the chemical affinity of the reactions describing the formation of the GaAsN compound is nonzero). Therefore, the effect of growth parameters could be determined only qualitatively.

In this study, we developed a thermodynamic approach to describe the growth of III–V compounds for the case of GaAsN based on analyzing the equilibrium between various phase components involved in the occurring chemical reactions. The results of calculations in terms of the given model are presented, demonstrating good agreement with the experimental data.

1063-7826/01/3505-0533$21.00

2. THERMODYNAMIC MODEL OF THE GROWTH OF GaN_xAs_{1-x} TERNARY COMPOUND

The proposed thermodynamic approach is based on the following assumptions. The MBE process is considered to be a process in which the equilibrium is established at the surface of a growing layer between the GaN_xAs_{1-x} solid phase and Ga, N, and As_2 gas phases, which allows the application of the law of mass action. The substrate temperature is taken as the temperature of the system, *T*. The pressures determined by reevaporation from the substrate surface of respective elements are taken to be the equilibrium partial pressures of the gas phase. The properties of the ternary compounds are described in terms of the model of regular solutions [10]. Also, we assume that deviations of the GaAsN growth from stoichiometry are negligibly small.

We assume that only atomic nitrogen formed in the decomposition of gaseous molecular nitrogen in the plasma source is incorporated into the growing layer. It is noteworthy that the model being developed is in fact universal since it deals with a flux of atomic nitrogen and, consequently, can be applied to any kind of plasma source.

The reaction between the main growth components can be represented as

$$\mathrm{Ga}(g) + x\mathrm{N} + 0.5(1-x)\mathrm{As}_2(g) \longleftrightarrow \mathrm{GaN}_x\mathrm{As}_{1-x}(s). \quad (1)$$

With the solid solution GaN_xAs_{1-x} regarded as a homogeneous mixture of binary components with appropriate activity coefficients, reaction (1) can be represented as a sum of the following two reactions

$$\begin{aligned} \mathrm{Ga}(g) + \mathrm{N}(g) &\longleftrightarrow \mathrm{GaN}(s), \\ \mathrm{Ga}(g) + 0.5\mathrm{As}_2(g) &\longleftrightarrow \mathrm{GaAs}(s). \end{aligned} \quad (2)$$

According to the model of regular solutions, the activity coefficients a_{GaAs} and a_{GaN} characterize the deviation from an ideal solution. Therefore, the law of mass action for these reactions has the form

$$\frac{P_{Ga}P_{As2}^{1/2}}{a_{GaAs}} = K_{GaAs}, \quad (3a)$$

$$\frac{P_{Ga}P_{N}}{a_{GaN}} = K_{GaN}, \quad (3b)$$

where K_i are the equilibrium constants of the reactions in which binary compounds are formed, and P_i are the equilibrium partial pressures corresponding to element fluxes reevaporated from the substrate.

Equations (3a) and (3b) are supplemented by the condition of stoichiometry

$$F_{Ga}^0 - F_{Ga} = 2(F_{As2}^0 - F_{As2}) + F_N^0 - F_N \quad (4)$$

and the expression describing the ratio of the fluxes of group V elements coming to form the epitaxial layer,

$$\frac{x}{1-x} = \frac{F_N^0 - F_N}{2(F_{As2}^0 - F_{As2})}, \quad (5)$$

where F_i^0 are the element fluxes incident onto the substrate and F_i are the element fluxes reevaporated from the substrate. The reevaporated fluxes F_i and the pressures P_i are related by

$$F_i = \frac{P_i}{\sqrt{2\pi m_i kT}}, \quad (6)$$

where m_i is the molecular weight, *k* is the Boltzmann constant, and *T* is the substrate temperature. As a result, we have a system of four equations, (3a), (3b), (4), and (5) with four unknowns (x, P_{Ga}, P_{As2}, and P_N). The analytical reduction of the system gives a system of irreducible transcendental equations, requiring a numerical solution:

$$\begin{aligned} &\frac{2\times 10^{-2}}{\sqrt{2\pi m_{As2}kT}}P_{As2}^{3/2} + \frac{10^{-2}}{\sqrt{2\pi m_N kT}}\frac{a_{GaN}}{a_{GaAs}}\frac{K_{GaN}}{K_{GaAs}}P_{As2} \\ &+ (F_{Ga}^0 - F_N^0 - 2F_{As2}^0)P_{As2}^{1/2} - \frac{10^{-2}}{\sqrt{2\pi m_{Ga}kT}}K_{GaAs}a_{GaAs} = 0, \end{aligned} \quad (7)$$

$$\begin{aligned} \frac{x}{1-x} = \Bigg(&F_N^0 \\ &- \frac{10^{-2}K_{GaN}a_{GaN}}{\sqrt{2\pi m_N kT}K_{GaAs}a_{GaAs}}P_{As2}^{1/2}\Bigg)\Big/2\left(F_{As2}^0 - \frac{10^{-2}P_{As2}}{\sqrt{2\pi m_{As2}kT}}\right), \end{aligned} \quad (8)$$

where [3, 9]

$$a_{GaAs} = (1-x)\exp\left[\frac{\alpha x^2}{RT}\right], \quad a_{GaN} = x\exp\left[\frac{\alpha(1-x)^2}{RT}\right],$$

$$K_{GaAs} = \exp\left[32 - \frac{4.86\times 10^4}{T}\right],$$

$$K_{GaN} = \exp\left[44 - \frac{1.08\times 10^5}{T}\right],$$

$\alpha = 2.16\times 10^5$ J/mol is the interaction parameter, and *R* is the universal gas constant; the pressures and fluxes are given in units: P_i [mbar], F_i [$cm^{-2}\ s^{-1}$].

Thus, the solution of the system of equations (7) and (8) yields the compositions *x* and pressures of reevaporated arsenic, P_{As2}. Further, we obtain with the use of expressions (3a), (3b), and (4) the pressures of reevaporated fluxes of gallium, P_{Ga}, and nitrogen, P_N, at given external fluxes F_{As2}^0, F_N^0, and F_{Ga}^0 and substrate temperature *T*. Thus, we established a relationship between

the quantities that can be set or measured in the course of growth and the composition of the growing compound.

The nitrogen incorporation efficiency can be written as the ratio of the incorporated part of the external flux to the total external flux:

$$\eta = \frac{F_N^0 - F_N}{F_N^0} \quad (9)$$

or, using Eqs. (5) and (6), relation (9) can be represented as follows

$$\eta = \frac{2}{F_N^0}\frac{x}{1-x}\left(F_{As2}^0 - \frac{10^{-2}P_{As2}}{\sqrt{2\pi m_{As2}kT}}\right). \quad (10)$$

The flow rate of molecular nitrogen is commonly measured in sccm (standard cm^3/min). If we assume that the flux diverges from the aperture uniformly into a solid angle 2π, then the flux of nitrogen atoms F_N^0 in $cm^{-2}\ s^{-1}$ units can be represented as

$$F_N^0 = \frac{2N_A}{22.4\times 10^3 \times 60 \times 2\pi d^2} f\beta. \quad (11)$$

Here, β is the degree of decomposition of molecular nitrogen into atoms in the plasma source, the parameter determined by the type and operation parameters of the sources (such as microwave power in the RF plasma source or direct current in the DC plasma source); f is the flow rate of molecular nitrogen in the source, measured in sccm; d is the source-to-substrate distance; and N_A is the Avogadro number.

3. EXPERIMENTAL

To compare the predictions of the proposed thermodynamic model with experimental data, we prepared and studied bulk GaAsN layers. The samples were grown by MBE in a standard unit with a solid source of arsenic. An RF plasma source was used as the nitrogen supply, which, according to the manufacturer, has a 20–70% degree of decomposition (activation) of molecular nitrogen into atoms, depending on the applied microwave power. It should be noted that it is impossible to determine the degree of decomposition (activation) and beam divergence precisely in terms of the thermodynamic model, and, therefore, the degree of decomposition plays the role of a fitting parameter. However, the important point is that it remains constant for a given power, irrespective of the values of the other variable parameters.

The typical growth rate V was 1 monolayer per second (ML/s), which corresponds, for unity gallium incorporation efficiency, to an incorporated flux of $6.19\times 10^{14}\ cm^{-2}\ s^{-1}$. The flux of arsenic, found from the rearrangement of a diffraction pattern, was 2.5–3.5 times the gallium flux. The nitrogen flow rate f was varied within 0.04–0.5 sccm. The substrate temperature ranged from 400 to 530°C. The content of incorporated nitrogen was found using X-ray diffraction analysis by taking rocking curves near the (004) reflection from GaAsN layers about 0.2 μm thick. The lattice constant of cubic GaN was taken to be 0.451 nm.

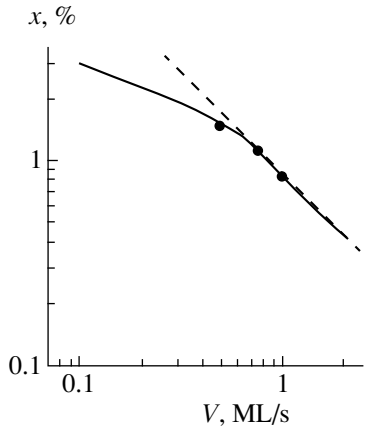

Fig. 1. Nitrogen content x of a growing GaN_xAs_{1-x} compound vs. growth rate V. The solid line represents the theoretical dependence, the dashed line corresponds to $x \sim 1/V$. The symbols represent experimental data. $F_{As2}^0 = 2.3 \times 10^{15}\ cm^{-2}\ s^{-1}$, $f = 0.15$ sccm, $\beta = 70\%$, $T = 460$°C.

4. RESULTS OF CALCULATION AND DISCUSSION

In this section we analyze the dependence of the composition (incorporation efficiency) on all four external parameters of the growth process (T, F_{As2}, f, V) and compare the results of calculation with the experimental data.

It has been established experimentally [11, 12] that, when compounds containing small amounts of nitrogen (<3%) are grown at a low external flow rate of nitrogen, the content of nitrogen in the solid solution is inversely proportional to the growth rate. The solid line in Fig. 1 represents the dependence of the composition (nitrogen content) x on the growth rate V, calculated in terms of the proposed model at fixed external fluxes of N_2 and As_2 and constant substrate temperature (460°C). It can be seen that the dependence observed in the range of growth rates typical of the MBE technique (0.6–1.2 ML/s) does agree with the inversely proportional dependence $1/V$ shown in Fig. 1 by a dashed line. The points in the figure represent the experimental data on nitrogen content in GaAsN layers grown at different rates (0.5 and 1.0 ML/s), obtained in this study. At a low growth rate (<0.5 ML/s) the dependence noticeably deviates from the inversely proportional behavior, exhibiting a tendency for the nitrogen content to level off. This is important for the growth of, e.g., In(Ga)AsN quantum dots, when the typical growth rates in these processes

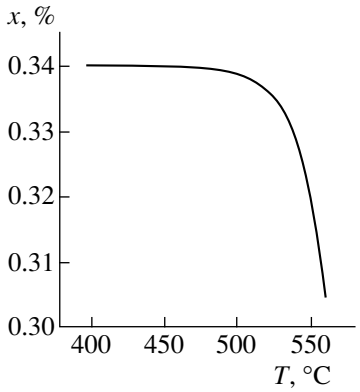

Fig. 2. Nitrogen content x of a growing GaN_xAs_{1-x} compound vs. substrate temperature T. $F^0_{As2} = 1.85 \times 10^{15}$ cm^{-2} s^{-1}, f = 0.05 sccm, β = 70%, V = 1 ML/s.

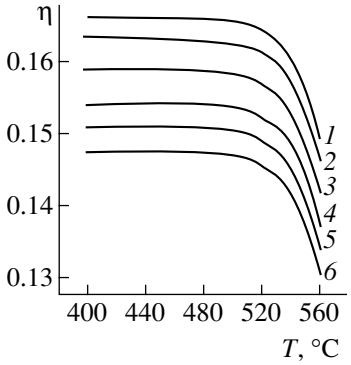

Fig. 3. Incorporation efficiency η vs. substrate temperature T. $F^0_{As2} = 1.85 \times 10^{15}$ cm^{-2} s^{-1}, β = 70%, V = 1 ML/s. Molecular nitrogen flow rate f in the source: (*1*) 0.05, (*2*) 0.1, (*3*) 0.15, (*4*) 0.2, (*5*) 0.25, and (*6*) 0.3 sccm.

are on the order of hundredths of a nanometer per second and the analysis of the nitrogen content of bulk layers is hindered by plastic strain relaxation.

Figure 2 shows the composition of the growing compound in relation to deposition temperature T at fixed external As_2 and N_2 fluxes and growth rate. A region of constant composition is clearly seen in the temperature range 400–480°C, in good agreement with experimental data [8]. At higher temperatures, the content of nitrogen decreases with increasing temperature, all other deposition conditions being the same. It is noteworthy that the x value starts to decrease long before the onset of intense reevaporation of Ga from the growth surface (~640°C).

A study of the dependence of the incorporation efficiency η on the substrate temperature allows a deeper insight into the nature of the above behavior. Figure 3 presents a family of $\eta(T)$ curves calculated by means of formula (10) for different external flow rates f of nitrogen and a fixed growth rate and arsenic flux. It can be seen that the incorporation efficiency shows the same behavior with temperature as the nitrogen content. At temperatures higher than ~570°C, it is virtually impossible to incorporate nitrogen into a growing layer. The strong temperature dependence of the incorporation efficiency in the range 520–560°C leads to the irreproducibility of the composition of layers grown under conditions of this kind and, possibly, to fluctuations of the nitrogen content during the growth process. Figure 3 shows that raising the flow rate of molecular nitrogen leads to a lower incorporation efficiency over the entire range of temperatures. Thus, the content of nitrogen depends on the nitrogen flow rate in an essentially nonlinear manner and it seems appropriate to study theoretically the dependence of x on f.

The calculated compositions of the growing layer in relation to the external flow rate of molecular nitrogen are presented in Fig. 4 in the form of theoretical dependences $x(f)$ at a fixed external flux of As_2, a fixed growth rate, and a substrate temperature of 460°C. The calculations were carried out for different decomposition factors β (different microwave powers fed into the plasma source). In addition, the figure presents experimental data on the growth of GaN_xAs_{1-x} layers under the prescribed conditions. A study aimed at correlating the experimental data with the results of theoretical calculations revealed that, under the assumption of a uniform divergence of the molecular nitrogen flow into a solid angle of 2π, the decomposition factor of the source β = 70%. Being an upper bound, this value falls into the range specified by the technical characteristics of the source when a certain directionality of the beam of nitrogen atoms is taken into account. Apparently, the dependence $x(f)$ tends to a constant value, in agreement with the experimental data. Thus, it is impossible to make the percentage of nitrogen higher in a growing layer by merely raising the rate of the external nitrogen flow in the source. At higher nitrogen flow rates, the content of nitrogen is mainly determined by the decomposition factor, i.e., by the source operation regime. The growth in this range is preferable as regards the reproducibility, since the microwave power can be controlled with high precision, whereas the nitrogen flow shows unavoidable fluctuations.

It is known that the experimental photoluminescence (PL) spectra and X-ray diffraction patterns of GaN_xAs_{1-x} are markedly broadened as compared with those of pure GaAs. For example, the typical width of the PL line is about 50 meV for GaN_xAs_{1-x} ($x \approx 2\%$) and is practically independent of the observation temperature. Phase decomposition of the growing solid solution is unlikely in the given case because of the low content of nitrogen. Thus, it may be assumed that the broadening is mainly caused by minor compositional fluctuations. With account of the fact that 1% nitrogen shifts the PL line to longer wavelengths by about 200 meV, the typical broadening corresponds to x fluctuation within approximately ±0.1%.

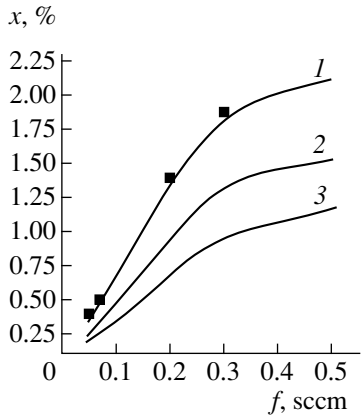

Fig. 4. Nitrogen content x of a growing GaN_xAs_{1-x} compound vs. flow rate f of molecular nitrogen. The solid lines represent theoretical dependences, symbols correspond to experimental data. $F^0_{As2} = 1.85 \times 10^{15}$ cm^{-2} s^{-1}, V = 1 ML/s, T = 460°C. Decomposition factor β: (*1*) 70, (*2*) 50, and (*3*) 35%.

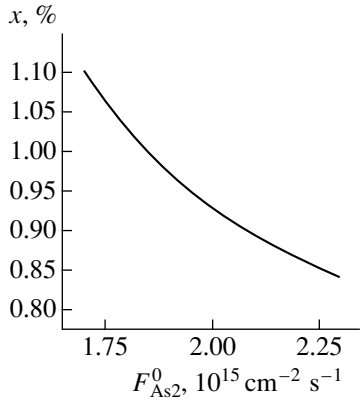

Fig. 5. Nitrogen content x of a growing GaN_xAs_{1-x} compound vs. external arsenic flux F^0_{As2}; β = 70%, V = 1 ML/s, f = 0.15 sccm, T = 460°C.

Modern MBE machines can maintain the growth rate with very high precision (no worse than 0.5%). The stability of the substrate temperature is somewhat poorer (±5°C). However, the weak temperature dependence of the nitrogen content in the range $T < 500$°C suppresses the composition fluctuations associated with this factor. As already mentioned, the instability of the nitrogen flow is suppressed by working in the range corresponding to weak $x(f)$ dependence. The only parameter that can noticeably affect the stability of the nitrogen content in the course of the growth process is the arsenic flux, which may fluctuate within 20%. This is due to (i) technical characteristics of the growth machine, especially in the case of solid-state effusion sources of arsenic; (ii) a rather large flux of arsenic, compared with other fluxes, the process being typically performed under As-rich conditions; and (iii) the high volatility of arsenic. In this context, finding the dependence of the nitrogen content on the As_2 flux is of particular importance.

Figure 5 demonstrates the dependence of the nitrogen content on the external arsenic flux in the vicinity of the typical values of the growth flow rate. It can be seen that the nitrogen content strongly depends on the arsenic flux. Varying the As_2 flux by 20% with respect to the mean value leads to composition fluctuations within 0.08–0.17%. This is in excellent agreement with the estimates based on the experimental broadening of PL lines. Thus, the arsenic flux instability may be one of the most important factors.

5. CONCLUSION

Thus, a thermodynamic model is proposed, describing the growth of GaAsN ternary solid solutions in relation to external growth parameters (flow rate of molecular nitrogen, flux of arsenic, growth rate, and substrate temperature). The model was used to demonstrate that the composition of the growing compound as a function of the growth rate in the range 0.6–1.2 ML/s is in good agreement with the experimentally observed inversely proportional dependence $x \propto 1/V$. At slower growth rates the dependence deviates from the inversely proportional behavior and x tends to a constant value, which should be taken into account in growing, e.g., In(Ga)AsN quantum dots. The temperature dependence of the composition x and incorporation efficiency η shows a plateau in the temperature range 400–480°C. At higher temperatures the nitrogen incorporation efficiency falls abruptly. This may lead to poor reproducibility of experimental results.

It is also shown that the $x(f)$ dependence levels off at high nitrogen flow rates and, thus, it is impossible to make the percentage of nitrogen higher in the growing layer, x, by merely raising the rate f of the external nitrogen flow in the source. Finally, it is demonstrated that the instability of the nitrogen flux may be an important factor responsible for PL line broadening with respect to the ideal case.

The proposed model can be applied to describe the growth of GaAsN compounds with any source of nitrogen atoms; it can also be extended to the case of molecular epitaxy from gas sources.

ACKNOWLEDGMENTS

The study was supported by the NATO Science for Peace Program (grant SfP-972484), "Physics of Solid-State Nanostructures" Program (project no. 99-2034), and CRDF grant (RE1-2221).

REFERENCES

1. R. Heckingbottom, in *Molecular Beam Epitaxy and Heterostructures*, Ed. by L. L. Chang and K. Ploog (Martimus Nishoff, Amsterdam, 1985; Mir, Moscow, 1989).

2. P. S. Kop'ev and N. N. Ledentsov, Fiz. Tekh. Poluprovodn. (Leningrad) **22**, 1729 (1988) [Sov. Phys. Semicond. **22**, 1093 (1988)].
3. A. Yu. Egorov, A. R. Kovsh, A. E. Zhukov, *et al.*, Fiz. Tekh. Poluprovodn. (St. Petersburg) **31** (10), 1153 (1997) [Semiconductors **31**, 989 (1997)].
4. V. M. Ustinov and A. E. Zhukov, Semicond. Sci. Technol. **15**, R41 (2000).
5. B. Bochert, A. Yu. Egorov, S. Illek, and H. Riechert, IEEE Photonics Technol. Lett. **12** (6), 597 (2000).
6. D. A. Livshits, A. Yu. Egorov, and H. Riechert, Electron. Lett. **36** (16), 1381 (2000).
7. Z. Z. Bandic, R. J. Hauenstein, M. L. O'Steen, and T. C. McGill, Appl. Phys. Lett. **68** (11), 1510 (1996).
8. Z. Pan, L. H. Li, W. Zhang, *et al.*, Appl. Phys. Lett. **77** (2), 214 (2000).
9. Y. Qiu, S. A. Nikishin, H. Temkin, *et al.*, Appl. Phys. Lett. **70** (21), 2831 (1997).
10. A. S. Jordan and M. Ilegems, J. Phys. Chem. Solids **36**, 329 (1975).
11. T. Kitatani, M. Kondow, K. Nakahara, *et al.*, J. Cryst. Growth **201/202**, 351 (1999).
12. B. V. Volovik, A. R. Kovsh, W. Passenberg, *et al.*, Pis'ma Zh. Tekh. Fiz. **26** (10), 88 (2000) [Tech. Phys. Lett. **26**, 443 (2000)].

Translated by M. Tagirdzhanov

Semiconductors, Vol. 35, No. 5, 2001, pp. 539–542. Translated from Fizika i Tekhnika Poluprovodnikov, Vol. 35, No. 5, 2001, pp. 560–563.

SEMICONDUCTOR STRUCTURES, INTERFACES, AND SURFACES

An Analysis of the Charge-Transport Mechanisms Defining the Reverse Current–Voltage Characteristics of the Metal–GaAs Barriers

S. V. Bulyarskiĭ and A. V. Zhukov*

Ul'yanovsk State University, Ul'yanovsk, 432700 Russia

**e-mail: avg@ulsu.ru*

Submitted September 11, 2000; accepted for publication September 19, 2000

Abstract—Reverse current–voltage characteristics of metal–GaAs contacts with a Schottky barrier were measured. Linear portions of the reverse-current dependence on the squared electric-field strength in the space-charge region of diodes were obtained. Such a dependence is related to electron interaction with the lattice vibrations. The reverse current of the Mo–GaAs:Si contacts is analyzed at different temperatures. Results of the analysis showed that measured current–voltage characteristics are controlled by the phonon-assisted electron tunneling from metal into semiconductor with the involvement of a deep center attributed to the *EL2* trap. A similar mechanism governs the reverse current–voltage characteristics of the Ni–GaAs:S Schottky diodes.

1. INTRODUCTION

An increase in the speed of response and a decrease in the power consumption are still urgent problems in the development of modern circuits for computer engineering and information processing. The first problem may be resolved by choosing semiconductor materials with a high carrier mobility and the second, by reducing the operating voltages of devices. In view of these circumstances, Schottky diodes based on the III–V materials are more and more widely used in microwave (MW) engineering and optoelectronics. Therefore, the current development of semiconductor MW electronics and integrated microcircuits, in which the field-effect transistors with a Schottky gate based on GaAs are used, reflects a necessity for more detailed study of the material itself and of the electron processes which occur in the space charge region (SCR) of devices.

The objective of this study was to gain insight into the mechanism of an increase in the probability of the electron transitions from deep-level centers in the SCR of semiconductor devices and into the influence of these effects on the reverse current–voltage characteristics of the metal–semiconductor contacts.

2. EXPERIMENT: THE REVERSE CURRENT DEPENDENCES ON THE ELECTRIC FIELD

We studied two series of samples. Among the first series were Schottky diodes fabricated by the electrochemical deposition of Ni on S-doped GaAs. The sample preparation was described elsewhere [1, 2]. Among the second series were commercial MW varicaps based on the Schottky diodes. The *n*-GaAs epilayer substrates were grown by vapor-phase epitaxy. The varicap structure consisted of three consecutively grown layers with concentrations of the doping impurity (Si) equal to 0.3×10^{18}, 4.1×10^{18}, and 0.3×10^{18} cm^{-3}. The Schottky barrier was fabricated by molybdenum vacuum deposition. The contact area was about 1 mm^2. Studies of the contact characteristics [1, 3] showed that these structures are Schottky diodes. The current–voltage (*I–V*) characteristics of the MW varicaps were measured at a reverse bias in a voltage range from 0 to 10 V and in a temperature range of 100–370 K (Fig. 1). We measured the current–voltage characteristics of the Ni–GaAs barriers at room temperature in the voltage range of 0–2 V.

It can be seen from Fig. 1 that, in a rather wide temperature range (from 125 to 243 K), the current in the samples of the second series (varicaps) is scarcely affected by temperature, but at the same time a strong field dependence exists. Such dependence of current is typical of the tunnel mechanism of charge transport [3]. In this case, the current is given by [4]

$$I_c = I_{0c}\exp\left[-\frac{4}{3}\frac{\sqrt{2m^*}}{eF\hbar}(E_+^*)^{3/2}\right], \quad (1)$$

where F is the electric field strength in the SCR, and E_+^* is the tunneling effective energy which depends on the energy depth of level. To verify an assumption concerning the tunnel mechanism of the charge transport, *I–V* characteristics were rearranged to the $I = f(1/F)$ coordinates. The reverse bias voltage applied to the sample was converted to the field strength in the SCR

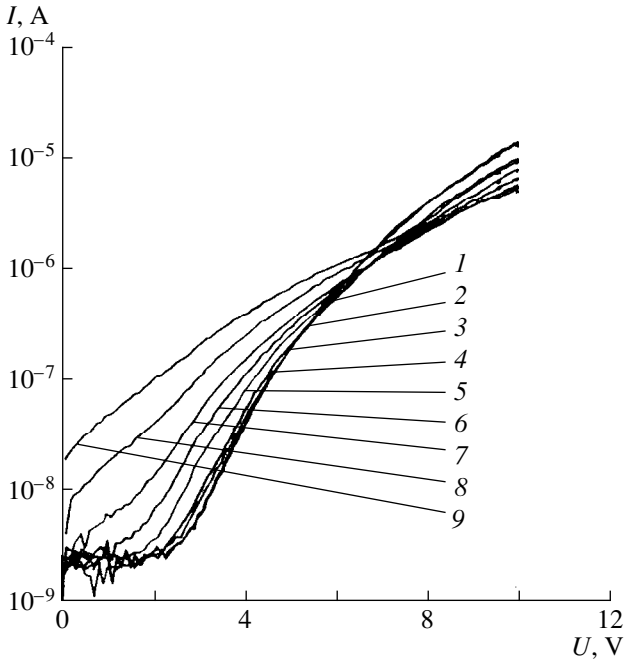

Fig. 1. Reverse current–voltage characteristics of microwave varicap at temperatures T = (*1*)125, (*2*) 168, (*3*) 209, (*4*) 243, (*5*) 275, (*6*) 307, (*7*) 338, (*8*) 351, and (*9*) 370 K.

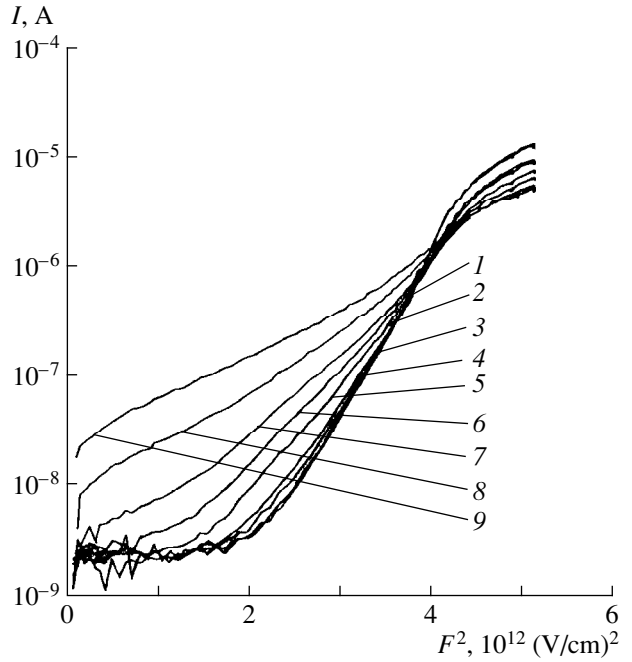

Fig. 2. Reverse current dependence of microwave varicap on the squared field strength in the space charge region at temperatures T = (*1*) 125, (*2*) 168, (*3*) 209, (*4*) 243, (*5*) 275, (*6*) 307, (*7*) 338, (*8*) 351, and (*9*) 370 K.

of the Schottky contact according to the relation [3]

$$F(U) = \frac{1}{\varepsilon\varepsilon_0 S}\int_{U-U_k}^{U} C(u)du, \qquad (2)$$

where integration was performed over the experimental dependence of the SCR capacitance (C) on the voltage (U) for forward (from $u = U - U_k$ to 0) and for reverse (from 0 to $u = U$) biases and S is the barrier area. This conversion is necessary because of the complexity of the doping profile of the samples under study [5].

I–V characteristics in the $I = f(1/F)$ coordinates are well approximated in the high field region by a straight line in the entire temperature range. The effective energy obtained from the slope is equal to 0.64 eV. It is evident that experimental results are well described by the tunneling model through the deep center. The energy depth of the center E_+ was calculated from the equation [4]

$$E_+^* = E_g\left\{\frac{3}{16}\left[\frac{\pi}{2} - \arcsin\left(1 - \frac{2E_+}{E_g}\right)\right] - \frac{3}{8}\left(1 - \frac{2E_+}{E_g}\right)\sqrt{\frac{E_+}{E_g} - \left(\frac{E_+}{E_g}\right)^2}\right\}^{2/3}, \qquad (3)$$

where E_g is the band gap, and was found to be 0.73 eV, which agrees well with the trap level *EL2* in GaAs.

In the low-field region, the current depends only slightly on field. Such I–V behavior is related to a predominance of the leakage currents in this region.

3. CALCULATION OF PARAMETERS OF THE PHONON-ASSISTED TUNNELING MODEL

Multiphonon processes are of considerable importance in nonradiative transitions [2, 6–8]. Electron–phonon interaction results in the temperature dependences of the capture coefficients and in an increase of the thermal emission rate in high electric fields. The vibration states of the impurity centers cause a similar effect which may explain the observed current increase with temperature. It is experimentally [2, 9] and theoretically [10–18] shown that the probability of these transitions in high electric fields increases exponentially with the squared electric-field strength. A similar strong increase in electric current (considering that $U \propto F^2$ for an abrupt p–n junction) can be seen in Fig. 2. According to Fig. 2, the electric field strength F exceeds 2×10^6 V/cm, which corresponds to high electric fields, in the SCR of the MW varicap. As can be seen from Fig. 2, a linear dependence of the logarithm of the current on F^2 is observed in the range from 10^{12} to 4×10^{12}(V/cm)^2 (abscissa axis).

If only one level exists in the band gap of a semiconductor, then the reverse current through the SCR with

the involvement of this level (irrespective of the charge transport mechanism) can be expressed as

$$I = Se\int_0^l \frac{W_1 W_2}{W_1 + W_2} dx \approx Se\frac{W_1 W_2}{W_1 + W_2} l, \qquad (4)$$

where l is the SCR width, and W_1 and W_2 are the probabilities of the electron transition from metal to the deep level and from this level to the conduction band. The probability of one of the transitions is usually higher. Assuming that the energy distance between the deep level and the bottom of the conduction band is $E_t > \varphi_b - E_t$, where φ_b is the barrier height, we obtain $W_2 \gg W_1$. In this case, formula (4) may be rewritten as $I \approx SeW_1 l$. Therefore, to an accuracy of the field dependence of the SCR width, we have $I(F, T) = \text{const}\, W_1(F, T)$.

In recent papers devoted to the study of multiphonon generation–recombination processes involving deep impurity centers based on the studies of Perel and Yassievich [15–19], the probability of tunnel multiphonon ionization as a function of the electric field is given by the relation [19]

$$W(F, T) = W(0, T)\exp(F^2/F_0^2), \qquad (5)$$

where

$$\frac{1}{F_0^2} = \frac{\tau_2^3 e^2}{3m^*\hbar}, \text{ but } \tau_2 = \frac{\hbar}{2kT} - \frac{\hbar}{2\hbar\omega}\ln\left(\frac{S\hbar\omega}{E_0}\right). \qquad (6)$$

Here S is a coefficient. Approximating the linear portions of the curve $\log I(F^2)$ (Fig. 2) by straight lines, we obtained the slopes of these portions $\frac{d\ln I}{d(F^2)}$. Then, after plotting the $\sqrt[3]{\frac{d\ln I}{d(F^2)}} = f\left(\frac{10^3}{T}\right)$ dependence, we analyzed the applicability of formulas (5) and (6) to describe the experimental curves (Fig. 3). Initially (at high temperatures) this dependence is well approximated by the straight line

$$y = (\tan\alpha_{\text{exp}})\frac{10^3}{T} - y_0.$$

The slope of this line is $\tan\alpha_{\text{exp}} = 3.24 \times 10^{-5}$. This result is in good agreement with the theoretical value obtained from (6):

$$\tan\alpha_{\text{theor}} = \frac{\hbar}{2k}\sqrt[3]{\frac{e^2}{3m^*\hbar}}\frac{1}{10^3} = 1.83 \times 10^{-5}.$$

It should be noted that so far we have not made any assumptions about the character of the deep center that is involved in this transition. We now assume that trap *EL2* is involved in this process. According to the above, we assume that the energy of the *EL2* level is $E_0 = 0.73$ eV. We used the local phonon energy as well as the Huang and Rhys factor as adjustable parameters. The cutoff value $y_0 = -1.51 \times 10^{-5}$ obtained from approximation by a straight line is in good agreement with the theoretical value calculated from the relation (6) for $\hbar\omega = 28$ meV and $S = 7$. This result differs only slightly from the data reported, for example, in [20] where

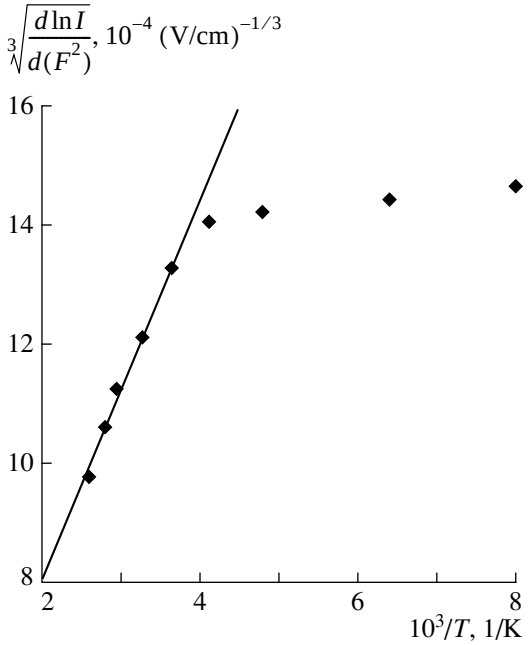

Fig. 3. Dependence of $[d\ln I/d(F^2)]^{1/3}$ on $10^3/T$.

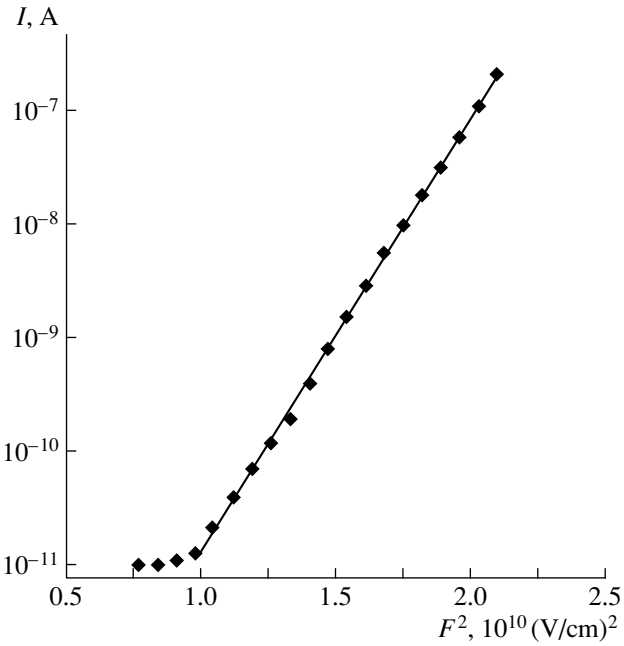

Fig. 4. Reverse current–voltage characteristic of the Ni–GaAs:S diode at $T = 295$ K.

$\hbar\omega = 20 \pm 5$ meV and $S\hbar\omega = 115 \pm 50$ meV. It should be noted that the deep center of the $V_{Ga}S_{As}$ complex, which we previously studied [2], either is not involved at all in the charge transport in the SCR of the reverse-biased diode or its contribution is negligible. This follows from the fact that the energy depth of this center is larger than the potential-barrier height of the Ni–GaAs contact.

A plot of the reverse current as a function of the squared field strength in the SCR of the Ni–GaAs:S diode is shown in Fig. 4. It can be seen that, in the squared-field range from 10^{10} to 2.5×10^{10} (V/cm)^2, the dependence of log$I$ on F^2 is linear. The slope in this portion of the curve is $d\ln I/d(F^2) = 8.81 \times 10^{-10}$, which agrees with the theoretical value

$$\frac{d\ln I}{d(F^2)} = 1/F_0^2$$

for parameters $\hbar\omega = 19.5$ meV and $S = 7$ (the calculation was performed on the assumption that *EL2* traps with the energy depth $E_0 = 0.73$ eV are involved in the process). This result agrees better with the data of [20], although due to the absence of the temperature-related measurements we cannot state that *EL2* traps exist. Nevertheless, an obvious linear current dependence on the squared field strength observed in all the samples studied enables us to state that a mechanism for phonon-assisted tunnel transport of charge carriers exists.

4. CONCLUSION

Thus, we measured the reverse current–voltage characteristics of the Ni–GaAs:S Schottky diodes, fabricated in the laboratory, and of commercial MW varicaps based on the Mo–GaAs:Si Schottky diodes. In both types of samples, linear portions of the reverse current dependences on the squared electric-field strength in the space charge region of diodes were observed. It is shown that such dependence is related to the interaction of electrons with the lattice vibrations. The reverse current of the MW varicaps is analyzed at different temperatures. Results of analysis showed that the current–voltage (*I–V*) characteristics are controlled by the phonon-assisted electron tunneling from metal into semiconductor with the involvent of a deep center attributed to the *EL2* trap. It is shown that a similar mechanism also governs reverse *I–V* characteristics of the Ni–GaAs:S Schottky diodes.

REFERENCES

1. S. V. Bulyarskiĭ and A. V. Zhukov, Uch. Zap. Ul'yanovsk. Gos. Univ., Ser. Fiz. **2** (5), 98 (1998).
2. S. V. Bulyarskiĭ, N. S. Grushko, and A. V. Zhukov, Zh. Éksp. Teor. Fiz. **116** (3), 1027 (1999) [JETP **89**, 547 (1999)].
3. S. V. Bulyarskiĭ and N. S. Grushko, *Generation–Recombination Processes in Active Elements* (Mosk. Gos. Univ., Moscow, 1995).
4. O. V. Kurnosova and A. A. Pakhomov, Fiz. Tekh. Poluprovodn. (Leningrad) **20** (10), 1868 (1986) [Sov. Phys. Semicond. **20**, 1171 (1986)].
5. A. S. Ambrozevich, S. V. Bulyarskiĭ, N. S. Grushko, and A. V. Zhukov, Uch. Zap. Ul'yanovsk. Gos. Univ., Ser. Fiz. **2** (7), 54 (1999).
6. Huang Kun and A. Rhys, Proc. R. Soc. London **204**, 406 (1950); in *Problems in Physics of Semiconductors*, Ed. by V. L. Bonch-Bruevich (Inostrannaya Literatura, Moscow, 1957).
7. S. I. Pekar, Usp. Fiz. Nauk **50**, 197 (1953).
8. V. A. Kovarskiĭ, *Kinetics of Nonradiative Processes* (Shtiintsa, Kishinev, 1968).
9. S. V. Bulyarskiĭ, N. S. Grushko, and A. A. Gutkin, Fiz. Tekh. Poluprovodn. (Leningrad) **9**, 287 (1975) [Sov. Phys. Semicond. **9**, 187 (1975)].
10. D. Pons and S. Makram-Ebeid, J. Phys. (Paris) **40** (12), 1168 (1979).
11. S. Makram-Ebeid and M. Lannoo, Phys. Rev. B **25** (10), 6406 (1982).
12. S. F. Timashov, Fiz. Tverd. Tela (Leningrad) **14**, 2621 (1972) [Sov. Phys. Solid State **14**, 2267 (1973)].
13. S. F. Timashov, Fiz. Tverd. Tela (Leningrad) **14**, 171 (1972) [Sov. Phys. Solid State **14**, 136 (1972)].
14. V. Karpus and V. I. Perel', Pis'ma Zh. Éksp. Teor. Fiz. **42**, 403 (1985) [JETP Lett. **42**, 497 (1985)].
15. V. Karpus, Pis'ma Zh. Éksp. Teor. Fiz. **44**, 334 (1986) [JETP Lett. **44**, 430 (1986)].
16. V. Karpus and V. I. Perel', Zh. Éksp. Teor. Fiz. **91**, 2319 (1986) [Sov. Phys. JETP **64**, 1376 (1986)].
17. V. N. Abakumov, I. A. Merkulov, V. I. Perel', and I. N. Yassievich, Zh. Éksp. Teor. Fiz. **89** (4), 1472 (1985) [Sov. Phys. JETP **62**, 853 (1985)].
18. V. N. Abakumov, O. V. Kurnosova, A. A. Pakhomov, and I. N. Yassievich, Fiz. Tverd. Tela (Leningrad) **30** (6), 1793 (1988) [Sov. Phys. Solid State **30**, 1030 (1988)].
19. S. D. Ganichev, I. N. Yassievich, and W. Prettl, Fiz. Tverd. Tela (St. Petersburg) **39** (11), 1905 (1997) [Phys. Solid State **39**, 1703 (1997)].
20. G. Martin and S. Makram-Ebeid, Phys. Rev. Lett. **54** (2), 416 (1986).

Translated by I. Kucherenko

Semiconductors, Vol. 35, No. 5, 2001, pp. 543–549. Translated from Fizika i Tekhnika Poluprovodnikov, Vol. 35, No. 5, 2001, pp. 564–570.

LOW-DIMENSIONAL SYSTEMS

Photoelectric Spectroscopy of InAs/GaAs Quantum Dot Heterostructures in a Semiconductor/Electrolyte System

I. A. Karpovich*, A. P. Gorshkov, S. B. Levichev, S. V. Morozov, B. N. Zvonkov, and D. O. Filatov

Nizhni Novgorod State University, pr. Gagarina 23, Nizhni Novgorod, 603600 Russia

** e-mail: get@phys.unn.runnet.ru*

Submitted July 18, 2000; accepted for publication October 23, 2000

Abstract—The photovoltaic effect in the semiconductor/electrolyte junction is an effective method for investigation of the energy spectrum of InAs/GaAs heterostructures with self-assembled quantum dots. An important advantage of this method is its high sensitivity. This makes it possible to obtain photoelectric spectra from quantum dots with high barriers for the electron and hole emission from quantum dots into the matrix even if the surface density of the dots is low (~10^9 cm^{-2}). In a strong transverse electric field, broadening of the lines of optical transitions and emission of electrons and holes from quantum dots into the matrix directly from the excited states are observed. The effect of the photovoltage sign reversal was detected for a sufficiently high positive bias across the barrier within the semiconductor. This effect is related to the formation of a positive charge at the interface between the cap layer and electrolyte and of the negative charge on impurities and defects in the quantum dot layer. © *2001 MAIK "Nauka/Interperiodica".*

1. INTRODUCTION

Photovoltaic spectroscopy, which is based on the investigation of the photovoltaic effect spectra for barriers of various types and photoconductivities, extends the range of optical methods for diagnostics of quantum well structures [1–7]. It permits a determination of the energy spectrum and some other characteristics of quantum objects (quantum wells (QWs), quantum dots (QDs), etc.) at low photoexcitation levels in a wide spectral range at room temperature. Photoelectric methods have a relatively low sensitivity to the type of band structure of the material (direct band gap or indirect band gap) and its imperfection. For the solution of various problems, this may be both an advantage and a disadvantage.

The efficiency of the methods of photoelectric spectroscopy was demonstrated mainly for the investigation of heterostructures with QWs. Application of these methods to heterostructures with self-assembled QDs, particularly of the InAs/GaAs type, involves certain difficulties. For this reason, they are rarely used for diagnostics of these structures [7]. One of the major difficulties is related to the smaller optical absorption coefficient for QDs compared to that for QWs at the usual QD surface density of ~10^{10} cm^{-2}. This hinders revealing the photosensitivity related to QDs against the background of the extrinsic photosensitivity of the structures. Another difficulty is related to the greater height of potential barriers compared to that of QWs. This restricts electron and hole emission into the matrix, which is necessary for the emergence of photoelectric effects.

One of the most convenient methods for photoelectric diagnostics of the QW structures is capacitor-photovoltage spectroscopy [6]. In this method, the surface photovoltage spectrum of a QW structure is measured within the capacitor with a pressed insulator (mica plate) and metal electrode. Due to the presence of the depletion layer at the natural GaAs surface, no artificial barrier (Schottky barrier or *p–n* junction) is required in the QW structure in order to observe the capacitor photovoltage. However, it is usually impossible to reveal QDs with a density of ~10^{10} cm^{-2} using this method [7].

In this study, the possibility for diagnostics of the InAs/GaAs QD heterostructures was investigated by a method related to the capacitor-photovoltage spectroscopy. This method includes photovoltage measurements for the semiconductor/electrolyte junction with a liquid electrolyte. This method was widely used for investigation of the surface properties of semiconductors [8]. It was also used for investigation of the energy spectrum for the structures with the InGaP/GaAs individual QWs, and a high spectral resolution was noted for this method [4]. It will be demonstrated below that the advantages of this method and its merits are of a special importance in some aspects compared to other photoelectric methods for the investigation of QD heterostructures. They adequately compensate certain inconveniences and restrictions related to the use of the liquid electrolyte.

2. EXPERIMENTAL

The electrolytic cell was fabricated by tightly pressing a Teflon ring with an inner diameter 5 mm and a

1063-7826/01/3505-0543$21.00 © 2001 MAIK "Nauka/Interperiodica"

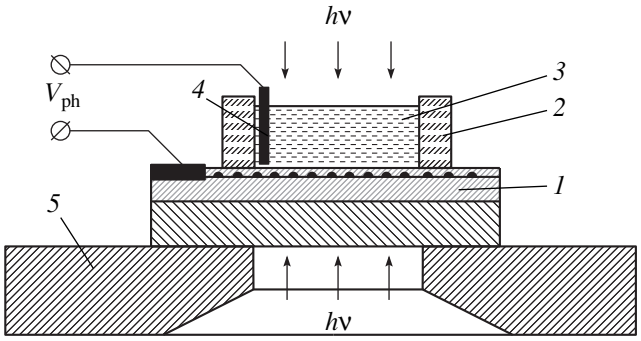

Fig. 1. Schematic representation of the electrolytic cell for investigation of the semiconductor/electrolyte photovoltage spectra. (*1*) QD heterostructure sample, (*2*) Teflon ring, (*3*) electrolyte, (*4*) Pt electrode, and (*5*) sample holder.

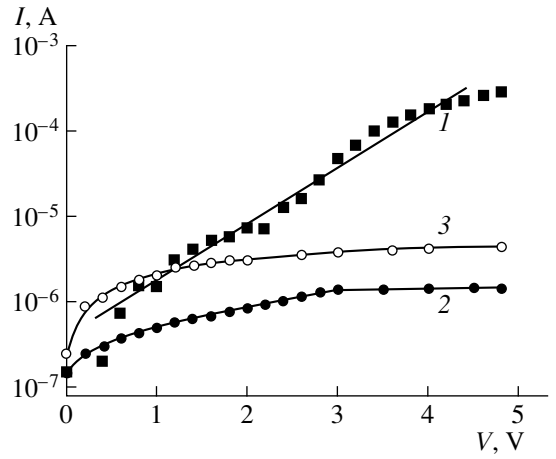

Fig. 2. Current–voltage characteristics of the (QD heterostructure)/electrolyte junction. (*1*) Forward bias (QD heterostructure is cathode); (*2*, *3*) reverse bias (QD heterostructure is anode), measurements (*2*) in dark and (*3*) under illumination.

height of 4 mm to the QD heterostructure deposited on the semi-insulating or conducting substrate. The ring and the sample served as the vessel for the electrolyte (Fig. 1). The electrolyte was a 0.5 M KCl solution mixed with glycerol in a 1 : 1 ratio. The reference electrode was a Pt wire embedded in the electrolyte. The cell design allowed for the illumination of the sample both through the electrolyte and the substrate. The latter variant was used if the electrolyte had a considerable absorption in the spectral range under investigation (at the photon energy $h\nu$ of <0.9 eV).

Photoelectric spectra were measured under a modulated illumination at a frequency of 800 Hz in a small-signal mode with synchronous detection of the signal.

The GaAs/InAs QD heterostructures obtained by vapor-phase epitaxy under atmospheric pressure using metalloorganic compounds of Ga, In, and arsine (MOCVD method) were investigated. The QD heterostructures were grown on the GaAs(100) surface misoriented by 3° to the [110] direction. A 0.8-μm-thick *n*-GaAs buffer layer was grown at 650°C, the temperature was further decreased to 530–510°C, and the QD InAs layer was deposited. Trimethylindium and arsine were separately supplied into the reactor at 4-s intervals for 6 and 2 s, respectively, with the number of cycles as large as 10. The estimated nominal thickness of the InAs layer was ~1.5 nm, i.e., about 5 monolayers. In the course of deposition, the QD layer was doped with bismuth, which allowed obtaining QDs with a higher size uniformity. The surface relief and photoelectronic properties of the Bi-doped QD heterostructures were investigated in detail in [9]. QD heterostructures both without the cap layer and with the GaAs cap layer ~15-nm thick were grown.

3. EXPERIMENTAL RESULTS AND DISCUSSION

3.1. General Characteristic of the Semiconductor/Electrolyte Photovoltage Method

Static current–voltage (*I–V*) characteristics of the (QD heterostructure)/electrolyte/Pt electrolytic cell (Fig. 2) are qualitatively similar to characteristics of the semiconductor photodiode with a Schottky barrier or a *p–n* junction. At a reverse bias across the barrier in the semiconductor, which corresponds to the *n*-type conduction of semiconductor (QD heterostructure is anode), saturation of the dark current and photocurrent is observed. The saturation current density is close to the calculated value for the Schottky barrier in *n*-GaAs with a barrier height of ~0.6 eV (the value corresponding to pinning of the Fermi level at the free surface was accepted). This indicates that at a reverse bias, the voltage drops mainly across the barrier of the depletion layer in the semiconductor electrode. Steady-state photovoltage in the open-circuit mode under monochromatic illumination in the intrinsic absorption region for GaAs ($h\nu$ = 1.5 eV) is ~0.3 V. This value agrees with the expected value for the barrier height mentioned. Similar values were obtained by the Kelvin method on the GaAs free surface [5].

For a forward bias (QD heterostructure is cathode), the voltage dependence of a current is almost exponential at low voltages (Fig. 2, curve *1*), and its leveling off at a sufficiently high voltage was observed. However, for an approximation of the forward current by the expression $I \propto \exp(qV/mkT)$, the nonideality factor for the *I–V* characteristic turns out to be very large ($m \approx 20$). This is apparently caused by a considerable voltage drop in the electrolyte and across the Pt/electrolyte contact.

The photoelectric spectra $V_{ph}(h\nu)$ obtained by various methods (photoconductivity, capacitor-photovoltage spectroscopy, and semiconductor/electrolyte photovoltage) are shown in Fig. 3. The spectra were obtained for the same Bi-doped QD heterostructure, in which the QD surface density was high enough ($\sim 2 \times 10^{10}$ cm^{-2}) for carrying out the spectrum measurements

by all these methods. Due to a high uniformity of the QDs in size and chemical composition, the major optical transition (a peak at $h\nu = 0.96$ eV) and transitions to the first and second excitation levels are well resolved and coincide in energy. The two latter peaks are spaced almost equidistantly by ~80 meV from the major peak. The energies of the photosensitivity peaks agree well with the photoluminescence (PL) spectra $J_{PL}(h\nu)$ for QDs (curve *6*). For the region of transparency for GaAs and electrolyte $0.9 < h\nu < 1.35$ eV, the semiconductor/electrolyte photovoltage spectra coincide for illumination from the electrolyte and substrate sides (curves *4*, *5*). The noticeable photosensitivity in the intrinsic absorption region for GaAs under illumination from the substrate side is related to the effect of scattered radiation. The photosensitivity band with the flattened portion close to 1.35 eV is related to the wetting layer.

The planar photoconductivity spectrum for the GaAs layer, which was obtained in similar conditions, is shown in Fig. 3 for comparison (curve *2*). It coincides with the photoconductivity spectrum of the QD heterostructure in the intrinsic absorption range for GaAs. It can be seen that the photosensitivity from the QD layer for $h\nu < 1.4$ eV exceeds the extrinsic photosensitivity for GaAs only by a factor of 2–3. It is known that the photoconductivity of the GaAs layers is barrier-controlled under usual conditions. It is governed by the modulation of the width of the surface and internal barriers (at the layer/substrate interface) under illumination [10]. For the weak-absorption region of GaAs at $h\nu < 1.4$ eV, the extrinsic photoconductivity related to the internal barrier is dominant, is determined mainly by the radiation absorption by the *EL*2 and *HL*1 deep centers in the semiconductor substrate, and has a photoelectric threshold at $h\nu \approx 0.75$ eV. The concentration of these centers in the epilayer is 1–2 orders of magnitude lower than that in the substrate and does not contribute noticeably to the photosensitivity. The background of the extrinsic photosensitivity from the substrate causes difficulties in detecting the QDs by the photoconductivity method if their concentration is $\lesssim 10^{10}$ cm^{-2}.

Upon measurement of the capacitor photovoltage in the capacitor, one of whose plates is the quasi-neutral region of the QD heterostructure itself, to which the nonrectifying contact is formed, the internal barrier seemingly should not manifest itself. However, because of both the small capacitance of the measuring capacitor and the spurious capacitive coupling of the substrate to the measuring capacitor, the background of the extrinsic photosensitivity from the substrate becomes only weaker, but does not disappear completely. This can be seen from a comparison of curves *1* and *3* in Fig. 3. As a result, the use of the capacitor-photovoltage spectroscopy makes it possible to reduce the lowest concentration for detecting the QDs down to the level of $\sim 5 \times 10^9$ cm^{-2} only. Approximately the same QD concentration is also necessary for using the method of photovoltage with the Schottky barrier.

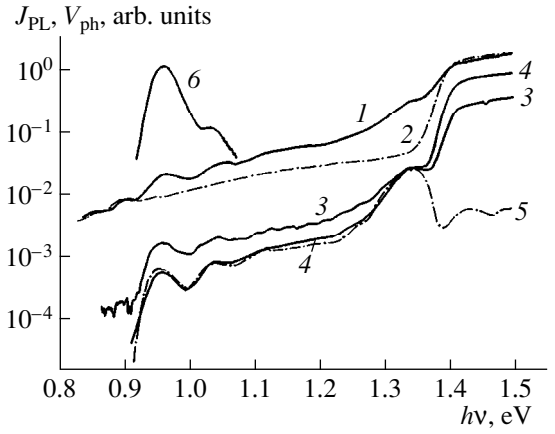

Fig. 3. Photoelectric spectra for the QD heterostructures obtained by various methods: (*1*) planar photoconductivity method, (*2*) same for uniform GaAs layer; (*3*) capacitor-photovoltage spectroscopy; (*4*) method of photovoltage in the (QD heterostructure)/electrolyte junction (illumination from the electrolyte side), and (*5*) the same for illumination from the substrate side. (*6*) Photoluminescence spectrum.

Characteristic features of the semiconductor/electrolyte photovoltage method are the practically complete absence of the background of the intrinsic photosensitivity from the substrate and a very low noise level, which is related to the high capacitance of the electrolytic capacitor. Due to these specific features of the method, its use ensures a reduction in the lowest detectable QD concentration by approximately an order of magnitude compared to other photoelectric methods. This is the major advantage of the method, which is especially valuable for investigation of QD heterostructures. In addition, the semiconductor/electrolyte photovoltage method, to some extent, combines the advantages of the capacitor-photovoltage spectroscopy and photovoltage at the Schottky barrier. In the former case, no preparation of the samples prior to measurements is required, and the surface is accessible for external effects. In the latter case, the current mode of measurements and electric-field strength variation in the vicinity of the quantum-confinement objects in a wide range are possible. The semiconductor/electrolyte photovoltage spectroscopy also provides certain unique possibilities of investigating the QD heterostructures, particularly the possibility of investigating *in situ* formation and passivation of defects in these structures, which are related to photoelectrochemical reactions on their surface.

3.2. Influence of the Electric Field on the Semiconductor/Electrolyte Photovoltage Spectrum

The influence of the transverse electric field on the semiconductor/electrolyte photovoltage spectra recorded in the mode of the current flow through the semiconductor electrode are shown in Figs. 4 and 5.

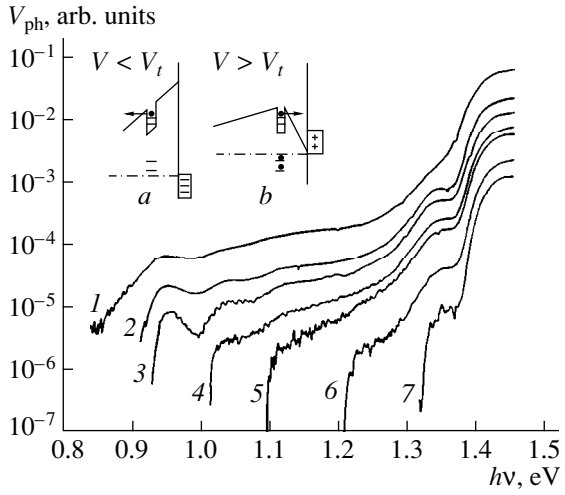

Fig. 4. Influence of the transverse electric field in the QD layer on the semiconductor/electrolyte photovoltage spectrum. *V*: (*1*) –4.0, (*2*) 0.0, (*3*) +1.4, (*4*) +1.8, (*5*) +2.1, (*6*) +2.7, and (*7*) +3.0 V. In insets, energy diagrams of the near-contact region of the semiconductor/electrolyte junction at a positive bias below the threshold bias V_t (*a*) and above the threshold bias (*b*) are shown.

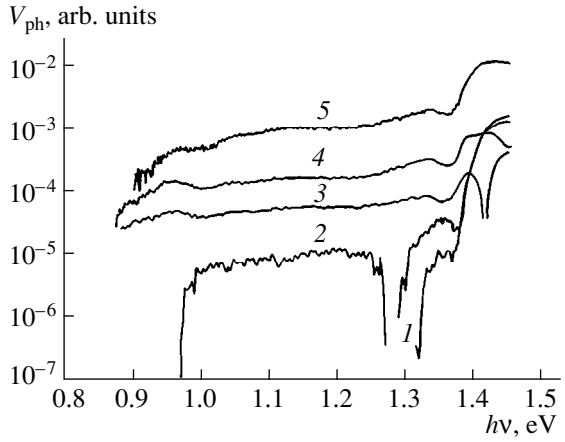

Fig. 5. Influence of the transverse electric field in the QD layer on the semiconductor/electrolyte photovoltage spectrum. *V*: (*1*) +3.0 (curve *7* in Fig. 4), (*2*) +3.2, (*3*) +3.4, (*4*) +4.0, and (*5*) +8.0 V.

At a reverse bias across the barrier, if the field strength in the space charge region and consequently in the QD layer increases with an increase in the bias, the photosensitivity increases. However, the resolution of the spectrum structure deteriorates significantly in this case (Fig. 4, curves *1*, *2*). The width of the major transition peak was determined from the shape of the photosensitivity edge. It increases at the voltage of –4 V by a factor of almost two compared to the peak width at the zero bias (40 meV). For a forward bias across the barrier, the photosensitivity decreases, whereas the spectral resolution increases (curve *3*).

For a forward bias that is sufficiently large, the sequential disappearance of the photosensitivity peaks and bands is observed with an increase in the voltage. First, the major transition peak disappears (Fig. 4, curve *4*), and then the peaks of transitions to the excitation levels disappear as well (curves *5* and *6*). For a bias voltage of +2.7 V (curve *6*), the photosensitivity band with the threshold of ≈1.22 eV indistinguishable in the complete spectrum is revealed. This band is related to the presence of another array of smaller QDs, which are usually formed in the QD heterostructures under investigation [9]. For this sample, a low-intensity PL peak at $h\nu \approx 1.3$ eV, which corresponds to this band, was observed at 77 K. For $V = +3$ V, the photosensitivity band in the QD heterostructure spectrum, which is related to QDs, disappears completely. The only remaining band is the one related to the QW of the wetting layer (curve *7*). We note that the PL peak from the wetting layer was rarely observed at 77 K in the PL spectra of the QD heterostructures under investigation. However, this band is always present in the photoelectric spectra even when QDs themselves do not noticeably contribute to the photosensitivity.

It was unexpected that the forward bias above the certain threshold value of $V_t = +3$ V for this structure affects the QD heterostructure spectrum (Fig. 5). The QD photosensitivity spectrum began to be recovered in this case. However, the photovoltage sign changes initially in the absorption region of QDs (curve *2*), then in the region of the wetting layer (curve *3*), and finally the entire absorption region of the QD heterostructures (curves *4*, *5*). In this case, the photosensitivity in the major transition region in QDs considerably exceeded the photosensitivity at the zero bias and even at a reverse bias. However, at a large forward bias, similarly to a large reverse bias, the fine structure of the spectrum disappeared almost completely and the noise level increased significantly. The effect described was observed only for QD heterostructures with the sufficiently thin cap layer (~15 nm).

Emission of electrons and holes from QDs into the matrix, which causes the semiconductor/electrolyte photovoltage phenomenon in the QD absorption region, is of tunneling nature. This is apparent from the necessity of embedding the QD layer into the high field region of the surface barrier in order to obtain the noticeable photosensitivity from QDs and its complete disappearance at a fairly large forward bias. Estimations demonstrate that a decrease in the activation energy of thermal emission because of the Schottky effect in the fields $\sim 5 \times 10^4$ V/cm could not account for the above. The photoelectron and photohole lifetimes at the QD excitation levels are generally controlled by the rates of three processes, namely, relaxation to the ground state, radiative and nonradiative recombination, and emission from the QDs into the matrix.

The effect of field on the line width of the optical transitions in QDs can be explained by the variation in

the transparency of the triangular barrier for tunneling emission. Since the QD layer is located nearly in the region of the surface-barrier top, the emission of electrons rather than holes plays a major part in the photovoltage emergence (see Fig. 4, inset *a*). The effective barrier width for origination and, consequently, its transparency depend on the field strength in the vicinity of the QD, namely, the barrier transparency increases for a reverse bias and decreases for a forward bias applied to the barrier. In this case, the lifetime for nonequilibrium electrons at the QD levels correspondingly increases or decreases, whereas the line-width for an optical transition changes inversely proportional to this time according to the uncertainty relation. For the uncertainty in energy to be comparable to the emission line width for the QD ensemble (~40 meV), the lifetime in relation to emission should be ~0.1 ps. The interlevel relaxation of carriers and their radiative recombination at QDs are characterized by considerably larger times (~10 and ~100 ps, respectively). We note that close to the disappearance threshold of the photosensitivity peak, apparent peak narrowing may be observed. This is caused by the fact that the photosensitivity from the larger points disappears at a lower bias voltage. It is noticeable in curve *3* (Fig. 4), where the major transition peak seems to be cut from the low energy side.

The field affects the line width not only for the major transition, but also for transitions into the QD excited states, and the emergence of the QD spectrum lines is sequential rather than simultaneous. These facts demonstrate that the emission of nonequilibrium electrons and holes from QDs into the matrix in a sufficiently strong electric field proceeds immediately from the QD excitation levels. This conclusion agrees well with the above estimations of various times, which can determine the lifetime of the excited state.

The QD photosensitivity is restored with the photovoltage sign reversal for an adequately large forward bias $V > V_t$. This fact can be explained by the change of the charge sign at the (QD heterostructure)/electrolyte interface. The sign reversal from negative to positive is due to electrochemical processes at the electrode. Protons from the electrolyte are neutralized at the semiconductor cathode, and atomic hydrogen evolves. For a sufficiently large current density, the positive charge can form at the QD heterostructure surface due to passivation of the surface states by atomic hydrogen and to the accumulation of protons at the surface. The absence of the QD layer in the surface barrier would lead to the change of the band-bending sign in the surface region to the opposite one, i.e., to the formation of the enriched layer at the surface. This is actually observed at the surface of certain semiconductors [8]. In our case, this does not occur since the enriched layer with the built-in QD layer forms. This should lead to occupation of the QD levels with electrons and disappearance of not only the photosensitivity, but also the emission absorption by QDs. We believe that an increase in the barrier height to a certain value leads to the emergence of a negative charge in the QD layer and formation of a double charged layer at the surface. The latter one is separated by the cap layer, which acts as an insulator. If the positive surface charge is sufficiently large, the electric field in this layer should make tunnel electron emission possible toward the surface rather than into the bulk of the semiconductor (Fig. 4, inset *b*). This explains the reversal of the photovoltage sign and recovery of the photosensitivity from the QD layer.

It is noteworthy that the negative charge in the QD layer cannot be localized directly at the QDs. The reason is that their surface density is too low to ensure a field strength of $\sim 5 \times 10^4$ V/cm, which is necessary for tunneling into the wetting layer. Considering that the distance from cluster vertices (QDs) to the cap layer surface is ~10 nm, a surface charge density of $\sim 3 \times 10^{11}$ cm^{-2} is required for the creation of such a field. It is evident that this charge can be localized only at impurities and defects in the QD layer (Fig. 4, inset *b*).

Photoexcitation in the intrinsic absorption region for GaAs with the presence of such a barrier leads to the emergence of the oppositely directed photocurrents. In spite of the small thickness of the cap layer, the photocurrent generated in this layer at a sufficiently large forward bias becomes larger than the oppositely directed photocurrent. However, due to the effect of compensation of photocurrents, photosensitivity at a large forward bias is almost an order of magnitude lower compared to the photosensitivity at a reverse bias.

3.3. Effect of the Emission Barrier in Quantum Dots on the Semiconductor/Electrolyte Photovoltage Spectrum

Certain specific features of the surface relief and photoelectronic properties of the QD heterostructures obtained by MOCVD have been investigated previously. In particular, low energies of the major transition in the QDs were related [9] to the formation of the transition layer of the solid solution at the QD boundary. This boundary plays the part of the internal QW in the QW/QD combined layers [11]. A decrease in the energy of the major transition implies an increase in the height of the barriers that control the rate of the electron and hole emission from the QDs into GaAs. For a sufficiently large height of these barriers, the photosensitivity from the QD layer should cease to exist.

Figure 6 demonstrates the PL and semiconductor/electrolyte photovoltage spectra of two QD heterostructures, namely, with the cap layer (curves *1*, *3*) and without it (curves *4*, *5*). Due to the optimization of deposition conditions, presumably one of the lowest values of the major transition energy in the InAs/GaAs QDs was obtained for the first structure at room temperature (0.85 eV). This value corresponds to a wavelength of 1.46 μm. In this case, the full width at a half-maximum (FWHM) for the PL peak QD1 is ~25 meV, which is indicative of the high uniformity of the QDs in size and

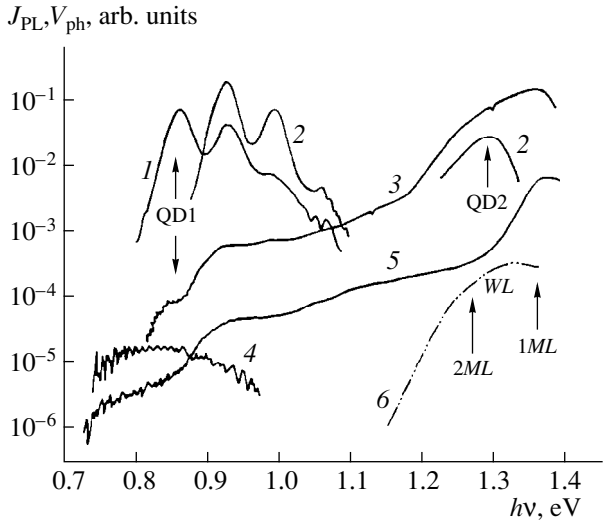

Fig. 6. Photoluminescence and photovoltage spectra for heterostructures with a low energy of the major transition in QDs. The QD heterostructure with the cap layer: (*1*) PL spectrum at 300 K, (*2*) the same at 77 K, and (*3*) the semiconductor/electrolyte photovoltage spectrum. The QD heterostructure without the cap layer: (*4*) PL spectrum at 77 K, (*5*) semiconductor/electrolyte photovoltage spectrum, and (*6*) extracted photosensitivity (absorption) spectrum of the wetting layer.

chemical composition. However, the QD surface density, which was estimated from the relationship between photosensitivity values in the absorption regions for the QDs and wetting layers [9], was low ($\sim 3 \times 10^9$ cm^{-2}). Because of this, it was possible to obtain the photosensitivity spectra from the QDs for this structure by the semiconductor/electrolyte photovoltage method only.

For the major transition energy in the QD $\lesssim 0.9$ eV, the electric field in the surface barrier in the QDs is too weak to ensure that the quantum efficiency of the photoelectron tunneling emission in the vicinity of the major transition is close to unity even for the thinnest cap layer (15 nm). For this reason, the photosensitivity peak in this region turns out to be considerably lower than the peak in the region of the transition to the first excitation level (Fig. 6, curve *3*). However, for the QD heterostructures with a high energy of the major transition, where this restriction is absent, the heights of these peaks are almost equal to each other (see Fig. 3). This fact confirms the conclusion that the photoelectrons and photoholes at the excitation levels have no time to relax to the ground level before their emission from the QDs.

For a QD heterostructure without a cap layer, the QD surface density measured directly using a scanning atomic force microscope turned out to be $\sim 7 \times 10^9$ cm^{-2}. Using the semiconductor/electrolyte photovoltage method at a reverse bias across the barrier, we managed to detect the photosensitivity from the surface QDs and to observe it close to the energy $h\nu \approx 0.75$ eV (Fig. 6, curve *5*). As should be expected for this low energy of the major transition, the photosensitivity close to the threshold turned out to be very low compared to the photosensitivity for the photon energy $h\nu > 0.9$ eV. At this energy, the quantum efficiency becomes close to unity. The presence of the broadened PL band peaked at $h\nu \approx 0.83$ eV, which was observed for this structure at 77 K (curve *4*), testifies that the threshold was attained. Allowing for the temperature shift, this peak corresponds to the photosensitivity threshold. A large red shift of the major transition energy in the surface QDs was observed previously [12]. This shift was explained by the elastic-stress relaxation in these QDs. Pronounced broadening of the PL band from the surface QDs is probably caused by an increase in the effective size variance for QDs because of their nonuniform oxidation. A similar phenomenon was also observed for the PL spectra of the partially oxidized surface QWs [5].

For the structure with a surface QD layer, the wetting layer, if it is formed, is completely oxidized as a result of exposure to air. For this reason, this layer does not manifest itself in the semiconductor/electrolyte photovoltage spectrum (curve *5*). An increase in the photosensitivity for $h\nu > 1.3$ eV is related to the fundamental-absorption edge for GaAs. For a structure with a cap layer (curve *3*), an increase in the photosensitivity for $h\nu > 1.15$ eV is related to the wetting layer. Making curves *5* and *3* for $h\nu < 1.15$ eV coincident and finding the difference, we should obtain the photosensitivity spectrum for the wetting layer, which also characterizes the optical absorption spectrum for this layer (curve *6*). The calculated values of the absorption edge for the strained InAs wetting layers one and two monolayers thick are indicated by arrows. A decrease in the photosensitivity (absorption) by a factor of more than two in the thickness range from one to two monolayers indicates that the probable thickness of the wetting layer is intermediate between these values.

It was mentioned above that along with the array of relatively large QDs, an array of smaller QDs is usually formed in the QD heterostructures investigated [9]. The base dimension and height for large and small QDs are ~40 and ~6 nm for large QDs, and ~30 and ~1.6 nm for small QDs, respectively. The PL peak QD2 at $h\nu \approx 1.29$ eV, which is usually observed at 77 K (curve *2*), is related to small QDs. The absence of any specific feature in curve *6* at $h\nu \approx 1.21$ eV (with the correction to the temperature shift of the major transition) can be explained by the relatively low surface density of the QDs of this type. They can be identified in the photosensitivity spectra measured at an optimal positive bias (Fig. 4, curve *6*).

CONCLUSION

The investigations carried out demonstrate that the spectroscopy of the photovoltaic effect in the semiconductor/electrolyte junction substantially extends the

capabilities of the photoelectric diagnostics of the heterostructures with quantum dots of the InAs/GaAs type. They were demonstrated by the measurement of the photoelectric spectra from the QDs with a large barrier height for the electron and hole emission for low QD surface concentration, and by the data on the field influence on the photosensitivity spectra. These investigations demonstrated that the transverse electric field affects the line width for optical transitions in the QDs, and the tunneling emission of electrons from the QDs into the matrix proceeds directly from the excitation levels. The use of the photoelectrochemical processes for the (QD heterostructure)/electrolyte junction opens prospects for controlling the surface state of these structures.

ACKNOWLEDGMENTS

We thank V.Ya. Aleshkin for his fruitful participation in the discussion.

This study was supported by the Russian Foundation for Basic Research (project nos. 98-02-16688 and 00-02-17598), Ministry of Education of the Russian Federation (project nos. 97-7.1-204 and 015.06.01.19), Interdisciplinary Scientific and Technological Program "Physics and Technology of Solid-State Nanostructures" (project no. 99-1141), and Joint Program of the Ministry of Education of the Russian Federation and CRDF (the BRHE Program, REC-001).

REFERENCES

1. P. Blood, J. Appl. Phys. **58**, 2288 (1985).
2. H. J. Polland, Y. Horikoshi, E. O. Gobel, *et al.*, Surf. Sci. **174**, 278 (1986).
3. I. A. Karpovich, V. Ya. Aleshkin, A. V. Anshon, *et al.*, Fiz. Tekh. Poluprovodn. (Leningrad) **24**, 2172 (1990) [Sov. Phys. Semicond. **24**, 1346 (1990)].
4. X. He and M. Razeghi, Appl. Phys. Lett. **262**, 618 (1993).
5. I. A. Karpovich, V. Ya. Aleshkin, A. V. Anshon, *et al.*, Fiz. Tekh. Poluprovodn. (St. Petersburg) **26**, 1886 (1992) [Sov. Phys. Semicond. **26**, 1057 (1992)].
6. I. A. Karpovich and D. O. Filatov, Fiz. Tekh. Poluprovodn. (St. Petersburg) **30**, 1745 (1996) [Semiconductors **30**, 913 (1996)].
7. B. N. Zvonkov, I. G. Malkina, E. R. Lin'kova, *et al.*, Fiz. Tekh. Poluprovodn. (St. Petersburg) **31**, 1100 (1997) [Semiconductors **31**, 941 (1997)].
8. Yu. Ya. Gurevich and Yu. V. Pleskov, *Photoelectrochemistry of Semiconductors* (Nauka, Moscow, 1983).
9. B. N. Zvonkov, I. A. Karpovich, N. V. Baĭdus', *et al.*, Fiz. Tekh. Poluprovodn. (St. Petersburg) **35** (1), 92 (2001) [Semiconductors **35**, 93 (2001)].
10. I. A. Karpovich, B. I. Bednyĭ, N. V. Baĭdus', *et al.*, Fiz. Tekh. Poluprovodn. (Leningrad) **23**, 2164 (1989) [Sov. Phys. Semicond. **23**, 1340 (1989)].
11. K. Nishi, H. Saito, S. Sugou, and J.-S. Lee, Appl. Phys. Lett. **74**, 1111 (1999).
12. H. Saito, K. Nishi, and S. Sugou, Appl. Phys. Lett. **73**, 2742 (1998).

Translated by N. Korovin

Semiconductors, Vol. 35, No. 5, 2001, pp. 550–553. Translated from Fizika i Tekhnika Poluprovodnikov, Vol. 35, No. 5, 2001, pp. 571–574.

LOW-DIMENSIONAL SYSTEMS

Manifestation of the Upper Hubbard Band in the Electrical Conductivity of Two-Dimensional *p*-GaAs–AlGaAs Structures

N. V. Agrinskaya, Yu. L. Ivanov, V. M. Ustinov, and D. A. Poloskin

Ioffe Physicotechnical Institute, Russian Academy of Sciences, Politekhnicheskaya ul. 26, St. Petersburg, 194021 Russia

Submitted October 19, 2000; accepted for publication October 23, 2000

Abstract—The Hall effect and electrical conductivity were studied in the temperature range of 1.7–300 K in Be-doped *p*-GaAs/AlGaAs multilayer structures with 15-nm-wide quantum wells. Doping of the well itself and the adjacent barrier layer was used to create a situation when the upper Hubbard band (the A^+ centers) was occupied with holes and electrical conduction proceeded over the states in this band. It is shown experimentally that the binding energy of A^+ centers increases significantly in the 15-nm-wide wells compared to this energy in the bulk, which is explained by the fact that the well size and the hole radius at the A^+ center are almost identical. The above radius was independently estimated from an analysis of the temperature dependence of the hopping conductivity. © *2001 MAIK "Nauka/Interperiodica"*.

INTRODUCTION

Recently, increased interest in electrical conductivity of two-dimensional (2D) structures has been evident. This is primarily caused by experimental observation of metallic-type low-temperature conductivity in the Si metal–oxide–semiconductor field-effect transistors (MOSFETs) and in the GaAs/AlGaAs-based heterostructures [1, 2].

Since, as is known, the scaling theory of delocalization predicts the insulator-like behavior for 2D structures in the low-temperature limit, the above observations are of fundamental importance. By now, three possible explanations of the observed behavior have been suggested. In the first, it is assumed that the conductivity is actually metallic down to the zero temperature, whereas a deviation from the predictions of the scaling theory for localization is related to the behavior different from that of the Fermi liquid; this behavior is caused by the contribution of electron–electron interactions, which is disregarded in the scaling theory of localization [3]. In the second version, it assumed that the observed behavior may be described by conventional theory of impure metals (and, thus, the transition to the insulator state is bound to be observed as temperature is lowered), whereas the metal-like behavior in the studied temperature range is caused by the temperature dependence of the structural disorder (for the Si-based MOSFETs, this factor was related to the scattering of electrons by the traps in Si) [4].

However, a unified mechanism for explaining all special features of the observed behavior for various systems has not been suggested so far. In connection with this, Kozub *et al.* [5] recently suggested a third variant of explanation of the observed behavior. This explanation may be treated as a modification of the second approach from the standpoint of interpreting the temperature dependences; however, it is based on a certain common factor, i.e., on the conductivity channel related to the upper Hubbard band [5].

However, by virtue of the fact that the structure of localized states is not quite clear in the systems under consideration, a quantitative comparison of predictions of the model with experimental data is difficult. In connection with this, the possibility of experimentally studying the electrical conductivity over the upper Hubbard band in a certain model system where the localized-state origin would be clear from the outset is of undeniable interest.

In the three-dimensional (3D) case, it is very difficult to distinguish the conductivity over the upper Hubbard band from the conduction-band conductivity; this is caused by the fact that the theoretical binding energy of a charged shallow-level impurity (A^+ or D^-) ε_- relative to the conduction-band bottom is fairly small ($\varepsilon_- = 0.055\varepsilon_0$, where ε_0 is the binding energy for isolated impurity). Thus, the conductivity over the upper Hubbard band was considered to be negligible compared to that over the conduction band. However, Dubon *et al.* [6] observed the conductivity over the upper Hubbard band for asymmetrically strained Ge:Cu, and it was noted that the Hubbard bands were separated from each other and from the valence band. In this situation, the Hubbard energy amounted to 3.7 meV in lightly doped samples and vanished when the impurity concentration approached the critical value. In addition, we should mention the data on magnetoresistance under the conditions of hopping conductivity in doped semiconductors; these data demonstrate reliably that there is a con-

1063-7826/01/3505-0550$21.00

tribution of the upper Hubbard band to the conductivity, with the binding energy being larger than the theoretical estimate [7]. Since in 3D semiconductors the number of doubly charged states cannot exceed the number of singly charged states (except for the U^- centers), these data may be treated as circumstantial.

Another situation arises in 2D systems with selective doping, in which case, using different doping methods and varying the gate bias voltage, it is possible to controllably change the electron concentration in a quantum well (QW) and, thus, vary the ratio between the concentrations of the D^- and D^0 centers.

In fairly narrow QWs (when the extension of the wave function is comparable to the QW size), the energies ε_- and ε_0 increase. It is clear that this increase in the binding energy is more appreciable for the D^- state than for the D^0 state due to the fact that the radius of the electron localization is larger in the former. For an ultimately narrow QW, the energies ε_- and ε_0 increase tenfold and fourfold, respectively, in comparison to the 3D case. In QWs with a finite width, we may have a situation when the state D^- descends, whereas the state D^0 remains at the same position; this can also reduce the Hubbard energy, which may facilitate a contribution from the upper Hubbard band and appreciably affect the physical phenomena in the systems under consideration.

We chose a GaAs/AlGaAs system with a QW width of about 15 nm; the system was doped with Be acceptor impurity whose localization radius (2 nm) was appreciably smaller than the QW width. By doping the QW itself and the adjacent barrier layer, we attained the situation when the upper Hubbard band was occupied with holes under the equilibrium conditions and electrical conduction proceeded over its states. In the temperature range 300–1.7 K, we studied the Hall effect and the impurity-related and hopping electrical conductivities. The experiments showed that the binding energy of A^+ centers increased significantly in 15-nm-wide QWs compared to that in the bulk, which is caused by the fact that the QW width and the hole radius were almost identical in an A^+ center. The above radius was estimated independently from an analysis of the temperature dependence of hopping conductivity.

EXPERIMENTAL

The structures to be studied were grown on the semi-insulating GaAs(100) substrates by the molecular-beam epitaxy using a Riber 32P system equipped with the solid-phase Ga, Al, As, and Be sources. We grew the structures under the conditions of As enrichment at the substrate temperature of 580°C. The growth rate was about 10 nm/min. The structures contained ten 15-nm-wide GaAs QWs separated by 15-nm-thick $Al_{0.3}Ga_{0.7}As$ barriers. Prior to the deposition of the first QW and after the deposition of the last QW, the 100-nm $Al_{0.3}Ga_{0.7}As$ confinement layers were deposited. Epitaxial growth was completed by depositing a cap GaAs layer with a thickness of 20 nm. In both of the studied samples, the QW middle region (with a thickness of 5 nm) was doped. In one of the samples (sample 293), the $Al_{0.3}Ga_{0.7}As$ barriers were undoped, whereas, in sample 213, the 5-nm-thick middle region of the barriers was doped. Thus, the thickness of undoped spacer layers on both sides of the barrier was 5 nm. As the *p*-type dopant, we used Be introduced with a concentration of 10^{17} cm^{-3}; the electron concentration measured at 300 K in samples 293 and 213 was 10^{17} cm^{-3}. Contacts to the samples were formed by firing the deposited Au layer (containing 3% of Zn) to the sample for 2 min at a temperature of 450°C.

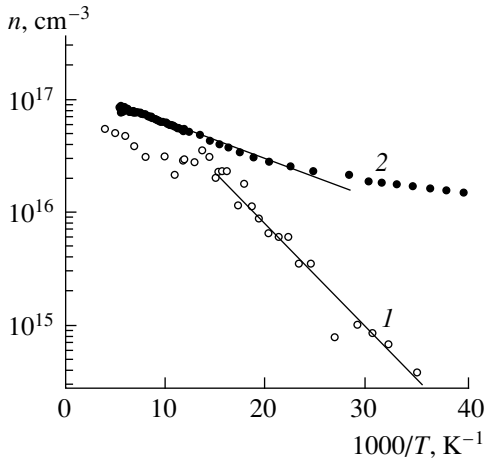

Fig. 1. Temperature dependences of the charge-carrier concentrations in (*1*) sample 293 and (*2*) sample 213. The concentrations were determined from the Hall effect measurements and were calculated by averaging over the volume, taking into account that the sample thickness was 150 nm (10 quantum wells with a width 15 nm each).

Figure 1 shows the temperature dependences of the charge-carrier concentration determined from Hall effect measurements in samples 293 and 213. The temperature range 50–300 K corresponds to excitation of holes from the acceptor level to the valence band. Fairly high values of mobility μ = 300–500 cm^2 V^{-1} s^{-1} at 300 K and the temperature dependence of mobility $\mu(T) \propto T^{3/2}$ are indicative of the charge-carrier transport over the valence band. In the low-temperature region, the charge-carrier concentration varies according to the Arrhenius equation; at the same time, a decrease in the slope of the dependence $\ln n = f(1/T)$ is observed at high temperatures, which may be indicative of depletion of the impurity. In particular, for sample 293, featuring a certain compensation (which is quite likely due to uncontrollable impurities or the states at the interfaces), a portion with the slope of E_a is observed in the carrier-concentration dependence, whereas a portion with a slope of $E_a/2$ is observed at higher temperatures, The ionization energies estimated from the slopes of the temperature dependences are found to be different for

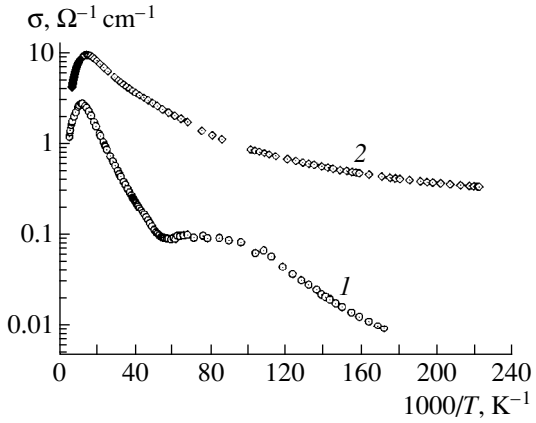

Fig. 2. Temperature dependences of electrical conductivity for samples (*1*) 293 and (*2*) 213.

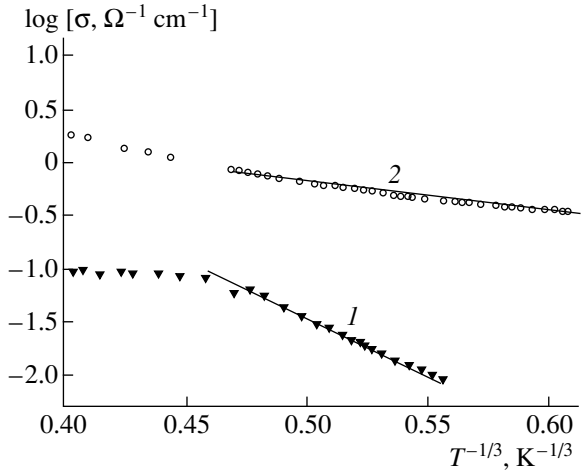

Fig. 3. Temperature dependences of electrical conductivity represented as plots of logσ vs. $T^{-1/3}$ for samples (*1*) 293 and (*2*) 213.

two types of the samples and amount to 7 and 21 meV for structures 213 and 293, respectively. Below T = 50 K (down to 1.7 K), the temperature dependence of electrical conductivity σ is indicative of the hopping mechanism of conductivity (Fig. 2). The slopes of dependences σ(T) plotted as logσ vs. $T^{-1/3}$ are found to be different for the two samples (Fig. 3).

DISCUSSION

According to the published data, the level depth for Be impurity in GaAs is ε_0 = 27 meV. From the experiment with sample 293 (only the GaAs layers were doped), we obtained the ionization energy E_a = 21 meV. The discrepancy with the published result may be attributed to the effect of the finite width of the impurity band W; according to theoretical predictions, we have the following expression for W in a lightly compensated sample:

$$W = e^2/\chi N^{1/3}.$$

Here, χ is the permittivity and N is the impurity concentration. Thus, for $N = 10^{17}$ cm^{-3}, we obtain W = 10 meV, which agrees closely with the doubled difference between ε_0 and the observed ionization energy E_a.

For sample 213 (both the GaAs layers and barriers were doped), we obtained a much lower ionization energy for acceptors (7 meV). In this situation, excess holes occupy the second charge state of the acceptor A^+ in the GaAs layers. Theoretically, the ionization energy of the acceptor A^+ is about $0.05\varepsilon_0$ in the 3D case. We obtained the value fivefold larger, which may be accounted for by the fact that the structure is 2D. Indeed, the radius of the ground state a_0 is 30 Å, which is much smaller than the QW width (15 nm), whereas the radius of the A^+ center may be much larger (ultimately, on the order of $4a_0$) and may approach the QW width. In turn, this causes the state of the A^+ center to become lower and the Hubbard energy (the gap between the states of the A^0 and A^+ centers) to decrease.

We can independently estimate the radii of the A^0 and A^+ centers by analyzing the low-temperature portion of electrical conductivity that corresponds to the variable-range hopping (VRH) conductivity. Since the hopping range at low temperatures indubitably exceeds the structure size, the VRH transport is 2D and is described by the expression

$$\sigma = \sigma_0 \exp\left(-\frac{T_0}{T}\right)^{1/3}.$$

Here, T_0 is a parameter related to the density of states at the Fermi level N_{E_F} and the localization radius as

$$T_0 = C(N_{E_F} a^2)^{-1},$$

where C = 13.8 is a numerical coefficient.

In Fig. 3, we show the low-temperature portions of electrical-conductivity curves as plots of logσ vs. $T^{-1/3}$. It can be seen that the plots yield the straight lines; the values of the parameter T_0 for samples 293 ($T_0 = 10^3$ K) and 213 ($T_0 = 1.8 \times 10^4$ K) were determined from the slopes of these straight lines. The ratio of these parameters yields the ratio between the radii of states for the two samples; i.e.,

$$\frac{T_{01}}{T_{02}} = \left(\frac{a_2}{a_1}\right)^{1/2}.$$

Thus, we find that the ratio between the radii of the A^0 and A^+ centers is equal to four; i.e., the radius of the A^+

center equals 8 nm, which is comparable to the QW width.

Thus, our experiments showed that the binding energy of the A^+ centers is much larger (by a factor of 5) in the 15-nm-wide QWs than in the bulk, which is explained by the fact that the QW width and the hole radius in an A^+ center have almost the same values.

ACKNOWLEDGMENTS

We are indebted to A.E. Zhukov for his help with growing the structures and to V.I. Kozub for his participation in discussion of the results.

This study was supported by the Russian Foundation for Basic Research, project nos. 00-02-16992, 00-15-96750, and 98-02-18403.

REFERENCES

1. S. V. Kravchenko, G. V. Kravchenko, J. E. Furneaux, *et al.*, Phys. Rev. B **50**, 8039 (1994).
2. D. Simmonian, S. V. Kravchenko, M. P. Sarachik, and V. M. Pudalov, Phys. Rev. Lett. **79** (12), 2304 (1997).
3. A. Perez-Garrido, M. Ortuno, E. Cuevas, *et al.*, Phys. Rev. B **55**, R8630 (1997).
4. B. L. Alsthuler and D. I. Maslov, Phys. Rev. Lett. **82**, 145 (1999).
5. V. I. Kozub, N. V. Agrinskaya, S. I. Khondaker, and I. Shimak, cond-mat/9911450 (1999).
6. O. D. Dubon, W. Walukiewicz, J. W. Beeman, and E. E. Haller, Phys. Rev. Lett. **78**, 3519 (1997).
7. N. V. Agrinskaya, V. I. Kozub, and T. A. Polyanskaya, Phys. Status Solidi B **218**, 159 (2000).

Translated by A. Spitsyn

Semiconductors, Vol. 35, No. 5, 2001, pp. 554–556. Translated from Fizika i Tekhnika Poluprovodnikov, Vol. 35, No. 5, 2001, pp. 575–577.

LOW-DIMENSIONAL SYSTEMS

Superlattice Conductivity under the Action of a Nonlinear Electromagnetic Wave

D. V. Zav'yalov and S. V. Kryuchkov

Volgograd State Pedagogical University, Volgograd, 400013 Russia

Received October 19, 2000; accepted for publication October 26, 2000

Abstract—The influence exerted by a nonlinear electromagnetic wave on the dc conductivity of a superlattice is analyzed. An essentially nonlinear current–voltage (*I–V*) characteristic is obtained. A portion of negative absolute conductivity appears in the *I–V* characteristic at certain nonlinear-wave parameters. A distinction is made between the given case and that of a monochromatic wave, when a large number of such portions may exist. For typical superlattice parameters, some of the negative absolute conductivity must appear at a nonlinear wave field strength $E_0 \approx 1.8 \times 10^3$ V/cm. © *2001 MAIK "Nauka/Interperiodica".*

The influence exerted by a monochromatic high-frequency (HF) electric field on the superlattice (SL) conductivity has been studied theoretically [1–4]. The effects of absolute negative conductivity, total self-induced transparency, and oscillatory dependence of the current on the HF field strength were demonstrated. Thereby, it was shown that a quantum SL must exhibit markedly nonlinear electromagnetic (EM) properties. The recent fabrication of high-quality SL samples and the possibility of generating femtosecond laser pulses enabled an experimental study of the nonlinear EM properties of SLs [5]. For instance, Bloch oscillations have been excited in a GaAs–$Al_{0.3}Ga_{0.7}As$ SL at room temperature by femtosecond laser pulses [6]. The possibility of tuning the oscillation frequency by means of an external dc electric field has been demonstrated. Self-excited oscillations of current in a SL under the action of a high dc electric field, induced by the periodic motion of field domains, were considered in [7]. It was shown that the application of an HF field gives rise to various nonlinear dynamic regimes. The conduction in a double-barrier heterostructure in a strong laser field was studied in [8]. The effect of negative absolute resistance was observed. EM waves in an SL can be described, in the approximation of rare conduction electron collisions with crystal structure irregularities, in terms of the sine-Gordon equation [9]. One of the most general periodic solutions of this equation is the solution expressed in terms of the Jacobi elliptic functions. Thus, the monochromatic EM field applied to a SL is transformed in the SL bulk into a nonlinear EM wave. This transformation of a monochromatic EM wave into a nonlinear one may lead to substantial changes in the electronic properties of a SL in the field of such a wave [10, 11]. That is why it is of interest to consider the influence exerted by the field of a nonlinear EM wave on the dc conductivity of the SL.

Let a uniform dc electric field of strength E be applied to the SL; in addition, let an EM wave polarized along the SL axis propagate parallel to the SL layers. The electric field strength can be written as

$$E(z, t) = E_0 cn\left[\frac{2K(k)\omega}{\pi}(t - z/\beta V), k\right] \text{ for } k \le 1, \quad (1)$$

$$E(z, t) = E_0 dn\left[\frac{2K(k)\omega k}{\pi}(t - z/\beta V), k^{-1}\right] \text{ for } k > 1. \quad (1a)$$

In expressions (1) and (1a), $k = eE_0 d|1 - \beta^2|^{1/2}/2\omega_p \hbar\beta$, $\omega = \pi\beta\omega_p/2K(k)|1 - \beta^2|^{1/2}$, $\beta = u/V$, u is the phase velocity of the wave, V is the velocity of the EM wave in the absence of electrons, E_0 is the peak field strength of the nonlinear wave, d is the SL period, $\omega_p^2 = 4\pi e^2 n_0 \Delta d^2 \hbar^{-2} I_1(\Delta/T)/I_0(\Delta/T)$, ω_p is the generalized electron plasma frequency in the miniband, n_0 is the electron density in the miniband, $I_m(x)$ is a modified Bessel function of the first kind of order m, T is temperature in energy units, and Δ is the half-width of the conduction miniband.

The solutions (1) and (1a) correspond to fast waves ($\beta > 1$), which will be the subject of further study (the results for slow waves are similar). The characteristic distance along which the field of the wave changes noticeably is assumed to greatly exceed the electron mean free path. This condition allows the field to be considered uniform and the spatial derivative of the distribution function to be neglected.

Then the dc component of the current flowing along the SL axis takes the form

$$j_x = j_0(J_1 + J_2) \quad \text{for} \quad k \le 1, \quad (2)$$

$$j_x = j_0 J \quad \text{for} \quad k > 1. \quad (2a)$$

1063-7826/01/3505-0554$21.00 © 2001 MAIK "Nauka/Interperiodica"

Here, $j_0 = \hbar\omega_p^2/4\pi ed$,

$$J_1 = \sum_{n=0}^{\infty} \frac{a_n^2(k)}{2} \frac{\nu\Omega(\nu^2 + \Omega^2 - 4n^2\omega^2)}{[\nu^2 + (2n\omega + \Omega)^2][\nu^2 + (2n\omega - \Omega)^2]}, \quad (3)$$

$$J_2 = \sum_{n=0}^{\infty} \frac{b_n^2(k)}{2} \times \frac{\nu\Omega[\nu^2 + \Omega^2 - (2n+1)^2\omega^2]}{\{\nu^2 + [(2n+1)\omega + \Omega]^2\}\{\nu^2 + [(2n+1)\omega - \Omega]^2\}}, \quad (4)$$

$$J = \sum_{n=0}^{\infty} \frac{a_{1n}^2(k) + b_{1n}^2(k)}{2} \times \frac{\nu\Omega(\nu^2 + \Omega^2 - 4n^2\omega^2)}{[\nu^2 + (2n\omega + \Omega)^2][\nu^2 + (2n\omega - \Omega)^2]}, \quad (5)$$

$$a_0(k) = \sqrt{2}\left(2\frac{E(k)}{K(k)} - 1\right),$$

$$a_{10}(k) = \sqrt{2}\left(1 - \frac{2}{k^2}\left[1 - \frac{E(k^{-1})}{K(k^{-1})}\right]\right),$$

$$a_n(k) = \frac{4n\pi^2}{K^2(k)} \frac{q^n}{1 - q^{2n}} \quad \text{for} \quad n \geq 1,$$

$$b_n(k) = \frac{2(2n+1)\pi^2}{K^2(k)} \frac{q^{n+1/2}}{1 + q^{2n+1}},$$

$$a_{1n}(k) = \frac{4n\pi^2}{K^2(k^{-1})k^2} \frac{q^n}{1 - q^{2n}} \quad \text{for} \quad n \geq 1,$$

$$b_{1n}(k) = \frac{4n\pi^2}{K^2(k^{-1})k^2} \frac{q^n}{1 + q^{2n}},$$

$$q = \exp[-\pi K(k')/K(k)], \quad k' = \sqrt{1 - k^2} \quad \text{for} \quad k \leq 1,$$

$$q = \exp[-\pi K(k')/K(k^{-1})], \quad k' = \sqrt{1 - k^{-2}} \quad \text{for} \quad k > 1,$$

$E(k)$ is a complete elliptic integral of the second kind, $K(k)$ is a complete elliptic integral of the first kind, Ω is the Stark frequency, and $\Omega = eEd/\hbar$ (E is the dc field strength). It is noteworthy that, in the limit $E_0 = 0$, expressions (2) and (2a) reduce to the static *I–V* characteristic reported in [12, 13].

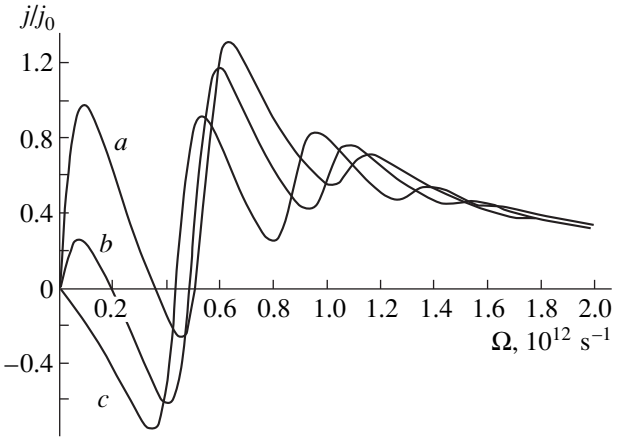

Static *I–V* characteristic of the superlattice under the action of a nonlinear electromagnetic wave for $k = 0.7$ (*a*), 0.8 (*b*), and 0.9 (*c*).

In the HF limit (provided that $\omega \gg \Omega, \nu$), expressions (3) and (4) are essentially simplified and (2) takes the form

$$j = j_0\nu^{-1}\Omega\left\{\frac{a_0^2(k)}{2}\frac{\nu^2}{\Omega^2 + \nu^2} - \frac{\nu^2}{2\omega^2}\left(\sum_{n=1}^{\infty}\frac{a_n^2(k)}{4n^2} + \sum_{n=0}^{\infty}\frac{b_n^2(k)}{(2n+1)^2}\right)\right\}. \quad (6)$$

The second term in the brackets is much smaller than the first; however, at those HF field strengths when k is equal to a root of the function $a_0(k)$ (or lies in close vicinity of this point), the first term vanishes (or becomes smaller than the second one) and the current j turns negative (it starts to flow against the applied dc field). Such a phenomenon, named the negative absolute conductivity, is characteristic of essentially nonequilibrium systems. In the present case, the nonequilibrium state is related to the pumping of the SL sample by an HF EM field. It is noteworthy that at $k \longrightarrow 0$ (i.e., in the limit of linear waves) (6) turns into the expression for the current in the HF case, reported in [1]. The presence and position of a negative absolute conductivity portion in the *I–V* characteristic is particularly clear in curves in the figure, plotted using formulas (2)–(5) at different k. It should be noted that quite a number of curve portions with negative absolute conductivity are present in the case of a monochromatic field, when the amplitude of the wave is independent of its frequency, but only a single portion is present in the case in question. The formal reason is that the $a_0(k)$ vanishes only once, and in the monochromatic case it goes over to the function $J_0(k)$ having an infinite set of roots.

Finally, let us make some numerical estimates. At $d \approx 10^{-6}$ cm, $\Delta \approx 10^{-2}$ eV, $n_0 \approx 10^{14}$ cm^{-3}, $T \approx 10^2$ K (then $\omega_p \approx 10^{12}$ s^{-1}), and $\beta \approx 1.2$, a portion with negative abso-

lute conductivity in the *I–V* characteristic would be expected to appear at $E_0 \approx 1.8 \times 10^3$ V/cm.

REFERENCES

1. A. A. Ignatov and Yu. A. Romanov, Phys. Status Solidi B **73** (1), 327 (1976).
2. A. A. Ignatov and Yu. A. Romanov, Izv. Vyssh. Uchebn. Zaved., Radiofiz. **21** (1), 132 (1978).
3. V. V. Pavlovich and É. M. Épshteĭn, Fiz. Tverd. Tela (Leningrad) **18** (5), 1483 (1976) [Sov. Phys. Solid State **18**, 963 (1976)].
4. V. V. Pavlovich and É. M. Épshteĭn, Fiz. Tekh. Poluprovodn. (Leningrad) **10** (10), 2001 (1976) [Sov. Phys. Semicond. **10**, 1196 (1976)].
5. S. A. Akhmanov, V. A. Vysloukh, and A. S. Chirkin, *The Optics of Femtosecond Pulses* (Nauka, Moscow, 1988).
6. T. Dekorsy, R. Ott, H. Kurtz, and K. Köhler, Phys. Rev. B **51** (23), 17275 (1995).
7. O. M. Bulashenko, M. J. Garcia, and L. L. Bonilla, Phys. Rev. B **53** (15), 10008 (1996).
8. Yu. Parhnovskii and H. Metiu, Phys. Rev. B **51** (7), 4193 (1995).
9. F. G. Bass, A. A. Bulgakov, and A. P. Tetervov, *High-Frequency Properties of Semiconductors with Superlattices* (Nauka, Moscow, 1989).
10. S. V. Kryuchkov and K. A. Popov, Fiz. Tekh. Poluprovodn. (St. Petersburg) **32** (3), 334 (1998) [Semiconductors **32**, 302 (1998)].
11. S. V. Kryuchkov and A. I. Shapovalov, Opt. Spektrosk. **81** (2), 336 (1996) [Opt. Spectrosc. **81**, 305 (1996)].
12. S. L. Ktitorov, G. S. Simin, and V. Ya. Sandalovskiĭ, Fiz. Tverd. Tela (Leningrad) **13** (8), 2229 (1971) [Sov. Phys. Solid State **13**, 1872 (1971)].
13. L. Esaki and R. Tsu, IBM J. Res. Dev. **14** (1), 61 (1970).

Translated by S. Ktitorov

Semiconductors, Vol. 35, No. 5, 2001, pp. 557–564. Translated from Fizika i Tekhnika Poluprovodnikov, Vol. 35, No. 5, 2001, pp. 578–585.

LOW-DIMENSIONAL SYSTEMS

Nonlinear Interaction of Waves in a Semiconductor Superlattice

A. A. Bulgakov* and O. V. Shramkova

Usikov Institute for Radiophysics and Electronics, National Academy of Sciences of Ukraine, Kharkov, 61085 Ukraine

** e-mail: bulgakov@ire.kharkov.ua*

Received September 20, 2000; accepted for publication November 13, 2000

Abstract—The nonlinear wave interaction in a periodic structure formed by alternating semiconductor and insulator layers has been studied. The translation symmetry of the structure is shown to be the reason for a number of peculiarities of the nonlinear interaction. Conditions of the resonance interaction between the first and second harmonics are analyzed. The excitation of the second harmonic via the interaction of the first spatial harmonics propagating in the opposite directions is considered for the first time. An explanation is given for the significant enhancement of the wave interaction near the passband edge. *© 2001 MAIK "Nauka/Interperiodica".*

1. INTRODUCTION

The tendency toward the miniaturization of modern devices for processing and transmission of information using electromagnetic waves from the optical to microwave ranges necessitates the application of solid-state structures over virtually the entire signal transmission–receiving path. The role played by nonlinear mechanisms in solids is, as a rule, relatively unimportant. However, their effect on the useful signal is rather strong and leads to undesirable consequences. The reasons are both the significant level of transmitted power and the great length of transmission lines. At the same time, nonlinear phenomena in solids are widely used for information processing (modulation and heterodyning), frequency multiplication, spectroscopy, studies of physical parameters of solid state structures, etc. Artificial materials in the form of multilayer structures and, in particular, semiconductor superlattices have received wide acceptance. That is why a study of the nonlinear interaction of electromagnetic waves in layered and, in particular, periodic structures is important both from the standpoint of physics and in view of the possible numerous applications.

The present work is concerned with the excitation of a second harmonic in a semiconductor superlattice in the vicinity of the plasma frequency of the semiconducting material. The nonlinearity under the study is due to the nonlinearity of the free carrier current. Constructing an appropriate theory is a difficult task since the nonlinearity of current arises from the nonlinearities of carrier velocity and density, which are induced by plasma wave propagation. The terms related to these nonlinearity mechanisms appear in Maxwell's equations and equations of motion and continuity. These nonlinearities cannot be represented in the expression for the insulator permittivity as squared modulus of the electric field strength $|\mathbf{E}|^2$, since they depend on the field components E_iE_k in a more general way.

Taking into account the smallness of the nonlinear terms by using the perturbation theory or, more precisely, the three-wave interaction theory [1–3] essentially simplifies the analysis. However, a difficulty arises in this case: different nonlinear mechanisms are operative in different layers and are described by terms appearing in different equations. It is necessary to formulate a rule that would allow a clear (and physically correct) description of all nonlinearities. For a homogeneous medium, this role is played by the orthogonality of the right-hand side of the algebraic system of equations to the solution of a transposed system. As a result, a system of abridged equations (or coupling equations) for slowly varying wave amplitudes is obtained. The physical meaning of this system is that the interaction energy is small compared with the wave energy and varies slowly (compared with the wave frequency) in the course of interaction. In the problem under consideration, the system of equations is differential because of the spatial inhomogeneity; therefore, Green's formula should be applied [4] (see below). The mathematical meaning consists in that the right-hand side of the system of differential equations must be orthogonal to the solution of the transposed differential system. The system of abridged equations is the same as in the case of a nonlinear homogeneous medium (and, therefore, is well described in the literature), with all specific features of the layered structure accounted for by the coefficients of this system. In the present study, we analyze these features and their dependence on the superlattice parameters.

The theory of weak nonlinear interactions was laid down in [1] in terms of the kinetic approach and developed in [2, 5]. It was later elaborated by many other authors (see, e.g., [3] and references therein). The

1063-7826/01/3505-0557$21.00

three-wave analysis was presented in [6] for bounded media and in monograph [7] for periodic systems. This theory was applied to periodic insulator lattices in [8].

It was shown in [9] for the model of coupling equations for a periodic medium that an essential enhancement of nonlinear interaction is possible at passband edges [9]. The authors believe that the resonance of spatial harmonics and the resulting increase in the interaction time are the reasons for this effect. It was demonstrated in [8] that a more complicated phenomenon takes place since the resonance conditions (Bragg resonance conditions for the whole period of the structure) are fulfilled in the stop band for electromagnetic waves. Therefore, the extent to which the nonlinear interaction is enhanced is determined by the closeness of the passband edge to the point of the Bragg resonance.

In this work, we consider a structure with layers exhibiting frequency dispersion. Consequently, the synchronism laws are essentially more complicated than those considered in [5, 8]. The laws of synchronism, characteristic of periodic structures, are studied, and it is shown that, in addition to the Bragg resonance, one more factor—a peculiar nonlinear resonance—strongly affects the effective interaction constant. This resonance is characterized by the zero algebraic sum of transverse (with respect to layer boundaries) wave vector components of interacting waves in one of the layers. In its physical meaning, this condition corresponds to the maximum energy stored by waves in this layer.

2. PROBLEM DEFINITION: DISPERSION RELATION

Let us consider a periodic structure with spacing d formed by the alternation of semiconductor layers of thickness d_1 and insulator layers of thickness d_2. We orient the system of coordinates so that the Oz axis is perpendicular to the layer boundaries. The layers are assumed to be uniform in the Ox and Oy directions; therefore, we can put $\partial/\partial y = 0$. This results in decoupling of Maxwell's equations into equations for two polarizations. The polarization with nonvanishing components E_x, E_z, and H_y of the electric and magnetic fields is studied in this work. The propagation of electromagnetic waves is described here by Maxwell's equations, the material relations for every layer, and the boundary conditions requiring that the tangential components of magnetic and electric field be equal at all of the boundaries. In order to derive the dispersion relation, we use the transfer matrix technique. The transfer matrix relates the field in the zero-point of a period to that in an arbitrary point z of the structure period [10]:

$$\begin{pmatrix} H_{y1}(0) \\ E_{x1}(0) \end{pmatrix} = M(z) \begin{pmatrix} H_{y2}(z) \\ E_{x2}(z) \end{pmatrix}.$$

The elements of the transfer matrix for $z = d$ are given in the Appendix.

Using the Floquet theorem, we get the dispersion relation for the unbounded periodic medium [7] (temporal and spatial dependence is assumed in the form $\exp(-i\omega t + ik_x x + ik_z z)$):

$$\cos \bar{k}d = \cos k_{z1}d_1 \cos k_{z2}d_2 - \frac{\varepsilon_1\varepsilon_2}{2k_{z1}k_{z2}}\left[\left(\frac{k_{z1}}{\varepsilon_1}\right)^2 + \left(\frac{k_{z2}}{\varepsilon_2}\right)^2\right]\sin k_{z1}d_1 \sin k_{z2}d_2, \quad (1)$$

where $k_{z1} = \sqrt{(\omega^2/c^2)\varepsilon_1 - k_x^2}$ and $k_{z2} = \sqrt{(\omega^2/c^2)\varepsilon_2 - k_x^2}$ are, respectively, the transverse wave numbers in the semiconductor and insulator layers (henceforth, the subscript "1" will refer to the semiconductor and "2" will refer to the insulator layer); k_x is the wave number in the Ox direction; $\varepsilon_1 = \varepsilon_{01}(1 - \omega_p^2/\omega^2)$ and $\varepsilon_2 = \text{const}$ are the insulator permittivities of the layers, with ε_{01} the lattice contribution to the insulator permittivity; ω_p is the plasma frequency; and $\bar{k}$ is the "averaged" so-called Bloch wave number replacing k_{z1} and k_{z2}. A numerical solution of (1) is presented in Fig. 1. The calculations were carried out for a structure with the following parameters, first layer: InSb semiconductor ($\varepsilon_{01} = 17.8$, $\omega_p = 10^{12}$ s^{-1}), $d_1 = 0.01$ cm; second layer: insulator ($\varepsilon_2 = 2$), $d_2 = 0.015$ cm. The $\bar{k}d = 0$ curve is shown in the figure by a dashed line; $\bar{k}d = \pi$, by a thin solid line. The passbands are shaded.

In what follows, we are interested in the region around the plasma frequency, in which the plasma properties of the semiconductor layers are manifested. Therefore, the figure shows three passbands (I, II, and III).

The two lower passbands for the electromagnetic waves (I, II), the so-called acoustic and optical branches of plasma polaritons [7], become narrower with an increasing $k_x d$, and their edges asymptotically approach the frequency of the surface plasmon at the interface between the semiconductor and insulator layers, $\omega_{ps} = \omega_p\sqrt{\varepsilon_{01}/(\varepsilon_{01} + \varepsilon_2)}$, at $k_x d \longrightarrow \infty$. The band of acoustic polaritons begins at $k_x = 0$ and $\omega = 0$, while the optical waves have a gap of width $\omega \approx \omega_p$ at $k_x \longrightarrow 0$.

3. DERIVATION OF THE COUPLING EQUATIONS

The aim of this study is to analyze the nonlinear interaction of waves in the superlattice. Nonlinear effects in solids are, as a rule, weak; therefore, the perturbation approach can be used to construct a theory. The analysis technique has been well developed for homogeneous media and extensively reported in the literature [11, 2, 3]. The situation is different in the inhomogeneous case. The problem is that in the case under study, the nonlinear system cannot be reduced to an algebraic set of inhomogeneous equations, as it is nec-

essary for the technique described in [2]. The equations remain differential (the derivatives $\partial/\partial z$ remain in the case under study), and conditions are to be formulated that would make it possible to clearly take into account the nonlinear mechanisms acting in different layers of the structure and, in addition, to meet the requirement of field continuity at all boundaries of the structure. The development of such a technique for analysis of nonlinear wave interactions in adjoining homogeneous media was started in [6]. The technique was applied to periodic structures in [8].

The method is based on the use of Green's formula [4]:

$$\int_a^b [\tilde{f}^*(\hat{L}f) - (\tilde{\hat{L}}\tilde{f})^* f]dv = f\tilde{f}\Big|_a^b, \qquad (2)$$

where $\hat{L}$ is the differential operator having the form of a square matrix composed of operators of the linearized set of equations, $\tilde{\hat{L}}$ is the transpose of $\hat{L}$, f and $\tilde{f}$ are eigenfunctions of these operators (the asterisk is used to denote complex conjugated values), a and b are boundaries of the integration domain, integration is done over the entire volume of the structure, and $\tilde{f}^*(\hat{L}f)$ stands for the scalar product. The nonlinear set of equations can be represented as

$$\tilde{L}f = \hat{H}(f, f), \qquad (3)$$

where $\tilde{H}(f, f)$ is the bilinear column operator formed by nonlinear terms of the initial set of equations. By substituting (3) into (2) and using the condition for weakness of the nonlinear interaction

$$\omega \gg \frac{d\ln C}{dt}, \qquad (4)$$

where C is the wave amplitude, we get the dynamic system of equations for the amplitudes of the interacting waves. The derivative with respect to the "slow time" in (4) is denoted by d/dt.

In the case under consideration, it is supposed that the nonlinear mechanisms are related to the nonlinearity of the current $\mathbf{j}_1 = en\mathbf{v}_1$ in semiconductor layers (n is the time-dependent electron density, and $\mathbf{v}_1$ is the carrier velocity in the semiconductor). The nonlinear set of equations consists of Maxwell's equations in which the nonlinear current is found from the continuity and carrier motion equations:

$$\mathrm{curl}\mathbf{H}_1 = \frac{\varepsilon_{01}}{c}\frac{\partial \mathbf{E}_1}{\partial t} + \frac{4\pi}{c}\mathbf{j}_1,$$

$$\mathrm{curl}\mathbf{E}_1 = -\frac{1}{c}\frac{\partial \mathbf{H}_1}{\partial t},$$

$$\frac{\partial \mathbf{v}_1}{\partial t} + (\mathbf{v}_1\mathrm{grad})\mathbf{v}_1 = \frac{e}{m}\mathbf{E}_1 + \frac{e}{mc}[\mathbf{v}_1\mathbf{H}_0] + \frac{e}{mc}[\mathbf{v}_1\mathbf{H}_1], \qquad (5)$$

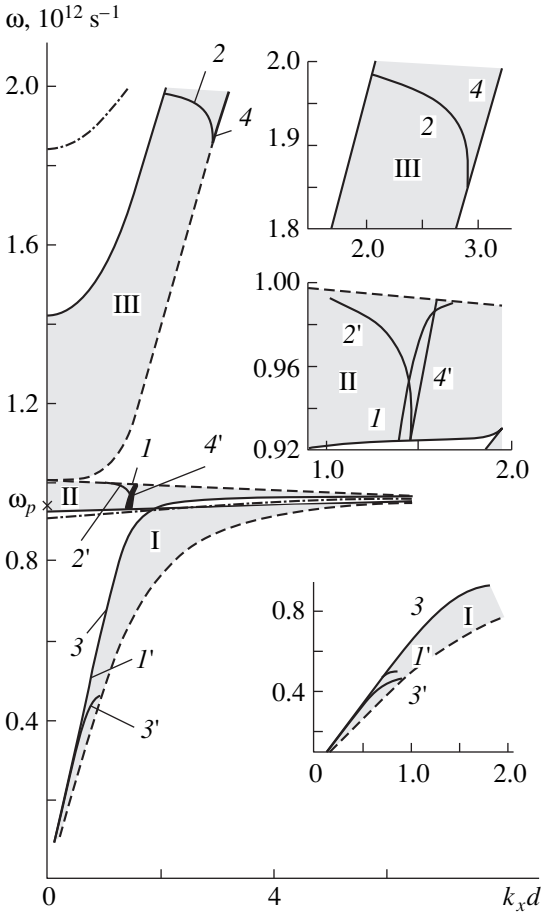

Fig. 1. Dispersion relation: $\varepsilon_0 = 17.8$, $d_1 = 0.01$ cm, $\varepsilon_2 = 2$, $D_2 = 0.015$ cm, $H_0 = 2.7 \times 10^{-6}$ A/cm.

$$\frac{\partial n_1}{\partial t} + \mathrm{div}(n_0 + n_1)\mathbf{v}_1 = 0,$$

$$\mathbf{j}_1 = e(n_0 + n_1)\mathbf{v}_1.$$

The equations for the insulator layer are constituted by Maxwell's equations with ε_2 taken instead of ε_{01} and $\mathbf{j} = 0$.

Applying formula (2) to the system (5), we seek its solution in the form

$$\mathbf{E} = \sum_{k_x=-\infty}^{\infty} C_k(t)[\mathbf{e}(z) + \mathbf{e}^{ad}]\exp(-i\omega_k t + ik_x x),$$
$$H_y = \sum_{k_x=-\infty}^{\infty} C_k(t)[h_y(z) + h_y^{(ad)}]\exp(-i\omega_k t + ik_x x), \qquad (6)$$

where $C(t)$ is the amplitude, slowly varying with time [owing to (4)], of a wave with frequency $\omega = \omega(k_x, \bar{k})$ and wave vector $\mathbf{k} = \{k_x, 0, \bar{k}\}$. The dependences $\mathbf{e}(z)$ and $h_y(z)$ account for the inhomogeneity of the structure

in the z-direction, and the additional terms $\mathbf{e}^{(ad)}$ and $h_y^{(ad)}$ describe deviations of the field directions from those in the linear case caused by the action of nonlinear mechanisms. These quantities have the same order of smallness as the nonlinear terms.

The operator $\hat{L}$ is obtained from the linearized system of equations for the semiconductor and insulator layers (5). The operator $\hat{H}$ consists of nonlinear terms describing the semiconductor layer and the time derivatives dC/dt of the wave amplitude, appearing in the equations for the first and second layers. It is noteworthy that dC/dt is a quantity of the same order of smallness as the nonlinear terms. Hence, e.g., $\partial E_{x2}/\partial t = -i\omega E_{x2} + dE_{x2}/dt$ (see [12]).

The eigenfunctions of the operators L and $\hat{L}$ are proportional, respectively, to $\exp(-i\omega t + ik_x x)$ and $\exp(i\tilde{\omega} t + i\tilde{k}_x x)$. Therefore, integration over t and x of the linear operators gives delta-functions $\delta(\tilde{\omega} - \omega)\delta(\tilde{k}_x - k_x)$, and integration over dz yields the boundary conditions. The frequencies and wave-vector x-components of the eigenfunctions of the operators L and $\tilde{L}$ must be equal; therefore, $k_z = \tilde{k}_z$. That is why all linear terms vanish upon integration. Only the terms with additional fields $\mathbf{e}^{(ad)}$ and $h_y^{(ad)}$ remain in the left-hand side of Eq. (2). As a result, we have

$$L(\partial/\partial z)C_k\varphi_k^{ad} = \frac{dC_k}{dt}\varphi_k$$

$$+ \sum_{k_x = k_x' + k_x''} C_{k'}C_{k''}\hat{H}_1(\varphi_{k'}, \varphi_{k''})e^{-i(\omega' + \omega'' - \omega)t},$$

where $\hat{H}_1$ is the operator comprising only nonlinear terms for the semiconductor layer and $\varphi_k^{(ad)}$ is the column vector formed by the field components $h_y^{(ad)}$, $\mathbf{e}^{(ad)}$.

To integrate nonlinear terms in formula (2) over dz, let us divide the path of integration so as to isolate domains of width $2\delta_i(\delta_i \longrightarrow 0)$ in the vicinity of each boundary [7]:

$$\int_{-\infty}^{\infty} = \lim_{\delta_i \to 0,\ i = 0, \pm 1, \ldots} \ldots + \int_{-\delta_0}^{\delta_0} + \int_{\delta_0}^{-\delta_1 + d_1}$$

$$+ \int_{-\delta_1 + d}^{\delta_1 + d_1} + \int_{\delta_1 + d_1}^{-\delta_2 + d} + \ldots,$$

where $d = d_1 + d_2$ is the structure period. In the integrals over each layer, we express fields in terms of the fields in the first period of the system, using the Floquet theorem; i.e., we reduce them to the sum

$$\sum_{n = -\infty}^{\infty} \exp[i(\bar{\mathbf{k}} + \bar{\mathbf{k}}'' - \bar{\mathbf{k}} + 2\pi n/d)z],$$

$$n = 0, \pm 1, \ldots,$$

which leads to the conservation law for the Bloch wave vector component

$$\bar{k}' + \bar{k}'' - \bar{k} + 2\pi n/d = 0, \tag{7}$$

and the remaining integrals are proportional to $2\delta_i$ or $\delta_i + \delta_{i+1}$ and vanish in the limit $\delta_i \longrightarrow 0$.

In order to meet the field continuity conditions, we are bound to assume that the additional fields satisfy the same conditions as the linearized fields. Then, only terms with dC/dt and nonlinear terms remain in Eq. (2). In what follows, the method used to derive the coupling equations coincides with the standard procedure [2].

If the resonance (synchronism) conditions are satisfied

$$\begin{cases} \omega' + \omega'' - \omega = 0 \\ k_x' + k_x'' - k_x = 0 \\ \bar{k}' + \bar{k}'' - \bar{k} + 2\pi n/d = 0, \end{cases} \tag{8}$$

we obtain the equation for the amplitude C_k [12]:

$$\frac{dC_k}{dt} = W_{k, k', k''}C_{k'}C_{k''}, \tag{9}$$

where

$$W_{k, k', k''} = \int_0^d dz m n_0 \left\{ \frac{1}{\omega}(\nabla' + \nabla'', v^*)(v' v'') \right.$$

$$\left. + \frac{1}{\omega'}(\nabla' v')(v^* v'') + \frac{1}{\omega''}(\nabla'' v'')(v^* v') \right\}.$$

Expression (9) is the equation for the amplitude of the kth wave. Equations for the amplitudes of the other two waves (C' and C'') can be obtained by interchanging the subscripts.

The nonlinear interaction related to the system periodicity exhibits the following specific features.

(1) The band structure of the spectrum consists in that the matrix element and the synchronism conditions make sense only within the passbands of the lattice.

(2) No synchronism condition exists for the z-components of the wave vector, and a relation for the Bloch components (7) of the wave vector, containing the term $2\pi n/d$, must be satisfied instead (apparently, this fact was first revealed on physical grounds in [13]).

(3) The matrix elements in (9) are complex quantities in contrast to the case of homogeneous media, where $W_{k, k', k''}$ is imaginary.

4. ANALYSIS OF THE COUPLING EQUATIONS

Let us analyze the conditions of interaction between the first and second harmonics with frequencies ω' and ω = 2ω'. The system of coupling equations (9) reads

$$\begin{cases} dC_k/dt = W_{2k', k'} C_{k'}^2 \\ dC_{k'}/dt = W_{k', 2k'} C_k C_{k'}^*. \end{cases} \tag{10}$$

To solve Eq. (10), we introduce the following designations: $C_k = Ce^{i\varphi}$, $C_{k'} = C'e^{i\varphi'}$, $W_{2k', k'} = We^{i\Theta}$, $W_{k', 2k'} = W'e^{i\Theta'}$, $\Phi = 2\varphi' - \varphi$. Then, the coupling equations take the form

$$\begin{cases} dC/dt = WC'^2 \cos(\Theta + \Phi) \\ dC'/dt = W'CC' \cos(\Theta' - \Phi) \\ d\Phi/dt = -W(C'^2/C)\sin(\Theta + \Phi) - 2W'C\sin(\Theta' - \Phi). \end{cases} \tag{11}$$

When W and W' are imaginary, i.e., $\Theta = \Theta' = 3/2\pi$, Eq. (11) is reduced to an elliptic integral and the solution is obtained in the form of elliptic functions:

$$C^2 = WK_1 \left\{ y_1 + (y_2 - y_1) \times \mathrm{sn}^2 \left[W'W^{1/2} K_1^{1/2} (t - t_0), \sqrt{\frac{y_2 - y_1}{y_3 - y_1}} \right] \right\}, \tag{12}$$

where $K_1 = [C^2(0)/W] + [C'^2(0)/W']$, $y_1 < y_2 < y_3$ are the roots of the cubic equation

$$y(1-y)^2 - K = 0 \quad K = \frac{K_2^2}{K_1^3 W (W')^2}.$$

When $C(0) < C'(0)$, we find the amplitudes of the first and second harmonics:

$$C^2 \approx \frac{W}{W'} [C'(0)]^2 \mathrm{sn}^2 [\sqrt{WW'} C'(0) t, 1 - \sqrt{K}],$$
$$C'^2 \approx [C'(0)]^2 \{1 - \mathrm{sn}^2 [\sqrt{WW'} C'(0) t, 1 - \sqrt{K}]\}. \tag{13}$$

It can be seen that the second-harmonic amplitude grows with increasing ratio W/W', and the period of the elliptic function is inversely proportional to $\sqrt{WW'}$. Thus, the physical characteristics of the interaction between the first and second harmonics can be obtained by analyzing the dependence of the nonlinear interaction coefficients W and W' on the structure parameters, which is done in the following section.

5. NONLINEAR EXCITATION OF THE SECOND HARMONIC

Excitation of the second harmonic, apart from being used in frequency multiplication and periodic medium spectroscopy, is of interest because of the possibility of analytical study and elucidation of physical features in the nonlinear interaction of waves.

The synchronism conditions for the interaction of the first and second harmonics read

$$\begin{cases} \omega = 2\omega' \\ k_x = 2k_x' \\ \bar{k} = 2\bar{k}'. \end{cases} \tag{14}$$

Here, k_x' and ω' are determined from the system of dispersion relations

$$\cos\bar{k}'d = \cos k_{z1}' d_1 \cos k_{z2}' d_2 - \frac{\varepsilon_1' \varepsilon_2}{2k_{z1}' k_{z2}'} \times \left[\left(\frac{k_{z1}'}{\varepsilon_1'} \right) + \left(\frac{k_{z2}'}{\varepsilon} \right)^2 \right] \sin k_{z1}' d_1 \sin k_{z2}' d_2,$$
$$\cos\bar{k}d = \cos k_{z1} d_1 \cos k_{z2} d_2 - \frac{\varepsilon_1 \varepsilon_2}{2k_{z1} k_{z2}} \times \left[\left(\frac{k_{z1}}{\varepsilon_1} \right)^2 + \left(\frac{k_{z2}}{\varepsilon_2} \right)^2 \right] \sin k_{z1} d_1 \sin k_{z2} d_2, \tag{15}$$

where $\varepsilon_1 = \varepsilon_{01}\{1 - \omega_p^2/4\omega'^2\}$ and $\varepsilon_1' = \varepsilon_{01}\{1 - \omega_p^2/\omega'^2\}$ (i.e., $\varepsilon_1 \neq \varepsilon_1'$, and, therefore, $k_{z1} \neq 2k_{z1}'$). Here lies the difficulty encountered in solving this system of equations analytically, in contrast to the case of a insulator lattice [8]. An analytical solution of the system (15) can be obtained only in the case of a resonance in the second layer, i.e., at $k_{z2}' d_2 = \pi m$ and $k_{z2} = 2k_{z2}'$, where $m = \pm 1, \pm 2, \ldots$. Then, the synchronism conditions (14) are satisfied for the first harmonics with frequencies ω' and wave numbers k_x':

$$k_x' = \frac{1}{2} \sqrt{\frac{\varepsilon_0}{c^2}(4\omega'^2 - \omega_p^2) - \left(\frac{d_1}{\pi m} \right)^2 \left[\frac{3}{2} \frac{\varepsilon_{01}}{c^2} \omega_p^2 + \left(\frac{\pi m}{d_1} \right)^2 \right]^2}.$$

The numerical solution of the system of Eqs. (14) and (15) is represented by thick solid lines in Fig. 1 for the first (*1'*, *2'*) and second (*1*, *2*) harmonics located within the passbands. It can be seen that the first and second harmonics are obviously located in different passbands. Curve *1* shows a transition from the acoustic to optical branch; curve *2*, from the optical branch to that located in the band above the plasma frequency ω_p. It is noteworthy that curves *1'* and *2'* end inside the relevant bands at $\bar{k}' = \pi/2$. With this value increasing, the

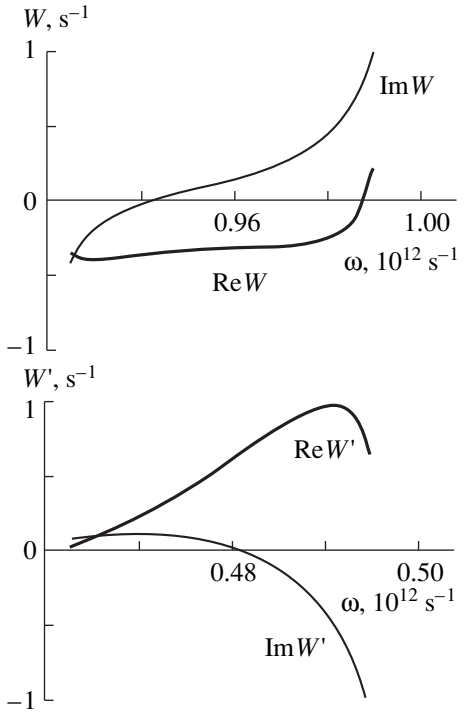

Fig. 2. Nonlinear interaction coefficients vs. frequency for curves *1*, *1*' in Fig. 1.

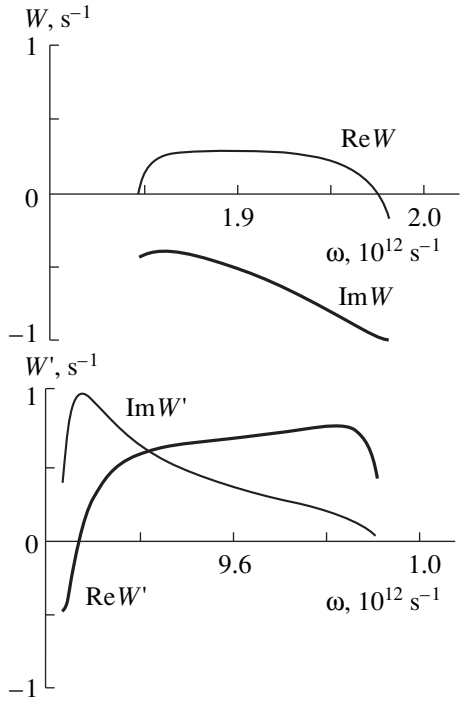

Fig. 3. Nonlinear interaction coefficients vs. frequency for curves *4*, *4*' in Fig. 1.

wave number of the second harmonic leads to a stop band for this harmonic, since $\bar{k} > \pi$.

In the periodic structure, a specific nonlinear interaction mechanism takes place. The point is that the sign of the Bloch wave number is not determined from the dispersion relation. This is why the synchronism conditions are satisfied for both $+\bar{k}'$ and $-\bar{k}'$. Therefore, the following kind of interaction is possible:

$$\begin{cases} \omega = 2\omega' \\ k_x = 2k_x' \\ \bar{k} \pm 2\pi n/d = \bar{k}' - \bar{k}'. \end{cases} \tag{16}$$

In this case, the second harmonic is excited with wave number $\bar{k} = \mp 2\pi n/d$ as a result of interaction of the spatial harmonics with frequency ω' propagating in counter-directions along the axis *Oz*. This kind of interaction is possible since the Bloch wave number is a "quasi-wave number" similar to the electron quasi-momentum in solids. Interest in this kind of interaction is due to the fact that, as shown below, the condition $\bar{k} = 2\pi n/d$ may lead to a substantial increase in the efficiency of the nonlinear interaction.

The numerical solutions of the dispersion relations for the resonance conditions (16) are presented in Fig. 1 by curves *3*', *3*, *4*', and *4*. Curves *3* and *3*' represent the interaction condition at which the first and second harmonics are located in the same passband. Curves *4* and *4*' are related to a process with harmonics belonging to different passbands.

Figures 2 and 3 show the dependences $W(\omega)$ and $W'(\omega)$ normalized to the maximum values: $\mathrm{Re}\,W'/\max(\mathrm{Re}\,W')$ and $\mathrm{Im}\,W'/\max(\mathrm{Im}\,W')$, and the same for *W*, for curves *1*' and *1*, *2*' and *2*, *3*' and *3*, and *4* and *4*' in Fig. 1.

In order to explain this behavior and gain an understanding of the physical factors governing the nonlinear interaction constants, it is necessary to take into account that, upon integration of the expression for *W*, each term in Eq. (9) gives four factors of the form

$$f_s \frac{\cos k_s d_1 - 1 + i \sin k_s d_1}{k_s}, \tag{17}$$

where f_s is a coefficient determined from the amplitudes of interacting waves and k_s is one of the combinations $k_{z1} + k_{z1}' + k_{z1}''$, $k_{z1} - k_{z1}' - k_{z1}''$, $k_{z1} + k_{z1}' - k_{z1}''$, $k_{z1} - k_{z1}' + k_{z1}''$.

Thus, one of the special features of the wave interaction in the periodic structure is that the *W*' and *W* coefficients are complex even when no account is taken of the dissipative processes. This leads to specificities in the dynamics of the interaction process. In order to correctly determine the signs of the real and imaginary parts of *W* and *W*', like signs of the power in the expo-

nentials $\exp(\pm i\bar{k}'d)$ and $\exp(\pm i\bar{k}d)$ should be chosen if a process of type (14) is under consideration. In case (16), a system of dynamic equations (9) instead of (10) should be used and different signs should be chosen for the first harmonics. Then, the sign of the second harmonic does not matter since $\bar{k}\,d = \pi n$. It is noteworthy that an incorrect choice of the signs leads to an unstable solution of the coupling equations.

The coefficients values are determined by two resonance conditions that are specific to a periodic medium. These are the Bragg resonance conditions for the whole structure period [8] and the "nonlinear resonance" [7].

The Bragg resonance makes the nonlinear interaction coefficients in a periodic medium significantly larger in absolute value than those in a homogeneous medium. The nature of this phenomenon consists in that the values of W and W' are affected by the field coefficients A_2 and A_2'. Expressions for these coefficients are given in the Appendix. The resonance manifests itself in that these coefficients become infinite at the points for which

$$m_{12}' = 0 \quad (\text{or} \quad m_{12} = 0). \tag{18}$$

Curves satisfying Eq. (18) are shown in Fig. 1 by the dash–dot lines.

In relations (17), one of f_s tends to infinity. As shown in [8], this is just the Bragg resonance condition for the whole period of the system. Solutions to these equations are located in the forbidden bands, since $(m_{11}' + m_{22}')/2 > 1$ (or $(m_1 + m_{22})/2 > 1$), where the synchronism laws are not satisfied. At the passband edge, the coefficients A_2 and A_2' are finite, with their values depending on the distance between the resonance point and the point satisfying the synchronism conditions and located at the band edge, i.e., $\bar{k} = 2\pi$ or $\bar{k}' = 0, \pi$. Since the solutions of (18) are different, the nonlinear interaction coefficients have maximums at different frequencies and wave number. Physically, this is related to the frequency dependence of the insulator permittivity of the semiconductor. In the insulator lattice, the peaks of W and W' coincide, since the Bragg resonance condition reads $m_{12}' = m_{12} = 0$ (see [8]). It should finally be noted that the possibility of a substantial increase in the nonlinear interaction coefficient was shown for the first time in [9] for a model problem.

The second factor affecting the W and W' coefficients is the possibility of one of k_s vanishing (no divergence appears in this case as seen from (17)). It is noteworthy that in the limit $k_s \longrightarrow 0$ the real part of the second factor in (17) is zero and the imaginary part is d_1. Therefore, only $\mathrm{Re}W'$ ($\mathrm{Re}W$) or $\mathrm{Im}W'$ ($\mathrm{Im}W$) will have a maximum. The vanishing of k_s means that the "total field" of the interacting waves is independent of the z coordinate within the semiconductor layers; i.e., the energy of these waves accumulated inside these layers is the highest for the parameters leading to the condition $k_s = 0$. As a result, the interaction constant is larger the closer the wave parameters are to this condition,.

Figure 2 presents the frequency dependences of the nonlinear interaction coefficients for the case of synchronism (14) (curves *1'*, *1* in Fig. 1). A decrease in k_s (approximately twofold) makes $\mathrm{Im}W'(\omega')$ lower and $\mathrm{Im}W(\omega)$ higher. The peak of $\mathrm{Re}W'(\omega')$ is related to the Bragg resonance for the first harmonic. The decrease in $\mathrm{Re}W'(\omega')$ at the band edge is related to the "competition" of two resonances. For the nonlinear interaction coefficient $W(\omega)$ of the second harmonic, only the Bragg resonance was found to be important in the given example.

Figure 3 presents the same frequency dependences for the case when the synchronism conditions (16) are satisfied (curves *4'* and *4* in Fig. 1). Here, the peaks associated with the "nonlinear" resonance are observed for the dependences $\mathrm{Im}W'(\omega')$ and $\mathrm{Im}W(\omega)$. This resonance leads to higher slopes of the curves for the first and second harmonics at low- and high-frequency ends. However, the resonance frequencies lie relatively far from the band edges; therefore, the increase in the coefficients W and W' is relatively small.

6. CONCLUSION

The aim of this study was to gain insight into the nonlinear interaction of waves in a periodic layered semiconductor–insulator superlattice. Green's formula (2) was applied to derive the dynamic equations which account for the nonlinear terms in the motion and continuity equations, leading to the nonlinear current in Maxwell's equations for the semiconductor layers. In addition, account is taken of the fact that nonlinear processes occur in the periodically arranged semiconductor layers rather than in the entire volume of the superlattice.

The synchronism conditions are analyzed for frequencies lying close to the semiconductor plasma frequency; i.e., the frequency dispersion of the insulator permittivity is taken into account. It is shown that the second harmonic can be excited in the interaction of first spatial harmonics propagating both in the same and opposite directions. The latter variant of interaction is possible only in periodic structures and has not been described previously.

The physical factors affecting the second-harmonic amplitude are revealed. They are related to the Bragg resonance of the structure period and nonlinear resonance, when one of the quantities $\pm 2k_{z1}'$, $\pm k_{z1}$ tends to zero. The Bragg resonance leads to divergence of the fields in the forbidden band. Therefore, the nonlinear interaction coefficient depends on closeness of this point to the passband edge. Physically, the occurrence of the resonance means that the duration of the nonlinear resonance effectively becomes longer. The nonlinear resonance means that the energy of the interacting

harmonics, accumulated in the semiconductor layers, is highest at the resonance point. It is this fact that leads to an increase in the nonlinearity coefficient. The "competition" between these two resonances leads to a rather complicated frequency dependence of the nonlinear interaction coefficients.

APPENDIX

Transfer matrix elements are given by

$$m_{11} = \cos k_{z1}d_1\cos k_{z2}d_2 - \frac{k_{z2}\varepsilon_1}{k_{z1}\varepsilon_2}\sin k_{z1}d_1\sin k_{z2}d_2;$$

$$m_{12} = -i\frac{\omega}{c}\frac{\varepsilon_1}{k_{z1}}\sin k_{z1}d_1\cos k_{z2}d_2 - i\frac{\omega}{c}\frac{\varepsilon_2}{k_{z2}}\cos k_{z1}d_1\sin k_{z2}d_2;$$

$$m_{21} = -i\frac{c}{\omega}\frac{k_{z1}}{\varepsilon_1}\sin k_{z1}d_1\cos k_{z2}d_2 - i\frac{c}{\omega}\frac{k_{z2}}{\varepsilon_2}\cos k_{z1}d_1\sin k_{z2}d_2;$$

$$m_{22} = \cos k_{z1}d_1\cos k_{z2}d_2 - \frac{k_{z1}\varepsilon_2}{k_{z2}\varepsilon_1}\sin k_{z1}d_1\sin k_{z2}d_2.$$

Expressions for fields are written as

$$E_{x1} = -i\frac{c}{\omega\varepsilon_1}A_1(-k_{z1}\sin k_{z1}z + A_2k_{z1}\cos k_{z1}z),$$

$$E_{x2} = -i\frac{c}{\omega\varepsilon_2}A_1(-B_1k_{z2}\sin k_{z2}z + B_2k_{z2}\cos k_{z2}z),$$

$$H_{y1} = A_1(\cos k_{z1}z + A_2\sin k_{z1}z),$$

$$H_{y2} = A_1(B_1\cos k_{z2}z + B_2\sin k_{z2}z),$$

where

$$B_1 = \cos k_{z1}d_1\cos k_{z2}d_1 + \frac{k_{z1}\varepsilon_2}{k_{z2}\varepsilon_1}\sin k_{z1}d_1\sin k_{z2}d_1 + A_2\left\{\sin k_{z1}d_1\cos k_{z2}d_1 - \frac{k_{z1}\varepsilon_2}{k_{z2}\varepsilon_1}\cos k_{z1}d_1\sin k_{z2}d_1\right\},$$

$$B_2 = \cos k_{z1}d_1\sin k_{z2}d_1 - \frac{k_{z1}\varepsilon_2}{k_{z2}\varepsilon_1}\sin k_{z1}d_1\cos k_{z2}d_1 + A_2\left\{\sin k_{z1}d_1\sin k_{z2}d_1 + \frac{k_{z1}\varepsilon_2}{k_{z2}\varepsilon_1}\cos k_{z1}d_1\cos k_{z2}d_1\right\},$$

$$A_2 = i\frac{\omega}{c}\frac{\varepsilon_1}{k_{z1}}\frac{m_{11} - e^{-i\bar{k}d}}{m_{12}}.$$

REFERENCES

1. B. B. Kadomtsev and V. I. Petviashvili, Zh. Éksp. Teor. Fiz. **43**, 2234 (1962) [Sov. Phys. JETP **16**, 1578 (1963)].
2. A. A. Galeev and V. I. Karpman, Zh. Éksp. Teor. Fiz. **44** (2), 592 (1963) [Sov. Phys. JETP **17**, 403 (1963)].
3. J. Weiland and H. Wilhelmsson, *Coherent Nonlinear Interaction of Waves in Plasmas* (Pergamon, Oxford, 1976; Énergoizdat, Moscow, 1981).
4. P. Hartman, *Ordinary Differential Equations* (Wiley, New York, 1964; Mir, Moscow, 1970).
5. N. Bloembergen, *Nonlinear Optics: a Lecture Note and Reprint Volum* (W. A. Benjamin, New York, 1965; Mir, Moscow, 1966).
6. A. A. Bulgakov, S. I. Khankina, and V. M. Yakovenko, Fiz. Tverd. Tela (Leningrad) **22** (8), 2536 (1980) [Sov. Phys. Solid State **22**, 1483 (1980)].
7. F. G. Bass, A. A. Bulgakov, and A. P. Tetervov, *High-Frequency Properties of Semiconductors with Superlattices* (Nauka, Moscow, 1989).
8. A. A. Bulgakov, S. A. Bulgakov, and L. Vazquez, Phys. Rev. E **58**, 7887 (1998).
9. V. É. Pozhar and L. A. Chernozatonskiĭ, Fiz. Tverd. Tela (Leningrad) **27** (3), 682 (1985) [Sov. Phys. Solid State **27**, 421 (1985)].
10. M. Born and E. Wolf, *Principles of Optics* (Pergamon, Oxford, 1969; Nauka, Moscow 1973).
11. N. N. Bogolyubov and Yu. A. Mitropol'skiĭ, *Asymptotic Methods in the Theory of Nonlinear Oscillations* (Nauka, Moscow, 1974, 4th ed.; Gordon and Breach, New York, 1962).
12. V. N. Tsytovich, *Nonlinear Effects in Plasmas* (Nauka, Moscow, 1967; Plenum, New York, 1970).
13. N. Blombergen and A. I. Silvers, Appl. Phys. Lett. **17** (11), 483 (1970).

Translated by S. Ktitorov

Semiconductors, Vol. 35, No. 5, 2001, pp. 565–572. Translated from Fizika i Tekhnika Poluprovodnikov, Vol. 35, No. 5, 2001, pp. 586–593.

LOW-DIMENSIONAL SYSTEMS

The Distribution Function of Hot Charge Carriers under Conditions of Resonance Scattering

A. A. Prokof'ev[1,2], M. A. Odnoblyudov[1,2], and I. N. Yassievich[1,2]

[1] *Ioffe Physicotechnical Institute, Russian Academy of Sciences, Politekhnicheskaya ul. 26, St. Petersburg, 194021 Russia*

[2] *Division of Solid-State Theory, Department of Physics, Lund University, SE-223 62 Lund, Sweden*

Submitted November 8, 2000; accepted for publication November 15, 2000

Abstract—A simple analytical method for solving the kinetic equation for charge carriers in the presence of resonance states in the streaming mode is suggested. The Breit–Wigner isotropic model for resonance scattering was used in an analysis of both the anisotropic energy distribution of charge carriers, which arises under the effect of an external electric field in a two- and three-dimensional gas of charge carriers, and the occupancy of the resonance state. The conditions for the origination of the intracenter population inversion are considered.

1. INTRODUCTION

On the basis of uniaxially stressed germanium in which the shallow-level acceptors give rise to the resonance states, a terahertz laser was developed; this laser operated by optical transitions between the resonance and localized states of the same impurity (see [1, 2] and the references therein). The emergence of a new type of population inversion induced by resonance states in semiconductors was considered previously [3] on the basis of the numerical solution of a kinetic equation for the streaming mode. A detailed theoretical study of resonance states introduced by shallow-level acceptors in uniaxially stressed semiconductors was reported recently [4].

In this paper, we suggest a simple analytical method for solving the kinetic equation for charge carriers in the presence of resonance states in the streaming mode. Using the Breit–Wigner resonance scattering as an example, we analyze the anisotropic distribution of charge carriers in energy, which arises under the effect of an external electric field on two-dimensional (2D) and three-dimensional (3D) systems of charge carriers; we also analyzed the occupancy of the resonance state. The conditions for the emergence of intracenter population inversion are discussed.

2. THE STREAMING MODE

We consider a simple model in which we restrict ourselves to the consideration of only the resonance scattering of charge carriers by impurities and the interaction of carriers with optical phonons.

If there is no resonance scattering, the so-called streaming mode comes into play [5, 6]. This mode takes place for the fields $F \geq \hbar\omega_o/el$, where l is the mean free path in reference to other mechanisms of scattering. If there is an electric field **F** applied along the z-axis, the charge carriers are accelerated and move in the k space until their energy becomes higher than the optical-phonon energy $\hbar\omega_o$. The charge carriers whose energy exceeds $\hbar\omega_o$ can emit an optical phonon, after which they return to the region of low kinetic energies $\varepsilon_\mathbf{k} \leq \epsilon_0$.

The kinetic Boltzmann equation for the distribution function of the charge carriers $f_\mathbf{k}$ in the wave vector **k** has the following form:

$$\frac{\partial f_\mathbf{k}}{\partial t} + \frac{eF}{\hbar}\frac{\partial f_\mathbf{k}}{\partial k_z} = S - D. \quad (1)$$

Here, $S(\varepsilon_\mathbf{k})$ stands for a charge-carrier source that differs from zero for $\varepsilon_\mathbf{k} \leq \epsilon_0$ and D accounts for drain of charge carriers for $\varepsilon_\mathbf{k} = \hbar\omega_o$. The drain can be taken into account in the simplest manner by introducing the boundary condition

$$f_\mathbf{k} = 0 \quad (2)$$

for $\varepsilon_\mathbf{k} = \hbar\omega_o$.

The dependence $S(\varepsilon_\mathbf{k})$ is determined from the condition that the arrival of the particle to the region of low energies $\varepsilon_\mathbf{k} \leq \epsilon_0$ is controlled by the emission of optical phonons due to deformation-related interaction. For the sake of simplicity, we assume that the source is isotropic and take into account the condition for the balance of fluxes: the total flux to the region of $\varepsilon_\mathbf{k} \leq \epsilon_0$ is equal to the flux through the surface $\varepsilon_\mathbf{k} = \hbar\omega_o$; i.e.,

$$J(\hbar\omega_o) \equiv \int S(\varepsilon_\mathbf{k}) d^3\mathbf{k} = \frac{e}{\hbar}\int f_\mathbf{k}(\mathbf{F}\cdot\mathbf{dS})|_{\varepsilon_\mathbf{k} = \hbar\omega_o}. \quad (3)$$

The resonance scattering is taken into account by introducing the collision integral I into the right-hand side of Eq. (1); we have

$$I = \sum_{\mathbf{k}} N_i W_{\mathbf{k}\mathbf{k}'}(f_{\mathbf{k}'} - f_{\mathbf{k}}), \tag{4}$$

where N_i is the number of impurity centers and the scattering probability $W_{\mathbf{k}\mathbf{k}'}$ is defined as

$$W_{\mathbf{k}\mathbf{k}'} = \frac{2\pi}{\hbar}|t_{\mathbf{k}\mathbf{k}'}|^2\delta(\varepsilon_{\mathbf{k}'} - \varepsilon_{\mathbf{k}}), \tag{5}$$

with $t_{\mathbf{k}\mathbf{k}'}$ standing for the resonance-scattering amplitude.

We consider the limiting case in which the resonance-level width $\Gamma/2 \ll E_0$, where E_0 is the energy position of the resonance level. In this case, the processes of capture by, and emission from, a resonance state and, correspondingly, of the resonance scattering occur in a narrow energy range and may be treated as taking place at a fixed energy E_0.

Thus, in the energy range of $\epsilon_0 < \varepsilon_{\mathbf{k}} < \hbar\omega_o$, we have free motion of charge carriers under the effect of an electric field and resonance elastic scattering for an energy of $\varepsilon_{\mathbf{k}} = E_0$, where E_0 is the resonance-level energy. In what follows, we will focus on the resonance-level occupancy, which is defined by

$$f_r = \sum_{\mathbf{k}} W_{\mathbf{k}} f_{\mathbf{k}}, \tag{6}$$

where $W_{\mathbf{k}}$ is the total probability for the capture of the free charge carrier with a wave vector $\mathbf{k}$ by the resonance state [3, 4].

The normalization condition for the distribution function is given by the equation

$$n = n_i f_r + \sum_{\mathbf{k}} f_{\mathbf{k}}, \tag{7}$$

where n is the total charge-carrier concentration and n_i is the impurity concentration (we disregard the fact that charge carriers have spin).

3. A SIMPLE ISOTROPIC MODEL OF RESONANCE SCATTERING

We derive a time-independent solution to Eq. (1) for isotropic scattering. In this case, both the elastic resonance scattering and the probability of capture of free charge carriers by the resonance state are specified by only two parameters (E_0 and Γ) and depend only on the magnitude of the wave vector of the particle (the Breit–Wigner model; see, for example, [7]).

The capture probability $W_{\mathbf{k}}$ and the amplitude of elastic resonance scattering $t_{\mathbf{k}\mathbf{k}'}$ are defined as

$$W_{\mathbf{k}} = \frac{1}{V}\frac{\pi\Gamma\hbar^2}{km}\frac{1}{(\varepsilon_{\mathbf{k}} - E_0)^2 + \Gamma^2/4}, \tag{8}$$

$$|t_{\mathbf{k}\mathbf{k}'}|^2 = \frac{1}{V^2}\frac{\pi^2\hbar^4\Gamma^2}{m^2k^2}\frac{1}{(\varepsilon_{\mathbf{k}} - E_0)^2 + \Gamma^2/4}, \tag{9}$$

where V is the normalization volume and m is the particle mass. These expressions may be derived following [3, 4].

Introducing the resonance-scattering cross section

$$\sigma_r(k) = \frac{\pi}{k_0^2}\frac{\Gamma^2}{(\varepsilon_{\mathbf{k}} - E_0)^2 + \Gamma^4/4}, \tag{10}$$

we can reduce the collision integral I to the following form:

$$n_i\sigma_r(k)\upsilon_k\frac{1}{2}\int_{-1}^{+1} d\eta'[f(\eta', \varepsilon_{\mathbf{k}}) - f(\eta, \varepsilon_{\mathbf{k}})]. \tag{11}$$

Here, $\upsilon_k = \sqrt{2\varepsilon_{\mathbf{k}}/m}$ is the particle velocity; also, a parameter $\eta = k_z/k$ is introduced.

If $\Gamma \ll E_0$, resonance scattering occurs only for the particles with the wave vector given by $k_0 = \sqrt{2mE_0/\hbar^2}$; i.e.,

$$\sigma_r(k) = \frac{2\pi^2\Gamma}{k_0^2}\delta(\varepsilon_k - E_0). \tag{12}$$

Since the momentum in the direction perpendicular to the field is preserved, it is convenient henceforth to introduce the dimensionless variables for the total energy ($y = \varepsilon_{\mathbf{k}}/E_0$) and the energy of transverse motion ($y_\perp = \varepsilon_\perp/E_0$); here, $\varepsilon_\perp = \hbar^2k_\perp^2/2m$ and $k_\perp^2 = k^2 - k_z^2$. It also convenient to introduce a function $f_1(\mathbf{k})$ defined in the region of $k_z > 0$ and a function $f_2(\mathbf{k})$ defined in the region of $k_z < 0$.

In isotropic models, the energy dependence of the charge-carrier source is given by [5]

$$S = S_0\sqrt{\frac{\varepsilon_{\mathbf{k}}}{\hbar\omega_o}}\left[1 - \left(\frac{\varepsilon_k}{\epsilon_0}\right)^{3/2}\right]\Theta(\epsilon_0 - \varepsilon_{\mathbf{k}}), \tag{13}$$

where it is convenient to determine the constant S_0 from the condition for the balance of fluxes (3) and the characteristic parameter ϵ_0 is defined [5, 6] by the following formula:

$$\epsilon_0 = \left(\frac{9}{2m_z}\right)^{1/3}\left(\frac{\omega_o}{\upsilon_A}eF\hbar\right)^{2/3}. \tag{14}$$

Here, υ_A is the parameter specifying the rate of optical-phonon emission $\upsilon_A = \sqrt{\varepsilon_{\mathbf{k}}/\hbar\omega_o - 1}$ by charge carriers with an energy of $\varepsilon_{\mathbf{k}} > \hbar\omega_o$. When calculating ϵ_0, we should use the value of the effective mass m_z inherent in the particle with an energy close to that of an optical phonon.

Equation (1) written in variables y and $y_\perp$ has the following form with expression (13) and the collision term taken into account:

$$\frac{\partial f_{1,2}(y, y_\perp)}{\partial y} = \pm A\frac{\delta(y-1)}{\sqrt{1-y_\perp}}[B - f_{1,2}(y, y_\perp)] \pm C\frac{\sqrt{y}}{\sqrt{y-y_\perp}}\left[1-\left(\frac{y}{y_0}\right)^{3/2}\right]\Theta(y_0-y). \quad (15)$$

Here, $y_0 = \epsilon_0/E_0$, the parameters A and C are given by

$$A = \frac{2\pi^2 n_i \Gamma}{eFk_0^2}, \quad (16)$$

$$C = \frac{S_0}{eF}\sqrt{\frac{mE_0}{\hbar}}, \quad (17)$$

and the parameter B is related to the value of the distribution function for $y = 1$ as

$$B = \frac{1}{4}\int_0^1 \frac{f_1(1, y_\perp) + f_2(2, y_\perp)}{\sqrt{1-y_\perp}}dy_\perp. \quad (18)$$

In expression (15), the plus sign refers to the function f_1, whereas the minus sign refers to the function f_2 (see Fig. 1).

The boundary conditions (2) imposed on the distribution functions can be rewritten as

$$f_1(y_1, y_\perp) = f_2(y_1, y_\perp) = 0, \quad (19)$$

where $y_1 = \hbar\omega_o/E_0$.

We note that, as follows from formulas (6) and (8) for $\Gamma \ll E_0$, it is the quantity B which specifies the occupancy of the resonance level f_r; i.e., we have

$$f_r = B. \quad (20)$$

Figure 1 illustrates the domains of definition of the functions f_1 and f_2 in the **k** space. Domains *1* and *1a* ($k_z > 0$) correspond to the acceleration of charge carriers by an electric field, whereas domains *2* and *2a* ($k_z < 0$) correspond to deceleration. Charge carriers undergo a pronounced elastic scattering at the surface $k = k_0$. Outside the source, the particles appear in domain *2* only as a result of scattering. There are no charge carriers at all in domain *2a*. All charge carriers that arrived in domain *1a* after gaining an energy exceeding $\hbar\omega_o$ emit an optical phonon and return to the source domain $\varepsilon_{\mathbf{k}} < \epsilon_0$.

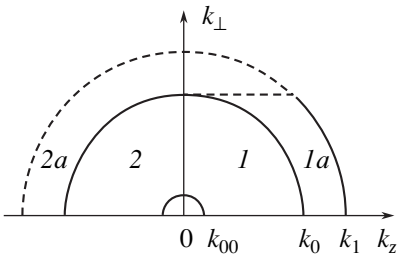

Fig. 1. The domains of the motion of charge carriers in the **k** space: $k_{00} = \sqrt{2m\epsilon_0}/\hbar$ restricts the source size; $k_0 = \sqrt{2mE_0}/\hbar$ defines the line of resonance scattering; $k_1 = \sqrt{2m\hbar\omega_o}/\hbar$, where $\hbar\omega_o$ is the optical-phonon energy; and *1* and *2* denote the definition domains for the functions f_1 and f_2, respectively.

Since the source is active only in the region of low energies $y < y_0$, we obtain a solution for the range of $y_0 < y < y_1$. For $y_0 < y < 1$, the functions f_1 and f_2 are independent of y, and we have

$$f_{1,2}(y, y_\perp) = C_{1,2}(y_\perp). \quad (21)$$

For $y > 1$, the solution of Eq. (15) yields

$$f_{1,2}(y, y_\perp) = C_{1,2}(y_\perp)\exp(\mp A/\sqrt{1-y_\perp}) + B[1 - \exp(\pm A/\sqrt{1-y_\perp})]. \quad (22)$$

The condition for the absence of particles in domain *2a* (see Fig. 1), i.e., the equality $f_2 = 0$ for $y > 1$, yields the following expression for C_2:

$$C_2(y_\perp) = B[1 - \exp(-A/\sqrt{1-y_\perp})]. \quad (23)$$

The flux of particles in the **k** space through the surface of constant energy ε is defined as

$$J(\varepsilon) = \frac{1}{(2\pi)^3}\int\frac{e}{\hbar}f_{\mathbf{k}}(\mathbf{F}\cdot\mathbf{dS}). \quad (24)$$

Here, we are dealing with the flux per unit volume of actual space. Rewriting integral (24) in the variables y and $y_\perp$, we obtain

$$J(y) = f\int_0^y [f_1(y, y_\perp) - f_2(y, y_\perp)]dy_\perp, \quad (25)$$

where

$$b = \frac{eFk_0^2}{8\pi^2\hbar}. \quad (26)$$

Since the source is active only for $y < y_0$, the flux J is constant for $y_0 < y < 1$; in contrast, the functions f_1 and f_2 depend only on $y_\perp$ [see Eq. (21)] in this region. We

then have $C_1(y_\perp) = C_2(y_\perp)$ for $y_\perp > y_0$, and we can represent C_1 as

$$C_1(y_\perp) = C_2(y_\perp) + \varphi(y_\perp), \tag{27}$$

where the function $\varphi(y_\perp)$ is nonvanishing only for $y_1 < y_0$ and is controlled by the flux from the source to the region $y > y_0$; i.e.,

$$J(y_0) = b\int_0^{y_0}\varphi(y_\perp)dy_\perp. \tag{28}$$

Using the function φ and taking into account formulas (21)–(23), we can write the distribution functions in the range of $y_0 < y < 1$ as

$$f_1(y, y_\perp) = \varphi(y_\perp) + B[1 - \exp(-A/\sqrt{1-y_\perp})], \tag{29}$$

$$f_2(y, y_\perp) = B[1 - \exp(-A/\sqrt{1-y_\perp})], \tag{30}$$

in the range of $1 < y < y_1$, we have

$$f_1(y, y_\perp) = \varphi(y_\perp)\exp(-A/\sqrt{1-y_\perp}) + B[1 - \exp(-2A/\sqrt{1-y_\perp})], \tag{31}$$

$$f_2(y, y_2) = 0. \tag{32}$$

We now consider the distribution function for charge carriers in the region of $y < y_0$, where Eq. (1) has the form

$$\frac{\partial f_{1,2}}{\partial y} = \pm C\frac{\sqrt{y}}{\sqrt{y-y_\perp}}\left[1 - \left(\frac{y}{y_0}\right)^{3/2}\right], \tag{33}$$

and C is defined by formula (17). We then have

$$\frac{\partial(f_1 - f_2)}{\partial y} = 2C\frac{\sqrt{y}}{\sqrt{y-y_\perp}}\left[1 - \left(\frac{y}{y_0}\right)^{3/2}\right]. \tag{34}$$

When integrating Eq. (34), we use the following equality as the boundary condition:

$$[f_1(y, y_\perp) - f_2(y, y_\perp)]\big|_{y = y_\perp} = 0.$$

As a result, we obtain

$$f_1(y, y_\perp) - f_2(y, y_\perp) = 2CM(y, y_\perp), \tag{35}$$

where

$$M(y, y_\perp) = \sqrt{y(y-y_\perp)} - \sqrt{y_0(y-y_\perp)} \times\left(\frac{2}{5}\frac{y^2}{y_0^2} + \frac{8}{15}\frac{yy_\perp}{y_0^2} + \frac{16}{15}\frac{y_\perp^2}{y_0^2}\right) + \frac{y_\perp}{2}\ln^2\left(\frac{\sqrt{y(y-y_\perp)} + 2y - y_\perp}{y_\perp}\right). \tag{36}$$

On the other hand, we have

$$f_1(y_0 + 0, y_\perp) - f_2(y_0 + 0, y_\perp) = \varphi(y_\perp);$$

thus, the condition for the continuity of the distribution function for $y = y_0$ yields

$$\varphi(y_\perp) = 2CM(y_0, y_\perp)\Theta(y_0 - y_\perp). \tag{37}$$

Using formula (25) and equating the fluxes for $y < 1$ and $y > 1$, we obtain the equality

$$\int_0^{y_0}\varphi(y_\perp)[1 - \exp(-A/\sqrt{1-y_\perp})]dy_\perp = B\int_0^1[1 - \exp(-2A/\sqrt{1-y_\perp})]dy_\perp, \tag{38}$$

which, when combined with expression (37), makes it possible to express the constant C in terms of B; i.e.,

$$C = \frac{1}{2}BI(A), \tag{39}$$

where

$$I(A) = \frac{\int_0^1[1 - \exp(-2A/\sqrt{1-y_\perp})]dy_\perp}{\int_0^{y_0}M(y_0, y_\perp)[1 - \exp(-A/\sqrt{1-y_\perp})]dy_\perp}. \tag{40}$$

Solving now Eqs. (33) and taking into account the continuity of the functions $f_1(y, y_\perp)$ and $f_2(y, y_\perp)$ at the boundary of the source $y = y_0$, we obtain the following expressions for the distribution functions for $y < y_0$:

$$f_{1,2}(y, y_\perp) = B\left[\frac{1}{2}I(A)(M(y_0, y_\perp) \pm N(y, y_\perp)) + 1 - \exp(-A/\sqrt{1-y_\perp})\right]. \tag{41}$$

Here, the signs "+" and "–" refer to the functions f_1 and f_2, respectively.

Formulas (29)–(32) and (41) define the functions $f_1(y, y_\perp)$ and $f_2(y, y_\perp)$ in the entire range of $0 < y < y_1$ to an accuracy of B.

The function of distribution of the charge carriers in total energy is obtained by integrating with respect to $y_\perp$; thus, we have

$$f(y) = \frac{1}{2}\int_0^y\frac{f_1(y, y_\perp) + f_2(y, y_\perp)}{\sqrt{y(y-y_\perp)}}dy_\perp. \tag{42}$$

The value of B can be determined from normalization condition (7), which has the following form in the variables y and $y_\perp$:

$$n = n_i f_r + \frac{k_0^3}{8\pi^2}\int_0^{y_1}\sqrt{y}\,f(y)dy. \quad (43)$$

It should be recalled that occupancy of a center is specified by the quantity B; i.e., $f_r = B$.

The functions of distribution of the charge carriers in total energy $f(y)$ and also the distribution function of the charge carriers with momentum directed along the electric field [$f(y, 0) = f_1(y, 0) + f_2(y, 0)$] and perpendicular to the field [$f(y, y) = f_1(y, y) + f_2(y, y)$] are shown in Figs. 2 and 3. All calculations were performed using the following parameters: E_0 = 20 meV, Γ = 2 meV, and $\hbar\omega_o$ = 36 meV (y_1 = 1.8). The function of distribution of charge carriers in the energy of transverse motion of particles with a total energy of $E_0(f(1, y_\perp))$ and $\hbar\omega_o(f(y_1, y_\perp))$ is shown in Fig. 4. Taking into account the possibility of using a simple isotropic model for the case of germanium under pressure, we used the effective mass of $m = 0.08m_0$ in the calculations, which corresponded to the density-of-state mass in the upper valence subband of compressed germanium (in the subband of light holes). When calculating ϵ with formula (14), we used the value of $m_z = 0.32m_0$.

4. A TWO-DIMENSIONAL SYSTEM OF CHARGE CARRIERS

In order to analyze the special features of the kinetics of the charge carriers confined in a quantum well (QW) under the conditions of resonance scattering, we consider the performance of the simple isotropic model in the case of the 2D system of charge carriers.

The Boltzmann kinetic equation for the distribution function of the 2D system of charge carriers is again defined by Eq. (1) taking into account the collision term that corresponds to the resonance scattering. However, it should be taken into account that **k** is now a 2D vector. Correspondingly, the density of states and the form of the source change. For the distribution of the source in energy, we now have

$$S = S_0\left(1 - \frac{\varepsilon_\mathbf{k}}{\epsilon_0^{(2D)}}\right)\Theta(\epsilon_0^{(2D)} - \varepsilon_\mathbf{k}). \quad (44)$$

Here, $\varepsilon_\mathbf{k}$ is the kinetic energy of 2D motion, and the source boundary $\epsilon_0^{(2D)}$ is now defined by the expression

$$\epsilon_0^{(2D)} = \frac{\omega_0}{\upsilon_A}\frac{2}{\pi}eFL, \quad (45)$$

where L is the QW width and υ_A is the same parameter as that specifying the emission rate of phonons in the 3D configuration. The effect of a QW on the phonon

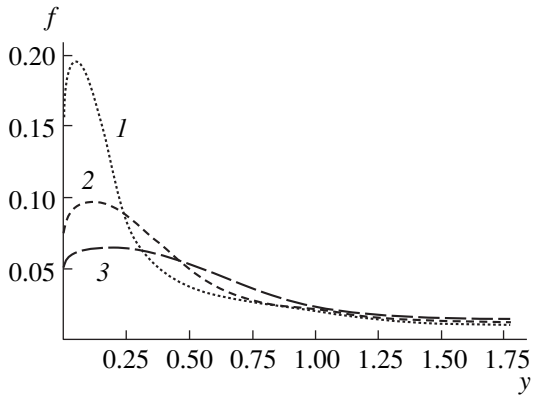

Fig. 2. The distribution function of charge carriers $f(y)$ for the impurity concentration of 5×10^{15} cm^{-3} and electric-field strengths F = (*1*) 300, (*2*) 1000, and (*3*) 2000 V/cm.

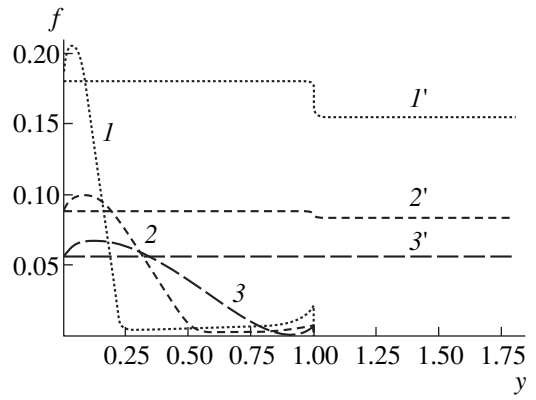

Fig. 3. The distribution function of charge carriers (*1*'–*3*') in the direction of the electric field $f(y, y_\perp = 0)$ (the step functions) and (*1*–*3*) in the direction perpendicular to the electric field $f(y, y_\perp = y)$ for the impurity concentration of 5×10^{15} cm^{-3} and the electric-field strengths of F = (*1*, *1*') 300, (*2*, *2*') 1000, and (*3*, *3*') 2000 V/cm.

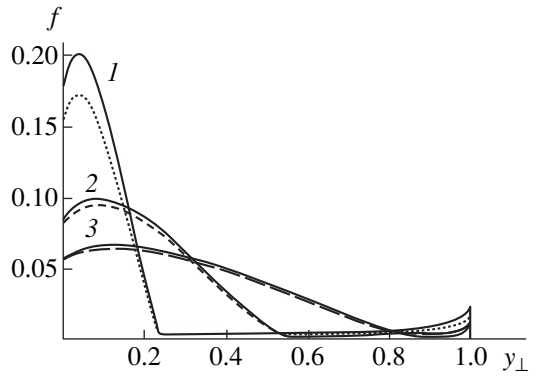

Fig. 4. The energy-distribution function for charge carriers moving transversely for the total energy $E_0 - 0$ (the solid lines) and $\hbar\omega_o - 0$ (the dashed lines) for the impurity concentration of 5×10^{15} cm^{-3} and electric-field strengths F = (*1*) 300, (*2*) 1000, and (*3*) 2000 V/cm.

spectrum is disregarded, and only the charge carriers at the first quantum-confinement level are considered in the approximation of infinitely high barriers. The parameter S_0 is determined from the condition for the balance of fluxes (3), where the fact that the charge-carrier system is 2D should be taken into account.

On the other hand, formula (4) may be used again for the collision integral; however, the scattering-probability amplitude is now defined as

$$\left|t_{\mathbf{kk'}}^{(2D)}\right|^2 = \frac{1}{S^2}\frac{\hbar^4 k}{m^2}\sigma_r^{(2D)}, \tag{46}$$

and, for the capture probability, we have

$$W_{\mathbf{k}}^{(2D)} = n_i^{(2D)}\upsilon\sigma_r^{(2D)}, \tag{47}$$

where $\upsilon = \hbar k/m$ is the charge-carrier velocity and $n_i^{(2D)}$ is the 2D impurity concentration. In the approximation of $\Gamma \ll E_0$, the resonance scattering occurs only if $k_0 = \sqrt{2mE_0\hbar^2}$ and formula (10) for the resonance-scattering cross section $\sigma_r^{(2D)}$ is replaced by

$$\sigma_r^{(2D)} = \frac{2\pi\Gamma}{k_0}\sigma(\varepsilon_k - E_0). \tag{48}$$

Introducing again the dimensionless variables $y = \varepsilon_{\mathbf{k}}/E_0$ and $y_\perp = \varepsilon_\perp/E_0$ and a parameter $y_0^{(2D)} = \epsilon_0^{(2D)}/E_0$, we obtain the following equation similar to Eq. (15):

$$\frac{\partial f_{1,2}(y, y_\perp)}{\partial y} = \pm A^{(2D)}\frac{\delta(y-1)}{\sqrt{1-y_\perp}}[B^{(2D)} - f_{1,2}(y, y_\perp)] \pm C^{(2D)}\frac{1 - y/y_0}{\sqrt{y - y_\perp}}\Theta(y_0^{(2D)} - y). \tag{49}$$

Here,

$$A^{(2D)} = \frac{2\pi\Gamma}{k_0}\frac{n_i^{(2D)}}{eF}, \tag{50}$$

$$B^{(2D)} = \frac{1}{2\pi}\int_0^1 \frac{f_1(1, y_\perp) + f_2(1, y_\perp)}{\sqrt{y_\perp}\sqrt{1-y_\perp}}dy_\perp. \tag{51}$$

The function of distribution in total energy $f(y)$ for a 2D system is related to $f_1(y, y_\perp)$ and $f_2(y, y_\perp)$ as

$$f^{(2D)}(y) = \frac{1}{2\pi}\int_0^y \frac{f_1(y, y_\perp) + f_2(y, y_\perp)}{\sqrt{y_\perp}\sqrt{y - y_\perp}}dy_\perp. \tag{52}$$

We call attention to distinctions between Eqs. (51) and (18) and between Eqs. (52) and (42); these distinctions are caused by the fact that the spectrum is 2D. The quantity $B^{(2D)}$ specifies the occupancy of the resonance state for a 2D system: $f_r^{(2D)} = B^{(2D)}$. We construct a solution of the kinetic equation by analogy with a 3D system; we express $C^{(2D)}$ in terms of $B^{(2D)}$ using the equation for the balance of fluxes, and we determine the quantity $B^{(2D)}$ itself from the normalization condition; i.e.,

$$n = n_i^{(2D)} f_r + \frac{k_0^2}{2\pi}\int_0^{y_1} f(y)dy. \tag{53}$$

A change in the form of energy dependence of the source affects the form of distribution function for low energies ($y < y_0^{(2D)}$) and the relation between $C^{(2D)}$ and $B^{(2D)}$. As a result, expression (39) is replaced by

$$C^{(2D)} = \frac{1}{2}B^{(2D)}I^{(2D)}(A), \tag{54}$$

where

$$I^{(2D)}(A) = \frac{\int_0^1 \frac{1}{\sqrt{y_1}}[1 - \exp(-2A/\sqrt{1-y_1})]dy_\perp}{\int_{y_0}^1 \frac{1}{\sqrt{y_\perp}}M^{(2D)}(y_0^{(2D)}, y_\perp)[1 - \exp(-A/\sqrt{1-y_\perp})]dy_\perp}, \tag{55}$$

$$M^{(2D)}(y, y_\perp) = 2\sqrt{y - y_\perp}\left(1 - \frac{1}{3}\frac{y}{y_0^{(2D)}} - \frac{2}{3}\frac{y_\perp}{y_0^{(2D)}}\right). \tag{56}$$

Below, we present the following final formulas defining the functions f_1 and f_2:

(i) in the range of $0 < y < y_0^{(2D)}$, we have

$$f_{1,2}(y, y_\perp) = B^{(2D)}\left\{\frac{1}{2}I^{(2D)}(A^{(2D)})[M^{(2D)}(y_0, y_\perp) \pm M^{(2D)}(y, y_\perp)] + 1 - \exp(-A^{(2D)}/\sqrt{1-y_\perp})\right\}; \tag{57}$$

(ii) in the range of $y_0^{(2D)} < y < 1$, we have

$$f_1(y, y_\perp) = B^{(2D)}[I^{(2D)}(A^{(2D)})M^{(2D)}(y_0^{(2D)}, y_\perp) + 1 - \exp(-A^{(2D)}/\sqrt{1-y_\perp})], \tag{58}$$

$$f_2(y, y_\perp) = B^{(2D)}[1 - \exp(-A^{(2D)}/\sqrt{1-y_\perp})]; \tag{59}$$

(iii) in the range of $1 < y < y_1$ ($y_1 = \hbar\omega_o/E_0$), we have

$$f_1(y, y_\perp) = B^{(2D)}[I^{(2D)}(A^{(2D)})M^{(2D)}(y_0^{(2D)}, y_\perp) \times \exp(-A^{(2D)}/\sqrt{1-y_\perp}) + 1 - \exp(-2A^{(2D)}/\sqrt{1-y_\perp})], \tag{60}$$

$$f_2(y, y_\perp) = 0. \tag{61}$$

The function of distribution of charge carriers in the total energy $f^{(2D)}(y)$ and also the distribution functions

for charge carriers with momentum directed along the electric field [$f(y, 0) = f_1(y, 0) + f_2(y, 0)$] and perpendicularly to the field [$f(y, y) = f_1(y, y) + f_2(y, y)$] are shown in Figs. 5 and 6.

The distribution function for charge carriers in reference to the energy of their transverse motion for the particles with total energy $E_0(f(1, y_\perp))$ and $\hbar\omega_o(f(y_1, y_\perp))$ is shown in Fig. 7. In calculations, we used the effective mass of $m = 0.1m_0$ and the QW width of $L = 5$ nm.

By the example of 2D configuration, we verified that the inclusion of the multiplier $(1 - f_\mathbf{k})$ into the collision terms is unimportant for the values of parameters we used. If the occupancy is high, the corresponding corrections are easily taken into account by iteration and result in an extension of the source region in the energy space.

5. DISCUSSION

First of all, we discuss the results obtained here from the standpoint of the feasibility of forming the intracenter population inversion. Figure 8 shows the dependences of the resonance-state occupancy on the electric-field strength for the 2D and 3D configurations.

For a 2D configuration, the occupancy of the resonance states is much higher. This is caused by a decrease in the number of states in the continuous spectrum up to an energy E_0, where the majority of particles are concentrated. Correspondingly, a decrease in the resonance energy brings about an increase in the occupancy of the resonance state.

It is noteworthy that the terahertz lasing by intracenter transitions have been observed for electric-field strengths that exceeded the impurity-breakdown threshold F_{thr} (for Ge, this threshold is on the order of 10 V/cm; in the strained Ge, the threshold is typically even lower due to a decrease in the binding energy of the ground state). Typically, the impurity breakdown is accompanied by current pinching. The simplest model making it possible to adequately describe the behavior of charge carriers under the conditions of impurity breakdown requires that at least two localized states be considered; these are the ground (E_0) and excited (E_1) states.

Following the breakdown of the ground state, the steady-state mode within the pinch is sustained by a typically lower electric-field strength, which ensures a dynamic equilibrium between the impact excitation of charge carriers from the state E_1 and the capture of carriers from the band by this state.

The Monte Carlo method has been used [8] to study in detail the impurity breakdown in *p*-Ge. Calculations were performed for the acceptor concentration of 10^{14} cm^{-3}. A value of 0.05 was obtained for the occupancy of the state E_1 in an electric field with a strength of 30 V/cm; as the field strength increased, the occupancy decreased to a value on the order of 10^{-3} in the fields with a strength higher than 1000 V/cm.

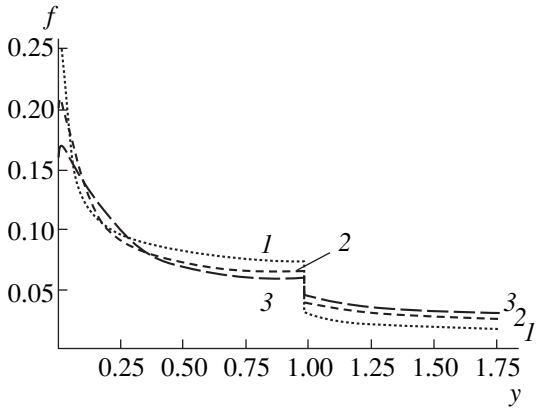

Fig. 5. The energy-distribution functions of charge carriers $f(y)$ in a two-dimensional configuration for the impurity concentration of 10^{11} cm^{-2} and electric-field strengths $F =$ (*1*) 300, (*2*) 1000, and (*3*) 2000 V/cm.

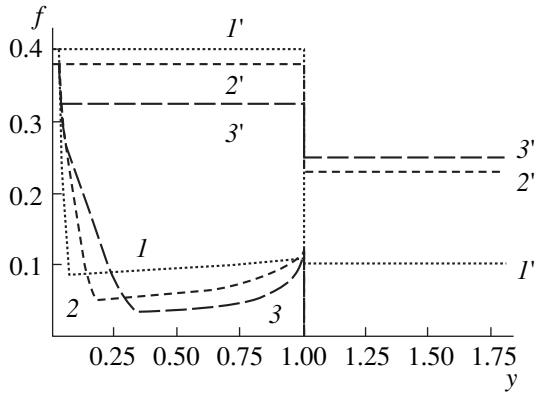

Fig. 6. The distribution functions for charge carriers moving (*1*'–*3*') in the direction along the electric field (the step functions) and (*1*–*3*) in the direction perpendicular to the field for the impurity concentration of 10^{11} cm^{-2} and the electric-field strengths of $F =$ (*1*, *1*') 300, (*2*, *2*') 1000, and (*3*, *3*') 2000 V/cm.

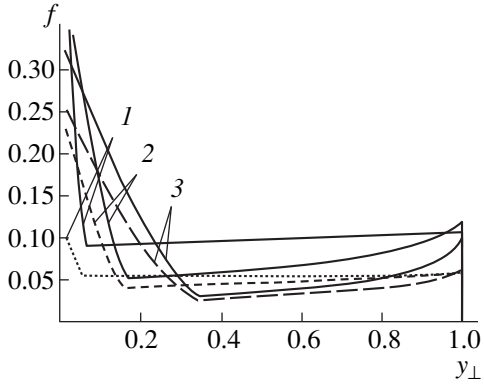

Fig. 7. The energy-distribution functions for charge carriers in a two-dimensional configuration; the carriers move transversely with total energy $E_0 - 0$ (the solid lines) and $\hbar\omega_o - 0$ (the dashed lines) in electric fields with a strength of $F =$ (*1*) 300, (*2*) 1000, and (*3*) 2000 V/cm. The impurity concentration is 10^{11} cm^{-2}.

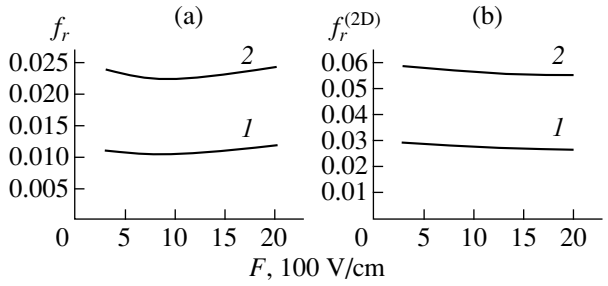

Fig. 8. Dependences of the resonance-state occupancy on the electric-field strength (a) for three-dimensional configuration and the impurity concentration equal to (*1*) 10^{15} and (*2*) 5×10^{15} cm^{-3} and (b) for two-dimensional configuration with the impurity concentration equal to (*1*) 5×10^{10} and (*2*) 10^{11} cm^{-2}.

Thus, we may expect that there is a range of field strengths such that the condition for the intracenter population inversion is satisfied.

Figures 3, 4, 6, and 7 demonstrate a pronounced asymmetry of the distribution function. This function has a conventional streaming-type form in the direction along the electric field, whereas, in the direction perpendicular to the field, it features characteristic peaks in the energy region in the vicinity of E_0. In the 2D configuration, these peaks are more pronounced.

6. CONCLUSION

In this paper, we suggested a method which makes it possible to derive an analytical solution to the kinetic equation for hot charge carriers in the presence of resonance scattering under the conditions of the streaming mode. The method was used to reveal special features of the distribution function for the 2D and 3D charge-carrier systems. We calculated the occupancy of resonance states and showed that it may be as high as 6% in a 2D configuration, which indicates that 2D extrinsic semiconductor structures may have potential in the development of unipolar laser operating at the terahertz frequencies.

ACKNOWLEDGMENTS

We thank V.I. Perel' and A.A. Andronov for their valuable comments and for their participation in discussions.

This study was supported by the Russian Foundation for Basic Research. I.N. Yassievich thanks the Stint Fellowships Programme (contract no. 99/527(00)) for financial support, and A.A. Prokof'ev thanks the Swedish Institute for providing a scholarship according to the grant "The New Wisby Programme."

REFERENCES

1. I. V. Altukhov, E. G. Chirkova, M. S. Kagan, *et al.*, Zh. Éksp. Teor. Fiz. **115**, 89 (1999) [JETP **88**, 51 (1999)].
2. Yu. P. Gousev, I. V. Altukhov, K. A. Korolev, *et al.*, Appl. Phys. Lett. **75**, 757 (1999).
3. M. A. Odnoblyudov, I. N. Yassievich, M. S. Kagan, *et al.*, Phys. Rev. Lett. **83**, 644 (1999).
4. M. A. Odnoblyudov, I. N. Yassievich, V. M. Chistyakov, and K. A. Chao, Phys. Rev. B **62**, 2486 (2000).
5. A. A. Andronov, Fiz. Tekh. Poluprovodn. (Leningrad) **21** (7), 1153 (1987) [Sov. Phys. Semicond. **21**, 701 (1987)].
6. A. A. Andronov, in *Spectroscopy of Nonequilibrium Electrons and Phonons*, Ed. by C. V. Shank and B. P. Zakharchenya (North-Holland, Amsterdam, 1992), Modern Problems in Condensed Matter Science, Vol. 35.
7. L. E. Landau and E. M. Lifshitz, *Course of Theoretical Physics*, Vol. 3: *Quantum Mechanics: Non-Relativistic Theory* (Nauka, Moscow, 1989, 4th ed.; Pergamon, New York, 1977, 3rd ed.).
8. W. Quade, G. Hupper, E. Schöll, and T. Kuhn, Phys. Rev. B **49**, 13408 (1994).

Translated by A. Spitsyn

Semiconductors, Vol. 35, No. 5, 2001, pp. 573–578. Translated from Fizika i Tekhnika Poluprovodnikov, Vol. 35, No. 5, 2001, pp. 594–599.

LOW-DIMENSIONAL SYSTEMS

Electron Transport in Silicon Carbide Natural Superlattices under the Wannier–Stark Quantization Conditions: Basic Issues and Application Prospects

V. I. Sankin* and P. P. Shkrebiĭ

Ioffe Physicotechnical Institute, Russian Academy of Sciences, ul. Politekhnicheskaya 26, St. Petersburg, 194021 Russia

** e-mail: sankin@widegap.ioffe.rssi.ru*

Submitted November 15, 2000; accepted for publication November 16, 2000

Abstract—Hot-electron transport in silicon carbide natural superlattices was investigated. Almost all of the theoretically predicted effects related to the Wannier–Stark localization, such as Bloch oscillations, Stark–phonon resonances, miniband-state localization, and resonance tunneling between the minibands, were observed for the first time. In n^+–n^-–n^+ structures optimized for the measurements at microwave frequencies, the formation of the mobile electric domain was observed in the electric-field range corresponding to the Bloch oscillation conditions; thus, the onset of the microwave oscillations in the 6*H*-SiC natural superlattice can be stated with a high degree of confidence. © *2001 MAIK "Nauka/Interperiodica".*

1. INTRODUCTION

Silicon carbide is a widely known material for high-power high-temperature radiation-resistant electronics. Today, SiC analogues exist for virtually all of the main Si-based devices. However, it seems that a more promising approach is related to the design of the devices utilizing the properties of SiC that are unique among other semiconductors. It is this problem that is the subject of the present study. From this point of view, the existence of SiC polytypes (different modifications of SiC crystals with enlarged unit cell) is of major interest. In most polytypes (with the exception of 3*C*- and 2*H*-SiC), in addition to the basic period equal to the lattice constant, there is an extra period several times (or even several factors of ten) greater than the lattice constant. This additional periodicity was called a natural superlattice (SL). It is of great interest to examine in which way the existence of the natural SL affects the electronic properties of the polytypes. It is well known that, in semiconductors with an SL, the phenomenon of the field-induced localization, or Wannier–Stark localization (WSL) [1], is the subject of investigation. This phenomenon can be described as follows. According to the principles of the quantum mechanics, electrons heated by an electric field and reaching the top of the allowed band experience a Bragg reflection, after which they move in the direction opposite to the field, losing kinetic energy and approaching the bottom of the band; then, the process repeats. Consequently, the electron motion becomes periodic (this is called the Bloch oscillations); thus, the electron spectrum transforms from quasi-continuous to discrete. With an increasing field, the discreteness becomes more pronounced, which means that the degree of electron localization increases. The major consequence of this new crystal state is the appearance of the negative differential conductance (NDC).

Most of the studies of the field-induced localization were carried out for the so-called artificial SLs, in particular, for the GaAs–AlAs heterostructure SLs. However, the experimental data obtained, especially those related to the studies of the quantum transport, cannot be considered unambiguous [2, 3].

In this study, we deal with transport phenomena in strong electric fields, namely, the WSL in natural SLs. The natural SLs have a number of advantages over artificial ones. They are free from the interface imperfections and the fluctuations in the layer thicknesses, which adversely affect the possibility of obtaining the WSL effects in artificial SL structures. This is probably the major reason why many of the WSL effects were experimentally observed for the first time in only the natural SLs of SiC polytypes [4].

Such important effects as NDC, electron–phonon resonance under Wannier–Stark quantization conditions, and resonance tunneling between the adjacent minibands observed in relation to the field-induced localization in natural SLs are the subject of this study. In addition, we report the data demonstrating the influence of WSL on practically important phenomena such as impact ionization and avalanche breakdown.

Along with their basic importance, the results of this study open alluring prospects for a number of possible

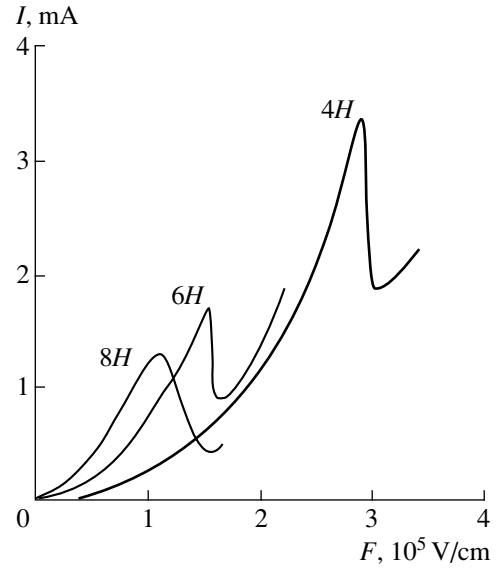

Fig. 1. Current–voltage characteristics of three-terminal structures based on 4*H*-, 6*H*-, and 8*H*-SiC.

applications of natural SLs of SiC polytypes. Here is a list of some of them.

(1) Observation of NDC opens the way for the development of microwave- and THz-range amplifiers and oscillators.

(2) Electron–phonon resonance can be utilized to create the THz-range radiation sources.

(3) Resonance tunneling effect represents a basis for the development of efficient ultrafast high-power switches.

Two types of structures were investigated. For the purpose of practical implementation of microwave oscillations in natural SLs (in addition to bipolar triode structures, which are best suited for DC measurements), SiC unipolar n^+–n^-–n^+ diode and vertical field-effect triode structures were fabricated. These structures satisfy the necessary requirements for the observation of the high-speed processes; unusual features in their current–voltage characteristics in a strong electric field will be also considered.

2. A BIPOLAR n^+–π–n^+ STRUCTURE

The necessity to use three-terminal structures instead of two-terminal ones resulted from the lack of epitaxial SiC layers with low impurity concentrations [4]. In such systems, the current can be controlled without needing to change the electric field. Later, this idea was used in the studies of artificial SLs as well.

To investigate the electron transport under the WSL conditions, an unconventional bipolar triode structure had been designed, which made it possible to satisfy the following requirements:

(1) the current through the sample is purely electronic;

(2) the electric field in the sample is uniform;

(3) the current in the sample can be controlled independently of the field;

(4) the field in the active region is oriented parallel to the SL axis for each of the polytypes examined ($F \parallel C$); and

(5) the current flows through the sample by the injection–transit mechanism.

Operation of this structure was described in detail else where [4]. Here, we consider only a few basic features. The structure consists of three regions: the emitter, the base, and the collector. The base region is the main one. It is composed of the polytype under study doped with a deep-level acceptor impurity (Sc), which results in very low free-hole concentration: $p \approx 10^{10}$ cm^{-3} at 300 K. Thus, the structure type is n^+–π–n^+. It is ensured that the electrons drift through the base of such a structure from the emitter to the collector under the conditions of quasi-uniform pulsed electric field. In this mode, effects in relatively low fields (from 100 to 500 kV/cm), such as Bloch oscillations and saturation of the drift velocity, were observed. In the other mode, the strength of the pulsed field in the base was fixed at a low level (about 50 kV/cm), and a high field of variable strength existed in the collector junction. After traveling through the base, the electrons enter the region of the collector field, whose average strength was varied from 500 to 2500 kV/cm. In this mode, electron–phonon resonances, localization in the first miniband, tunneling between the minibands, and other effects were observed.

3. EXPERIMENTAL RESULTS OBTAINED FOR BIPOLAR THREE-TERMINAL STRUCTURES

3.1. Bloch Oscillations

Figure 1 displays the *I–V* curves obtained for three SiC polytypes (4*H*, 6*H*, and 8*H*). A salient feature of all three curves is the existence of an NDC region. This kind of NDC may result from two distinct mechanisms characterized by considerably different critical fields: electron reflection from the region with negative effective mass and reflection from the miniband edge, or Bloch oscillations. In order to estimate the critical fields, we have to know the scattering times under the strong-field conditions; these were derived from the experimentally determined drift velocities. Comparing the estimated critical-field values with those experimentally measured (equal to 290, 150, and 110 kV/cm), we concluded that the data obtained can be more adequately described in the context of the Bloch oscillation

mechanism. The relationships between the critical fields for different polytypes (see above) qualitatively agree with the ratios between the periods of the corresponding natural SLs.

3.2. Stark–Phonon Resonances

With an increase in the electric field, the region of electron localization eventually becomes smaller than the electron free path length. Then, the current can flow only by the tunneling hopping mechanism, and resonance effects may exist. One such effect occurs when the Stark energy is equal to the phonon energy. It should be noted that such strong fields can be attained only in the collector junction. Electrons, after traveling through the base, enter the collector region, where the highest field can be varied from 600 to 4100 kV/cm; the mean field, whose values are laid off along the horizontal axis in Fig. 2, is twice as low. Experimental data for SiC polytypes 6*H* and 4*H* are given in Figs. 2 (curves *1*–*3*) and 3, respectively. For the same phonon energies, the resonance field values differ significantly for the two polytypes; this is explained by a difference of a factor of 1.5 in the corresponding periods of the natural SL.

3.3. Complete Localization of the Electrons in the First Miniband

According to the theory [5], complete localization of the electrons in the first miniband takes place if the Stark energy exceeds the half-width of the miniband, and the NDC region appears in a wide range of electric fields. We observed this effect in the 6*H*-SiC polytype, which is illustrated by curve *4* in Fig. 2. We note that similar effect in the 4*H* polytype should occur in the field range beyond the breakdown threshold but cannot be observed for this reason. In the 8*H* polytype, and in several others as well, this effect was not observed due to the microplasma breakdown that leads to a significant reduction of the collector-junction field. The observation of this effect enabled us to experimentally determine, for the first time, the width of the first miniband in 6*H*-SiC, which amounted to $E_1 = 256$ meV.

3.4. Tunneling between the Minibands

We now consider curve *5* in Fig. 2. The run of this curve could be ascribed to the electrical breakdown if not for the sharp reduction in the current following the current surge, a feature that is not typical at all of the breakdown *I–V* characteristics. The data can be explained in the following way. The region of a sharp increase in electron current occurs due to the resonance tunneling of electrons from the discrete levels in the first miniband to the second miniband (whose spectrum is still quasi-continuous). The subsequent current drop is probably related to the onset of the Bloch oscillations in the second miniband. In the simplest case, the second

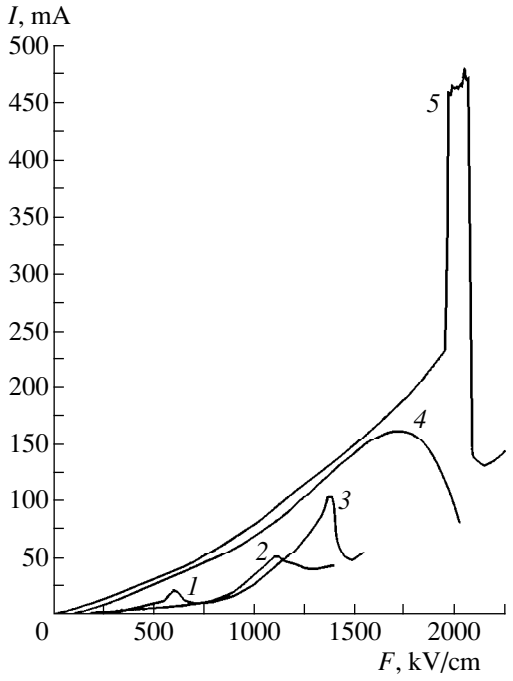

Fig. 2. Resonances resulting from the Wannier–Stark localization in the 6*H*-SiC natural SL and related to: (*1*) hopping assisted by transverse acoustic phonons, 46 meV; (*2*) hopping assisted by longitudinal acoustic phonons, 77 meV; (*3*) hopping assisted by longitudinal optical phonons, 103 meV; (*4*) complete localization in the first miniband; and (*5*) resonance tunneling between the first and the second minibands.

miniband is wider than the first one approximately by a factor of 4; thus, in the field range considered, the spectrum in the second miniband is still quasi-continuous, and the electron Bloch oscillations mechanism can be operative. It is known that interminiband resonance tunneling becomes possible when the Stark energy is equal to the energy gap E_{12} between the minibands.

It is reasonable to assume that the maximum (rather than the average) value of electric field in the space-charge region should be used to characterize the resonance tunneling. Consequently, the Stark energy corresponding to the tunneling between the minibands amounts approximately to 303 meV; this is equal to the sum $E_1/2 + E_{12}$, so that $E_{12} \approx 175$ meV. The sum $E_1 + E_{12} + E_2 \approx 1.46$ eV, which agrees well with the spectral position of the absorption band originating from the transitions between the first and the second minibands [6].

3.5. On the Mechanism of Electron Impact Ionization

Previously, it was established that the electron contribution to the impact ionization is strongly suppressed for $F \parallel C$ [7]. A number of experiments demonstrated that this is an entirely orientation-dependent effect

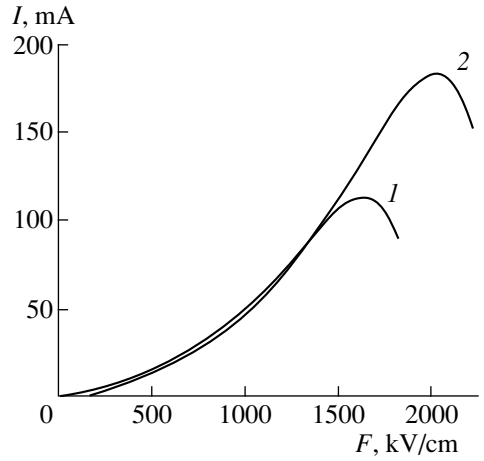

Fig. 3. Stark–phonon resonances in 4*H*-SiC SLs: (*1*) longitudinal acoustic phonons, 77 meV and (*2*) longitudinal optical phonons, 103 meV.

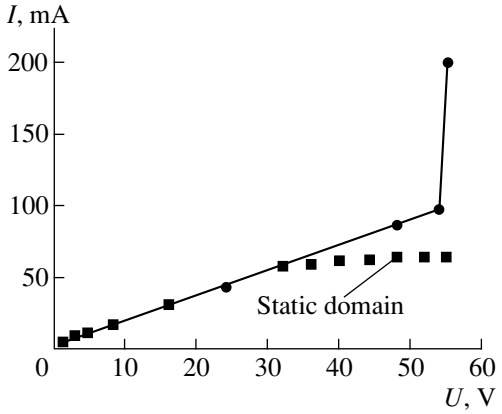

Fig. 4. Current–voltage characteristic of the two-terminal 6*H*-SiC n^+–n^-–n^+ structure with a natural SL.

related to the existence of a natural SL. On the other hand, it was demonstrated that the electron heating does take place in anomalously high fields, exceeding the theoretically predicted value of breakdown field by a factor of 2 [8]. While the issue of the suppression of electron heating in a narrow band was almost completely understood, the mechanism leading to electron heating in the case of a miniband spectrum remained unclarified. Based on the data presented here, we may suggest that electrons can tunnel to the upper miniband (see Fig. 2, curve *5*) and become quasi-free, after which their heating proceeds by the classical mechanism.

4. STUDIES OF THE BLOCH OSCILLATIONS IN 6*H*-SiC TWO-TERMINAL n^+–n^-–n^+ STRUCTURES

The special-purpose structure described in Sections 2 and 3, representing a bipolar transistor with the base of specific design, unfortunately is not suited by its speed characteristics for use in the microwave range. Thus, unipolar n^+–n^-–n^+ diode structures were engineered; their development was made possible by the recent advances in the epitaxial growth of the layers with low concentration of the donor impurities. The n^--type base of these structures has the electron concentration $N_d - N_a$ from 2×10^{15} to 5×10^{16} cm^{-3}, and the two heavily-doped n^+ contact layers are characterized by $N_d - N_a$ from 3×10^{18} to 10^{20} cm^{-3}. The structure was processed into a mesa with the cross-sectional dimensions of 25–40 μm; the base width was 3–5 μm. The *I–V* characteristic for such a structure is shown in Fig. 4. It is linear and exhibits no unusual features up to a certain voltage, where a sharp increase in the current is observed, which is accompanied by the emission of light. The spectrum of this emission coincides with the spectrum of emission observed under the breakdown conditions in *p–n* junctions. It should be noted that the field strength estimated for the case of uniform field distribution does not exceed 150 kV/cm, which is more than an order of magnitude lower than the smallest reported values for the breakdown field in 6*H*-SiC. Probably, the field strength is increased due to the electric-field domain formation in the base region. It is known that such domains can be formed in the crystal under the NDC conditions. As described above, we did observe the NDC at the field of 150 kV/cm, which is related to the Bloch oscillations.

Having adopted the picture of the domain formation, one needs to specify further if the domain is mobile or immobile. The *I–V* curve of Fig. 4 gives an argument in favor of the former possibility. In the case of a static domain, the *I–V* characteristic should contain a leveled-off region, as depicted in Fig. 4.

5. STUDIES OF THE BLOCH OSCILLATIONS IN 6*H*-SiC THREE-TERMINAL n^+–n^-–n^+ STRUCTURES

Another experiment was carried out to obtain more convincing evidence of the supposed electric-field domain formation. For this purpose, we fabricated for the first time a SiC unipolar three-terminal structure forming a static-induction transistor (SIT) with a *p–n* junction gate; it was fabricated from the n^+–n^-–n^+ structure by a special technology. A layout of such a SIT is shown in Fig. 5. The conduction channel with geometric dimensions $40 \times 20 \times 3$ μm, which is similar in design to the diode-type n^+–n^-–n^+ structure considered above, is located between the two regions of the *p–n* junction field. The junction field has a distinct component transverse to the direction of the current flowing in the channel from the source to the drain. For the gate voltage $V_g = 0$, the current–voltage characteristic of such a channel (Fig. 6) is similar to that of the diode structure (Fig. 4). Application of the voltage to the gate

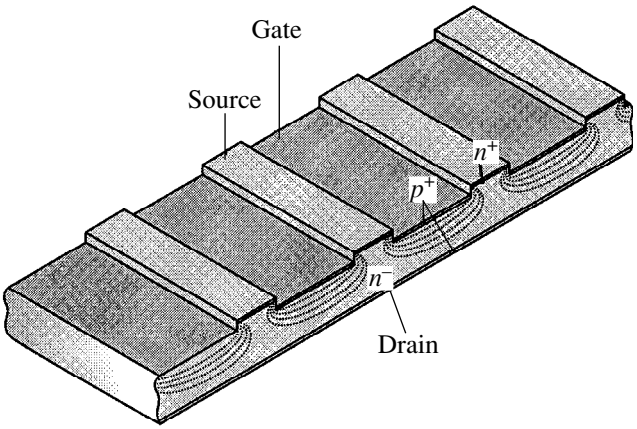

Fig. 5. A layout of the static-induction transistor with the *p–n* junction gate.

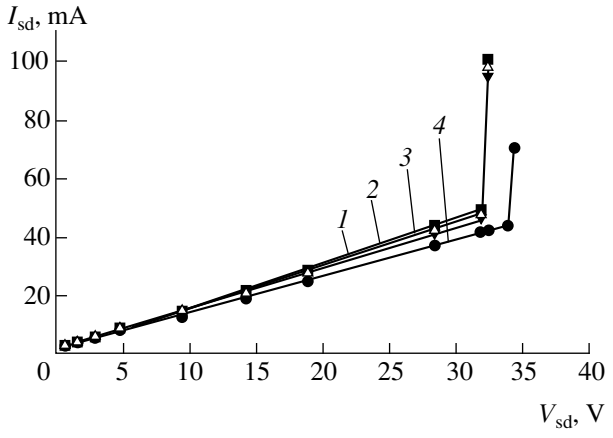

Fig. 6. Current–voltage characteristics of a unipolar vertical three-terminal structure (static-induction transistor) under the gate voltage V_g = (*1*) 0, (*2*) –1, (*3*) –2, and (*4*) –3 V.

has a markedly different effect on the linear and breakdown portions of the *I–V* curve. In the linearity region, a change typical of SIT is observed: the current decreases with the gate field at a rate given by the transconductance S = 2–4 mA/V, which is in agreement with the channel parameters. On the other hand, in the breakdown region, the decrease in the current is characterized by the transconductance S = 40–60 mA/V (see Fig. 6). In the SIT with geometric parameters similar to the parameters of silicon SITs, the values of the transconductance increase nearly 50 times with respect to those just presented. Such a gigantic and sharp drop in the current can be explained by the destruction of the domain under the influence of electric field oriented perpendicularly to the domain field. Obviously, the breakdown is suppressed with the domain destruction, which leads to a sharp reduction in the current. The results obtained also corroborate the assumption of the mobile domain formation: due to the design of the SIT (Fig. 5) under study, the considerable effect of the gate field appears only in the channel region approximately 1 μm from the source; thus, the static domain, which is localized near the source, would remain unaffected.

Unfortunately, this mode of operation is not suited for the detailed investigations of microwave oscillations, since the through current cannot be stabilized and rapid structure degradation takes place. On the other hand, we observed a new effect that is probably no less useful for the applications than the microwave-signal generation. The observed sharp decrease in the large-amplitude current can be used to design fast high-power switching devices. Unfortunately, the structure degradation again hinders the utilization of this effect for practical needs in the immediate future. However, there is a good chance that this difficulty, which is most probably related to the inhomogeneity of the n^--SiC layer, will be eliminated. It is common in material science that such a problem can be resolved after the studies aimed at enhancing the material quality. There is also the possibility that this drawback is specific to the material grown in a certain technological unit; then, material fabricated in other units should be tried. Presumably, the task is not very difficult, taking into account that the scope of investigations in the area of SiC technology becomes ever wider.

6. CONCLUSION

In this paper, we report the results indicating that natural SL in SiC polytypes decisively affects the electron transport in strong electric fields. This is manifested in a number of effects presenting the first strong evidence of the existence of Wannier–Stark localization in crystalline solids. It should be stressed that this was not yet observed in artificial SLs. Furthermore, the results obtained open the way for very interesting and promising developments of SiC devices, which is confirmed by the observation of the electric-field domain formation under the conditions close to the appearance of NDC caused by Bloch oscillations and the domain destruction accompanied by a fast current switching. According to the experimental data, the domain is mobile; thus, there is good reason to believe that the microwave oscillations take place in the crystal. Direct observation of the oscillations will be the subject of the future studies. The effect of the domain destruction resulting in a fast current switching also provides the basis for promising application developments.

ACKNOWLEDGMENTS

This study was supported by the Russian Foundation for Basic Research (project no. 00-02-16943) and the Interdisciplinary Research Program “Physics of the Solid-State Nanostructures” (project no. 97-1038).

REFERENCES

1. G. H. Wannier, Phys. Rev. **11**, 432 (1960).
2. A. Sibille, J. F. Palmier, H. Wong, *et al.*, Phys. Rev. Lett. **64**, 52 (1990).
3. F. Bettram, F. Capasso, D. L. Sivco, *et al.*, Phys. Rev. Lett. **64**, 3167 (1990).
4. V. I. Sankin and I. A. Stolichnov, Fiz. Tekh. Poluprovodn. (St. Petersburg) **31**, 577 (1997) [Semiconductors **31**, 489 (1997)].
5. R. Tsu and G. Dohler, Phys. Rev. B **12**, 680 (1975).
6. G. B. Dubrovskii, A. A. Lepneva, and E. I. Radovanova, Phys. Status Solidi B **57**, 423 (1973).
7. A. P. Dmitriev, A. O. Konstantinov, D. P. Litvin, and V. I. Sankin, Fiz. Tekh. Poluprovodn. (Leningrad) **17**, 1093 (1983) [Sov. Phys. Semicond. **17**, 686 (1983)].
8. V. I. Sankin, Yu. A. Vodakov, and D. P. Litvin, Fiz. Tekh. Poluprovodn. (Leningrad) **18**, 2146 (1984) [Sov. Phys. Semicond. **18**, 1339 (1984)].

Translated by M. Skorikov

Semiconductors, Vol. 35, No. 5, 2001, pp. 579–582. Translated from Fizika i Tekhnika Poluprovodnikov, Vol. 35, No. 5, 2001, pp. 600–603.

AMORPHOUS, VITREOUS, AND POROUS SEMICONDUCTORS

Silicon Network in *a*-Si:H Films Containing Ordered Inclusions

O. A. Golikova*, E. V. Bogdanova*, M. M. Kazanin*, A. N. Kuznetsov*, V. A. Terekhov, V. M. Kashkarov**, and O. V. Ostapenko****

** Ioffe Physicotechnical Institute, Russian Academy of Sciences, Politekhnicheskaya ul. 26, St. Petersburg, 194021 Russia*

*** Voronezh State University, Voronezh, 394026 Russia*

Submitted September 12, 2000; accepted for publication September 14, 2000

Abstract—*a*-Si:H films with inclusions of $(SiH_2)_n$ clusters or Si nanocrystals have been grown by magnetron-assisted SiH_4 decomposition (dc-MASD). The films were characterized by the microstructural parameter R = 0.7–1.0. Ultrasoft X-ray emission spectroscopy was applied to establish the effect of these inclusions on the increasing ordering of Si network. It is shown that, irrespective of the nature of the inclusions, their effect is strongest for films of intrinsic material deposited at high temperatures (up to 400°C). © *2001 MAIK "Nauka/Interperiodica".*

1. INTRODUCTION

It has been reported [1, 2] that dc magnetron-assisted silane decomposition (dc-MASD) yields films of amorphous hydrogenated silicon (*a*-Si:H) containing ordered inclusions of varied nature—$(SiH_2)_n$ clusters (dihydride chains) or Si nanocrystals. When ordered inclusions are formed, one would expect a change in the structure of the amorphous matrix of the films, compared with the "standard" *a*-Si:H and, in particular, in the degree of ordering of the network constituted by silicon atoms. Nevertheless, though being important for the understanding of the reasons for modification of electronic parameters of inhomogeneous amorphous films, a focus of recent attention, the question as to whether these changes do occur has not been considered previously. This study is a step in the direction of obtaining an answer to this question.

2. EXPERIMENTAL PROCEDURE

The technological parameters of the processes employed to deposit *a*-Si:H films containing dihydride chains $(SiH_2)_n$ or nanocrystalline Si inclusions have been reported elsewhere [1, 2].

As an object of study, films containing $(SiH_2)_n$ chains obtained at a deposition temperature T_s varied between 50 and 400°C were examined. The hydrogen content of these films (C_H) ranged from 30 to 8 at. %, respectively. The microstructure parameter R, determined in the conventional way [1], did not vary significantly with T_s, averaging $R \cong 0.7$. This means that a considerable part of hydrogen was present in the amorphous matrix in the form of monohydride complexes SiH. With growing C_H, the optical gap E_g increased from 1.7 to 2.1 eV; however, judging from the activation energies ΔE of electrical conductivity, the Fermi level was always close to $E_g/2$. For example, at T_s = 300°C, the activation energy was 0.85 eV, which corresponds to an "intrinsic" material.

Films with nanocrystalline Si inclusions were deposited at a constant temperature T_s = 390°C. The C_H values for these films were 3–4 at. %, and the R values were close to unity; i.e., practically the entire amount of hydrogen was incorporated in SiH_2 complexes. The films had an energy gap E_g = 1.85 eV, but the activation energies of electrical conductivity ΔE were not the same: both "intrinsic" and "pseudodoped" materials were obtained (ΔE = 0.96 and 0.6–0.7 eV, respectively). This is probably associated with changes in the pressure of the silane–argon mixture (2.5–3.5 mTorr) at T_s = const. It is noteworthy that here ΔE is the activation energy of electrical conductivity at elevated temperatures, when the charge transport is governed by the amorphous phase.

The obtained films were studied by ultrasoft X-ray emission spectroscopy. $L_{2,3}$ spectra of Si furnish information about the partial densities of all filled *s* states in Si, i.e., states lying below the Fermi level, and are highly "sensitive" to changes in the ordering of the Si network [3]. First, the shape of the $L_{2,3}$ spectra related to valence band states changes depending on the degree of network ordering. Second, data on valence band "tails," whose intensity also depends on the degree of network ordering, can be directly obtained from the $L_{2,3}$ spectra. $L_{2,3}$ spectra of Si were measured using an

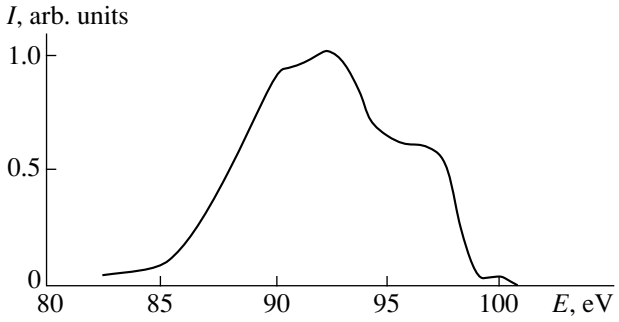

Fig. 1. Si-$L_{2,3}$ spectrum of a "conventional" "intrinsic" *a*-Si:H film deposited at T_s = 350°C.

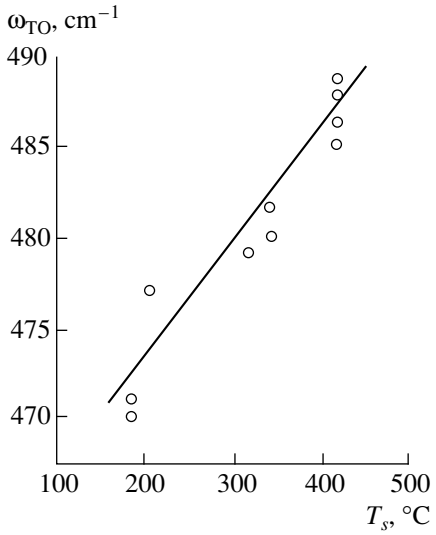

Fig. 2. Raman frequency of transverse optical (TO) phonons, ω_{TO}, in conventional *a*-Si:H vs film deposition temperature T_s.

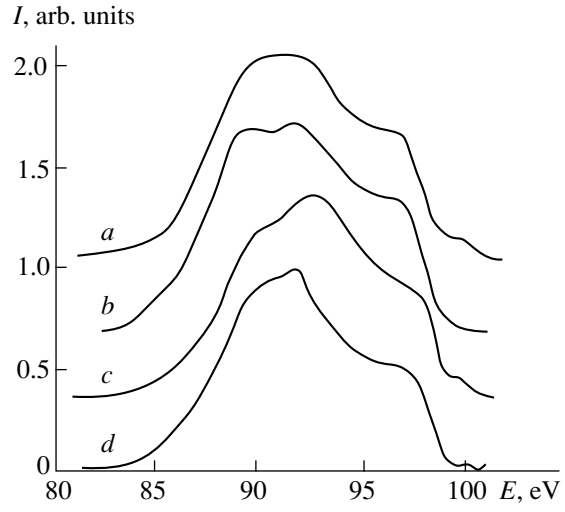

Fig. 3. Si-$L_{2,3}$ spectra of *a*-Si:H films with $(SiH_2)_n$ inclusions, deposited at T_s: (*a*) 50, (*b*) 150, (*c*) 320, and (*d*) 400°C.

RSM-500 spectrometer at an electron energy of 3 keV, corresponding to analysis depth of 50 nm.

Together with performing electrical conductivity (dark conductivity σ_d) measurements, for some films we measured the temperature dependence of photoconductivity (σ_{ph}) at an incident photon energy ε = 2 eV and a carrier generation rate $G = 10^{19}$ cm^{-3} s^{-1}.

3. RESULTS AND DISCUSSION

We studied *a*-Si:H films that contained ordered inclusions of a varied nature and which were deposited both at T_s = var and at T_s = const. Therefore, we first dwell upon the results concerning changes in the degree of network ordering for "conventional" (inclusion-free) *a*-Si:H films. This, in our opinion, will allow a more substantiated judgment about the influence of inclusions.

The ultrasoft X-ray emission spectra taken from *a*-Si:H films deposited at low T_s show a broad main peak at $E_V - E$ = 7–9 eV (E_V is the valence band edge) [3], whereas in the spectra of films deposited at elevated temperatures this peak exhibits a fine structure (Fig. 1). We believe that this occurs because of a certain ordering of the Si network through its thermal relaxation. Raman spectra support this conclusion.

Indeed, as seen in Fig. 2, the Raman frequency of the TO phonon band (ω_{TO}) grows with an increasing T_s. It is known [4] that

$$\omega_{TO} = \omega_0 - c(\Delta\omega_{TO})^2,$$

where ω_0 is the frequency of the TO phonon band in the absence of internal strain in the film, $\Delta\omega_{TO}$ is the half-width of the TO band, and c is a constant. Therefore, an increase in ω_{TO} means that $\Delta\omega_{TO}$ decreases with increasing T_s. The $\Delta\omega_{TO}$ value is a measure of Si–Si bond angle variance: its decrease indicates structural ordering on the short-range order level. However, in all probability, this also leads to a higher degree of network ordering on the medium-range order level, meaning a lower variance of dihedral angles or a higher order in the arrangement of Si tetrahedra [5].

In [5], the peak intensity of the TA phonon band, normalized to the peak intensity of the TO phonon band (I_{TA}/I_{TO}), was used as a parameter characterizing the medium-range order, with a decrease in this parameter indicating Si network ordering on the medium-range order level. It should be noted that at T_s = const, the $\Delta\omega_{TO}$ and I_{TA}/I_{TO} values fall simultaneously, depending on the shift of the Fermi level with respect to the conduction band edge, reaching their minimum values for the intrinsic material [5].

Let us now consider ultrasoft X-ray emission spectra taken for *a*-Si:H films containing $(SiH_2)_n$ chains (Fig. 3). As mentioned in the preceding section, all

these films are nearly "intrinsic." Therefore, any relationship between the obtained results and the Fermi level position is ruled out and only their relationship with the decreasing T_s remains. An analysis of these spectra demonstrated that the spectrum related to valence band states is strongly smoothed at a low deposition temperature T_s = 50°C, and a weakly pronounced structure in the form of 2 peaks appears near the main peak at T_s = 150°C. At T_s = 320°C, the height of the peak closest to the valence band bottom decreases, becoming approximately equal to that in Si crystal [3]. This indicates that a significant network ordering occurs with an increasing T_s. At T_s = 400°C, this effect is preserved but the intensity of the spectrum in the upper part of the valence band ($E_V - E \le 4$ eV) decreases, also indicating an ordering of the silicon atom network.

However, comparing these results with those obtained in studying conventional *a*-Si:H deposited at the same temperatures shows their significant difference (see, e.g., the spectrum in Fig. 1 and spectrum *c* in Fig. 3). Therefore, it may be concluded that the presence of $(SiH_2)_n$ chains makes the Si network more ordered, with this effect appearing at T_s = 150°C and becoming increasingly pronounced with growing T_s. It is noteworthy that the growing T_s also leads to a lower density of states in the valence band tails. Nevertheless, these films are somewhat inferior in photoconductivity to *a*-Si:H films of device quality [1].

Let us consider ultrasoft X-ray emission spectra taken for three films deposited at T_s = 390°C and containing nanocrystalline Si inclusions ($d_{\text{Raman}} \simeq 5$ nm, $X_c \simeq 20\%$): spectra *a*, *b*, and *c* for film 1, 2, and 3 (Fig. 4). These films differ from one another: films 1 and 2 are pseudodoped films and film 3 is intrinsic. The temperature dependences of σ_d in Fig. 5 are similar to those reported in [2]. Despite the high temperature of T_s, the ultrasoft X-ray emission spectra of films 1 and 2 broaden substantially (Fig. 4), resembling spectrum *a* in Fig. 3 for a film that contains $(SiH_2)_n$ clusters and is deposited at T_s = 50°C. For film 3, the ultrasoft X-ray emission spectrum, by contrast, has a pronounced structure resembling spectrum *d* in Fig. 3. Therefore, it may be assumed that the pattern of change in Si network ordering with the position of the Fermi level in the conventional *a*-Si:H at T_s = const [5] is also valid for films containing Si nanoinclusions. Then, the formation of nanoinclusions leads to even stronger ordering of the network in the intrinsic film, exerting no significant influence on the strongly disordered networks of pseudodoped layers. It is noteworthy that this situation is similar to that observed for films containing $(SiH_2)_n$ nanoinclusions. Indeed, these inclusions have no effect on the strongly disordered network of a film deposited at T_s = 50°C (Fig. 3, spectrum *a*).

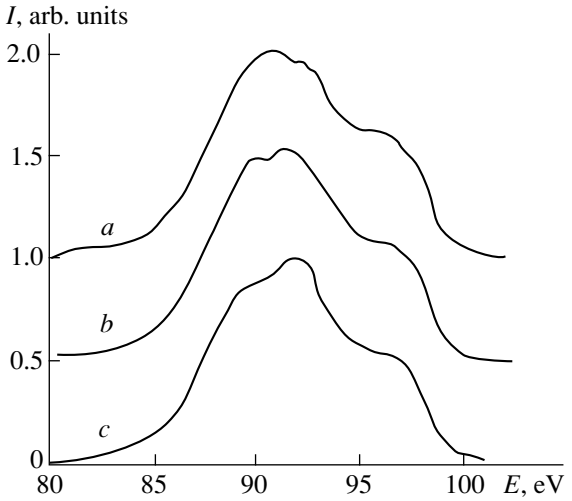

Fig. 4. Si-$L_{2,3}$ spectra of *a*-Si:H films with nanocrystalline Si inclusions, deposited at T_s = 390°C: (*a*, *b*) pseudodoped films 1 and 2, respectively; (*c*) intrinsic film 3.

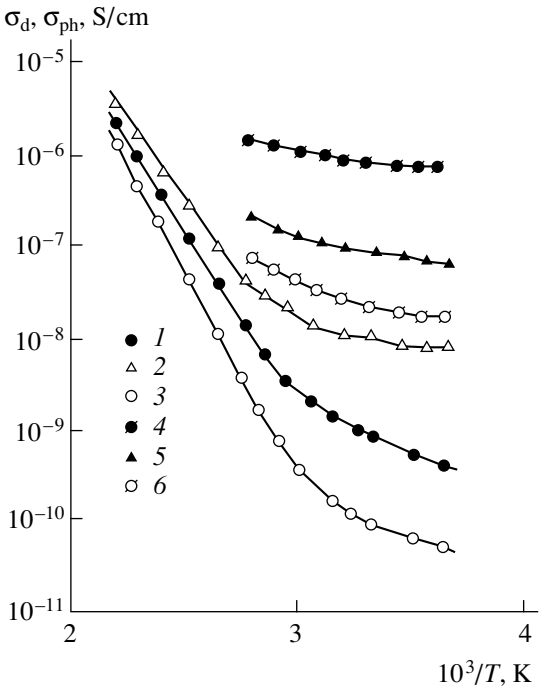

Fig. 5. Temperature dependences of (*1–3*) dark conductivity σ_d and (*4–6*) photoconductivity σ_{ph} of *a*-Si:H films with nanocrystalline Si inclusions: (*1*, *4*) film 1, (*2*, *5*) film 2, and (*3*, *6*) film 3.

The ratio $(\sigma_{ph}/\sigma_d)_{300\text{ K}}$ is 10^3, 10, and 10^2 for films 1, 2, and 3, respectively (Fig. 5). According to [2], this parameter decreases with an increasing contribution to the conductivity from the crystalline phase, depending on how current paths are formed at equal X_c, which in turn depends on the distribution of Si nanoinclusions in

the films. However, no methods for controlling this distribution have been proposed.

4. CONCLUSION

In this study, the effect of ordered inclusions of varied nature in *a*-Si:H films—$(SiH_2)_n$ clusters and Si nanocrystals—on the increasing ordering of the Si network has been established for the first time. The investigations were done by means of ultrasoft X-ray spectroscopy. The obtained experimental results were analyzed with account taken of the effects of thermal relaxation (at T_s = var) and pseudodoping (at T_s = const) on the network ordering. It is shown that, irrespective of the nature of the inclusions, their influence is the strongest for intrinsic films deposited at the highest temperatures.

REFERENCES

1. O. A. Golikova, A. N. Kuznetsov, V. Kh. Kudoyarova, and M. M. Kazanin, Fiz. Tekh. Poluprovodn. (St. Petersburg) **31**, 816 (1997) [Semiconductors **31**, 691 (1997)].
2. O. A. Golikova, M. M. Kazanin, A. N. Kuznetsov, and E. V. Bogdanova, Fiz. Tekh. Poluprovodn. (St. Petersburg) **34** (9), 1125 (2000) [Semiconductors **34**, 1085 (2000)].
3. V. A. Terekhov, Asuthor's Abstract of Candidate's Dissertation (Voronezh, 1994).
4. R. Tsu, J. Non-Cryst. Solids **97/98**, 163 (1987).
5. O. A. Golikova and V. Kh. Kudoyarova, Fiz. Tekh. Poluprovodn. (St. Petersburg) **32**, 876 (1998) [Semiconductors **32**, 779 (1998)].

Translated by M. Tagirdzhanov

Semiconductors, Vol. 35, No. 5, 2001, pp. 583–587. Translated from Fizika i Tekhnika Poluprovodnikov, Vol. 35, No. 5, 2001, pp. 604–608.

AMORPHOUS, VITREOUS, AND POROUS SEMICONDUCTORS

Excitation of Luminescence in Porous Silicon with Adsorbed Ozone Molecules

S. N. Kuznetsov*, V. B. Pikulev, A. A. Saren, Yu. E. Gardin, and V. A. Gurtov

Petrozavodsk State University, Petrozavodsk, 185640 Russia

** e-mail: snkuzn@mainpgu.karelia.ru*

Submitted September 20, 2000; accepted for publication October 26, 2000

Abstract—A new effect of the excitation of luminescence in porous silicon during adsorption of ozone from the gaseous phase was investigated. The signals of ozone-induced luminescence and photoluminescence decay with time of ozone exposure in a strictly correlated way; simultaneously, an oxide-phase growth is observed in porous silicon. A linear relationship was found between the luminescence intensity and the amount of oxide phase formed in the presence of ozone. Correlated shifts in the spectra of ozone-induced luminescence and photoluminescence are observed if the porosity of silicon varies. A mechanism for this effect is proposed. According to this mechanism, in the case of the dissociative adsorption of ozone, the exothermic reaction of oxidation of backbonds of a silicon atom takes place on the surface of nanocrystallites. Energy released is spent for the excitation of electron spectrum of silicon crystallites. The radiative relaxation in the case of ozone excitation proceeds similarly to that of the photon excitation of luminescence in porous silicon. © *2001 MAIK "Nauka/Interperiodica".*

INTRODUCTION

The investigation of optical luminescence in porous silicon (por-Si) began with using photon excitation, i.e., photoluminescence (PL) [1], in which case nonequilibrium electron–hole pairs or excitons are generated when photons are absorbed in por-Si nanodimensional fragments. Thereafter, two varieties of the injection method for supplying excess charge carriers of opposite signs in silicon nanocrystallites were invoked from solid [2] and electrolytic [3] contacts to porous silicon. The above ways of generating an excited state in crystallites are basically similar, because they lead to a nonequilibrium population of the electron-state spectrum by charge carriers.

In our study [4], we pioneered in discovering an unconventional method of excitation of por-Si luminescence using the adsorption of ozone from the gaseous phase. It is noteworthy that, in our previous paper [5], we reported the excitation of por-Si luminescence using a corona discharge in air; however, this was interpreted at that time as the manifestation of the injection mechanism of excitation. At the first stage of studying the new effect, the following essential features of the process remained unclarified: (1) the possible role of the classical chemiluminescence mechanism proceeding in the case of excitation and radiative relaxation of atomic-scale local centers, and (2) an excitation-energy source of the ozone-induced radiation. The results of this study deal with these problems confirming the quantum-size model [1] of optical luminescence in por-Si, which prevails in relevant publications. The data obtained are indicative of the collective character of the luminescence process in por-Si nanocrystallites under ozone excitation; therefore, it should be more justified to call the investigated effect adsorboluminescence.

EXPERIMENTAL

Our samples were prepared on polished crystalline *p*-Si substrates [1 Ω cm, (100) face] and *n*-Si [0.3 Ω cm, (111) face]. The substrates were anodized in a mixture of $HF : H_2O : C_2H_5OH = 1 : 1 : 2$ in the galvanostatic mode and under illumination with a halogen lamp. The substrates were etched for several minutes with a current density of 25 and 100 mA/cm^2 for *p*-Si and *n*-Si, respectively. Immediately after forming, the por-Si samples were transferred into a vacuum chamber, in which the photo-induced and ozone-induced luminescence was measured. The elimination of rinsing and the use of high-rate vacuum drying minimized the oxidation of the por-Si layer. The thickness of the layers was ~10 μm for a porosity higher than 70%.

The PL spectra were measured at a pressure of ~1 Pa and the excitation in a narrow photon-energy range near $h\nu \approx 4$ eV with a power of ~1 mW/cm^2. We used the automated grating spectrometer in the photon counting mode; the spectra were corrected for spectrometer sensitivity.

The adsorboluminescence spectra of por-Si were detected in the flux of the ozone–oxygen mixture at a pressure of ~100 Pa. Ozone was generated in flowing gas reactors of two types in an atmosphere of pure oxygen (99.9%). In the first reactor, ozone was produced by ultraviolet radiation from a deuterium lamp. The efficiency of ozone generation amounted to several percent. In the other setup, a high-frequency discharge

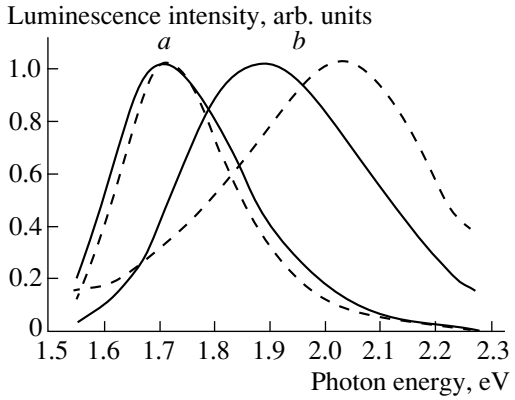

Fig. 1. Normalized spectra of adsorboluminescence (solid lines) and photoluminescence (dashed lines) for por-Si samples on *p*-Si with various porosities: (*a*) original porosity (~70%); and (*b*) enhanced porosity as a result of additional etching (~80%).

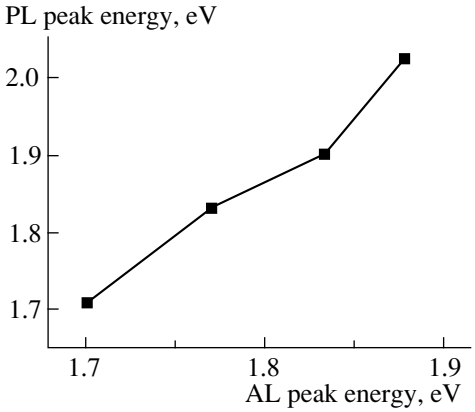

Fig. 2. Correlation between peak energies in the spectra of adsorboluminescence (AL) and photoluminescence (PL) for por-Si samples with a porosity in the range of 70–85%.

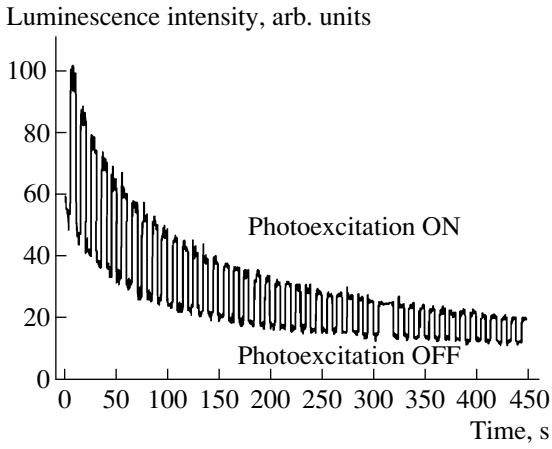

Fig. 3. Kinetics of the luminescence response in a por-Si layer on *n*-Si for continuous exposure to ozone and the modulated photoexcitation. The depth of modulation is 100%; the integral detection of the response is in the wavelength range of 600–850 nm.

with inductive coupling was used. This type of reactor made it possible to also obtain atomic fluxes of other gases (hydrogen and nitrogen).

We studied the correlation between the intensities of PL and adsorboluminescence signals using our installation for measuring the PL-excitation spectra described in detail elsewhere [6]. A luminescence signal was detected in the wavelength range of 600–850 nm. In this case, the flow of ozonized dry air was at atmospheric pressure.

Relative variations in the concentrations of hydride and oxide complexes of silicon in por-Si layers were observed by the infrared (IR) transmission of samples using a Specord M-80 two-beam spectrophotometer and a substrate without the por-Si layer placed in the channel of comparison. In this study, the experimental data were obtained at room temperature.

RESULTS

The intensity of adsorboluminescence signal depends directly on the ozone-molecule concentration. At a high concentration, the signal varies burstlike with exposition time; the kinetics of decay of intensity is close to exponential for a low concentration of ozone. Furthermore, the adsorboluminescence signal is controlled by the original state of the por-Si layer: it is lower for an oxidized surface. Therefore, the correct measurement of the adsorboluminescence spectrum is possible for an as-prepared sample (in our case, the IR-measurement data show no oxide phase) at low ozone pressure. In Fig. 1, we display the normalized spectra of adsorboluminescence and PL of different-porosity por-Si layers on *p*-Si. Case *b* corresponds to a higher porosity of the sample than case *a*; this porosity was attained by additional photoetching of the original sample in forming the electrolyte with a floating potential across the substrate. It can be seen that the luminescence bands virtually coincide for less porous layers; for highly porous layers, the PL spectrum is shifted to shorter wavelengths and is broadened compared to the adsorboluminescence band. In Fig. 2, the tendency for positions of the peaks to diverge with increasing porosity is shown in more detail. It is important to stress that the shift of the PL band to shorter wavelengths with an increase in the layer porosity is accompanied by a steady shift of the adsorboluminescence spectrum in the same direction, which suggests a close relation between both processes.

In addition to the spectral correlation, the quantitative relationship between the adsorboluminescence and PL intensities is observed when the efficiency of emission from the same por-Si sample varies. The indicated relation was obtained for the simultaneous excitation of por-Si luminescence by photons and ozone molecules, with the ozone action leading to a steady degradation of luminescence properties, as was noted above. The 100% modulation of the exciting photos flux enables us

to single out the luminescence responses from both actions in one run of the same experiment. In Fig. 3, the time dependence of the luminescence response from a porous layer on *n*-Si in the case of combined excitation is shown. The relationship between both components of the luminescence signal is shown in Fig. 4. It can be seen that the correlation of the photoluminescence and adsorboluminescence intensities is quasi-linear and it is valid when the components vary almost by an order of magnitude.

An adsorboluminescence-signal decay observed in the case of ozone adsorption is indicative of the accumulation of irreversible changes in the por-Si layer. The character of these changes is associated with the process of oxidation of the layer. The qualitative observations of the adsorboluminescence-signal kinetics in the ozone atmosphere with an addition of HF gives a direct confirmation: the decay rate reduces abruptly in the presence of an oxide etchant. Moreover, there is a qualitative relationship between the illumination flux and the amount of the oxide phase formed in the presence of ozone. The ratio between these quantities was determined by measuring the adsorboluminescence kinetics interrupted periodically for detecting the IR absorption in the range of 1000–1200 cm^{-1}. The absorption of por-Si in this band is governed by the concentration of the Si–O–Si bonds [7]. In the case of oxidation in ozone, the band peak is at ~1070 cm^{-1}, and its height can serve as a measure of the oxide-phase amount. The adsorboluminescence flux emitted for the time of ozone action is found by integrating the adsorboluminescence signal intensity with respect to time. The results of measurements carried out for the por-Si layers on *n*-Si and *p*-Si are shown in Fig. 5. We may conclude that the results correspond satisfactorily to the linear dependence between the indicated quantities. In other words, the number of photons emitted in the presence of ozone is proportional to the number of Si–O–Si bonds formed in the por-Si layer.

On the other hand, the data in Fig. 4 indicate that the PL intensity decreases as irreversible modifications accumulate in por-Si as a result of the adsorption of ozone; i.e., the PL quantum efficiency reduces when the oxide phase is formed. The form of this dependence can be established in much the same way it was done in the previous case; however, here we control only the intensity of the PL component of the total luminescence signal. For convenience in the following discussion, the data obtained are shown in Fig. 6 in intensity–inverse-absorption coordinates for both types of substrates. Thus, the PL efficiency of por-Si decreases with an increase in the number of siloxane bridges generated by ozone according to the hyperbolic law. We note that a similar relation is valid for the adsorboluminescence intensity by virtue of its proportionality to the PL signal (Fig. 4). This conclusion does not contradict the data in Fig. 5, as is shown below.

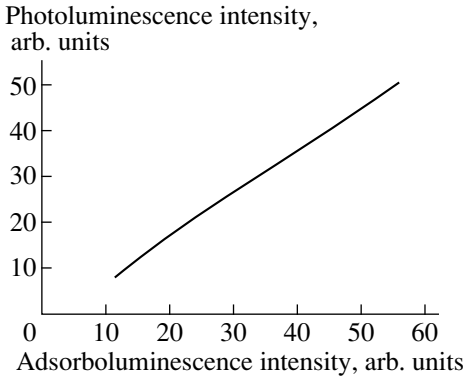

Fig. 4. Correlation between the integrated intensities of adsorboluminescence and photoluminescence in the case of combined excitation of por-Si (from data in Fig. 3).

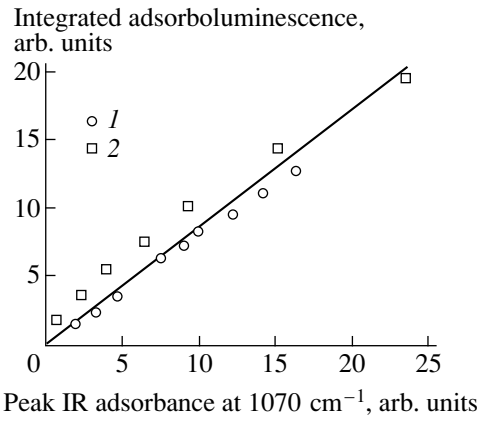

Fig. 5. Dependence of the light flux emitted in the case of adsorboluminescence of por-Si on the amplitude of IR absorption in the band corresponding to the Si–O–Si bonds formed by the ozone action: (*1*) *p*-Si and (*2*) *n*-Si.

DISCUSSION

The mechanism of luminescence in porous silicon with the ozone-molecule adsorption is explained by addressing two key questions.

(1) What reaction supplies the energy necessary for emitting the photons of the optical spectrum? It is evident that the nature of adsorbents and adsorbates point to the process of silicon oxidation. From Fig. 1, it follows that the exothermic reaction energy yield must be comparable to a photon's highest energy of ~2.0 eV observed in the adsorboluminescence spectrum. The data on the energy of the Si–Si bonds (1.8 eV) and the Si–O bonds (3.8 eV) (taken from [8]) testify that the indicated condition is met. From this point of view, the process of oxidation of the end Si–H_n groups passivating the por-Si surface in the as-prepared sample (a binding energy of 3.1 eV) is less probable. In fact, our observations of the IR absorption in por-Si layers show, in the case of ozone adsorption, that an increase in the siloxane-bridge concentration is accompanied by

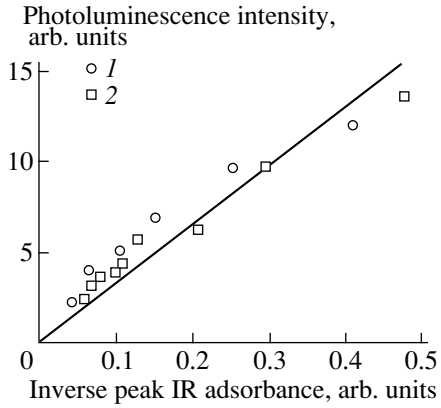

Fig. 6. Dependence of the photoluminescence intensity in por-Si on the inverse magnitude of the IR absorption in the band of the Si–O–Si bonds formed by the ozone action: (*1*) *p*-Si and (*2*) *n*-Si.

the appearance of increasing absorption by the O_3–Si–H (2250 cm^{-1}) and O_2–Si–H (2190 cm^{-1}) complexes with a simultaneous decrease in the absorption in the Si–H_n band (2087, 2114, and 2140 cm^{-1}). This means that ozone virtually does not break the hydride bonds (for the exposure doses studied by us) but induces the oxidation of backbonds in Si surface atoms with a nanocrystallite volume in the por-Si matrix [9]. The activation energy for oxidizing the por-Si backbonds is high and amounts to 1.2 eV [10], which is less than the enthalpy of ozone-molecule formation equal to 1.5 eV. If we compare these values, the special role of ozone in the adsorboluminescence effect becomes clear. At the first stage, ozone is adsorbed on a por-Si surface with the following dissociation of a metastable molecule and formation of an oxygen atom in the excited state: $O_{3ads} \longrightarrow O_2 + O^*$. From a dissociated ozone molecule, atomic oxygen acquires an energy of ~1.5 eV, sufficient for overcoming the activation barrier of 1.2 eV in the reaction of backbond oxidation. At the second stage, an oxygen atom closes the dangling Si–Si bond, thus forming the siloxane bridge Si–O–Si with an energy gain of ~2 eV. With a certain probability, the energy released can be spent for excitation of luminescence in the por-Si layer.

(2) Does the event of luminescence-photon radiation occur at the local (atomic) level or on a collective scale (i.e., realized via an intermediate stage of excitation of the electron system of an atomic ensemble)? In other words, we have an alternative: intracenter luminescence or radiative band-to-band recombination in the excited electron system of silicon crystalline nanofragments in por-Si.

For intracenter luminescence, a radiation spectrum with a small half-width is characteristic: for example, in the PL of unbounding silicon–oxygen centers $O_3{\equiv}Si{-}O^{\bullet}$ in amorphous SiO_2(NBOHC), this value is smaller than 0.2 eV. On the contrary, our data show a considerable width of the adsorboluminescence spectrum comparable to the corresponding width of the PL-spectrum band.

Even more indicative is the correlation between the adsorboluminescence and PL peaks when the por-Si porosity is varied (Fig. 2). This fact has a convincing explanation in the quantum-confinement model of visible-region luminescence in por-Si [1] under the assumption that the oxidation-reaction energy for the Si-crystallite surface in ozone excites the radiative transitions in these crystallites. A long-wavelength shift of the adsorboluminescence band with respect to the PL band can be assigned to the thickness nonuniformity of the investigated por-Si layers. The por-Si layers are characterized by a certain gradient of porosity, because the upper part of the layer is etched stronger in forming, especially the in the photoinduced one. Nanocrystallites with a larger characteristic size than those lying near the surface are located closer to the inner boundary. In our case, the PL was excited by ultraviolet-radiation photons, and the PL response was formed by the outer area of the por-Si layer. It is evident that the degree of deviation of the PL spectrum from the adsorboluminescence spectrum is higher the greater the porosity gradient is in the object under investigation.

In the quantum-confinement concept of optical luminescence in por-Si, the problem of the competing nonradiative process of recombination is of great significance owing to its masking role. On the basis of the published results of investigating por-Si by the method of electron spin resonance, the most probable defects generated during the oxidation of a por-Si layer are the so-called P_b centers [11, 12]. A P_b center represents a dangling bond of a surface silicon atom at the Si–SiO_2 boundary. It is known that this defect can exhibit the electrical activity as the center of capture and (or) recombination for charge carriers. We may assume that, under the conditions of forced oxidation of the Si-nanocrystallite surface by ozone, the P_b-centers are formed more efficiently than under the thermal oxidation of silicon or aging in air. As a result, the efficiency of nonradiative recombination of charge carriers increases abruptly, while the luminescence efficiency of the ozone-treated por-Si layer decreases (Fig. 3). However, this fact refers both to the PL response and to the adsorboluminescence signal by virtue of the strict correlation found between them (Fig. 4). Thus, the final phase of this effect of adsorboluminescence in por-Si under the action of ozone proceeds by a mechanism identical to that of the PL.

In conclusion, we discuss the found photon flux emitted in the adsorboluminescence and the PL intensity in relation to the amount of oxide phase produced by ozone in por-Si (Figs. 5, 6). On the one hand, the quantum efficiency of adsorboluminescence, i.e., the number of emitted photons in the case of forming a single siloxane bridge, is independent of the degree of oxidation of the por-Si layer. On the other hand, the PL

intensity (and, consequently, the adsorboluminescence intensity, due to the linear relation between them, see Fig. 4) is inversely proportional to the degree of oxidation. Is there a contradiction between these observations? A simple calculation shows that this situation is possible if the oxide phase grows with time t as $t^{1/2}$, which is characteristic of the diffusion-limited processes. We take into account that, for Si crystallites of nanometer size, the surface-to-volume ratio is rather large. If only one nonradiative defect (of the P_b-center type) is formed on the cluster surface, the probability of the radiative relaxation in it becomes negligible. We may assume that, in the case of adsorption, the ozone molecules diffuse deep into the por-Si layer and react consecutively with the defect-free crystallites and a single photon is generated in every formation of a siloxane bridge. The number of degraded crystallites increases as the diffusion front propagates, which leads to a reduction in the PL and adsorboluminescence intensities.

CONCLUSION

We studied systematically new effect in porous silicon; this effect consists in the excitation of luminescence under the adsorption of ozone molecules from the gaseous phase. We studied the spectral, kinetic, and infrared spectroscopic characteristics of the process. It was established that the source of excitation for the visible radiation in por-Si is the exothermic reaction of oxidation accompanying the dissociation of ozone admolecules. On the basis of the obtained correlations between the photoluminescence and adsorboluminescence characteristics of por-Si layers, a conclusion was made about the unified mechanism of radiative relaxation of excited state in a system of nanometer silicon crystallites.

REFERENCES

1. L. T. Canham, Appl. Phys. Lett. **57**, 1046 (1990).
2. N. Koshida and H. Koyama, Appl. Phys. Lett. **60**, 347 (1992).
3. A. Halimaoui, C. Oules, G. Bromchil, *et al.*, Appl. Phys. Lett. **59**, 304 (1991).
4. S. N. Kuznetsov, V. B. Pikulev, A. N. Skorokhodov, *et al.*, Appl. Surf. Sci. **140**, 239 (1999).
5. S. N. Kuznetsov, V. B. Pikulev, I. V. Klimov, *et al.*, Phys. Rev. B **51**, 1601 (1995).
6. V. B. Pikulev, S. N. Kuznetsov, Yu. E. Gardin, and V. A. Gurtov, J. Porous Mater. **7**, 253 (2000).
7. J. E. Olsen and F. Shimura, J. Appl. Phys. **66**, 1353 (1989).
8. P. O'Keeffe, S. Komuro, T. Morikawa, and Y. Aoyagi, J. Non-Cryst. Solids **198–200**, 969 (1996).
9. Y. Yasuda, H. Ikeda, and S. Zaima, Appl. Surf. Sci. **113–114**, 579 (1997).
10. J. Salonen, V.-P. Lehto, and E. Laine, Appl. Phys. Lett. **70**, 637 (1997).
11. B. Pivac, B. Rakvin, and L. Pavesi, Appl. Phys. Lett. **65**, 3260 (1994).
12. P. K. Kashkarov, E. A. Konstantinova, and V. Yu. Timoshenko, Fiz. Tekh. Poluprovodn. (St. Petersburg) **30**, 1479 (1996) [Semiconductors **30**, 778 (1996)].

Translated by V. Bukhanov

Semiconductors, Vol. 35, No. 5, 2001, pp. 588–590. Translated from Fizika i Tekhnika Poluprovodnikov, Vol. 35, No. 5, 2001, pp. 609–611.

AMORPHOUS, VITREOUS, AND POROUS SEMICONDUCTORS

Drift Mobility of Carriers in Porous Silicon

N. S. Averkiev, L. P. Kazakova*, É. A. Lebedev, and N. N. Smirnova

Ioffe Physicotechnical Institute, Russian Academy of Sciences, Politekhnichiskaya ul. 26, St. Petersburg, 194021 Russia

** e-mail: kazakova@pop.ioffe.rssi.ru*

Submitted November 3, 2000; accepted for publication November 4, 2000

Abstract—The drift mobility of carriers in porous silicon has been studied in a wide temperature range (190–360 K) at electric field strengths of 2×10^3–3×10^4 V/cm. An exponential temperature dependence of the hole drift mobility with an activation energy of $d \sim 0.14$ eV was established. The density of localized states controlling the transport is evaluated. © *2001 MAIK "Nauka/Interperiodica".*

The optical and photoelectric properties of porous silicon have been extensively studied in view of the prospects for practical use of this material. Much less attention has been given to the carrier transport, despite the fact that the information about the electron and hole mobilities and the energy spectrum of localized states is important for the understanding of various properties of porous Si and, in particular, the mechanism of electroluminescence [1–5].

In this study, we analyzed the drift mobility of carriers in porous Si in a wide range of temperatures (T = 190–360 K) and electric field strengths ($F = 2 \times 10^3$–3×10^4 V/cm).

The drift mobility was studied by the time-of-flight technique [6]. The excess concentration of carriers in a sample was created by a pulse of light with a wavelength of 0.337 μm and duration of ~8 ns generated by an LGI-21 nitrogen laser. A voltage pulse of duration ~1 ms was applied to the sample with a delay of ~100 μs between the instants of application of voltage and light. The measurements were done in the strong injection regime, when the influence of the electric field of the drifting carrier packet could not be neglected. The time constant of the input circuit of the amplifier was much shorter than the transit time.

Porous silicon layers of thickness $L \approx 10$ μm were grown electrochemically on a polished surface of *p*-type silicon with resistivity of 2–7 Ω cm. The samples studied had a "sandwich" structure. Crystalline silicon served as one electrode, and a semitransparent aluminum film vacuum-deposited onto porous Si served as the other. The sample resistance was 10^9–10^{10} Ω, with top electrode area of $(3–7) \times 10^{-2}$ cm^2.

Figure 1 presents oscillograms of photocurrent pulses observed in hole drift. The drift of electrons could not be observed because of the small signal amplitude.

As can be seen from Fig. 1, the shape of the obtained oscillograms of the transient current $I(t)$ is typical of a space-charge-limited current (SCLC) [7]. The dependences $I(t)$ are characterized by the initial (I_0) and peak (I_m) currents. The time t_m corresponding to the current peak was inversely proportional to the voltage applied to the sample. The I_0 and I_m values increased with voltage by a nearly quadratic law $I \propto U^2$. The signal amplitude was independent of the injecting light intensity.

The hole drift mobility μ_h was determined in two ways. In the first case, the drift mobility was calculated using the formula

$$\mu_h = L^2/t_T U, \quad (1)$$

where t_T is carrier transit time under conditions of weak injection related to t_m by $t_m = 0.8t_T$ [7]. The drift mobility of holes obtained by this method was $\sim 6.5 \times 10^{-3}$ cm^2/(V s) at T = 290 K and $F = 10^4$ V/cm.

In the second case, the mobility was determined using the expression for the density of the initial photocurrent under SCLC conditions [7]:

$$j_0[\text{A/cm}^2] = I_0/S = \mu_h \varepsilon U^2/(2.25 \times 10^{13} L^3), \quad (2)$$

where ε is the dielectric constant. Previously, a value of ε = 4.8 was obtained for PS in [3]. With this value, formula (2) yielded a hole mobility $\mu_h = 7.4 \times 10^{-3}$ cm^2/(V s), which practically coincides with the μ_h value calculated from the transit time by means of formula (1).

These μ_h values were close to those obtained in [4] on porous Si samples fabricated by the anodization method in a regime not strongly different from that used in the present work.

The investigations demonstrated that the μ_h value is independent of the electric field strength in the range 10^3–10^4 V/cm.

We also studied the temperature dependence of the drift mobility in the interval T = 190–360 K. The measurements were done in a vacuum chamber with residual pressure of ~10^{-2} Torr. Under the conditions of a vacuum, the room-temperature drift mobility decreased 3- to 4-fold. On performing several cycles of sample

heating–cooling, the hole mobility increased, tending to a constant value $\mu_h = 10^{-1}$ cm^2/(V s). It was found that this stable value is thermally activated

$$\mu = A\exp\left(-\frac{E_a}{kT}\right), \quad (3)$$

where $E_a \cong 0.14$ eV (Fig. 2). The crosses in Fig. 2 represent μ_h values obtained at the reverse temperature run.

It should be noted that the mobility determined in porous Si is low, which is characteristic of substances with disordered structure and carrier transport commonly controlled by trapping into localized states. Mention of the analogy between the electrical properties of these materials was made in [8]. These facts suggest a similarity between the mechanisms of carrier transport in porous Si and substances with disordered structure. Thus, the activation energy of drift mobility in porous Si can be related to the energy position of traps controlling the carrier transport.

The assumption we made is confirmed by an estimate of the preexponential factor ($A \approx 50$ cm^2/(V s)) obtained from formula (3) using the experimentally established values of mobility and its activation energy. It is known [9] that such a value of the preexponential factor indicates a carrier transport controlled by trapping into localized states. In this case, with a discrete level of localized states present, the mobility is described by

$$\mu = \mu_0\frac{N_c}{N_t}\exp\left(-\frac{E_a}{kT}\right), \quad (4)$$

where μ_0 is the carrier mobility in extended states and N_c and N_t are the effective density of states in the allowed band and density of localized states, respectively.

Recently, a temperature-independent electron mobility $\mu \approx 2$–4 cm^2/(V s) has been found [4]. This fact suggests that the carrier mobility at the allowed band edge in porous silicon is $\mu_0 \approx 1$ cm^2/(V s). If this μ_0 value is used in formula (4) and $N_c = 10^{19}$ cm^{-3} is taken, then the concentration of localized states can be estimated at $N_t = 2 \times 10^{17}$ cm^{-3}.

It follows from the obtained data that multiple cycles of heating–cooling in a vacuum markedly affect the drift mobility of carriers and its activation energy. These changes can be attributed to a strong interaction of atmospheric oxygen with the surface of porous silicon. This assumption is confirmed, e.g., by the results obtained in [10, 11].

Thus, the following results were obtained in studying the drift mobility in porous Si:

(i) the drift mobility of holes $\mu_0 = (6.5$–$7.4) \times 10^{-3}$ cm^2/(V s) at $T = 290$ K and $F = 10^4$ V/cm;

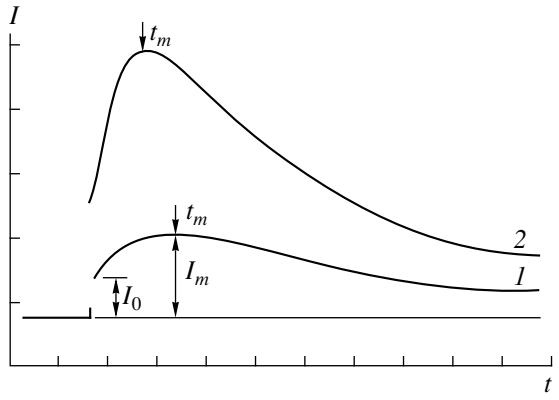

Fig. 1. Oscillograms of transient photocurrent $I(t)$ corresponding to drift of holes in a 10-μm-thick porous Si layer. Voltage U: (*1*) 3 and (*2*) 6 V. Scale: abscissa, 20 μs/div; ordinate, 0.4 μA/div.

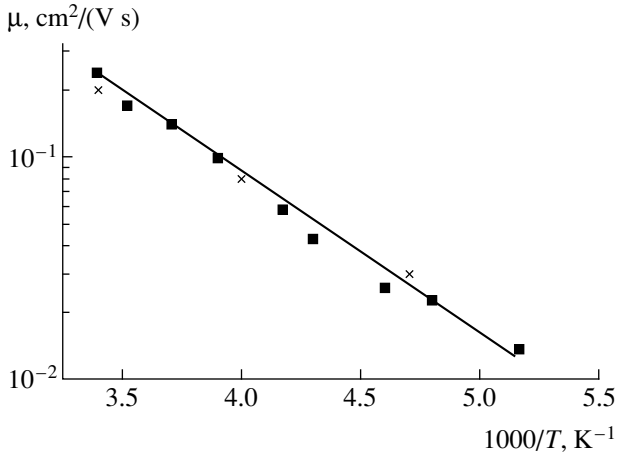

Fig. 2. Arrhenius plot of the drift mobility of holes at $L = 10$ μm and $F = 5 \times 10^3$ V/cm. The crosses correspond to the reverse run of the temperature.

(ii) μ_0 is practically independent of the electric field in the range $F = 2 \times 10^3$–3×10^4 V/cm;

(iii) the drift mobility shows an exponential temperature dependence with activation energy of ~0.14 eV;

(iv) multiple sample heating–cooling cycles strongly affect the drift mobility and its activation energy;

(v) the mechanism of drift mobility can be understood in terms of the model of carrier transport controlled by carrier trapping into localized states;

(vi) the density of localized states controlling the mobility was evaluated.

ACKNOWLEDGMENTS

We thank P.S. Yakovlev for his help in experimental data processing.

The study was supported by the Program of the Ministry of Science of the Russian Federation "Physics of Solid-State Nanostructures" (project nos. 97-1039 and 99-1107).

REFERENCES

1. O. Klima, P. Hlinomaz, A. Hospodkova, *et al.*, J. Non-Cryst. Solids **162–164**, 961 (1993).
2. É. A. Lebedev, G. Polisskiĭ, and V. Petrova-Koch, Fiz. Tekh. Poluprovodn. (St. Petersburg) **30**, 1468 (1996) [Semiconductors **30**, 772 (1996)].
3. L. P. Kazakova, A. A. Lebedev, and É. A. Lebedev, Fiz. Tekh. Poluprovodn. (St. Petersburg) **31**, 609 (1997) [Semiconductors **31**, 517 (1997)].
4. E. A. Lebedev, E. A. Smorgonskaya, and G. Polisski, Phys. Rev. B **57**, 14607 (1998).
5. P. Rao, E. A. Schiff, L. Tsybeskov, and P. M. Fauchet, in *Abstracts of the Int. Conference "Porous Semiconductors—Science and Technology", Mallorca, 1998*, p. 53.
6. W. E. Spear, J. Non-Cryst. Solids **1**, 197 (1969).
7. M. A. Lampert and P. Mark, *Current Injection in Solids* (Academic, New York, 1970; Mir, Moscow, 1973).
8. M. Ben-Chorin, F. Möller, F. Koch, *et al.*, Phys. Rev. B **51** (4), 2199 (1995).
9. N. F. Mott and E. A. Davis, *Electronic Processes in Non-Crystalline Materials* (Clarendon Press, Oxford, 1979; Mir, Moscow, 1982).
10. S. P. Kobeleva, T. N. Bakhtigaraev, E. A. Petrova, and A. F. Orlov, in *Proceedings of the 2nd All-Russia Conference on Science of Materials and Physicochemical Foundations of Doped Silicon Crystal Technology, Moscow, 2000*, p. 348.
11. E. A. Petrova, K. N. Bogoslovskaya, L. A. Balagurov, and G. I. Kocharadze, in *Proceedings of the 2nd All-Russia Conference on Science of Materials and Physicochemical Foundations of Doped Silicon Crystal Technology, Moscow, 2000*, p. 365.

Translated by M. Tagirdzhanov

Semiconductors, Vol. 35, No. 5, 2001, pp. 591–597. Translated from Fizika i Tekhnika Poluprovodnikov, Vol. 35, No. 5, 2001, pp. 612–618.

AMORPHOUS, VITREOUS, AND POROUS SEMICONDUCTORS

The Effect of Bombardment with Carbon Ions on the Nanostructure of Diamond-like Films

I. A. Faĭzrakhmanov*, V. V. Bazarov, V. A. Zhikharev, and I. B. Khaĭbullin

Kazan Physicotechnical Institute, Kazan Scientific Center, Russian Academy of Sciences, Sibirskiĭ trakt 10/7, Kazan 29, 420029 Tatarstan, Russia

**e-mail: fiak@dionis.kfti.kcn.ru*

Submitted October 9, 2000; accepted for publication November 16, 2000

Abstract—The effect of irradiation with carbon ions on the nanocluster structure of diamond-like carbon films was studied. It is shown that the electronic properties (optical absorption and electrical conductivity at low temperatures) of the films depend heavily on the ion dose, which is a consequence of the quantum confinement effect. Variations in the optical band gap and in the activation energy for hopping conductivity are indicative of an increase in the size of π clusters whose concentration remains unchanged in the entire range of ion doses of 3×10^{14}–1.2×10^{17} cm^{-2}. The process of defect production in the clusters is shifted to higher ion doses compared to that in structurally homogeneous materials. The optical absorption in the π clusters, their concentration in the samples, the tunneling parameters for initial and completely "graphitized" films, and the width of the barrier layer between the clusters were estimated; the width of the band of defect states was determined. It is shown that the known dependence of the optical band gap of the π clusters on their size should be modified for large clusters ($E_g \leq 1$ eV). © *2001 MAIK "Nauka/Interperiodica".*

INTRODUCTION

It is known that the films of amorphous carbon *a*-C and hydrogenated amorphous carbon *a*-C:H have an inhomogeneous structure, which is formed by carbon atoms with different coordinations. The relative content of 3- and 4-coordinated carbon atoms and partially 2-coordinated carbon atoms depends significantly on the methods and conditions of the film deposition and eventually controls the entire set of physical properties of these materials. Carbon films with a significant content of the diamond-like phase have properties close to those of diamond and are referred to as diamond-like carbon films. Their extreme hardness, chemical inertness, and transparence in the infrared region of the spectrum are qualities that underlie a wide range of practical applications for these films. However, the interest of researchers in these materials extends further. The main special feature of these materials is their nanocluster structure. This radically differentiates them from other elemental amorphous semiconductors (such as *a*-Si and *a*-Ge) and is of fundamental interest in its own right, especially in view of the rapid progress in the fields of nanoeletronics and the physics of nanostructures.

A special feature of the nanometer-size particles consists in the fact that their electronic structure depends appreciably on particle size. Therefore, the quantum size effects may be expected to manifest themselves in nanocluster materials. In connection with this, the development of methods for forming nanostructures and for controlling the sizes and concentration of nanoparticles is a topical problems. Ion bombardment may become one of these methods according to the published data [1]. However, the course of irradiation-induced processes in such media and their effect on physical properties may differ drastically from those in the known and well-studied bulk materials. On the one hand, due to the small size of nanoparticles, radiation defects can diffuse rapidly to the nanoparticle surface and recombine there. In addition, the free energy of a nanoparticle is invariably higher than the corresponding value for the bulk material and decreases as the nanoparticle size increases. All this makes the nanoparticle a very stable formation. On the other hand, if a structural defect somehow becomes stabilized within the particle, this may radically affect the electronic structure of a particle, due again to small size of the particle. Therefore, we believe that studying the radiation-induced processes in the media under consideration is interesting and important.

The objective of this study was to gain insight into the effect of bombardment with carbon ions on graphite-like clusters in diamond-like carbon films. We studied the diamond-like carbon films irradiated with carbon ions. The choice of these ions is related to the fact that the elemental composition of the films does not change as a result of carbon implantation. This makes it possible to study the film-structure variations related to radiation effects.

EXPERIMENTAL

It is known [2] that the electronic properties of diamond-like films, in particular, optical absorption in the visible and near ultraviolet regions of the spectrum and

electrical conductivity, are controlled by the presence of graphite-like nanoclusters (the π clusters) in these films. This makes it possible to use relatively simple and available experimental methods to monitor the changes in the sizes and concentration of nanoclusters that result from external factors affecting the medium. We studied optical properties and the temperature dependence of electrical conductivity of the films.

In a certain range of photon energies E (typically, in the region corresponding to $\alpha > 10^4$ cm^{-1}, where α is the absorption coefficient), the spectral dependence of the imaginary part of the dielectric constant (ε_2) in diamond-like carbon films is described by the Tauc formula typical of a number of amorphous semiconductors; i.e.,

$$E^2\varepsilon_2 = B_2(E - E_{gT})^2. \quad (1a)$$

If the refractive index $\bar{n} \approx$ const, we may rewrite formula (1a) as

$$E\alpha = B_1(E - E_{gT})^2, \quad (1b)$$

where E_{gT} is the Tauc optical gap to be determined experimentally. For amorphous semiconductors, dependences (1a) and (1b) are based on the direct and indirect band-to-band transitions between the delocalized states [3]. Strictly speaking, the quantity E_{gT} does not have any definite physical significance in the model of the energy-band structure of an amorphous semiconductor [4, 5]. The situation is different if the medium consists of nanoclusters that have different values for the optical band gap E_g. In this situation, as will be shown below, the quantity E_{gT} has the meaning of the average value of E_g for an ensemble of nanoclusters, and the coefficient B_1 in (1b) is proportional to their concentration. According to [2], the value of E_g for graphite-like nanoclusters is governed by the number of hexagonal rings N that form the cluster; i.e., we have

$$E_g = 2\beta/\mathrm{N}^{0.5} \quad (2)$$

for compact clusters and

$$E_g = 2\beta/\mathrm{N} \quad (3)$$

for linear clusters (here, $\beta = 3$ eV). Therefore, by studying the optical properties of diamond-like films, it is possible to determine the mean size of the nanoclusters and monitor variations in their concentration.

Useful information can be also obtained from the studies of low-temperature electrical conductivity in nanocluster systems and, in particular, in carbon films [6, 7]. It is known that, in these materials, the charge transport at low temperatures is accomplished by the mechanism of the variable-range hopping conductivity; thus, the resistance is given by

$$R = R_0\exp(T_0/T)^m, \quad (4)$$

where $m < 1$. If the density of localized states in the vicinity of the Fermi level is constant, the temperature dependence of resistance is described by the classical Mott law [8] with $m = 1/4$. In this case, the quantity T_0 is controlled by the tunneling parameter α_* and the density of localized states in the vicinity of the Fermi level $N(E_F)$; i.e., we have

$$T_0 = 16\alpha_*^3/kN(E_F), \quad (5)$$

where k is the Boltzmann constant. The value of $\alpha_*^{-1} = 1.2$ nm has been typically used in studies of the electrical conductivity in diamond-like carbon films. This value was determined previously [6] for carbon films that were produced by graphite sputtering and contained ~95 at. % of carbon in the sp^2 state. However, a diamond-like phase is inevitably present in diamond-like carbon films; this phase forms a tunneling barrier between the nanoclusters. The width of this barrier is governed by the ratio between the concentrations of the sp^3 and sp^2 states and by the nanocluster sizes. Therefore, the electron-localization radius α_*^{-1} is a function of the nanocluster size as in the case of granular metal–insulator systems [9]; thus, the value of $\alpha_*^{-1} = 1.2$ nm should be regarded as the largest possible. For diamond-like carbon films, the situation is more complicated, because the defect-free nanoclusters themselves act as potential barriers whose height depends on the nanocluster sizes. Consequently, not only the optical band gap E_{gT} but also the parameter T_0 depend on the mean size of the nanoclusters, with the dependence for T_0 being heavier. Another parameter on which T_0 depends is the density of states in the vicinity of the Fermi level $N(E_F)$. This density is proportional to the concentration of nanoclusters which have states near the middle of the band gap E_g. These nanoclusters may be represented by those with an odd number of carbon atoms (the nanoclusters containing the pentagonal and heptagonal rings) [2]. Furthermore, the ion bombardment gives rise to an additional number of defect-containing nanoclusters, which also reduces the value of T_0.

Thus, we may conclude from the above brief analysis that studies of optical and electrical properties make it possible to obtain information about the nanocluster structure of diamond-like carbon films.

Thin diamond-like carbon films with a thickness of $d_0 \approx 50$–70 nm were deposited on glass substrates by ion sputtering of graphite [10]. The as-deposited films were studied using optical and electrical measurements; in addition, the electron diffraction patterns of the films annealed in a vacuum chamber for 30 min at $T_a = 450$°C were analyzed. The films had optical and electrical characteristics typical of the diamond-like carbon films: $E_{gT} = 1.1$–1.2 eV, a refractive index $\bar{n} = 2.0$, an extinction coefficient $\bar{k} < 0.1$ (for a wavelength

$\lambda = 600$ nm), and a resistivity of $\rho \geq 10^6\ \Omega$ cm at room temperature. The electron diffraction pattern for the films corresponded to a cubic structure (with a lattice constant of 0.357 nm) close to that of diamond. The reflections corresponding to the diamond phase had the highest intensity. Other reflections forbidden for the diamond structure had much lower intensities.

The optical parameters of the films were determined from the reflection $R^*(\lambda)$ and transmission $T^*(\lambda)$ spectra, which were measured using a Hitachi-330 two-beam spectrophotometer in the wavelength range of 350 nm $\leq \lambda \leq$ 1000 nm. Using the values of d_0, $T^*(\lambda)$, $R^*(\lambda)$, and the approximation of a thin film on a transparent substrate, we calculated the spectral dependences $\bar{n}(\lambda)$ and $\bar{k}(\lambda)$ and the real $\varepsilon_1 = \bar{n}^2 - \bar{k}^2$ and imaginary $\varepsilon_2 = 2\bar{n}\bar{k}$ parts of the dielectric constant of the medium.

The temperature dependence of resistivity of the films was measured in the temperature range of T = 20–300 K using two probes. The silver contacts were deposited by thermal evaporation in vacuum.

We studied the structure of the films by high-energy electron diffraction using an ÉMR 125 electron microscope.

The films were implanted with C^+ ions with an energy of 20 keV (the projected range of ions in C was R_p = 46 nm, and the corresponding standard deviation was ΔR_p = 15 nm) in the dose range of 3×10^{14}–3×10^{17} cm^{-2}; an ILU-3 ion accelerator was used. The ion-current density was no higher than 2 μA/cm^2. The samples were mounted on a water-cooled holder.

ESTIMATION OF OPTICAL ABSORPTION IN THE π CLUSTERS

At present, there are no theoretical estimates available for optical absorption in individual π clusters. In the majority of experimental studies (see, for example, [11]), the results are discussed in terms of a model energy-band structure for an amorphous semiconductor. In accordance with this model, the dependence $\alpha(E)$, under certain conditions, has the form suggested by Tauc [see (1a) or (1b)]. The coefficient B_1 involves the squared matrix element of momentum $|p|^2$ and the effective electron masses in the valence and conduction bands. All these parameters are unknown. In addition, as was mentioned above, the quantity E_{gT} has no definite physical meaning in this model. Robertson and O'Reilly [2] calculated the electronic structure of compact π clusters in relation to their size, and Robertson [12] calculated the spectral dependences $J(E)/E$ ($\alpha(E) \propto J(E)/E$ under the assumption that $|p|$ = const; here, $J(E)$ is the combined density of states); however, the dependence $\alpha(E)$ was not calculated. We note that

$$J(E) = \int N_c(E')N_v(E' - E)dE', \qquad (6)$$

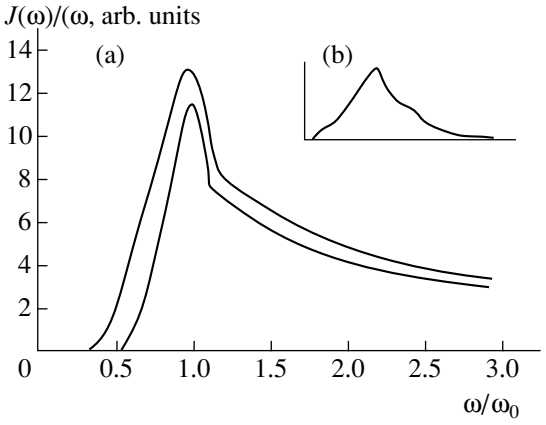

Fig. 1. The dependence $J(\omega)/\omega$ (a) simulated in this study and (b) calculated previously [12].

where $N_c(E')$ and $N_v(E')$ are the density of states in the cluster's conduction and valence bands, respectively. We can estimate the optical absorption of a nanocluster on the basis of the special features of the electron density of states, which follow from calculations by Robertson and O'Reilly [2, 12]. These feature are as follows:

(i) The total width of the energy range within which the π-electron states of a cluster are distributed is 6β.

(ii) The density of states is continuous, at least for N > 18.

(iii) The maximum of the function $J(E)$ is located at $E_0 = 2\beta$ and is independent of the cluster size.

(iv) $E_g = 2\beta/N^{0.5} = E_0/N^{0.5}$.

In addition, we assume that $|p|$ = const for allowed transitions. Thus, the absorption coefficient of a medium containing a single cluster may be represented as

$$\alpha(\omega) = (\pi e^2/m_e c)\varphi(\omega)J(\omega). \qquad (7)$$

Here, $\varphi(\omega)$ is the oscillator strength given by

$$\varphi(\omega) = 2g_n\hbar|p|^2/3g_m m_e\omega,$$

where g_m and g_n are the degrees of degeneracy of the ground and excited levels, m_e and e are the mass and charge of an electron, and ω is the cyclic frequency of incident light.

In order to calculate $\alpha(\omega)$, we need to know the combined density of states of π electrons $J(\omega)$; the latter dependence generally has the shape shown in Fig. 1b. In what follows, we construct a function that at least qualitatively describes correctly both the energy distribution of the combined density of states for the π electrons and its dependence on the cluster size. We now separate the dependence $J(\omega)$ into three portions,

each of which is approximated by a specific function; i.e.,

$$\begin{aligned}&\text{(I) } J_1(\omega) = J_0 B(\omega - \omega_g)^2 \quad (\omega_g \le \omega \le \omega_1),\\ &\text{(II) } J_2(\omega) = J_o\gamma/[(\omega - \omega_0)^2 + \gamma^2/4] \quad (\omega_1 < \omega \le \omega_2),\\ &\text{(III) } J_3(\omega) = J_0[B_2(\omega - 3\omega_0)^2 + a] \quad (\omega_2 < \omega \le 3\omega_0).\end{aligned} \tag{8}$$

In view of the condition for continuity of the function $J(\omega)$ at the points ω_1 and ω_2, we obtain

$$\begin{aligned}B &= (64/27)\gamma^{-3};\\ \gamma &= (\omega_0 - \omega_g)/\sqrt{2};\\ \omega_1 &= (3\omega_0 + \omega_g)/4;\\ B_2 &= 0; \quad a = 3/\gamma;\\ \omega_2 &= \omega_0 + \gamma/2\sqrt{3}.\end{aligned} \tag{9}$$

Thus, we derived the function of the combined density of states, which is controlled by a single cluster parameter, i.e., by the position of the absorption edge ω_g. The value of the normalization factor J_0 can be determined from the rule of sum as

$$\int_0^\infty \alpha(\omega)d\omega = (2\pi^2 e^2/m_e c)nZ, \tag{10}$$

where n is the atomic density and Z is the number of electrons per atom involved in the absorption event. In the case under consideration, $Z = 1$ and n is the number of carbon atoms in a cluster; i.e.,

$$n = 4\mathrm{N} + 2 = 4(\omega_0/\omega_g)^2 + 2. \tag{11}$$

Thus, we obtain the following expression for the absorption coefficient of a π cluster in the photon-energy range of $E_g < E < E_1$:

$$\begin{aligned}E\alpha(E) = (13.4\pi e^2 h/m_e c)[(2E_0^2/E_g^2 + 1)/I(E_0 - E_g)^3]\\ \times (E - E_g)^2 = B(E - E_g)^2.\end{aligned} \tag{12}$$

Here,

$$I = (1/J_0)\int_{E_g}^{3E_0} [J(E)/E]dE.$$

The results of numerical calculations of the parameter B may be approximated as

$$\begin{aligned}B(E_g)[\mathrm{eV}^{-1}\ \mathrm{cm}^{-1}] = 0.5 \times 10^{-16}(E_0/E_g)^{3/2}\\ (E < 3\ \mathrm{eV}).\end{aligned} \tag{13}$$

We now assume that the π-cluster distribution in E_g is rectangular. As a result,

$$E\alpha(E) = (N_0/2\Delta E_g)\int_{E_{g0} - \Delta E_g}^{E} B(E_g)(E - E_g)^2 dE_g, \tag{14}$$

where N_0 is the cluster concentration, E_{g0} is the mean value of E_g, and ΔE_g is the half-width of the distribution. The calculations show that, in the range of photon energies of $E_{g0} - \Delta E_g \le E \le E_{g0} + \Delta E_g$, the function $[E\alpha(E)]^{1/2}$ cannot be approximated by a linear dependence. This absorption region is similar to the Urbach tail in amorphous semiconductors. If $E > E_{g0} + \Delta E_g$, the function $[E\alpha(E)]^{1/2}$ may be approximated by a linear dependence of the type suggested by Tauc in a certain energy range; however, the parameters of this function also depend on the distribution half-width ΔE_g. Even if the cluster distribution is not excessively narrow (when the condition $\Delta E_g/E_{g0} < 1$ is satisfied), the experimentally measured Tauc optical band gap corresponds to the mean value of E_{g0}; i.e., we have

$$E\alpha(E) = N_0 B(E_{g0})(E - E_{g0})^2 \tag{15}$$

in the range of

$$E_{g0} + \Delta E_g < E < E_1 = (3E_0 + E_{g0})/4. \tag{16}$$

As might be expected, the parameter B_1 in expression (1b) is specified by the concentration N_0 of the π clusters. In addition, B_1 also depends on E_{g0}. This dependence is most important in the region of $E_{g0} \le 1$ eV. However, as is evidenced by experimental data (not only those obtained by us), B_1 depends on E_{gT} only slightly, at least in the range of $0.4\ \mathrm{eV} \le E_{gT} \le 1.4$ eV, although, as follows from formula (13), we have $B_1(0.5\ \mathrm{eV}) = 3B_1(1\ \mathrm{eV})$. This significant disagreement with the experiment may be overcome if we assume that E_g decreases more rapidly than according to the law $\mathrm{N}^{-0.5}$ with increasing π-cluster size. For example, the dependence $E_g \propto \mathrm{N}^{-1}$ results in the relation $B \propto (E_0/E_g)^{0.7}$; i.e., the dependence on E_g becomes less pronounced. In our opinion, the latter assumption is quite reasonable. In this case, we can obtain the following expression for the clusters with $E_g \le 1$ eV:

$$E\alpha(E) = 5.2 \times 10^{-16} N_0 (E - E_{g0})^2. \tag{17}$$

This relationship makes it possible to estimate the concentration N_0 of π clusters in the sample and the concentration N_C of carbon atoms included in the nanoclusters. Typically, the samples we studied had the values $E_{gT} = 1.0$–1.2 eV and $B_1 = 6.2 \times 10^4\ \mathrm{eV}^{-1}\ \mathrm{cm}^{-1}$. As a result, we obtain $N_0 = 1.2 \times 10^{20}\ \mathrm{cm}^{-3}$ and $N_\mathrm{C} = 2 \times 10^{22}\ \mathrm{cm}^{-3}$, which are quite reasonable values, at least on the order of magnitude.

Finally, the linear dependence of $[E\alpha(E)]^{1/2}$ on energy is observed experimentally only in a certain

range of photon energies. The lower bound is shifted significantly to lower energies E as E_{gT} decreases. Such behavior follows directly from condition (16).

Thus, the above approximate calculations of optical absorption in the π clusters describe adequately the experimental data on optical absorption of diamond-like carbon films; the estimations of the cluster concentration based on these calculations yield quite realistic values.

RESULTS AND DISCUSSION

The structure of diamond-like films is very sensitive to external factors. At relatively low annealing temperatures T_a = 350–400°C, thin films are crystallized. As a result, an electron-diffraction pattern characteristic of these films emerges [13, 14]. Crystallization is also observed when the films irradiated with electrons are examined using an electron diffractometer. Such a structural instability of the films also manifests itself in the case of irradiation of the films with low doses of C^+ ions. For the doses of $\sim 3 \times 10^{14}$ cm^{-2}, a distinct diffraction pattern is observed. As the ion dose increases, the diffraction pattern becomes gradually more diffuse and, for doses of $\sim 10^{15}$ cm^{-2}, ceases to exist, which indicates that the films are amorphized. Thus, we observe a sequence of structural transformations characteristic of semiconductor materials with the diamond structure. As will be clear from what follows, these structural modifications refer only to the diamond-like matrix.

Figure 2 shows the Tauc dependences for the as-grown samples and the samples irradiated with the C^+ ion doses of 3×10^{15} and 1.2×10^{17} cm^{-2}. It can be seen that, in the entire dose range, the slope of the Tauc dependences $B_1^{1/2}$ remains unchanged and has the same value as in the as-grown samples: $B_1 = 6.2 \times 10^4$ eV^{-1} cm^{-1} ($B_2 = 2.3$). This indicates that the π-cluster concentration remains unchanged under the carbon-ion irradiation and, according to the above estimations, amounts to $\sim(1–2) \times 10^{20}$ cm^{-3}.

Figure 3 shows the dose dependence of the optical band gap, which reflects variations in the mean size of the clusters. As can be seen from Fig. 3, three characteristic portions may be separated out. For doses of $D \le 6 \times 10^{14}$ cm^{-2}, the mean π-cluster size remains unchanged. In the range of 6×10^{14} cm$^{-2} \le D \le 1.8 \times 10^{16}$ cm^{-2}, a rapid decrease in E_{gT} from 1.2 to ~0.43 eV is observed. In the region of $D > 1.8 \times 10^{16}$ cm^{-2}, a slow (almost linear with dose) decrease in E_{gT} is observed.

The observed dose dependence of E_{gT} may be qualitatively explained in the following manner. To this end, we should bear in mind that the as-grown films constitute a two-phase system, which consists of the π clusters (which, in the case under consideration, may be treated as stable nuclei of the thermodynamically equilibrium graphite phase) surrounded by the metastable

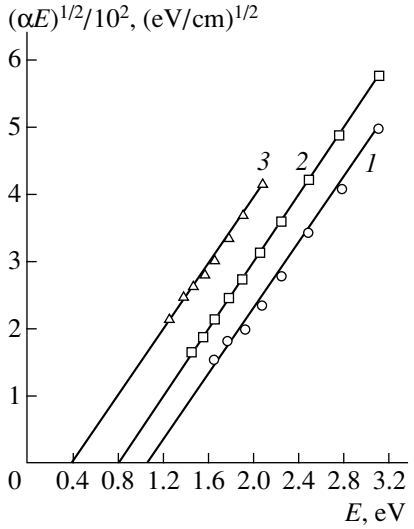

Fig. 2. The Tauc dependence for (*1*) the as-deposited sample and the samples irradiated with carbon ions with the doses of D = (*2*) 3×10^{15} and (*3*) 1.2×10^{17} cm^{-2}.

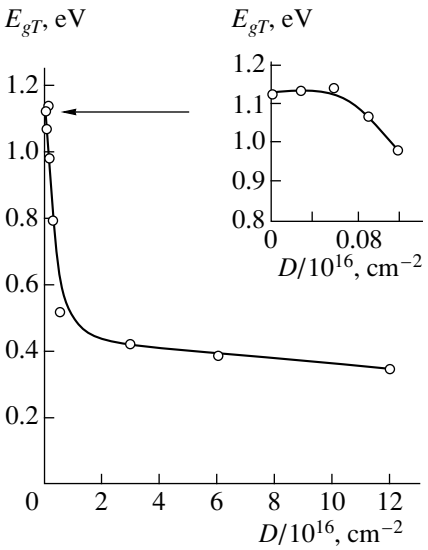

Fig. 3. Dependence of the Tauc optical band gap E_{gT} on the dose D of implanted carbon ions. The region of low doses ($D < 10^{15}$ cm^{-2}) is illustrated in the inset.

diamond-like phase. The clusters can grow according to two mechanisms, depending on whether the clusters are conjugate to the matrix or their peripheral bonds are saturated with hydrogen. In the first case, the growth may proceed by spontaneous transition from the sp^3 to sp^2 configuration in the boundary cluster region due to an increased vacancy concentration. In the second case, the growth may proceed by attachment of carbon atoms from the surrounding matrix to the peripheral dangling bonds that appear owing to the hydrogen effusion. In any case, a certain preliminary stage ($D \le 10^{14}$ cm^{-2}) is needed in order for such a growth process to set in. In

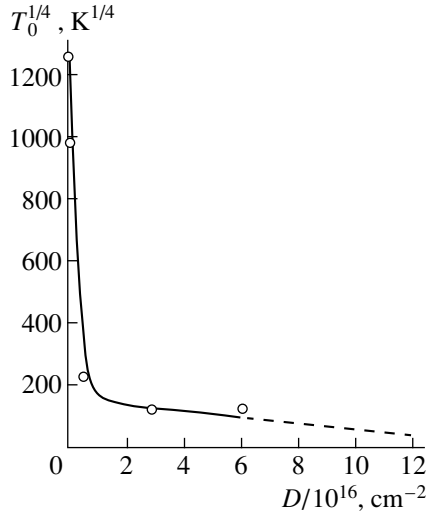

Fig. 4. The dependence of parameter $T_0^{1/4}$ on the dose D of implanted carbon ions.

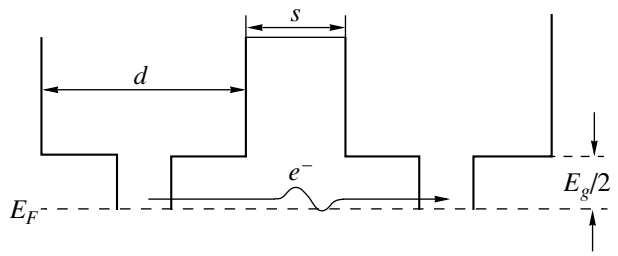

Fig. 5. A model of tunneling barriers for a diamond-like film.

addition, both these processes are limited only by the generation rate of radiation defects and therefore proceed rather rapidly. Obviously, a decrease in the growth rate is related to the fact that all, or the vast majority of, carbon atoms are bound by the clusters. In fact, the clusters with $E_g = 0.43$ eV contain ~350 carbon atoms, which yields the concentration of ~$(4–7) \times 10^{22}$ cm^{-3}. This is comparable to the atomic density of diamond-like films. Therefore, in the region of $D > 1.8 \times 10^{16}$ cm^{-2}, the cluster size can increase owing predominantly to the implanted carbon atoms; i.e., this increase is approximately proportional to the ion dose.

Figure 4 shows the dose dependence of the parameter $T_0^{1/4}$. The as-deposited films had a very high resistance ($R > 10^6$ MΩ at $T = 300$ K), which made it impossible to measure the temperature dependence of resistance. As a result of implantation with doses $D < 6 \times 10^{14}$ cm^{-2}, the resistance of the samples decreases somewhat ($R \approx 3 \times 10^5$ MΩ at $T = 300$ K); however, a large spread in the data is observed. Thus, it is impossible to accurately determine the dose dependence of $T_0^{1/4}$ in this region as well. For higher doses, the parameter $T_0^{1/4}$ depends heavily on the dose; this dependence is qualitatively similar to the dependence $E_{gT}(D)$. This suggests that we also have here a manifestation of the size effect related to the tunneling parameter. In diamond-like films, there are at least two types of tunneling barriers (Fig. 5); one of these is related to the diamond-like matrix, whereas the other is related to the nanoclusters themselves. For the hops over the distances of $r > d$, we may write

$$\alpha_* = \alpha_{*1} s/(d + s) + \alpha_{*2} d/(d + s), \qquad (18)$$

where α_{*1} and s are the tunneling parameter and the width of the tunneling barrier formed by the diamond-like phase and $\alpha_{*2} = 2\pi(2m_e\Delta E_2)^{1/2}/h = 2\pi(m_2 E_g)^{1/2}/h$ is the tunneling parameter for the barrier formed by a nanocluster with a diameter of d. We express E_g in terms of the cluster diameter as

$$d[\text{nm}] \approx (16/n_0\pi)^{1/2}(E_0/E_g) \approx 2.2/E_g\ [\text{eV}], \qquad (19)$$

where $n_0 \approx 38.2$ nm^{-2} is the cluster's atomic density. According to our assumption, we have $E_g \propto 1/\text{N}$ for the clusters with $E_g \le 1$ eV. In this situation,

$$d[\text{nm}] \approx 2.2/(E_g[\text{eV}])^{1/2}. \qquad (20)$$

Introducing these formulas into (18), we obtain the following expression for the tunneling parameter α_*:

$$\alpha_* \approx \alpha_{*1} s/(d + s) + 8/(d + s). \qquad (21)$$

It follows from this expression that the tunneling parameter consists of two terms: the first term depends on the dose in terms of the parameters α_{*1} and s, whereas the second term is dose-independent in the region of low and medium doses because $d + s = \text{const}$.

Similarly to the case of the dependence $E_{gT}(D)$, we can identify three characteristic regions in the dependence $T_0^{1/4}(D)$.

(I) The region of $D < 6 \times 10^{14}$ cm^{-2}. In this region, as was ascertained above, the nanocluster sizes remain unchanged; however, the diamond-like matrix is amorphized owing to the generation and accumulation of radiation defects. Origination of these defects in the region of tunneling barrier brings about a decrease in the barrier height, i.e., a decrease in α_{*1}.

(II) The range of 6×10^{14} cm$^{-2} < D < 1.8 \times 10^{16}$ cm^{-2}. In this dose range, the predominant process is an increase in the diameter of nanoclusters due to the adsorption of the barrier layer. This results in a decrease in the thickness s of the barrier layer from a certain initial value to zero and in a corresponding decrease in the parameter $T_0^{1/4}$.

(III) The region of $D > 1.8 \times 10^{16}$ cm^{-2}. In this region, $s \approx 0$.

It can be seen from Fig. 4 that the transition to the weaker dependence occurs for $D \approx 1.8 \times 10^{16}$ cm^{-2}. For this dose, we may assume that $s = 0$, $E_{gT} = 0.42$ eV, and $d = 3.4$ nm. Substituting these values into (21), we obtain $\alpha_*^{-1} = 0.45$ nm, which is approximately three times smaller than the value determined previously [6] ($\alpha_*^{-1} = 1.2$ nm). The data we obtained also make it possible to estimate the average distance between nanoclusters in the as-deposited samples at $s \approx 1.6$ nm and $\alpha_* = 7$ nm^{-1} (if we assume that $\alpha_{*1} \approx 10$ nm^{-1}).

Estimations based on expression (5) show that the observed increase in the parameter T_0 by more than three orders of magnitude cannot be assured by a change in the tunneling parameter α_* alone. It follows from the estimates that, simultaneously with an increase in the tunneling parameter, the concentration of defect-containing clusters over which the charge transport occurs should increase by at least an order of magnitude. According to these estimates, the defect production is the predominant cause of the decrease in T_0 in the region of $D > 1.8 \times 10^{16}$ cm^{-2}.

Finally, the dependence of log$R$ on $T^{-1/4}$ deviates significantly from a linear one at $T > 28$ K for the samples implanted with $D = 1.2 \times 10^{17}$ cm^{-2}, which indicates that the conduction mechanism is changed. As the estimates show, for these samples, one of the conditions for manifestation of the variable-range hopping conductivity is violated; i.e., we have

$$r = (3/8\alpha_*)(T_0/T)^{1/4} > d.$$

The temperature dependence of resistance in the range of 28 K < T < 100 K can be approximated by an exponential law with an activation energy of $\Delta E \approx 0.03$ eV. We may assume [15] that, in this temperature range, electrical conduction is accomplished by hops of electrons or holes to the nearest states of defects and that the value of ΔE is on the order of the half-width of the band of states related to defects. Knowing this value, we can estimate the concentration of the defect-related states over which the charge transport occurs. This concentration is of the same order of magnitude as the concentration of defect-containing clusters; i.e.,

$$N_{ds} \approx 2N(E_F)\Delta E.$$

For example, for $D = 6 \times 10^{16}$ cm^{-2}, we have $N_{ds} \approx 1.4 \times 10^{18}$ cm^{-3}, which is by about two orders of magnitude smaller than the concentration of clusters in the sample. This indicates that the π clusters have high radiation resistance.

CONCLUSION

Thus, optical and electrical properties of diamond-like films depend heavily on the dose of irradiation with carbon ions, which is a consequence of the size effect. It is ascertained that bombardment with carbon ions brings about a certain sequence of interrelated structural transformations in the matrix and the nanoparticle system, as a result of which the vast majority of carbon atoms become bound by more stable π clusters. The process of the defect production in the clusters is shifted to higher doses compared to that in structurally homogeneous materials. The initial π-cluster concentration, which, according to our estimations, amounts to (1–2) $\times 10^{20}$ cm^{-3}, remains unchanged under the implantation conditions used in this study. The known dependence of E_g on the π-cluster size should be modified for the clusters with $E_g \leq 1$ eV. The experimental and theoretical results obtained made it possible to estimate the tunneling parameters for as-deposited and completely graphitized samples ($\alpha_*^{-1} \approx 0.14$ and 0.45 nm, respectively): the thickness of the barrier layer between the nanoclusters in the as-deposited samples $s \approx 1.5$–2 nm, which was unknown previously, and the width of the band of defect-related states ~0.06 eV.

REFERENCES

1. G. F. Kachurin, I. E. Tyschenko, W. Skorupa, *et al.*, Fiz. Tekh. Poluprovodn. (St. Petersburg) **31**, 730 (1997) [Semiconductors **31**, 626 (1997)].
2. J. Robertson and E. P. O'Reilly, Phys. Rev. B **35**, 2946 (1987).
3. A. Frova and A. Selloni, in *Tetrahedrally-Bonded Amorphous Semiconductors*, Ed. by D. Adler and H. Fritzsche (Plenum, New York, 1985), p. 271.
4. D. Dasgupta, F. Damichelis, C. F. Pirri, and A. Tagliaferro, Phys. Rev. B **43**, 2131 (1991).
5. J. Robertson, Prog. Solid State Chem. **21**, 199 (1991).
6. J. J. Hauser, J. Non-Cryst. Solids **23**, 21 (1977).
7. J. C. Dawson and J. Adkins, J. Phys.: Condens. Matter **7**, 6297 (1995).
8. N. F. Mott and E. A. Davis, *Electronic Processes in Non-Crystalline Materials* (Clarendon Press, Oxford, 1971; Mir, Moscow, 1974).
9. O. Entin-Wohlman, Y. Gefen, and Y. Shapira, J. Phys. C **16**, 1161 (1983).
10. I. A. Faĭzrakhmanov and I. B. Khaĭbullin, Poverkhnost', No. 5, 88 (1996).
11. N. Savvides, J. Appl. Phys. **59**, 4133 (1986).
12. J. Robertson, Adv. Phys. **35**, 317 (1986).
13. H. Vora and T. J. Moravec, J. Appl. Phys. **52**, 6151 (1981).
14. L. S. Palatnik, M. B. Guseva, V. G. Babaev, *et al.*, Zh. Éksp. Teor. Fiz. **87**, 914 (1984) [Sov. Phys. JETP **60**, 520 (1984)].
15. E. A. Davis, Philos. Mag. **22**, 903 (1970).

Translated by A. Spitsyn

Semiconductors, Vol. 35, No. 5, 2001, pp. 598–604. Translated from Fizika i Tekhnika Poluprovodnikov, Vol. 35, No. 5, 2001, pp. 619–625.

PHYSICS OF SEMICONDUCTOR DEVICES

Light Emitting Diodes for the Spectral Range λ = 3.3–4.3 μm Fabricated from InGaAs and InAsSbP Solid Solutions: Electroluminescence in the Temperature Range of 20–180°C (Part 2[1])

M. Aĭdaraliev, N. V. Zotova, S. A. Karandashev, B. A. Matveev*, M. A. Remennyĭ, N. M. Stus', and G. N. Talalakin

Ioffe Physicotechnical Institute, Russian Academy of Sciences, Politekhnicheskaya ul. 26, St. Petersburg, 194021 Russia

** e-mail: bmat@iropt3.ioffe.rssi.ru*

Submitted October 5, 2000; accepted for publication October 6, 2000

Abstract—Light-emitting diodes (LEDs) based on *p–n* homo- and heterostructures with InAsSb(P) and InGaAs active layers have been designed and studied. An emission power of 0.2 (λ = 4.3 μm) to 1.33 mW (λ = 3.3 μm) and a conversion efficiency of 30 (InAsSbP, λ = 4.3 μm) to 340 mW/(A cm^2) (InAsSb/InAsSbP double heterostructure (DH), λ = 4.0 μm) have been achieved. The conversion efficiency decreases with increasing current, mainly owing to the Joule heating of the *p–n* homojunctions. In DH LEDs, the fact that the output power tends to a constant value with increasing current is not associated with active region heating. On raising the temperature from 20 to 180°C, the emission power of the (λ = 3.3 and 4.3 μm) LEDs decreases, respectively, 7- and 14-fold, to become 50 (at 1.5 A) and 7 μW (at 3 A) at 180°C. © *2001 MAIK "Nauka/Interperiodica".*

1. INTRODUCTION

In some applications, optoelectronic devices are required to operate at elevated temperatures. As shown previously [1], LEDs with an active region based on narrow-gap InGaAs (wavelength λ = 3.3 μm) and InAsSbP (λ = 4.3 μm) solid solutions retain their "classical" features at temperatures of up to 180°C: the temperature dependence of the reverse current in the saturation regime is governed by the increasing intrinsic carrier concentration, in accordance with the Shockley theory; emission spectra are described under the assumption of direct band-to-band transitions, spherically symmetrical bands, and thermalized charge carriers; the emission power decreases exponentially with increasing temperature, which is typical of Auger processes.

This study, proceeding from investigations started in [1], is concerned with the electroluminescence (EL) from InGaAs *p–n* homojunction LEDs (λ = 3.3 μm) and InAsSbP (λ = 4.3 μm) and with InAsSb/InAsSbP double heterostructure (DH) LEDs (λ = 4.0 μm) in the temperature range 20–180°C. The effect of electron confinement on the conversion efficiency of (λ = 4.0 μm) LEDs is demonstrated, and data on the long-term stability of (λ = 3.3 μm) LEDs at elevated temperatures are presented.

[1] For Part 1, see Semiconductors, **34**, 104–107 (2000).

2. EXPERIMENTAL

Samples were grown by liquid-phase epitaxy on (111) (*n*, *p*)-InAs substrates with carrier a concentration of ~2×10^{16} cm^{-3}. $In_{0.95}Ga_{0.05}As$ (λ = 3.3 μm) and $InAs_{0.87}Sb_{0.12}P_{0.01}$ (λ = 4.3 μm) solid solutions similar to those described previously [1, 2] were used as active layers in LEDs based on *p–n* homostructures. Layers of *p*-type were formed by doping the melt with zinc or manganese; the concentration of free holes was $p \approx (1–2) \times 10^{17}$ cm^{-3}. Epilayers of *n*-type with electron concentration $n \approx (1–2) \times 10^{17}$ cm^{-3} were nominally undoped. *n*-InGaAs and *p*-InAsSbP layers were 5–10 μm thick. Chips of (λ = 3.3 μm) LEDs ~100 μm thick were mounted in TO-18 packages, with the *p*-substrate underneath. In this case, the voltage was applied to the LED through a U-shaped gold contact deposited onto the chip surface at the cathode (see Fig. 1 in [1]), thus ensuring the absence of current lines near the inactive *p*-InAs surface. In the (λ = 4.3 μm) LEDs, the substrate and part of the wide-gap layer were etched off, and the chips were mounted, with the *p*-layer underneath, onto a silicon holder $0.4 \times 1.5 \times 1.7$ mm^3 in size; the radiation was emitted through the wide-band part of the 50- to 80-μm-thick *n*-InAsSbP graded layer, as in [1].

LEDs with an emission peak at λ = 4.0 μm were fabricated in the form of double heterostructures (DHs) comprising an undoped (111) *n*-InAs substrate ($n = (1–2) \times 10^{16}$ cm^{-3}) and three epilayers: (i) *n*-$InAs_{1-x-y}Sb_xP_y$ ($0.05 \le x \le 0.09$, $0.09 \le y \le 0.18$) wide-gap confinement

1063-7826/01/3505-0598$21.00 © 2001 MAIK "Nauka/Interperiodica"

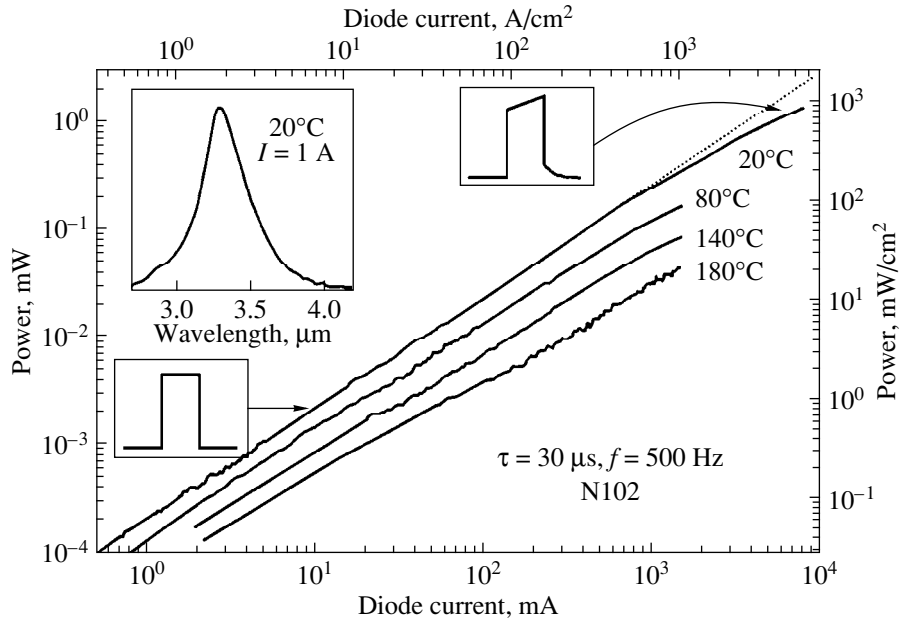

Fig. 1. Emission power vs. current for (λ = 3.3 μm) InGaAs *p–n* homojunction LED at T = 20, 80, 140, and 180°C. Inserts: emission spectrum at T = 20°C, I = 1 A; oscillograms of the photodetector output signal.

layer, adjoining the substrate; (ii) *n*-$InAs_{1-w}Sb_w$ ($w \approx 0.07$) active region; and (iii) *p*(Zn)-$InAs_{1-x-y}Sb_xP_y$ ($0.05 \le x \le 0.09$, $0.09 \le y \le 0.18$) wide-gap emitter. The active region was grown from a melt containing X^1_{Gd} = 0.004–0.005 at. % of gadolinium, which ensures the lowest concentration of residual impurities and the highest carrier mobility [3]. The thicknesses of the wide-gap layers were 3–5 μm, and that of the active region, 6 μm; the substrate, initially 350 μm thick, was ground and/or etched to 100 μm. Chips were mounted *p*-side down onto a silicon holder; the radiation was emitted through the substrate.

The EL was measured in the pulse regime, with τ = 30–500 μs as the pulse width and f = 500 Hz as the repetition rate, on samples with mesas 430 μm in diameter. The emission spectra were recorded using an InSb photodiode cooled to 77 K. The light–current (*L–I*) characteristics were measured with a calibrated HgCdTe photodiode cooled to 77 K, with due regard for the directional pattern of a LED.

3. RESULTS

3.1. (λ = 3.3 μm) InGaAs p–n Homojunction LEDs

Figure 1 shows *L–I* characteristics of InGaAs *p–n* homojunction LEDs at temperatures T = 20, 80, 140, and 180°C. The inserts present the LED emission spectrum at T = 20°C, the working current I = 1 A, and oscillograms of the photodetector output signals in the linear and sublinear portions of the *L–I* characteristic. The maximum room-temperature emission power was 1.33 mW (917 mW/cm^2) at I = 8 A. The *L–I* characteristic is linear up to I = 1 A, with a conversion efficiency (CE) of 167 mW/(A cm^2) and a quantum efficiency of 0.07%; at higher currents, the *L–I* characteristic is sublinear, and the CE decreases to 50 mW/(A cm^2) at I = 8 A. On extending the pulse width from 30 to 500 μs, the upper limit of the linear portion of the *L–I* characteristic decreases to I = 0.4 A, and the characteristic almost levels off at I = 1 A. In the linear portion of the *L–I* characteristic, the photodetector signal is rectangular, reproducing the shape of the pumping current pulse (see inset in Fig. 1). In the sublinear portion, the shape of the photodetector signal is not rectangular, exhibiting a sawtooth component and an exponential decay after the end of the current pulse (see insert in Fig. 1). After having passed the LED emission through a sapphire plate absorbing radiation with λ ≤ 5.5 μm, the photodetector signal became rectangular.

When the temperature increases to $T \approx 150$°C, the output power decreases exponentially: $P = P_0\exp(E_A/kT)$, where P_0 is the room-temperature power, E_A is a characteristic energy, and k is the Boltzmann constant (see Fig. 2). The characteristic energy E_A = 43 meV is close to the value typical of CHCC Auger processes [4]. When the temperature is elevated from 20 to 180°C, the quantum efficiency and CE decrease seven fold, to, respectively, 0.01% and 24 mW/(A cm^2). The emission spectra are shifted to longer wavelengths because of the temperature narrowing of the band gap, with temperature coefficient dE_g/dT, determined from the spectra, equal to 3.6×10^{-4} eV/K.

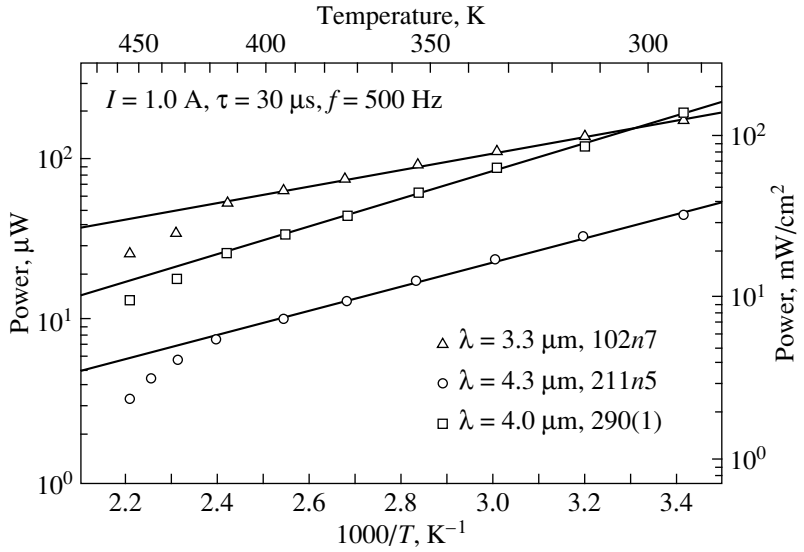

Fig. 2. Emission power vs. temperature for (λ = 3.3, 4.0, and 4.3 μm) LEDs at I = 1 A.

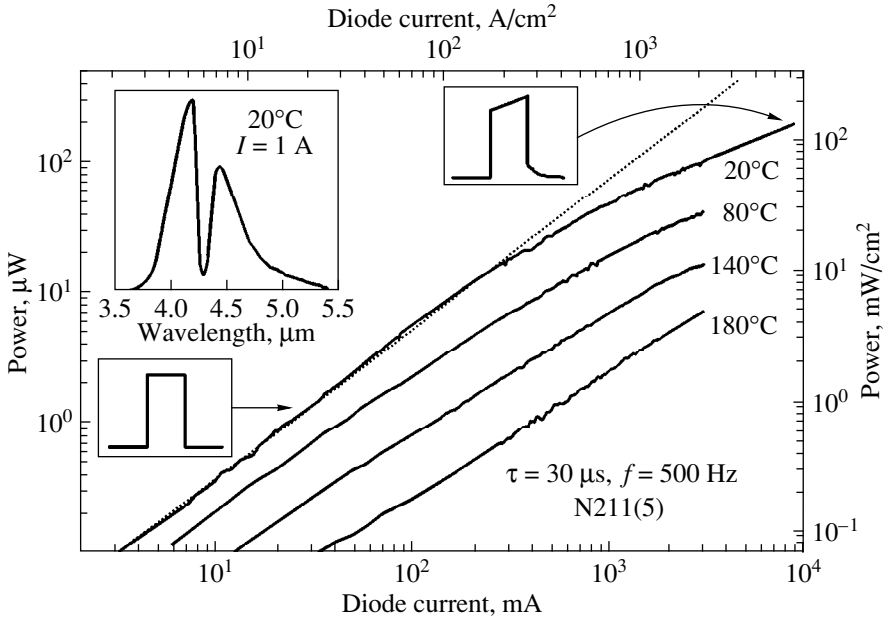

Fig. 3. Emission power vs. current for (λ = 4.3 μm) InAsSbP *p–n* homojunction LED at T = 20, 80, 140, and 180°C. Inserts: emission spectrum at T = 20°C, I = 1 A; oscillograms of the photodetector output signal.

3.2. (λ = 4.3 μm, 20°C) LEDs Based on the p–n Homojunction in an InAsSbP Graded Layer

Figure 3 presents the *L–I* characteristics of LEDs based on the *p–n* homojunction in an InAsSbP graded layer for T = 20, 80, 140, and 180°C; the insets show the LED emission spectrum at T = 20°C and at a working current of 1 A they also show the oscillograms of the photodetector output signals in the linear and sublinear portions of the *L–I* characteristic. The maximal output power at room temperature was 0.2 mW (140 mW/cm^2) at I = 8 A. The *L–I* characteristic is linear up to I = 250 mA, with a CE of 30 mW/(A cm^2) and a quantum efficiency of 0.02%; at higher currents, the *L–I* characteristic is sublinear; the CE falls to 9.4 mW/(A cm^2) at I = 8 A. Extending the pulse width to 500 μs diminishes the CE at $I \geq 1.5$ A, with the *L–I* curve leveling off at I = 3 A. In the linear and sublinear portions of the *L–I* characteristic, the shape of the signals at the photodetector output have the same specific features as for the (λ = 3.3 μm) LEDs (see the inset in Fig. 2). When the temperature is elevated from 20 to 180°C, the quantum efficiency, CE, and the output

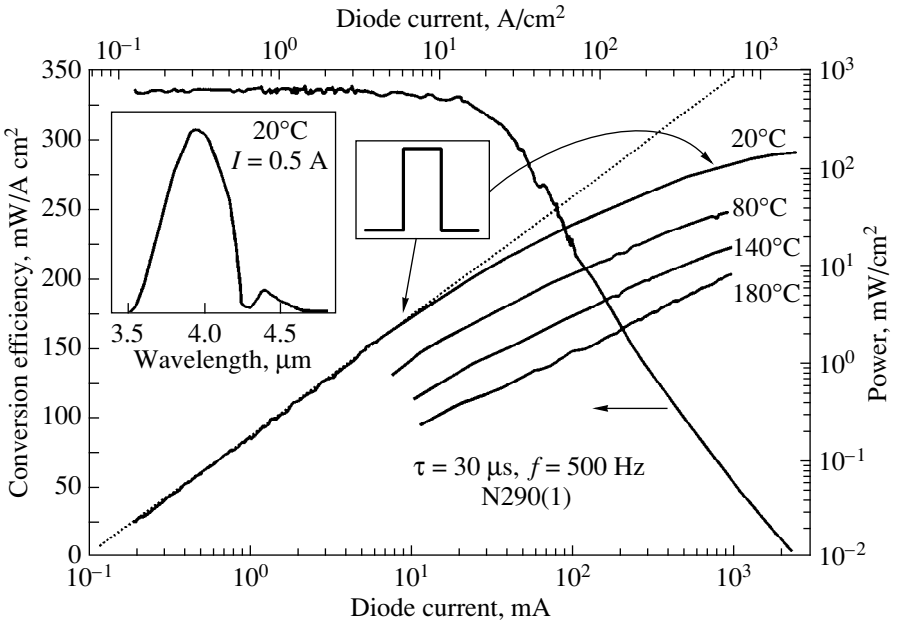

Fig. 4. Emission power vs. current for (λ = 4.0 μm) InAsSb/InAsSbP DH LED at T = 20, 80, 140, and 180°C, and the conversion efficiency vs. current at T = 20°C. Inserts: emission spectrum at T = 20°C, I = 1 A; oscillograms of the photodetector output signal.

power fall to 0.0014%, 5 mW/(A cm^2), and 2.5 μW (I = 1 A), respectively (see Fig. 2). The emission spectra are shifted to longer wavelengths owing to the temperature narrowing of the band gap with a temperature coefficient dE_g/dT of 3.5×10^{-4} eV/K.

3.3. (λ = 4.0 μm, 20°C) InAsSb(Gd)/InAsSbP DH LEDs

Figure 3 presents the L–I characteristics of InAsSb(Gd)/InAsSbP DH LEDs at T = 20, 80, 140, and 180°C, and the dependence of the CE on the current at T = 20°C; the insets show an emission spectrum at T = 20°C and I = 1 A, and oscillograms of the photodetector output signals in the linear and sublinear portions of the L–I characteristic. The maximum emission power obtained at room temperature was 0.23 mW (156 mW/cm^2) at I = 2.5 A. The L–I characteristic is linear up to I = 20 mA (current density j = 15 A/cm^2), with a CE equal to 340 mW/(A cm^2) and a quantum efficiency of 0.2%. Extending the pulse width to 500 μs has no effect on the L–I characteristic. The shape of the photodetector output pulse remains rectangular in both linear and sublinear portions of the L–I characteristic (see the inset in Fig. 4). When the temperature is elevated from 20 to 180°C, the quantum efficiency and the output power decrease to 0.017% and 12 μW (I = 1 A), respectively (see Fig. 2).

3.4. Stability of λ = 3.3 μm LEDs

Figure 5 presents data on the long-term variation of the properties of the (λ = 3.3 μm) LEDs. The upper graph shows the times for which the LEDs under study operated at several ambient temperatures. The samples operated at currents I = 0, 0.5, 1, 2 A for 150 h at room temperature, 450 h at T = 130°C, and 800 h at T = 180°C. The LEDs were cooled to room temperature and heated again to T = 130°C eight times and to 180°C three times. The lower graph shows the output power as a function of the working time. As can be seen, the output power decreased, on average, by 25% after 1400 h of operation. It is noteworthy that the working current strength has no effect on the degradation of the LEDs. With increasing working time, the reverse currents at a bias U = 1 V increased from 0.5–1 mA (0 h) to 3–4 mA (1400 h). On "cleaning" the sample surface by etching in CP-4, the reverse current returned to its initial values, and the output power tended to regain its initial value: P(1400 h) = (0.85–0.9)P(0 h).

4. DISCUSSION

Figure 6a presents the spectral dependence of the CE at T = 20°C for the (λ = 3.3–5.5 μm) p–n homojunction and DH LEDs. The experimental value corresponding to λ = 5.5 μm was obtained with an InAsSb LED similar to the one described in [5]. As can be seen, the CE of p–n homojunction LEDs decreases exponentially with increasing wavelength, presumably because of the growing contribution from nonradiative Auger recombination in the materials with narrower band gaps.

The L–I characteristic of p–n homojunction LEDs is linear up to currents of 0.25–1 A; at higher currents, the CE decreases. The LED emission spectrum is the sum

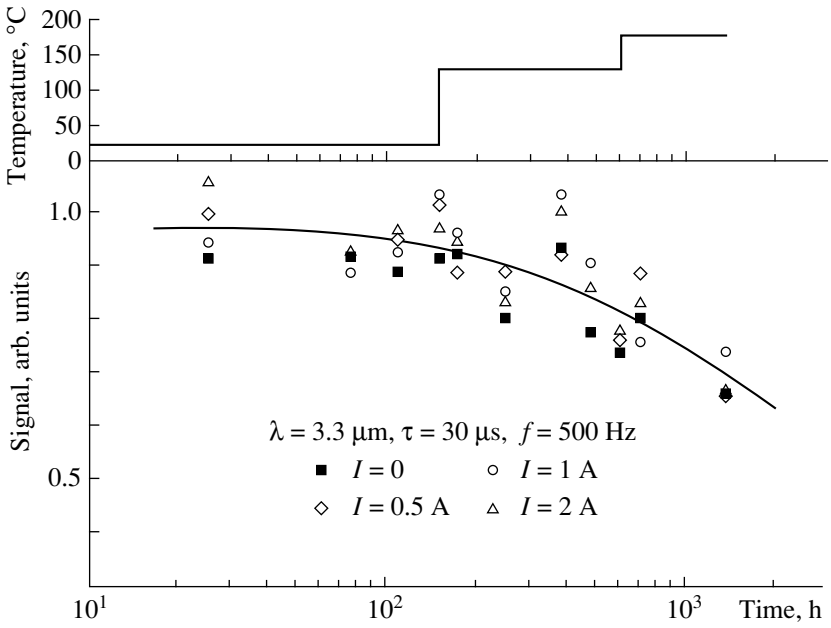

Fig. 5. Degradation of (λ = 3.3 μm) LEDs at *I*, A: 0 (2 samples), 0.5 (2 samples), 1 (2 samples), 2 (4 samples). *T* = 20, 130, and 180°C.

of the EL spectrum and the spectrum of a heated body. Consequently, the emission decay after the pumping current pulse has ended, typical of the sublinear portion of the *L–I* characteristic, indicates that they LED is warming up. The presence of a "thermal signal" is also manifested in the rise in the emission intensity during the pulse (i.e., in the sawtooth shape of the optical signal). It is noteworthy that the thermal signal decays in a very short time owing to the high thermal conductivity of III–V materials. Evaluations taking into account the thermal signal and the overlapping of the heated-body spectrum with the spectrum of HgCdTe photodetector sensitivity demonstrated that during a 30-μs pulse the LED warms up by ΔT = 20–50°C. The comparison of the warming-up value obtained with the temperature dependence of the emission power suggests that it is the warm-up that makes the decisive contribution to the decrease in the CE at high currents. It should be noted that the design of the (λ = 3.3 μm) LEDs is not the optimal, since it includes a relatively thick (~100 μm) *p*-InAs layer giving rise to high series resistance and making the active region lie farther from the heat sink. Both these features contribute to LED warm-up. In contrast, the *p*-layer thickness in the longer wavelength (λ > 4 μm) LEDs is less than 10 μm, which, combined with higher conductivity of *n*-layers, provides a series resistance 2–3 times lower compared with that in the (λ = 3.3 μm) LEDs. In addition, the proximity of the heat sink for the LEDs mounted on the holder with the *p*-layer underneath should ensure good heat removal and make the output parameters of LEDs independent of the duration and amplitude of the pumping current pulses.

Indeed, the specific behavior described above, typical of LEDs heated by pumping current, was not observed in the (λ = 4.0 μm) LEDs. The record-breaking CE value of 340 mW/(A cm^2) was obtained in a (λ = 4.0 μm) InAsSb/InAsSbP DH LED (structure 290(1) in Fig. 6a). The high efficiency of the DH LEDs is presumably due to the occurrence of the radiative recombination in the *n*-type active region, where the Auger recombination is weaker than in the *p*-type material which is "active" in homo-LEDs owing to the high electron mobility. Further, the electric confinement in a DH results in that the emission only occurs in a narrow region, less than 6 μm thick, and, therefore, lower self-absorption of light emitted from the active region would be expected. In homo-LEDs, the large width of the recombination region, determined by the electron diffusion length and constituting several tens of micrometers [6], leads to high absorption losses. Among the reasons for the high CE in DH-based LEDs, mention should also be made of the lower rate of non-radiative recombination, caused by the gettering effect of rare-earth dopants [3], which reduces the density of defects (non-radiative centers) and free carriers in the crystallizing solid phase.

However, the advantages of DH LEDs are limited to a range of small currents—I < 20 mA (15 A/cm^2)—with a substantial reduction in the CE observed at higher currents. Presumably, the electrical confinement in DH causes a significant increase in the concentration of injected carriers, with the corresponding enhancement of the Auger recombination. A similar situation was observed in [7], with a CE of 400 mW/(A cm^2) obtained for (λ = 3.45 μm) LEDs at currents below 3 mA

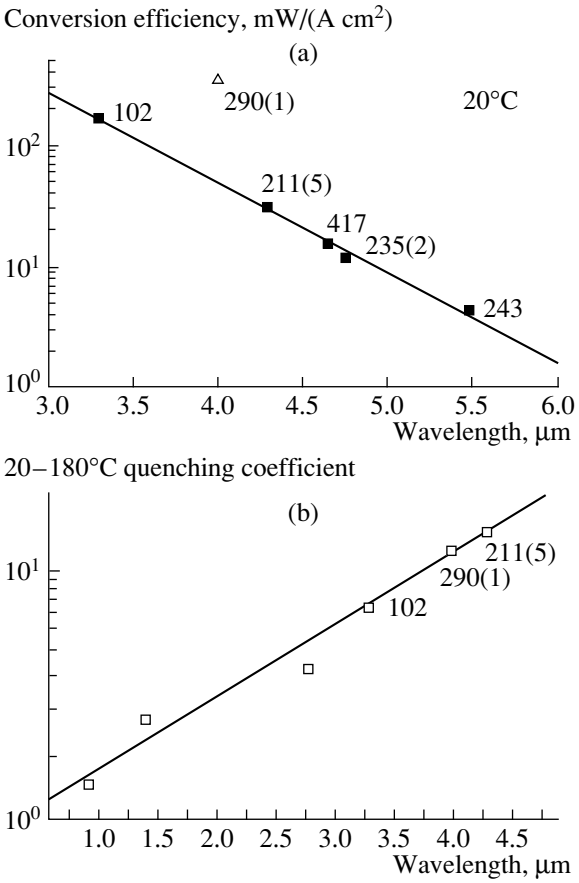

Fig. 6. (a) Conversion efficiency at 20°C and (b) power quenching coefficient (20–180°C) vs. wavelength, for DH (290 (1)) and *p–n* homojunction LEDs.

(10 A/cm^2). In homo-LEDs, the carriers are distributed over a larger volume, with the influence of the Auger processes being weaker and the sublinearity of the *L–I* characteristics, insignificant.

It is necessary to admit that the above considerations fail to explain in sufficient detail the behavior of the LED output power. For example, the active region warms up in (λ = 4.3 μm) LEDs, although these LEDs were mounted with their *p*-side on the heat sink. The dependence of the output power starts to level off with the pulse width increasing to 500 μs at a higher current than it does in the (λ = 3.3 μm) LEDs; on the other hand, the decrease in CE at short pulses starts at lower currents for the (λ = 4.3 μm), compared with the (λ = 3.3 μm) LEDs. In all probability, there are two reasons for the decrease in CE, namely, the warming-up and the Auger recombination, in the (λ = 4.3 μm) LEDs. It is noteworthy that the warming-up of the active region was also mentioned as the main factor limiting the power of (λ = 4.3 μm) LEDs at currents over 100 mA in [8].

The decrease in output power with increasing temperature in the range 20–180°C cannot be described by a single exponent, which indicates that several mechanisms are operative, e.g., Auger recombination and absorption by free carriers. Therefore, to describe the temperature variations of the LED power, it is convenient to introduce a "power quenching coefficient" (PQC) defined as the ratio of the room-temperature power to that at T = 180°C. Figure 6b shows the PQC for LEDs emitting in the range λ = 0.87–4.3 μm. The LED current was 2 A, the data for the wavelengths λ = 0.87 and 1.2 μm (T = 20°C) were obtained with GaAlAs/GaAs and InGaAsP/InP DH LEDs, respectively, and those for λ = 2.9 μm, with InGaAs *p–n* homojunction LEDs. As seen, the PQC grows exponentially with increasing wavelength. This indicates that the enhancement of the Auger recombination is the main reason for the power reduction with increasing temperature. It is worth noting that the PQC was 7 and 14 for the (λ = 3.3 μm) and (λ = 4.3 μm) LEDs, respectively, i.e., the halved values obtained in our previous study [1], which is due to the improved post-growth treatment.

5. CONCLUSION

To the authors' knowledge, the obtained output power of 1.33 mW (917 mW/cm^2, I = 8 A) is the highest achieved for (λ = 3.3 μm) LEDs; the obtained CE of 167 mW/(A cm^2) is nearly 1.5 times the value of 115 mW/(A cm^2), reported for (λ = 3.3 μm) LEDs in [9]. In (λ = 4.3 μm) LEDs, the obtained CE of 30 mW/(A cm^2) is close to the values reported for LEDs based on InAs/InAsSb superlattices: 18 mW/(A cm^2) [10] and 40 mW/(A cm^2) [11]. The CE of 340 mW/(A cm^2) obtained for the (λ = 4.0 μm) DH-based LEDs is seven times the CE for *p–n* homojunction LEDs expected from Fig. 6a for the same wavelength.

The CE and, correspondingly, the output power of *p–n* homojunction LEDs decreases exponentially with increasing wavelength, thus reflecting the enhancement of the nonradiative Auger recombination with a narrowing band gap in the active region. The decrease in the CE and the output power with increasing current in *p–n* homojunction LEDs is mainly due to the warming-up of the LED's active region, while the leveling-off of the *L–I* characteristic in the DH LEDs has a nonthermal nature.

When the wavelength increases, the temperature quenching of the LED output power is enhanced, which reflects the enhancement of the Auger recombination with the narrowing of the band gap.

ACKNOWLEDGMENTS

We are grateful to Schlumberger Oilfield Services Co. for their support of this study.

This study was supported by the US Foundation for Civil Research and Development for the CIS countries.

REFERENCES

1. M. Aĭdaraliev, N. V. Zotova, S. A. Karandashev, *et al.*, Fiz. Tekh. Poluprovodn. (St. Petersburg) **34** (1), 99 (2000) [Semiconductors **34**, 104 (2000)].
2. M. Aĭdaraliev, N. V. Zotova, S. A. Karandashev, *et al.*, Pis'ma Zh. Tekh. Fiz. **17** (23), 75 (1991) [Sov. Tech. Phys. Lett. **17**, 852 (1991)].
3. N. V. Zotova, S. A. Karandashev, B. A. Matveev, *et al.*, Fiz. Tekh. Poluprovodn. (St. Petersburg) **33** (8), 1010 (1999) [Semiconductors **33**, 920 (1999)].
4. S. Kim, M. Erdtmann, D. Wu, *et al.*, Appl. Phys. Lett. **69** (11), 1614 (1996).
5. M. Aĭdaraliev, N. V. Zotova, S. A. Karandashev, *et al.*, Pis'ma Zh. Tekh. Fiz. **24** (6), 88 (1998) [Tech. Phys. Lett. **24**, 243 (1998)].
6. http: //www.ioffe.rssi.ru/SVA/NSM/Nano/index.html
7. M. J. Kane, G. Braithwaite, M. T. Emeny, *et al.*, Appl. Phys. Lett. **76** (8), 943 (2000).
8. A. A. Popov, M. V. Stepanov, V. V. Sherstnev, and Yu. P. Yakovlev, Pis'ma Zh. Tekh. Fiz. **24** (2), 34 (1998) [Tech. Phys. Lett. **24**, 596 (1998)].
9. M. K. Parry and A. Krier, Electron. Lett. **30** (23), 1968 (1994).
10. M. J. Pullin, H. R. Hardaway, J. D. Heber, *et al.*, Appl. Phys. Lett. **74** (16), 2384 (1999).
11. A. Allerman, R. M. Biefeld, and S. R. Kurtz, Appl. Phys. Lett. **69** (22), 465 (1996).

Translated by D. Mashovets

Semiconductors, Vol. 35, No. 5, 2001, pp. 605–607. Translated from Fizika i Tekhnika Poluprovodnikov, Vol. 35, No. 5, 2001, pp. 626–628.

PHYSICS OF SEMICONDUCTOR DEVICES

A New Structure of the CdS-Based Surface-Barrier Ultraviolet Sensor

S. Yu. Pavelets, Yu. N. Bobrenko, A. V. Komashchenko, and T. E. Shengeliya

Institute of Semiconductor Physics, National Academy of Sciences of Ukraine, Kiev, 03028 Ukraine

Submitted July 30, 2000; accepted for publication October 23, 2000

Abstract—High-resistivity CdS or ZnSe layers were grown in the CdS surface region during sensor fabrication. The results of comparative investigations are presented for known CdS ultraviolet sensors and $Cu_{1.8}S$–CdS junctions with interlayers. The layers incorporated in the space-charge regions reduce the tunnel diode currents by more than three orders of magnitude, with the high quantum efficiency of the structures being retained in the ultraviolet spectral region. © *2001 MAIK "Nauka/Interperiodica".*

The $Cu_{1.8}S$–CdS photoconverters are the most sensitive sensors of ultraviolet (UV) radiation. Having a high quantum efficiency, the CdS sensors rank below the best surface-barrier structures in electric parameters. In this paper, we report the results of developing and investigating a photoconverter structure, which makes it possible to considerably improve electrical characteristics of the CdS sensor while retaining a high photosensitivity.

The $Cu_{1.8}S$–CdS photoconverter constitutes a polycrystalline layer of cadmium sulfide onto which copper sulfide (its stable modification is $Cu_{1.8}S$ [1–5]) is sputtered in vacuum. Thicknesses of CdS and $Cu_{1.8}S$ layers are 7 μm and 15 nm, respectively. The structure indubitably incorporates a surface barrier: a pulling electric field is almost completely concentrated in the CdS photosensitive component owing to a strong asymmetry of conductivity (a hole concentration in $Cu_{1.8}S$ is $p = 5 \times 10^{21}$ cm^{-3} and an electron concentration in CdS is $n = 10^{15}$ cm^{-3}). The samples are illuminated from the $Cu_{1.8}S$ side. It should be stressed that, in contrast to the Schottky diodes, a highly degenerate $Cu_{1.8}S$ is used instead of a metal. The basic advantage of using a highly degenerate semiconductor consists in the possibility of the practicality of the photoeffect associated with generation of hot charge carriers [5]. Unsatisfactory electrical parameters of sensors are the consequence of the tunnel current shunting a junction. A high probability of dominance of the tunnel processes is caused by the multistage tunneling with the participation of deep levels in the space-charge region (SCR) [2–4].

In this paper, we propose to incorporate a thin ($\lesssim$0.1 μm) layer of a less defective material into the SCR for blocking the tunnel component. This is possible, for example, by introducing a high-resistivity CdS layer with a composition approaching the stoichiometric one in the SCR. Thus, the probability of tunneling is expected to be reduced as a result of the decreasing number of defects participating in the process of forming the tunneling current.

In correspondence with the above, we fabricated the following structure of the basic photosensitive layer. A low-resistivity ($n = 10^{15}$ cm^{-3}) CdS layer ~7 μm thick was grown on a metallic substrate by the quasi-closed-volume method; thereafter, a high-resistivity ($n = 10^{13}$ cm^{-3}) CdS layer $\lesssim$0.1 μm thick was deposited; a low-resistivity CdS layer was then grown again. On the structure obtained, a barrier-forming $Cu_{1.8}S$ film was deposited. The SCR extent was ~0.7 μm. The thickness of the high- and low-resistivity layers were ~0.1 μm; i.e., they were completely within the SCR.

In the case of CdS sensors, the interlayer blocking the tunnel component of current can also be formed from zinc selenide (a wide-gap II–VI compound). Actually, the ZnSe high-resistivity layer deposited in the common technological cycle can be obtained without violating the basic parameters of the technological process of depositing CdS. In addition, it is of prime importance that ZnSe forms a continuous series of solid solutions $(CdS)_x(ZnSe)_{1-x}$ with CdS [6]. Thus, growing ZnSe on CdS with a transition variable-gap layer, we can prevent the formation of additional defects in the SCR associated with a mismatch between the crystalline lattices of ZnSe and CdS.

The photoconverter with a ZnSe intermediate layer was fabricated similar to those described above with the mandatory growth of the low-resistivity layer. The role of the low-resistivity interlayer was discussed previously [7, 8]. The main requirements to this layer are the following: it must be reasonably thin to avoid screening the contact difference of potentials as well as to provide the sufficient pulling electric field near the illuminated surface and, consequently, to preserve a high quantum efficiency.

Below, we report the results of comparative investigations of the $Cu_{1.8}S$–CdS junctions obtained using the

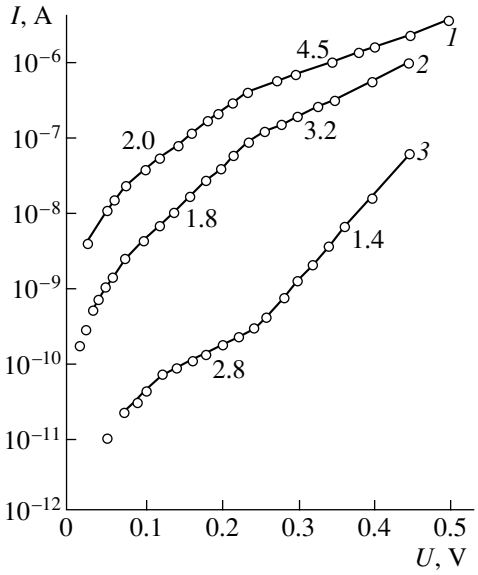

Fig. 1. Forward current–voltage characteristics of the $Cu_{1.8}S$–CdS junctions: (*1*) without intermediate layers, (*2*) with high-resistivity CdS layer, and (*3*) with a ZnSe layer. Values of β are indicated.

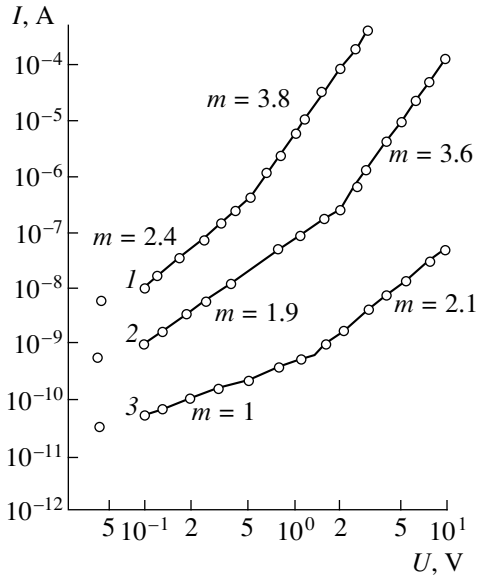

Fig. 2. Reverse current–voltage characteristics of the CdS sensors: (*1*) without intermediate layers, (*2*) with an intermediate high-resistivity CdS layer, and (*3*) with an intermediate ZnSe layer.

known technologies [1–5, 7, 8] and the $Cu_{1.8}S$–CdS junctions with high-resistivity interlayers. We studied the forward and reverse current–voltage (*I–V*) characteristics *I*(*U*) and the spectra of external quantum efficiency $Q(\lambda)$.

In Fig. 1, we show the forward *I–V* characteristics, which can be functionally written as $I = I_0\exp(\alpha U)$, where $\alpha = e/\beta kT$ if the thermal processes are dominant. Values of β (shown in Fig. 1) for curves *1* and *2* and an unusual variation in the slope of the *I–V* characteristic on the semilogarithmic scale (when the slope of straight lines decreases instead of increasing with the forward voltage) are typical of the junctions with *p*-$Cu_{1.8}S$ [2] in which the recombination–tunneling currents are prevalent. The presence of a high-resistivity CdS layer in the SCR reduces the shunting currents almost by an order of magnitude compared to the structure without a high-resistivity CdS layer (curves *2* and *1*, respectively).

The aforementioned currents decrease by more than three orders of magnitude if a ZnSe interlayer is used. Furthermore, as can be seen from Fig. 1 (curve *3*), for bias voltages $U > 0.3$ V, the overbarrier dark currents for which $\beta = 1.4$, $I_0 < 10^{-12}$ A (the sample surface area is 25 mm^2) prevail.

Special features of the reverse *I–V* characteristics (Fig. 2) are also indicative of a decrease in the currents as a result of the decreasing probability of tunneling. For the reverse *I–V* characteristics, the current can be written as $I \propto U^m$. In Fig. 2, two portions with parameters of *I–V* characteristics inherent in the junctions of this type [3] are observed for straight lines *1* and *2*: prebreakdown portions with $m = 1.9$–2.4 and the portions of soft tunnel breakdown with $m > 3.5$. When the ZnSe interlayer is used, there is no tunnel breakdown ($m < 3$, curve *3*) up to the bias voltage $U = 10$ V. For these structures, the generation currents with $m = 1$ are dominant up to $U = 1$ V. As can be seen from Fig. 2, for $U = 1$ V, the current decreases by four orders of magnitude compared to the junctions without the high-resistivity interlayers (curve *1*).

In Fig. 3, we show the spectra of the external quantum efficiency of CdS sensors. Curve *1* is a typical spectrum for efficient CdS-based photoconverters. Curves *2* and *3* are the spectral distributions of sensitiv-

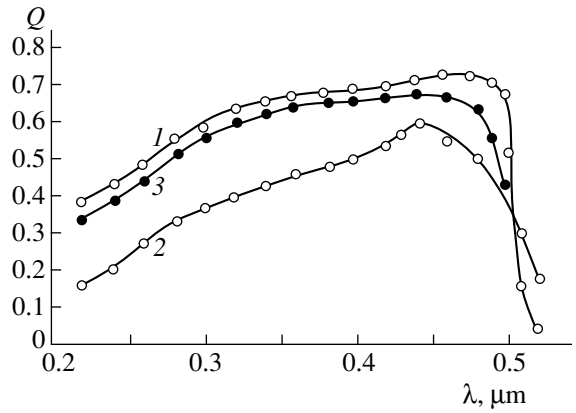

Fig. 3. Spectral distribution of quantum efficiency $Q(\lambda)$ for the $Cu_{1.8}S$–CdS surface-barrier sensor: (*1*) without high-resistivity intermediate layers, (*2*) with a high-resistivity ZnSe layer, and (*3*) with a low-resistivity layer and a ZnSe layer.

ity of junctions with only the high-resistivity ZnSe and the photoconverters with intermediate high-resistivity ZnSe and low-resistivity CdS layers, respectively. It can be seen that the presence of the low-resistivity surface layer considerably enhances the quantum efficiency within the entire spectral region.

Thus, the investigations of the *I–V* characteristics and the spectra of quantum efficiency show that the consecutive growth of high- and low-resistivity layers arranged in the SCR of the surface-barrier contact makes it possible to considerably improve the electrical parameters and to retain a high quantum efficiency of the CdS sensors. It should be stressed that the *I–V* characteristic parameters attained in this study for the thin-film polycrystalline structures do not rank below those inherent in the best single-crystalline analogues. A high photosensitivity and optimal electrical characteristics close to the limiting ones make the developed structures the best among the known UV sensors.

REFERENCES

1. V. N. Komashchenko, S. Yu. Pavelets, and G. A. Fedorus, Poluprovodn. Tekh. Mikroélektron. **32**, 40 (1980).
2. S. Yu. Pavelets, T. M. Svanidze, and V. P. Tarasenko, Ukr. Fiz. Zh. **28**, 581 (1983).
3. S. Yu. Pavelets, T. M. Svanidze, and V. P. Tarasenko, Fiz. Tekh. Poluprovodn. (Leningrad) **17**, 1330 (1983) [Sov. Phys. Semicond. **17**, 843 (1983)].
4. Yu. N. Bobrenko, U. U. Kishyuk, K. U. Kolezhuk, *et al.*, Sol. Energy Mater. Sol. Cells **33**, 83 (1994).
5. Yu. N. Bobrenko, A. M. Pavelets, S. Yu. Pavelets, and V. M. Tkachenko, Pis'ma Zh. Tekh. Fiz. **20** (12), 9 (1994) [Tech. Phys. Lett. **20**, 477 (1994)].
6. I. B. Mizetskaya, G. S. Oleĭnik, L. D. Budennaya, V. N. Tomashik, and N. D. Oleĭnik, *Physicochemical Foundations of Synthesis of Semiconductor Single-Crystal Solid Solutions of II–VI Compounds* (Naukova Dumka, Kiev, 1986).
7. A. I. Marchenko, R. I. Marchenko, S. Yu. Pavelets, *et al.*, Optoélektron. Poluprovodn. Tekh. **17**, 85 (1990).
8. Yu. N. Bobrenko, A. M. Pavelets, S. Yu. Pavelets, and V. M. Tkachenko, Optoélektron. Poluprovodn. Tekh. **31**, 74 (1996).

Translated by V. Bukhanov

Semiconductors, Vol. 35, No. 5, 2001, pp. 608–611. Translated from Fizika i Tekhnika Poluprovodnikov, Vol. 35, No. 5, 2001, pp. 629–632.

PHYSICS OF SEMICONDUCTOR DEVICES

Impact Ionization Wave Breakdown of Drift Step Recovery Diodes

V. A. Kozlov*, A. F. Kardo-Sysoev, and V. I. Brylevskiĭ

Ioffe Physicotechnical Institute, Russian Academy of Sciences, Politekhnicheskaya ul. 26, St. Petersburg, 194021 Russia

** e-mail: alx@helen.ioffe.rssi.ru*

Submitted November 8, 2000; accepted for publication November 8, 2000

Abstract—High frequency IMPATT oscillations followed under certain conditions by reversible impact ionization wave breakdown of the p^+–n–n^+ diode structure have been experimentally observed for the first time in a drift step recovery diode operating in the avalanche breakdown mode after a fast voltage restoration of the p–n junction. © *2001 MAIK "Nauka/Interperiodica".*

The reversible impact ionization wave breakdown in semiconductors underlies the operation of at least two types of semiconductor devices incorporating the p^+–n–n^+ diode structure as an active switching semiconductor element. Devices of the first type, avalanche switching diodes [1], are in fact avalanche transit time diodes operating in the so-called TRAPATT (trapped plasma avalanche triggered transit) mode. These diodes, proposed as far back as 1967 [2], are currently used for microwave generation at frequencies of several GHz, with a pulse output power up to 10^3 W. The second type of the devices, known as silicon avalanche shapers (SAS), was proposed in 1979 after the discovery of reversible breakdown in semiconductors with the formation of a delayed impact ionization wave [3]. The devices of the second type are also widely used nowadays for the generation of extremely high-power high-voltage electrical pulses with amplitudes of tens of kilovolts and pulse powers over 10^7 W at voltage build-up times less than 10^{-10} s. In both types of diode structures, the impact ionization wave breakdown of the lightly doped base of the device is triggered by applying a short high-power overvoltage pulse from an external source to the initially reverse-biased p–n junction. In this case, the efficiency of the impact ionization wave formation is largely determined by the parameters of the external "triggering" pulse (mainly by its amplitude and form), by the initial reverse bias applied to the p–n junction, and by other factors (p–n junction temperature, illumination of the structure, etc.).

In this paper, we report the first experimental observation of the wave breakdown in p^+–n–n^+ diode structures in the mode when the bias applied to the p–n junction is switched from forward to reverse. In contrast to the modes described above, the pulsed reverse overvoltage across the structure is not produced by the triggering pulse from the external source, but is formed by the p^+–n–n^+ structure itself. The pulse of the reverse overvoltage across the p–n junction arises in the device during abrupt (in the matter of several nanoseconds) recovery of the blocking properties of the p–n junction after the depletion of the electron–hole plasma stored in the base layers of the p^+–n–n^+ structure during the injection phase of the forward-biased p^+–n and n^+–n junctions. This effect has been observed in the so-called drift step recovery diodes (DSRD) [4], for which the step recovery of the p–n junction blocking capacity is the basic mode of operation in circuits generating high-voltage nanosecond pulses [5].

In our experiments, we used DSRDs fabricated by the conventional diffusion technology on n-Si(111) wafers with a resistivity of $\rho \approx 35\ \Omega$ cm. The total thickness of the p^+–n–n^+ DSRD structures was ~250 μm, with the p^+–n and n^+–n junctions lying at depths of ~70 and 30 μm, respectively. The working area of the p^+–n junction was ~3.3 cm^2, the hole lifetime in the n-base at low injection level was ~40 μs, and the static voltage of the avalanche breakdown in a p–n junction was $U_{BR} \approx 1300$ V.

The DSRDs were studied in a discharge L–C oscillatory circuit commonly used to form nanosecond pulses in DSRD-based circuits (Fig. 1a). During the forward pumping phase $\tau_+ = 200$ ns long, the injection current flows through the p^+–n–n^+ DSRD structure, modulating the n-base conductance and leading to accumulation of the excess charge of injected carriers in the base (Fig. 1b). Beginning at the instant of time t_1, the diode current reverses and the charge stored in the structure starts to decay. In this stage, the electrical resistance of the diode remains low until the instant t_2, when the space-charge layer arising near the p^+–n junc-

1063-7826/01/3505-0608$21.00

tion cuts off the current flow through the structure in a time $\tau_R \approx W_R/V$. Here, W_R is the width of the space charge layer under the appearing reverse bias U_R, and V is the drift velocity of charge carriers in silicon. The parameters of the *L–C* circuits in Fig. 1a are chosen so that all the energy of the circuits is stored in the inductors L_1 and L_2 at the instant of time $t = t_2 = (3/2)t_1$. Then, with the current through the DSRD interrupted, the current in the *L–C* circuits starts to flow through the load resistance *R* connected in parallel with the diode. The switchover of the current into the load upon recovery of the blocking capacity of the p^+–n–n^+ structure is accompanied by a sharp increase in the voltage across the DSRD and the load to a value U_{max} that may exceed the U_{BR} of the diode structure. The overvoltage across the DSRD structures can be controlled by varying the amplitude of the current I_R interrupted at the instant t_2 and the load resistance *R*, since the maximum voltage across the load may reach a value $U_{max} = I_R R$ (if $U_{max} < U_{BR}$). The circuit used in the experiments allowed gradual variation of I_R in the range 50–400 A at $R = 30\ \Omega$, which enabled the breakdown mode for diodes with U_{BR} in the range 1–6 kV. Pulses of current through the DSRD and voltage across the p^+–n–n^+ structures during their switching were recorded using a Tektronix TDS-380 two-channel digital oscilloscope with 1-ns time resolution or an S7-19 high-speed oscilloscope when transient processes with duration less than 1 ns were to be analyzed.

Figure 2 presents oscillograms of voltage pulses across the DSRD and current through the p^+–n–n^+ structure in the stage of restoration of the blocking capacity of the p^+–n-junction after the decay of the charge accumulated in the base during the injection stage (the accumulation stage is not shown in Fig. 2). At the instant of interruption of the DSRD current with amplitude $I_R = 100$ A, the voltage across the p^+–n–n^+ structure does not yet exceed the voltage of avalanche breakdown of the p–n-junction and the voltage pulse is bell-shaped (curve *1*), which is typical of DSRD operation in circuits forming nanosecond voltage pulses. The rate of rise of the reverse voltage across the p^+–n junction on interrupting a 100-A current is $\sim 1.6 \times 10^{11}$ V/s. This is still far from the maximum possible value of $(dU/dt)_{max} = (1/2)[(E_{BR}/V_S)] \approx 6.5 \times 10^{11}$ V/s, where E_{BR} is the breakdown electric field for silicon, and V_S is the saturated drift velocity of charge carriers.

As the amplitude of the interrupted current increases, the rise in the voltage across the diode becomes faster owing to an increased drift velocity, which attains a value V_S at an interrupted current density of $j_{RS} = qN_DV_S$, equal to about 200 A/cm^2 for the DSRDs under study (q is the electron charge, and N_D is the donor concentration in the n-base of the p^+–n–n^+ structure). However, V is virtually close to the limiting

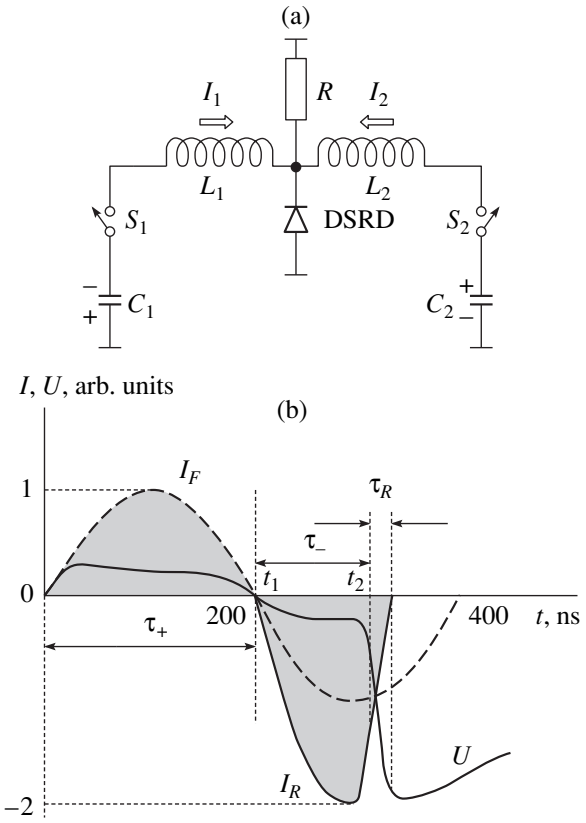

Fig. 1. (a) Simplified electric circuit for DSRD studies in the mode of nanosecond voltage pulse formation and avalanche breakdown in the p–n junction. C_1 and C_2 are storage capacitors that represent the sources of energy in the circuits; L_1 and L_2 are intermediate magnetic storages of energy in the circuits; S_1 and S_2 are power switches in the charging and discharge circuits, respectively; and R is the load resistor. (b) Diagrams of the current through and the voltage across DSRD operating in the mode of symmetric *L–C* circuits, with $L_1 \approx L_2$ and $C_1 \approx C_2$ (see Fig. 1a); τ_+, τ_-, and τ_R are, respectively, the durations of the charge pumping, charge decay, and DSRD current interruption and voltage rise stages; and I_F and I_R are the forward and reverse currents.

value for silicon at current densities over ~100 A/cm^2. On cutting off a current of 240 A ($j_R = 70$ A/cm^2), the dU/dt at the edge of the reverse voltage pulse across the p^+–n–n^+ structure is $\sim 5 \times 10^{11}$ V/s (curve *2*). In this case, the voltage across the $R = 30\ \Omega$ load, the maximum possible for the *L–C* circuit, could be ~3.5 kV with account taken of the energy loss for commutation. This exceeds the breakdown voltage of the p^+–n–n^+ structure. Consequently, the device connected in parallel with the load resistor starts to limit the voltage across the load to $\sim U_{BR} = 1.3$ kV and enters the mode of deep avalanche breakdown in the p^+–n junction with a breakdown current of ~150 A. In this mode, the voltage across the p^+–n–n^+ structure and the current through it oscillate at a frequency of ~280 MHz, with the oscillations decaying as the average voltage across

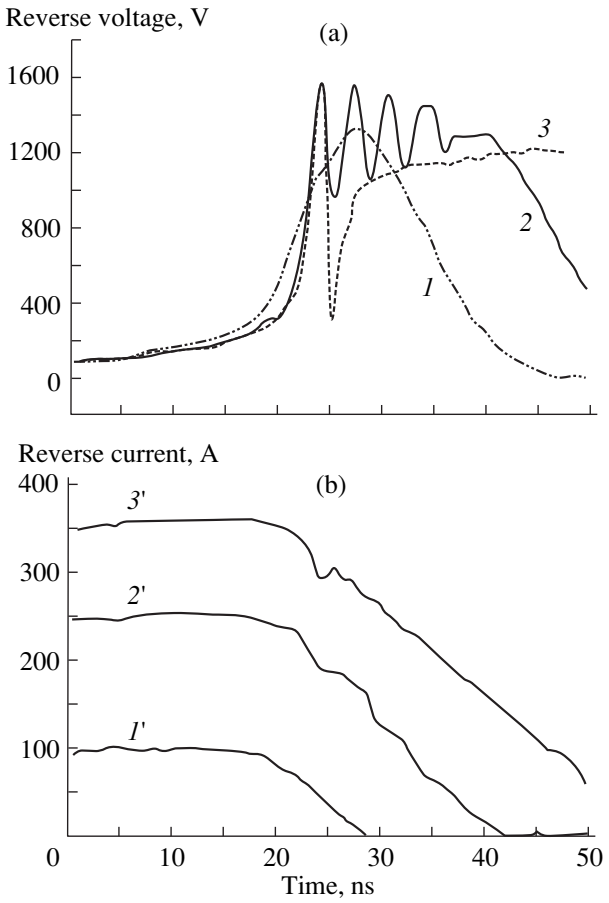

Fig. 2. Pulse oscillograms of (a) voltage across and (b) current through DSRD in the process of recovery of the p^+–n junction blocking capacity and its avalanche breakdown at several values of the reverse current I_R: (*1*, *1*') 100, (*2*, *2*') 240, and (*3*, *3*') 350 A. The static breakdown voltage of the p^+–n junction U_{BR} = 1320 V.

the p^+–n-junction decreases to ~U_{BR} of the diode. The observed character of oscillations and their frequency indicate the transition of the DSRD to the mode of IMPATT (impact avalanche transit time) oscillations, similar to those observed in the case of avalanche breakdown in power p–i–n diodes operating with an inductive load in the mode of the diode current reversal [6].

With the amplitude of reverse current through the DSRD increasing further and, with increasing consequently avalanche breakdown current density in the p^+–n junction in the IMPATT oscillatory mode, the oscillatory stage becomes longer and the rate of rise of the voltage across the p^+–n–n^+ structure reaches a value of ~6×10^{11} V/s at j_R = 100 A/cm^2. Beginning with this j_R value equal to ~$(1/2)j_{RS}$, even a minor further increase in the reverse current amplitude leads to an abrupt change in the nature of DSRD operation in the avalanche breakdown mode. As soon as the charge in the n-base of the structure decays and the first peak is reached, the voltage across the DSRD falls abruptly (in less than 1 ns) to a level of ~300 V and then rises gradually without IMPATT oscillations to a value ~U_{BR} of the p^+–n junction (Fig. 2, curve *3*). The abrupt fall of the voltage in curve *3* has a duration of ~1 ns because of the insufficient time resolution of the recording TDS-380 digital oscilloscope, whereas the value measured with an S7-19 high-speed S7-19 oscilloscope is 380 ps. Such a fast decrease in the voltage across the DSRD p^+–n–n^+ structure to a value substantially lower than the U_{BR} of the p–n junction suggests that the n-base of the structure is filled with electron–hole plasma with a carrier concentration of ~3×10^{13} cm^{-3} (provided that the carrier distribution in the volume of the n-base is uniform). In this case, the time of this filling is much shorter than the time of carrier drift through the n-base at a saturated velocity, the latter time being about 1.5 ns for the diodes under study. This indicates that the carrier generation and transport mechanisms in the p^+–n–n^+ structure change from avalanche transit to impact ionization wave breakdown, similar to that occurring in silicon avalanche shaper structures. It is worth noting that further studies in a special discharge circuit ensuring a reliable recording of this process in the course of time are necessary for the correct determination of the velocity of the impact ionization wave and a more detailed analysis of the observed effect. In the case in question, the discharge circuit, the DSRD, and the load have been designed for recording processes with a duration greater than 1 ns. The spurious inductance of the circuit does not allow precise measurements of processes with durations of about $t = L/R \approx$ 300 ps, which is comparable with the measured decay time of the voltage across the DSRD during the formation and traveling of the impact ionization wave.

To conclude, we have presented the first experimental evidence that drift step recovery diodes operating with avalanche breakdown in the p–n junction can enter the mode of IMPATT oscillations of the current through and the voltage across the device, with reversible impact ionization wave breakdown in the p^+–n–n^+ diode structure induced on further increasing the avalanche breakdown current density. A detailed study of the effect, including its stability and homogeneity over the structure area, its influence on the reliability of in-series connected DSRDs, and its possible practical applications, will be the goal of further experimental research.

ACKNOWLEDGMENTS

We are indebted to I.A. Smirnova for the fabrication of DSRD structures. This study was supported by the Russian Foundation for Basic Research, project no. 98-02-18217.

REFERENCES

1. M. Shur, in *Physics of Semiconductor Devices* (Prentice-Hall, Englewood Clifs, 1990; Mir, Moscow, 1992), Vol. 2, Chap. 6.
2. H. J. Prager, K. K. N. Chang, and S. Weisbrod, Proc. IEEE **55**, 586 (1967).
3. I. V. Grekhov and A. F. Kardo-Sysoev, Pis'ma Zh. Tekh. Fiz. **5**, 950 (1979) [Sov. Tech. Phys. Lett. **5**, 395 (1979)].
4. I. V. Grekhov, V. M. Efanov, A. F. Kardo-Sysoev, and S. V. Shendereĭ, Pis'ma Zh. Tekh. Fiz. **9**, 435 (1983) [Sov. Tech. Phys. Lett. **9**, 188 (1983)].
5. A. F. Kardo-Sysoev, V. M. Efanov, and I. G. Tchashnikov, in *Proceedings of the X Pulsed Power Conference, Albuquerque, 1995*, p. 342.
6. K. Mayaram, C. Hu, and D. O. Pederson, Solid-State Electron. **43**, 677 (1999).

Translated by D. Mashovets